EFFECTS OF BLOOM-FORMING ALGAE ON FOULING OF INTEGRATED MEMBRANE SYSTEMS IN SEAWATER DESALINATION

BY

DAVID ALLEN LADNER

B.S., New Mexico Institute of Mining and Technology, 2003
M.S., University of Illinois at Urbana-Champaign, 2005

DISSERTATION

Submitted in partial fulfillment of the requirements
for the degree of Doctor of Philosophy in Environmental Engineering in Civil Engineering
in the Graduate College of the
University of Illinois at Urbana-Champaign, 2009

Urbana, Illinois

Doctoral Committee:

Professor Mark M. Clark, Chair
Associate Professor Eberhard Morgenroth
Professor Steve Granick
Dr. Kishore Rajagopalan, Illinois Sustainable Technology Center

ABSTRACT

Combining low- and high-pressure membranes into an integrated membrane system is an effective treatment strategy for seawater desalination. Low-pressure microfiltration (MF) and ultrafiltration (UF) membranes remove particulate material, colloids, and high-molecular-weight organics leaving a relatively foulant-free salt solution for treatment by high-pressure reverse osmosis (RO). An integrated membrane system is severely challenged, however, when an algal blooms occurs. This research investigated important factors for and mechanisms of fouling by bloom-forming algae in integrated membrane systems.

In order to study RO fouling by algae, bench-scale testing protocols were evaluated. A method was developed to measure concentration polarization and intrinsic membrane permeability in a single experimental test. This laid the groundwork for accurately measuring flux decline from fouling. Natural seawaters (not under the influence of algal blooms) did not cause flux decline through buildup of organic foulants even though organic matter did deposit on the membranes.

Significant deposition of algae and algogenic organic matter (AOM) was observed on RO membranes. Dissolved AOM caused little flux decline, but when particulate material was present the flux declined by ten percent over 24 hours. The organic-matter cake layers that formed on the membrane surface caused some resistance to flow, but it was small compared to the intrinsic membrane resistance. Modeling showed an interplay between two fouling mechanisms: cake-enhanced concentration polarization (CECP) and hydraulic resistance. For foulant cakes with low porosity and small particle size, hydraulic resistance may be more important than CECP.

Foulant deposition on RO membranes was greatly affected by the feed spacer but was also affected by the shape of the permeate carrier. A permeate carrier with a fine mesh resulted in more spatially homogeneous foulant deposition and lower fouling propensity from AOM. A coarse permeate carrier caused foulants to deposit in a pattern defined by the feed spacer and flux decline was exacerbated. It is suggested here that both the feed spacer and the permeate carrier are important in determining the hydrodynamics that lead to foulant deposition.

Unlike RO membranes, low-pressure microfiltration (MF) and ultrafiltration (UF) membranes were severely fouled by algae. Pore blocking was the dominant mechanism for the early stages of MF and cake filtration dominated during later stages as irreversibly blocked pores became unavailable. Cake filtration was the dominant mechanism in UF where the pores were smaller and foulants were excluded.

Hydrodynamic shear applied to algal cells was detrimental to low-pressure filtration because of the release of highly-fouling organic matter. The highly fouling fraction was material large enough to be retained on a 0.22-μm microfilter but small enough that it was not removed by centrifugation or coarse (glass fiber) filtration. The algal cells themselves did not fall within this fraction since they were easily removed by centrifugation, but particulate material derived from broken algae did fall into the highly fouling fraction. Bacteria were also included in the highly-fouling fraction and were shown to be a major factor in fouling during an algal bloom. Adsorption of dissolved AOM was not a significant fouling mechanism on the hydrophilic membranes used here that are similar to the most common full-scale low-pressure membranes.

To Miriam and Isaac

ACKNOWLEDGMENTS

"No man is an Iland, intire of it selfe; every man is a peece of the Continent, a part of the maine."[1] I am the latest data point that supports this long-standing hypothesis; many people have contributed support and guidance for the work represented by this document. First and foremost, I thank my advisor Mark M. Clark for the trust he has placed in me over the last several years. He gave me the freedom to work in the manner I saw fit and gave me encouragement and guidance. In moments of discouragement he knew just what to say to get me back on the horse. More important than knowledge, Mark helped me gain experience, for which I am grateful.

My fellow graduate students provided great advice, thoughtful conversation, and quite a bit of food (at the office and in their homes). Manish Kumar and Won-Young Ahn are two fellow PhD students in the Clark research group to whom I will look up for the rest of my career. Other office mates were Adrienne Menniti, Kim Milferstedt, Katie Thompson, Li Liu, Xinyu Zhang, Fangqiong Ling, Nick Wiehardt, Sean Poust, Michelle Marincel, and Fabian Itel. Office #4125 was a great place to be because of these friends. Melvin Koh, Angela Koh, and Susana Kimura weren't lucky enough to be in #4125, but they did work in lab #4124 and I appreciate them, too. Shaoying Qi, manager of the Environmental Engineering labs kept everything running smoothly on the fourth floor and was the first source of help with equipment; along the way he became a good friend. Marvis Orzek knew answers to all my department-related questions and taught me a great deal about go-cart racing. Steve Daley is an amazing financial officer. Sue Lowry and Bobby Vance make an excellent ordering and reimbursing duo. Kathy Hepler sorted out many administrative fellowship issues. One's quality of life is highly dependent on the quality of people who surround them; my quality of life at Newmark Civil Engineering Laboratory was high.

Undergraduate students working with me were Nathan Lester, Paul St. Aubyn, Derek Vardon, Esvina Choo Mei Seng, and John Jurevis. On one hand they eased my dish-washing burden, and on the other they did important work I could not have

---

[1] Donne, John. 1624. Meditation XVII in *Devotions upon Emergent Occasions.*

performed myself. I wish them the best in their future careers and I hope I've had a positive impact on their view of Environmental Engineering.

Collaborators at MWH are thanked for their help in securing research funding and designing experiments to make them relevant to real-world problems. Manish Kumar first served in that capacity then Arun Subramani took over. Samer Adham led the group during our collaboration.

I am continually amazed at how willing people are to answer questions and provide support when I call them to ask for help, even when they are unrelated to the project. Robert Cheng and Tai Tseng from Long Beach Water Department supplied a seawater sample. Jess Brown and Chance Lauderdale from Carollo Engineers collected a red-tide phytoplankton sample. Gary Kirkpatrick at the Mote Marine Laboratory provided useful information about phytoplankton culture methods. Further culture information was given by Robert Andersen at the Provasoli-Guillard National Center for Culture of Marine Phytoplankton. Timothy Selle of Dow-Filmtech, Russ Steinhilber of Millipore, Rich Franks of Hydranautics, and Peter Hover of Koch supplied membranes. Bill Mickols of Dow-Filmtech provided helpful conversations about concentration polarization. Peter Eriksson of GE helped troubleshoot my membrane setup. There are certainly others who I've forgotten who patiently answered my phone calls and provided advice.

The first funding source for this project was obtained through the United States Department of the Interior, Bureau of Reclamation, Desalination and Water Purification Research and Development Program, assistance agreement #05FC811169. Additional support was provided through the United States Environmental Protection Agency, Science to Achieve Results (STAR) fellowship program. The WateReuse Foundation funded grant number WRF-06-014 to MWH on which the University of Illinois was a subcontractor. Lastly, the AWWA Research Foundation (now the Water Research Foundation) supported this work under funding agreement 04201.

My doctoral committee is thanked for their input and patience. They do not realize how much the short conversations I had with them have remained on my mind and steered my thinking. They are Eberhard Morgenroth, Kishore Rajagopalan, and Steve Granick.

My family is the reason I am here. My dad, Kenneth Ladner, taught me how to do unit conversions and an innumerable array of other practical, useful things. My mother Kathy Ladner gave me a home environment where I could flourish mentally and physically. My siblings Carol Roth and Bryan Ladner are my continual friends.

Lastly, but most importantly, I must thank my wife, Miriam Nibley Ladner. My life with her began at the same time my PhD program began. She stayed with me when her formal education finished so that I could finish mine. Now she is the mother of our beautiful son, Isaac. Research is great, but Miriam makes my life complete.

TABLE OF CONTENTS

1 INTRODUCTION... 1

2 LITERATURE REVIEW 4

2.1 MEMBRANE FOULING 4

2.1.1 Cake-enhanced concentration polarization.. 6

2.2 ALGAL BLOOMS AND MEMBRANE FOULING 8

2.2.1 Marine algal blooms 8

2.2.2 Industry experience with algal fouling 9

2.2.3 Algal fouling laboratory studies... 11

2.2.4 Effects of shear on algal fouling 12

2.3 STUDYING FOULING AT THE BENCH SCALE.................................. 13

2.3.1 Low-pressure membrane testing 13

2.3.2 High-pressure membrane testing 13

2.4 FIGURES 17

3 EXPERIMENTAL MATERIALS AND METHODS..................................... 18

3.1 REVERSE OSMOSIS.. 18

3.1.1 Bench-scale RO testing apparatus 18

3.1.2 Test Configurations... 19

3.1.3 Membranes.. 21

3.1.4 Algal fouling experiments.. 21

3.2 MICROFILTRATION AND ULTRAFILTRATION.................................. 21

3.2.1 Dead-end cell setup... 21

3.2.2 Membranes.. 22

3.3 SEAWATER 23

3.4 ALGAL CULTURE 24

3.5 ANALYTICAL METHODS 24

3.5.1 Algal and bacterial enumeration 24

3.5.2 Flow cytometry 26

3.5.3 Bulk fluorescence 27

3.5.4 Ultraviolet absorbance 27

3.5.5 Total organic carbon 27

3.5.6 Carbohydrates 28

3.5.7 Proteins 29

3.5.8 Size-exclusion chromatography 29

3.5.9 Visual image analysis of fouled membranes 29

3.5.10 Laser-scanning cytometry 30

3.5.11 Infrared spectroscopy 30

3.5.12 Scanning electron microscopy 31

3.5.13 Atomic force microscopy 31

3.6 TABLES 32

3.7 FIGURES 33

4 BENCH-SCALE EVALUATION OF REVERSE OSMOSIS 36

4.1 EVALUATION OF TEST CONFIGURATION OPTIONS 37

4.1.1 BaIReMT 37

4.1.2 Transient recovery 39

4.1.3 Full recycle 40

4.1.4 Comparison of configurations 40

4.2 TRANSPORT PARAMETER DETERMINATION 42

4.3 OSMOTIC PRESSURE DETERMINATION 44

4.4 SEAWATER FRACTIONATION EXPERIMENT 46

4.5 TRANSPORT PARAMETER RESULTS 47

4.6 SEAWATER FRACTIONATION RESULTS 49

4.7 SEAWATER SOURCE COMPARISON 50

4.8 CONCLUSIONS REGARDING BENCH-SCALE TESTING 52

4.9 TABLES 55

4.10 FIGURES 56

5 REVERSE OSMOSIS FOULING BY MARINE ALGAE 70

5.1 DESIGN OF EXPERIMENTS 71

5.2 FLUX DECLINE CAUSED BY ALGAE 72

5.3 AOM CHARACTERIZATION 72

5.4 FOULED MEMBRANE AUTOPSY 74

5.4.1 Visual and fluorescence image analysis 74

5.4.2 Scanning electron microscopy 76

5.4.3 Infrared spectroscopy 77

5.5 FOULING MECHANISMS 78

5.6 CONCLUSIONS REGARDING REVERSE OSMOSIS FOULING BY AOM 85

5.7 FIGURES 88

6 LOW-PRESSURE MEMBRANE FOULING BY MARINE ALGAE 99

6.1 FOULING BY DIRECT ALGAL FILTRATION 100

6.2 EFFECTS OF SHEAR ON LOW-PRESSURE MEMBRANE FOULING BY ALGAE 103

6.2.1 Shearing 103

6.2.2 Cell breakup characterization 105

6.2.3 MF/UF experiments for testing shear effects 107

6.2.4 Size fractionation 107

6.2.5 Determination of the level of shear 109

6.2.6 Effects of shear on algal cells 111

6.2.7 Effects of shear on flux 114

6.2.8 Flux modeling results 114

6.2.9 Organic-matter rejection 116

6.2.10 Fractionation Flux Results 118

6.2.11 Fractionation Analytical Results 119

6.3 THE IMPORTANCE OF BACTERIA 127

6.3.1 Simulated algal bloom 127

6.3.2 Membrane Filtration Tests 128

6.3.3 Algal bloom life cycle results 129

6.4 CONCLUSIONS REGARDING LOW-PRESSURE FOULING 131

6.5 TABLES 135

6.6 FIGURES 138

7 CONCLUSIONS AND SUGGESTIONS FOR FUTURE RESEARCH 165

7.1 OVERVIEW OF THE PROJECT 165

7.2 BENCH-SCALE EVALUATION OF REVERSE OSMOSIS 167

7.2.1 Conclusions 167

7.2.2 Future research 168

7.3 REVERSE OSMOSIS MEMBRANE FOULING BY MARINE ALGAE 169

7.3.1 Conclusions 169

7.3.2 Future research 170

7.4 LOW-PRESSURE MEMBRANE FOULING BY MARINE ALGAE 171

7.4.1 Conclusions 171

7.4.2 Future research 172

7.5 FINAL THOUGHTS 173

REFERENCES.. 174
AUTHOR’S BIOGRAPHY.. 183

1 INTRODUCTION

Seawater reverse osmosis (SWRO) is gaining momentum as a viable treatment technology to provide municipal drinking water. Currently only one municipal SWRO plant (Tampa, Florida) is operational in the United States, but pilot tests are being performed and plans are underway for full-scale facilities in southern California and the Texas Gulf Coast. SWRO is already a major source of drinking water for other areas of the world like the Middle East where water is scarce and energy (oil) is cheap. Further, nations like Spain and Australia are building and operating some of the world's largest full-scale SWRO plants to relieve their current water shortages.

One of the most important technical problems with SWRO is membrane fouling that reduces performance and increases operating cost. Feed water must be pretreated to remove the particulate and organic matter responsible for fouling. Filtration with low-pressure microfiltration (MF) and ultrafiltration (UF) membranes is one pretreatment technique that can provide good removal of foulants. These low-pressure membranes coupled with high-pressure reverse osmosis (RO) membranes constitute an integrated membrane system that can reliably provide drinking water from seawater.

An occasion when integrated membrane systems are particularly challenged is when marine algal blooms occur. The most common bloom-forming algae are unicellular photosynthetic flagellate species called dinoflagellates. Dinoflagellates have properties that make them good membrane foulants; they form blooms with very high concentration (on the order of 10^6 cell/ml), they swim and move vertically in the water column making them difficult to remove by settling techniques, and they contain a variety of proteins and polysaccharides that can absorb to membrane pores or surfaces. Both low-pressure pretreatment membranes (where water flows through pores) and high-pressure desalination membranes (where water diffuses through the polymer lattice) could be damaged by algal blooms.

This project sought a more complete understanding of how marine bloom-forming algae affect integrated membrane systems. The study began with emphasis on the high-pressure RO membranes. An important part of the early phase was to establish membrane testing protocols that could accurately evaluate membrane fouling at the bench scale.

Several techniques from the literature were attempted and the advantages and disadvantages of each method were explored. It became apparent that fouling data could be easily confounded in RO experiments because the measured flux was much more sensitive to salt concentrations at the membrane surface than it was to the degree of fouling. It was important to accurately determine both the level of concentration polarization and the inherent membrane resistance. A method was developed to determine these parameters in a single experiment using an appropriate transport model. This enabled evaluation of membrane fouling by natural seawaters and led the way for analysis of fouling by algae.

The objective of RO algal fouling experiments was to determine the extent to which membrane performance would be diminished in the presence of algae and their associated organic matter. In reports of pilot-scale studies it was unclear whether the observed flux decline was caused by algogenic organic matter (AOM) deposition or by biological growth enhanced by AOM. Here we focused on determining whether organic matter deposition was in and of itself sufficient for flux decline. Part of this work included developing techniques to determine the morphology of deposited materials including Fourier transform image analysis and laser-scanning cytometry (LCS). A side result of this effort was an interesting finding that the permeate spacer geometry was important in determining the way the feed spacer affected foulant deposition.

Regarding low-pressure pretreatment membranes, our first hypothesis was that the algal cells themselves would not be as important to fouling as the dissolved and colloidal AOM. If the cells were sheared and released their AOM to the water matrix, fouling would be exacerbated. Algae were exposed to hydrodynamic shear and cell breakup was characterized. Sheared and non-sheared samples were tested to determine changes in flux decline with shear and to determine how organic matter rejection diminished. Rejection by pretreatment membranes was an important consideration since any reduction in rejection would mean diminished performance in downstream RO membranes of an integrated system. In experiments with sheared algae it was possible to elucidate the highly fouling size fraction of AOM by separating the various fractions and performing subsequent flux decline experiments. These tests were also useful for investing whether fouling occurred by pore blocking due to material larger than the membrane pores or whether the dissolved organic matter was capable of causing flux decline by an adsorptive mechanism.

The last question posed in this dissertation came about as a real-world scenario was envisioned. During an actual bloom in a marine environment bacteria consume dying algae and bacterial numbers soar. How would low-pressure membranes be affected during this algal bloom life cycle? A bloom cycle was mimicked and both algal and bacterial numbers were tracked. Low-pressure filtration experiments were undertaken along the time frame of the mimicked bloom to determine how filtration would be affected.

2 LITERATURE REVIEW

The problem of fouling by algae in integrated membrane systems requires background in several arenas. It is useful to explore what is known about fouling phenomena in general from text-book presentations after decades of fouling studies and industry experience. Often the phenomena that are seen in the low-pressure regime (where fouling studies have been more extensive) are also applicable to the high-pressure case; both are treated together here. Mechanisms of membrane fouling like pore blocking, adsorption, and cake-enhanced concentration polarization are discussed.

Because of the applied nature of the algal fouling problem it is important to evaluate bench-, pilot-, and full-scale data from studies with natural waters. Most natural-water fouling tests are performed with fresh surface and river waters. Insight from some of those studies is presented here, but the focus is on seawater literature, which is sparser. Also sparse are reports of fouling by algae in seawater desalination systems, since seawater desalination for municipal drinking water is still rarely used (especially in the United States) and algal blooms occur sporadically. There have been enough cases, however, to suggest that algal blooms will become a bigger problem as seawater desalination becomes more wide-spread. Here we will present case studies of pilot and full-scale facilities that have experienced bloom problems. We will also explore the small body of research papers that have investigated algal fouling in the laboratory.

The body of knowledge from oceanographic and biological research is also useful. Much has been accomplished in the way of characterizing marine algal blooms like the notorious “red tide” events that plague coastal areas. Information about species types and bloom dynamics from oceanographic research can give clues to the engineering community on how to mitigate fouling problems by algal blooms.

Lastly, one of the thrusts of this research was to develop appropriate methods for studying RO fouling by natural seawaters. Literature on testing methods was explored.

2.1 MEMBRANE FOULING

Membrane fouling has been an important issue for as long as membranes have been employed for water treatment. Several textbooks that deal with water treatment and/or membranes contain sections or chapters on fouling and readers are referred there for a big-picture view of the body of fouling knowledge (Mulder 1991; Cheryan 1998; Duranceau 2001; Crittenden et al. 2005). A concise literature review of membrane fouling in water treatment was published recently that discusses advancements in fouling understanding over the past several years (Escobar et al. 2005). A short summary of this "textbook" knowledge about fouling is presented here, with a focus on information that is directly applicable to algal fouling problems.

Fouling is defined as the buildup of material on the membrane surface that causes a reduction in flux. Reversible fouling is flux decline that can be recovered with a backwash of the membrane. Irreversible fouling is longer-term fouling that is not recovered with a backwash. The distinction between reversible and irreversible fouling is only relevant for low-pressure membranes, since high-pressure membranes have such low intrinsic permeability that they cannot be backwashed.

Fouling depends heavily on the membrane material, with hydrophobic membranes generally fouling more readily than hydrophilic membranes (Laine et al. 1989; Jucker and Clark 1994; Howe and Clark 2002). Membrane surface morphology is also important; rough surfaces are usually more easily fouled than smoother surfaces (Elimelech et al. 1997; Vrijenhoek et al. 2001; Li et al. 2007). Low pH and high ionic strength can increase fouling, especially for extracted natural organic matter (NOM) (Jucker and Clark 1994; Braghetta et al. 1998). All material rejected by the membrane (including foulants) build up in the concentration polarization layer (DiGiano et al. 2000). When flux is increased, the balance of forces in the concentration polarization layer favors compaction of the foulant layer and increased concentrations; at some point, a "critical flux" may be reached. Beyond this critical flux, foulants interact more heavily with the membrane, often causing irreversible fouling (Zhu and Elimelech 1997).

Calcium has been shown to be quite important in natural-water fouling. Calcium appears to form a bridge between the membrane surface and the organic foulants (Ahn et al. 2008). Additionally, aluminum and silica have been identified in surface-water foulants (Howe et al. 2002). These results are consistent with previous research claiming that both inorganic and organic foulants should be studied simultaneously (Schafer et al. 2000). Calcium would be expected to be important in seawater studies, since it is so abundant; however, the high concentration of other salts may change the impact of calcium on fouling.

Natural waters contain particular size fractions of NOM that have more fouling propensity than the bulk NOM. In one lake water study, only a small fraction of dissolved organic matter (DOM) falling between 3 and 20 nm in size, caused fouling of UF membranes (Howe and Clark 2002). It has been shown that high-molecular-weight NOM consisting of biopolymers may be the main cause of fouling in wastewater treatment (Jarusutthirak and Amy 2006).

2.1.1 Cake-enhanced concentration polarization

One fouling mechanism unique to high-pressure salt-rejecting membranes deserves special attention here: cake-enhanced concentration polarization (CECP). As mentioned above, concentration polarization is the buildup of salts at the membrane surface. Salt buildup is balanced by back-diffusion of salts toward the bulk feed solution and back-diffusion is enhanced by crossflow. Under the CECP model the foulant layer hinders back-diffusion because the solute travel path is more tortuous and because crossflow is diminished (Hoek and Elimelech 2003). A diagram comparing concentration polarization to CECP is shown in Figure 2-1. Note that CECP would not occur in low-pressure membrane systems since salts are not rejected.

The first few studies to investigate the importance of CECP focused on monodisperse 100-nm latex particles as model colloidal foulants (Hoek et al. 2002; Hoek and Elimelech 2003). Flux decline was caused mainly by heightened osmotic pressure rather than by hydraulic resistance in the foulant layer. In natural seawaters, especially under algal bloom conditions, the foulants will not be monodisperse and it is unclear whether hydraulic resistance or CECP would dominate. Fouling by combined colloidal and dissolved materials is different than fouling by either colloidal or dissolved material alone (Li and Elimelech 2006).

Since the introduction of the CECP concept several investigators have applied the model to their membrane fouling studies. In most cases CECP is simply cited as a most-probable fouling mechanism with little effort at finding evidence for whether it was indeed present. Other workers, however, have verified that CECP does occur. Chong and

Fane (2007) used a novel NaCl tracer test whereby they found that CECP did in fact elevate the NaCl concentration at the membrane surface and cause decreased flux. The test was done in a dead-end mode where CECP would be more prevalent since crossflow was not present to aid back-diffusion. Lee et al. (2005) found that CECP was not always dominant; for their particular case with NF membranes NOM-calcium complexation that reduced hydraulic permeability was more important.

The CECP concept has been extended to biofouling with what was dubbed “biofilm-enhanced osmotic pressure” (Herzberg and Elimelech 2007). The new name adds no new insight except to stress that CECP is occurring in a biofilm. An interesting finding was that CECP was more dominant compared to hydraulic resistance for early biofilms and dead bacterial cells. With living cells in a well-established biofilm hydraulic resistance played a more important role. EPS filling the voids between bacterial cells caused a decrease in hydraulic resistance without greatly changing the level of CECP. This finding was supported with the evidence that salt rejection was the same for the two biofilms while the EPS-filled biofilm showed greater flux decline.

Some investigators have taken a mathematical approach at modeling the CECP phenomenon to determine how various parameters affect it. For a model biofilm CECP was enhanced because extracellular polymeric substances (EPS) retard back-diffusion of salts more than would be seen with hard-spheres particles (Kim et al. 2006). Tortuosity, (which is the reason that back-diffusion of salts is hindered) in a random, irregular structure like a biofilm is more drastic (Kim and Chen 2006).

Ng and Elimelech (2004) showed that CECP caused a decrease in trace-contaminant rejection; intrinsic membrane rejection was constant, but because the contaminants built up in the cake layer a higher concentration was available for permeation.

From the papers on CECP mentioned above, it appears that CECP is an important mechanism for flux decline in high-pressure systems. Hydraulic resistance is often downplayed as a mechanism, perhaps because the paper that introduce CECP emphasized that hydraulic resistance was significantly less important (Hoek and Elimelech 2003); however, hydraulic resistance was important in a few of the cases above, specifically for colloids coated with NOM and for biofilms with EPS. One of the challenges remaining in high-pressure fouling studied is to find ways to measure the relative contributions of CECP and hydraulic resistance to overall flux decline, especially in natural-water systems where the foulants are not well-characterized.

2.2 ALGAL BLOOMS AND MEMBRANE FOULING

2.2.1 Marine algal blooms

One potentially severe membrane foulant for seawater desalination is algae introduced to the feed water during a bloom. Marine algal blooms are caused by a few classes of phytoplankton, dinoflagellates being the most common. The dinoflagellate species *Lingulodinium polyedrum* has been the cause of massive red tide events in coastal California (Kahru and Mitchell 1998; Moorthi et al. 2006). In the Gulf of California, *Dinophysis caudate* and *Alexandrium catenella* have been identified (Lechuga-Deveze and Morquecho-Escamilla 1998). *Karenia brevis* (previously known as *Gymnodinium breve* and *Ptychodiscus brevis*) is a dinoflagellate causing toxic red-tide blooms in coastal Florida (Kirkpatrick et al. 2004; Kirkpatrick et al. 2006). *Heterocapsa pygmaea, Prorocentrum minimum*, and many others, have been identified (Johnsen et al. 1997; Trigueros and Orive 2000; Heil et al. 2005; Maso and Garces 2006). Even in waters where blooms are rarely seen, like the San Francisco Bay, dinoflagellate species can sometimes find just the right water quality and weather conditions to make a cameo appearance (Cloern et al. 2005).

Blooming dinoflagellates are in a size range (10 to 50 µm) that would easily pass through inlet screens. Their neutral buoyancy and ability to swim also make settling chamber removal impractical, though certain types of coagulation/flocculation or floatation-based methods may be worth considering (Edzwald 1993; Sengco et al. 2001; Pierce et al. 2004; Sengco and Anderson 2004). Dinoflagellates are easily rejected by microfiltration (MF) and ultrafiltration (UF) membranes, but a bloom with high cell concentration (on the order of 10^5 cells per ml) will quickly form a thick cake layer and impede water passage. If cells are damaged, either through natural death cycles, or through shear in the pumping system, they may release organic matter that passes through the pretreatment system to the RO membranes. Organic matter can directly foul the RO membrane and/or serve as substrate for bacterial species in biofouling.

As an algal bloom life cycle peaks and decays, a significant amount of organic material is released upon cell death (Whipple et al. 2005). Also, bacteria feed on the decaying material and release their own extracellular polymeric substance (EPS) that has the potential to foul pretreatment and RO membranes (Asatekin et al. 2006; Rosenberger et al. 2006). It is possible that the material from decomposition could have more of an impact on membrane fouling than the algal cells themselves.

2.2.2 Industry experience with algal fouling

Fouling by algae in full-scale membrane systems is a topic that has recently come to the forefront of the discussion among industry personnel working on seawater desalination. Much of the available knowledge is found in conference proceedings, news reports, and personal communications. These are presented here with a recognition that such sources are probably less reliable than peer-reviewed papers, but they give us a feel for the breadth of the problem and the mitigation strategies that are currently being employed.

MF and UF pretreatment systems are often effective for mitigation of fouling in seawater RO (Wilf and Klinko 1998; Drioli et al. 1999; Brehant et al. 2003; Teng et al. 2003). UF membranes, especially, are able to remove many organic constituents released by phytoplanktonic organisms; however, in one study even UF pretreatment did not prevent RO fouling at high flux (Glucina et al. 2000). It was assumed that the foulant was organic material small enough to pass through the UF membrane. From oceanographic studies, it is known that there exists a large fraction of seawater DOC smaller than the molecular-weight cutoffs of UF membranes (Aluwihare et al. 1997).

The author’s first knowledge about algal bloom problems experienced in seawater desalination came through discussions with representatives at the US Navy’s Port Hueneme, CA, desalination test facility and with their collaborator at the Orange County Water District, CA (Ishida 2006). They experienced a red tide event during testing of an integrated membrane system (MF followed by RO). The worst damage occurred on the MF membranes, which were subsequently taken off-line for extensive cleaning. The membranes were coated with an orange-yellow fouling layer and infrared absorption analysis revealed peaks for carbohydrates and proteins. It was suspected that large macromolecules, as opposed to the whole algal cells themselves, were the main fouling culprit.

The French water company Degrémont has been active in designing desalination plants and have published their ideas of combating algal blooms and low-quality water sources, in general. A pilot test for a proposed plant in Chile experienced algal bloom problems early in the testing phase (Petry et al. 2007). Dual-media filtration (DMF) was insufficient in removing algae. Dissolved air flotation (DAF) was added before the filtration step, but performance was still inadequate. The final design called for DAF followed by two stages of DMF in order to achieve sufficient water quality during algal blooms. With such aggressive pretreatment RO membrane fouling was not observed.

Degrémont representatives more recently reported their cost analysis of using MF or UF for RO pretreatment (Bonnélye et al. 2008). A conventional treatment train using DMF was more cost effective when the seawater quality was good, since DMF capital and operating costs were lower than MF/UF. For poor water quality as found during an algal bloom, however, MF/UF became economically viable because it was better at removing foulants and protecting the downstream RO elements.

In a Korean pilot study sand filtration was inadequate to remove red-tide algae so MF was installed (Kim et al. 2007). The MF membranes were able to effectively remove the algae and RO membranes performed well; however, the authors did not describe whether MF performance was affected by algae.

The most recent report found of a seawater desalination plant being affected by an algal bloom was a facility in Fujairah, United Arab Emirates (Sambidge 2008). DMF filters were overloaded with solids (algal biomass) during the event and the facility had to be shut down until the bloom subsided. The algal species in that case was a golden-brown *Heterosigma* species at a concentration of 1,800 to 2,400 cells/ml (Marquis and Trick 2008). *Heterosigma* is of the raphidophyte class which is similar to dinoflagellates in that it is unicellular and motile.

In several of the cases mentioned above DMF was not effective for algal removal, but in a Gibraltar seawater desalination plant chlorophyll-a and its breakdown product pheophytin were removed through a single-stage DMF. It is expected that the difference was due to foulant concentration. The Gibraltar plant did not experience bloom conditions so the low levels of algae present could be removed. It is important to recognize this dependence on concentration when considering the removal efficiencies reported for different systems.

An integrated membrane treatment plant using UF and RO for surface-water treatment in the Netherlands experienced increased biofouling of UF membranes when algal blooms were present (Kamp et al. 2000). Membranes were cleaned with a more alkaline solution to improve flux after the fouling event. Biofouling of the RO elements was also reported. Cell fragments (assumed to be bacterial/biofilm cells in this case) passing the UF system contributed to the RO-element biofilm growth.

The reports and case studies mentioned here are sufficient to conclude that algal fouling of integrated membrane systems is a problem in seawater desalination. RO membranes can be protected by MF and UF membranes, which are better at removing cells than conventional media filtration; however, the MF/UF membranes are then themselves fouled.

2.2.3 Algal fouling laboratory studies

A few investigations of membrane fouling by algae have been performed in the laboratory. Her et al. (2004) used blue-green algae (cyanobacteria) for NF fouling. They determined that AOM was more detrimental to the membranes than Suwannee River humic acid (SRHA). The AOM molecular weight was highly heterogeneous (high polydispersivity) and had a high hydrophilic fraction (57%) compared to SRHA. The authors concluded that the heterogeneously-sized hydrophilic material was responsible for the exacerbated fouling by AOM. The AOM was comprised of 68% protein, 22% carbohydrate, 5% lipid, and 3% chlorophyll *a* (according to the supplier); both proteins and carbohydrates were found in the foulant layer.

Fouling of UF membranes by the fresh-water cyanobacterial species *Microcystis aeruginosa* was studied to determine how cells interacted with NOM in the foulant layer (Kwon et al. 2005). Cells and NOM had a synergistic effect on fouling; the combined flux decline was greater than the sum of each component’s flux decline. It should be noted that though cyanobacteria are called blue-green algae, they are a bacterial species and their cell size (~3 μm) is smaller than most bloom-forming marine algae (10 to 50 μm). Still, it is possible that a synergistic effect between cells and organic matter occurs in any algal fouling event.

In an effort to optimize MF for removal of red-tide algae one team reported that crossflow filtration was more effective than dead-end, which would be expected for a high-biomass sample (Kim and Yoon 2005). Two algal species were used and different fouling propensity was observed; the dinoflagellate species *Prorocentrum micans* produced more soluble microbial products (SMP) and caused more fouling than the diatom *Thalassiosira* sp. even though *P. micans* was larger (35-70 μm) than *Thalassiosira* (10-50 μm). The authors hypothesized that SMP penetrated into the membrane matrix and blocked pores more dramatically than the whole algal cells on the membrane surface. Interestingly, however, the membrane used here was reported to have a pore size of 2 to 3 μm, which is quite large for microfiltration. SMP was detected by carbohydrate measurements alone and the size distribution was not determined. It is possible that the measured SMP contained particles in the 2 to 3 μm range that were not actually soluble, but that did enhance fouling.

2.2.4 Effects of shear on algal fouling

One concern that has been lightly addressed in algal fouling studies is the release of internal organic material when cells are broken by hydrodynamic shear forces. Shear is important in the release of toxins from some algal types (Himberg et al. 1989) and the release of taste-and-odor-causing compounds from others (Jenkins et al. 1967). Cells can withstand various levels of shear based on their cell wall structure (Joshi et al. 1996) which varies among different species. Some have a strong cell wall and thecal plates that constitute a type of "armor." Others, like the Gulf of Mexico red tide culprit *Karenia brevis* are unarmored and fragile enough to be broken apart by wave action (Kirkpatrick et al. 2004). Efforts have been made to quantify the shear forces experienced by algae for different pump and valve configurations (Jaouen et al. 1999; Vandanjon 1999) and to determine the individual species' shear threshold.

Small particles and colloidal material released from algae could be more detrimental to filtration than the whole algal cells. Small particles and colloids are likely to produce greater flux decline because of enhanced pore blocking and a less porous cake layer. Such a phenomenon has been seen in membrane fouling studies using bacterial organic matter (Shimizu et al. 1994). Similarly, studies have shown that coagulants forming more compact bacterial floc structures result in more dramatic cake-layer resistance than less-dense floc formations (Wang et al. 2008). Fouling could also be exacerbated with shear due to increased availability of dissolved and colloidal organic material that fouls by an adsorption mechanism. In MF and UF filtration of fresh surface waters it has been shown that the small dissolved colloidal fraction is the most important foulant due to its specific adsorptive interaction (Howe and Clark 2002). Some size fraction of algal organic matter could also have a specific interaction with membranes and be the principal foulant.

2.3 STUDYING FOULING AT THE BENCH SCALE

2.3.1 Low-pressure membrane testing

Testing of MF and UF membranes at the bench scale is fairly straightforward because of the low pressures involved (typically 5 to 50 psi). The simplest setup is a dead-end cell where water is fed to a flat-sheet membrane and pressurized with an air tank. Such a configuration has been used by many researchers and just a few examples are cited here (Ho and Zydney 2000; Lee et al. 2004; Koh et al. 2005). Cross-flow filtration with flat-sheet membranes has also been used (Lee and Clark 1998), but since most full-scale MF/UF installations are dead-end, crossflow is not representative. Full-scale systems now most often employ hollow-fibers. Bench-scale testing with small hollow-fibers is becoming more prominent. In a side-by-side comparison, flat-sheet tests sometimes give different results than hollow fibers, suggesting that hollow-fiber testing is better, since it is more like the full-scale system (Howe et al. 2007). However, the ease of dead-end flat-sheet tests make them more attractive.

2.3.2 High-pressure membrane testing

Testing of RO and NF membranes is inherently more difficult than MF/UF because of the high pressures required. Also, crossflow configurations are necessary to minimize concentration polarization and simulate the full-scale system. Because high-pressure tests require so much effort, alternate tests with low-pressure membranes are often used to determine water quality even for high-pressure installations. Membrane manufacturers often stipulate that source waters be pretreated to meet a specified Silt Density Index (SDI), a simple dead-end filtration test using a microfiltration membrane. This provides a relative indication of fouling potential, but gives no clear indication of fouling rate or long term performance (Wilf and Klinko 1998). Like the SDI, alternate methods such as the Modified Fouling Index (MFI) and the Mini Plugging Factor Index (MPFI) are based on batch microfiltration through a 0.45-μm microfilter, which is often insufficient for prediction of organic fouling (Yiantsios and Karabelas 2003). Another technique, the “UF-MFI” method employs an ultrafiltration membrane, instead of a microfilter (Boerlage et al. 2003). While this may be a more adequate predictor of fouling potential, it is still heavily affected by particulate deposition and gives little or no indication of the effect of dissolved constituents. A better index for determining fouling potential is needed. This will most likely be based on one or a few water quality parameters characterizing the nature and size of dissolved organic matter.

Currently in the seawater desalination field there is impetus to establish reliable methods for rapid evaluation of membranes and natural waters. Rapid bench-scale membrane tests (RBMT) have been used for evaluation of nanofiltration membranes in surface-water applications (Allgeier and Summers 1995; DiGiano et al. 2000) and similar tests have been employed for nanofiltration of seawater (Harrison et al. 2007). Bench-scale tests have been used to determine boron rejection for various membranes and operating conditions (Hyung and Kim 2006; Koseoglu et al. 2008). These studies highlight one of the attractive features of bench-scale studies: they can be used to quickly gain insight about membrane permeability, solute rejection, and fouling.

RO bench-scale tests with seawater have also been employed for determining the effects of various pretreatment methods on RO fouling potential (Kumar et al. 2006; Kumar et al. 2007). These tests were performed in eight hours with a scheme called the Batch Internal-Recycle Membrane Test (BaIReMT) that was first introduced for evaluating NF fouling (DiGiano et al. 2000). The BaIReMT method was designed to simulate later elements in a full-scale membrane treatment train. Later elements receive elevated foulant and solute levels because some amount of clean water is removed by the early stages. In the BaIReMT this is simulated through a unique setup where internal recycle lines (as opposed to complete recycle to the feed tank) allow solute concentrations to build up over time. The method was effective for fresh-water NF studies because natural organic matter (NOM) concentrations and membrane fouling increased over a short time period.

When the BaIReMT was employed for seawater RO, short-term flux decline was also apparent (Kumar et al. 2006). However, the results are suspect because in seawater reverse osmosis a buildup of solutes will dramatically reduce the flux not only by foulant accumulation, but simply through enhanced osmotic pressure. The osmotic pressure can be accounted for by plotting the “specific flux,” or the flux per unit driving force; however, the true driving force is somewhat difficult to ascertain because of concentration polarization from the increased salt concentration and osmotic pressure at the membrane wall. Determining the true driving force (applied pressure minus osmotic pressure) requires knowledge of the extent of concentration polarization in the bench-scale test system. Only then can the investigator determine whether flux variation in a BaIReMT is due to fouling, compaction, or simply increased osmotic pressure.

Various methods are used for determining concentration polarization in laboratory experiments. An early study in desalination via RO recognized the importance of determining the extent of concentration polarization and theoretical calculations were made based film theory (Sherwood et al. 1965). It was recognized that the extent of concentration polarization in real systems would depend greatly on local mixing. In order to improve performance predictions by film theory, semi-empirical models have been employed where viscous drag on channel walls and spacers, as well as directional losses due to flow changes around spacers have been taken into account in determining mass transfer coefficients (Da Costa et al. 1994). An “eddy constant” associated with the spacer configuration has also been employed (Bhattacharyya et al. 1990). Such semi-empirical models have proven effective in predicting concentration polarization for spiral-wound reverse osmosis elements where a sufficient number of experiments were performed to estimate parameters (Mariñas and Urama 1996). Computational fluid dynamics has recently been employed to determine the spatial variability of concentration polarization in laboratory test cells (Kim and Hoek 2005; Subramani et al. 2006; Lyster and Cohen 2007). Entrance and exit effects in small-scale systems caused significant variation in local concentration polarization and film theory methods were shown to be inadequate to account for these effects. Spacers installed for turbulence promotion also added to the complexity and difficulty in polarization calculation. While spacers induce an overall increase in flux by disturbing the concentration polarization layer (Ma and Song 2006), they also cause stagnation zones that could lead to locally elevated concentration polarization (Subramani et al. 2006). Stagnation areas in the corners of test cells are also of concern (Tarabara and Wiesner 2003).

Because of the complexity in modeling concentration polarization (and therefore flux) in real systems, transport parameters must be measured and not simply modeled. Typically, several experiments are needed in order to define the system (Mariñas and Urama 1996). At minimum, two filtration steps are typically employed: a clean-water test and a test with a known salt concentration as feed. For better accuracy, several experiments at different salt concentrations are used. From the clean-water test, one can find the intrinsic membrane permeability, while by comparing results from the salt-water tests, the extent of concentration polarization can be determined (Sutzkover et al. 2000; Kim and Hoek 2005). The clean-water test method for membrane permeability determination is somewhat suspect in high-pressure desalination because the flow regime is quite different from one test to the other; if flux is held constant for the two cases, the pressure will be different; if pressure is held constant, the flux will be different. It would be more appropriate to use a test that determines membrane transport parameters in the pressure and flux regime of interest. Just such a test is presented in Chapter 4.

2.4 FIGURES

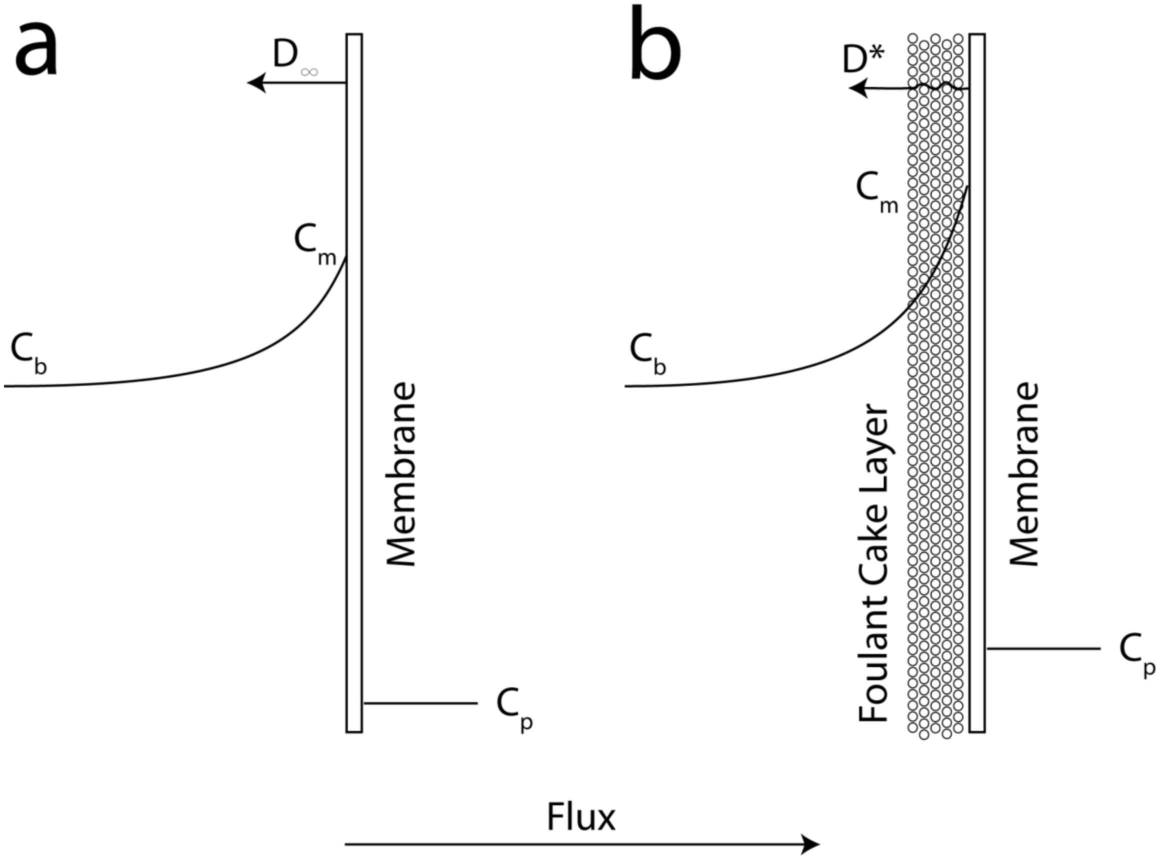

Figure 2-1. (a) Concentration polarization in operation of salt-rejecting membranes. C_b is the bulk salt concentration and C_m is the concentration at the membrane wall, which is always higher than C_b. Salt diffuses away from the membrane according to the bulk diffusion coefficient D_∞. C_p is the permeate salt concentration. (b) The cake-enhanced concentration (CECP) model predicts that salt diffusion is hindered when fouling occurs resulting in a lower diffusion coefficient D^*. Both C_m and C_p are elevated compared to the non-fouled case.

3 EXPERIMENTAL MATERIALS AND METHODS

3.1 REVERSE OSMOSIS

3.1.1 Bench-scale RO testing apparatus

The bench-scale reverse osmosis (RO) testing apparatus was designed according to the diagram in Figure 3-1. The key components were the membrane test cell, pump, motor, pressure gauges, temperature control unit, valve, balance, and data acquisition equipment. Specifications for these components are given in Table 3-1. The membrane test cell (SEPA II, GE Osmonics, Minnetonka, MN) is a commonly-used apparatus designed to simulate spiral-wound modules in industrial RO applications. Wetted parts of the cell were 316 stainless steel, as were the tubing and wetted parts of the high-pressure pump. This grade of steel was necessary because of the high corrosion propensity of seawater. The only components not comprised of 316 stainless steel were two Tygon tubes used for the inlet to the pump and the outlet of the temperature control heat exchanger. The motor chosen was a 2-horse power variable frequency drive motor capable of 20:1 turndown at constant torque. It was an inverter-duty motor, meaning the insulation was sufficient to prevent failure as the motor temperature rose under low-frequency conditions. For motor control, a phase inverter was used with a a 0-10 volt signal from the computer. A metering valve designed for low flow rates (around 800 ml/min) was installed in the concentrate line immediately after the membrane cell to provide pressure control.

Permeate flow rate was measured with a flow meter with a voltage signal output. The flow meter proved to be somewhat unreliable, however, because of interference from bubbles and drift over time. To ensure proper flux measurement the permeate was also fed into a collection vessel held by a balance. Balance measurements were sent to the computer through an RS232 signal. For continuous balance measurements, a self-emptying collection vessel was used, as depicted in Figure 3-1. Temperature control was provided by a heat exchanger made in the laboratory. Three meters of stainless steel tubing was coiled and connected to the concentrate outlet of the membrane cell. The coil was immersed in a water bath, with cooling water circulated through a temperature control unit. To ensure adequate cooling, pump feed temperature was recorded manually or via a voltage signal from a thermocouple and transmitter.

Data acquisition and control was achieved with a personal computer running Labview software. The controller program featured continuous monitoring of feed conductivity, pressure, and temperature, as well as permeate flow rate from the flow meter and permeate mass measurements from the balance. Automated speed control was implemented to maintain the target pressure in the event of pressure spikes. Data were recorded in ten-second intervals. Post-processing was performed with programs written in Matlab (Mathworks, Natick, MA).

3.1.2 Test Configurations

The first goal of the bench-scale membrane tests for this project was to evaluate fouling by natural waters under conditions similar to those found in full-scale desalination processes. One testing protocol found in the literature seemed to hold promise for accomplishing this goal, the batch internal recycle membrane test, denoted BaIReMT (DiGiano et al., 2000; Kumar et al., 2006). The main advantage of the BaIReMT was that full-scale recovery could be simulated. Full-scale recovery, defined as the amount of clean water obtained per amount of seawater treated, would be 30 to 50%. This is achieved with a process train of several reverse osmosis elements, each recovering a small percentage to make up the total. Bench-scale systems do not typically achieve such recovery because of their small membrane area. When high recovery is achieved at bench scale, the crossflow velocity must be set quite low—much lower than the full-scale system. The BaIReMT achieves a simulated high recovery with a realistic crossflow rate by recycling the concentrate and permeate streams in a well-defined way (described below). Early efforts in protocol optimization sought to implement the BaIReMT in a stable and reproducible manner. Limitations of the BaIReMT were discovered and alternate testing methods were employed. The optimization work resulted in several testing protocols that could be used, depending on the requirements of a given experiment. The details of each protocol, the results of experiments performed, and the positive and negative points of their implementation are explored below.

3.1.2.1 BaIReMT

The basic schematic of the BaIReMT is shown in Figure 3-2. This conceptual model is quite simple, but several key elements had to be incorporated in the design in order to make the RO unit function at the appropriate flow rates and pressures to mimic a full-scale RO system. The most important full-scale parameter to mimic was recovery, defined as the amount of clean water produced per salt water entering the system. Higher recovery meant higher salt and foulant concentration in the concentrate stream. Mimicking full-scale recovery, then, involved setting up the bench-scale system so that the membrane feed ran at the appropriate concentration (C_{mf}), which was always higher than the feed tank concentration (C_f). A mathematical model of the system was developed to determine the operating parameters necessary for a given recovery (see Section 4.1.1).

3.1.2.2 Transient recovery

The main advantage of the BaIReMT setup was that the feed salt concentration was elevated to mimic full-scale recovery. During the initial few hours of the test, however, the salt concentration increased to reach the desired set point. Instead of the complex setup of the BaIReMT procedure, with a break tank and a peristaltic pump, a new procedure was devised where a single small feed tank was used, with no break tank. The permeate was wasted for a period of time until the feed tank concentration increased to the desired level. Then the permeate tube was fed back to the feed tank for full recycle operation. With that, the break tank concentration was sure to remain constant, assuming no leaks, evaporation, or other upsets. This would allow for steady runs where fouling effects would be less varied. Also, it would provide a more stable system so that a minimal amount of modeling would be required to interpret the data. Further, flux measurements could be made more readily; when the permeate was wasted continuously, the operator only needed to switch beakers occasionally. This procedure was not given an acronym designation; it was simply called the transient recovery test. The flow schematics are given in Figure 3-3.

3.1.2.3 Full recycle

The full recycle test setup is shown in Figure 3-4. Both concentrate and permeate were recycled back to the feed tank in order to provide constant water quality in the membrane feed. This method was not capable of simulating full-scale recovery because the membrane feed concentration was always kept at its initial value.

3.1.3 Membranes

Reverse osmosis membranes were obtained from two manufacturers: SW30HR from Filmtec a wholly owned subsidiary of the Dow Chemical Company (Midland, Michigan), and SWC4 from Hydranautics a Nitto-Denko company (Oceanside, California). Membranes were received as flat sheets and were stored dry in sealed plastic bags protected from light. Coupons for experiments were cut and placed in DI water, then stored at 4˚C with DI water replaced regularly.

3.1.4 Algal fouling experiments

In order to test fouling by algae and their associated organic matter, a series of experiments was performed where RO membranes were challenged with a direct spike of algal-laden seawater. During the tests AOM was released as cells were sheared in the pump and valve. After the direct-spike test the water was filtered through an MF membrane (0.45-um mixed cellulose ester, Millipore, Billerica, MA). Filtration was performed on a flat-sheet cell (Amicon) in dead-end mode at 30 psi. Algal material caused a significant flux decline, so several runs were performed to filter all of the water sample. The microfiltered AOM sample was then re-run on the bench-scale RO unit with a fresh membrane coupon to determine the effects of dissolved AOM. Further details of these tests including flow rates, pressures, etc., are described in Chapter 5.

3.2 MICROFILTRATION AND ULTRAFILTRATION

3.2.1 Dead-end cell setup

MF and UF flux tests were performed at room temperature (21 ± 1°C) using circular membrane coupons in an unstirred dead-end cell. Two cell sizes were used, depending on the volume of feed to be processed. The larger cell (Amicon model 8050, Millipore) had a 50-ml fluid capacity and 11.9 cm^2 active membrane area. The smaller cell (Amicon model 8010, Millipore) had a 10-ml fluid capacity and 3.6 cm^2 active membrane area. Pressure varied according to the experiment, but 69 kPa (10 psi) for MF and 207 kPa (30 psi) for UF were typical (actual pressures used are given in the discussion of each experiment). Membrane coupons were soaked at least over night in deionized water to remove soluble processing chemicals. To provide extra support and resistance against membrane deformation a mesh screen was placed under the coupon. The screen was cut from the permeate carrier of a spiral-wound nanofiltration module (ESNA-1 LF, Hydranautics, Oceanside, CA). The membrane cell was fed by a one- or four-liter feed tank pressurized with a nitrogen cylinder. Membrane flux was determined by recording the mass of permeate collected over time on a top-loading balance (Model PB3002-S, Mettler-Toledo, Inc., Columbus, OH) using data acquisition software (Winwedge Standard, TAL Technologies, Inc., Philadelphia, PA) and a macro written into Microsoft Excel.

A clean-water flux run preceded each MF or UF filtration. The clean-water flux was tested by filtering ultrapure (18 MΩ-cm) water purified through a system of ion exchange and carbon adsorption cartridges (NANOpure, Barnstead-Thermolyne, Dubuque, IA). Clean-water flux was measured after accumulation of two liters of permeate (for 0.45-µm and 0.22-µm membranes) or after 30 minutes (for 0.1-µm, 100-kDa, and 30-kDa membranes). The clean-water flux run served as a control for the experimental setup; an abnormally high clean-water flux indicated an integrity breach and flux decline indicated contamination. Thus, if more than 5% variation in flux was seen over the last two-thirds of the clean-water run, the membrane was replaced. Experiments were performed at room temperature (typically 21 ± 1°C). Sample temperature for both clean water and fractionated samples was monitored to ensure it was within that range.

3.2.2 Membranes

A set of four membranes, two MF and two UF, constituted the majority of low-pressure membranes used during this research. MF membranes had pore sizes of 0.45 µm (cellulose acetate, Millipore) and 0.22 µm (cellulose acetate, GE Water & Process

Technologies, Minnetonka, MN). UF membranes had molecular-weight-cutoffs of 100 and 30 kilo-Dalton (kDa) (both were regenerated cellulose, Ultracel PLC, Millipore). These cellulose acetate and regenerated cellulose membranes are designated by the manufacturers as low protein binding membranes suited for filtration of biological samples. These low-fouling membranes were chosen for experiments where low adsorption was desired, like when pore blocking was studied and when organic-matter fractionation was performed.

Another membrane used had a 0.1-μm pore size and was made of material described as “hydrophilic PVDF” (Millipore VVLP). These membranes are similar in pore size and material to hollow-fiber membranes used in full-scale applications. The PVDF material is not itself hydrophilic but was modified to increase the hydrophilicity. The exact modification procedure used is proprietary, but is likely graft-polymerization of a polymerizable monomer such as hydroxyalkyl acrylate or methacrylate (Steuck 1984; Momtaz et al. 2005).

The final membrane used was a 0.45-μm membrane made of mixed cellulose esters (Millipore MCE). This was used for removal of particulate material in natural seawater samples and for other routine lab filtration.

3.3 SEAWATER

Seawater from San Diego Bay was collected by project consultants at MWH (Pasadena, California). Four 200-liter, low-density polyethylene (LDPE) barrels were collected and shipped via refrigerated carrier. The barrels were stored in a walk-in refrigerator at 4˚C. Other, smaller samples were collected from the West Basin Municipal Water District (southwest Los Angeles County, California), Carlsbad Desalination Project (Carlsbad, California), and Tampa Bay Desalination Plant in (Tampa, Florida). These samples were shipped over night in 20-liter LDPE collapsible containers in ice chests with cold packs. These were also stored in the walk-in refrigerator until use. Raw water quality was measured for West Basin, Carlsbad, and Tampa Bay seawater samples by MWH labs (Pasadena, CA). Methods used, as well as values obtained are given in Table 4-1.

Synthetic seawater was used for some experiments as an organic-free control. It was made by adding the major inorganic seawater species to deionized water in the following concentrations: 23.9 g/l NaCl, 4 g/l Na_2SO_4, 0.7 g/l KCl, 0.2 g/l $NaHCO_3$, 0.1 g/l KBr, 10.8 g/l $MgCl_2 \cdot 6H_20$, and 1.5 g/l $CaCl_2 \cdot 2H_2O$. The recipe was suggested by previous workers who were mimicking the composition of "standard seawater" defined to have a salinity of $35x10^{-3}$ (Grasshoff et al. 1983).

3.4 ALGAL CULTURE

The algal species used throughout this project was *Heterocapsa pygmaea*, designated CCMP1132, purchased from the Provasoli-Guillard National Center for Culture of Marine Phytoplankton (West Boothbay Harbor, ME). The initial sample was spiked into several culture tubes containing f/2 medium (Andersen 2005) prepared with 0.45-µm-filtered and autoclaved (121°C) San Diego seawater. Cultures were grown in glass bottles and Erlenmeyer flasks in volumes of 200 to 900 ml. They were exposed to a constant mercury-florescent light source (Sylvania Premium Cool White, 40W, 4100K) at a distance of approximately 30 cm. The light was attenuated with a plastic covering to yield an average intensity of 19 µmol photons m^{-2} s^{-1}. Growth was monitored weekly with a SpectraMax Gemini fluorescence microplate reader (Molecular Devices, Sunnyvale, CA). Cell concentrations were periodically verified with a hemacytometer and visible-light microscopy. A batch culture rotation was carried out by waiting two to four weeks for algae to reach a cell concentration of roughly 100,000 to 300,000 cells/ml then spiking a small volume of that culture into a fresh bottle of f/2 media at a dilution of 6:100 (i.e. 30 ml of algal culture into 500 ml of f/2 media). The batch culture rotation process was repeated throughout the time of the project.

3.5 ANALYTICAL METHODS

3.5.1 Algal and bacterial enumeration

Algal cells were counted manually via hemacytometry. Approximate 10 µl samples were placed on side-by-side grids (0.9 mm^3 volume per grid) of the hemacytometer (Hausser Scientific, Horsham, PA). Counts were performed with a visible-light microscope (Zeiss Jena Laboval, Maple Grove, MN) using a 10x objective and 10x eyepiece for at total of 100x magnification. Only whole, clearly-identifiable cells were counted even when material was present that appeared to be derived from cells.

Fluorescence microscopy was used to directly count and compare algal and bacterial cell concentrations. Preparation of slides began by filtering a small volume (150 to 2000 µl) of algal culture onto a 0.2-µm pore size, track-etched black polycarbonate membrane (Isopore, Whatman, Florham Park, NJ). A backing filter cut from a 0.45-µm membrane of mixed cellulose esters (type HAWP, Millipore) provided extra support. Filtration was performed using vacuum suction at about 2 kPa. After filtration 400 µl (enough to cover the 1.9 cm^2 active membrane surface) of a DAPI staining solution (1 mg/l of 4',6-diamidino-2-phenylindole in phosphate buffered saline) was applied for three minutes. The staining solution was then filtered through and the membrane was immediately placed on a microscope slide cleaned with 70% ethanol. Several drops of anti-fade solution (type AF1, Citifluor, London, United Kingdom) were placed on the membrane and a cover slip (also cleaned with 70% ethanol) was applied. The anti-fade solution adhered the cover slip to the slide with the membrane between. In some cases the slide was sealed with fingernail polish on two sides to prevent movement of the specimen, but later this was shown to be unnecessary.

Immediately after preparation of slides, algal cells were observed under the microscope (Zeiss Axioscope, Carl Zeiss AG, Maple Grove, MN). An X-Cite 120 fluorescent bulb (EXFO, Mississauga, Canada) was used for illumination. The filter set for algal detection (autofluorescence) was a Chroma 41001 (Rockingham, VT). In the set was an excitation filter with 480-nm center wavelength and 40-nm bandwidth, a beamsplitter with 505-nm longpass cutoff, and an emission filter centered at 535 nm with a 50-nm bandwidth. Images were captured using an Axiocam MRm digital camera (Carl Zeiss AG, Maple Grove, MN). Twenty-one images were collected for each slide using 100x magnification. Observation began at one edge of the active filter area and images were collected along a transect until reaching the other edge. Twenty-two images were typically collected along the transect.

After algal counts, bacteria were observed on the same slide. Magnification was switched to 1000x and immersion oil (Immersol 518 F, Zeiss) was placed between the objective and the slide. The filter set was switched to one optimal for DAPI stain detection (Chroma 31000). The set included an excitation filter with a 360-nm center and 40-nm bandwidth, a beamsplitter with 400-nm longpass cutoff, and an emission filter centered at 460 nm with 50-nm bandwidth. At least fifteen images were collected at random locations on the slide.

The number of cells on the membrane in most cases was counted by the operator. In some cases an image processing program written in Matlab was used. The program detected all pixel values above a certain threshold (set by the user) and found the total intensity of those pixels. Typically five images per slide were counted manually for use as a calibration. The user counted the number of cells present and entered the value. Then, the other images were automatically counted with the program using the calibration information. After the number of objects per image was determined, the data were adjusted to cell concentration using the known volume filtered and area per membrane. Several images were chosen at random and counted manually after analysis to verify the accuracy of automated counts. The variability associated with automated counting was always lower than the variability caused by random and non-uniform cell dispersion.

In some experiments only bacteria were enumerated. The procedure was as above but without the steps for algal enumeration. In other cases fluorescence microscopy was used simply to examine cells and capture images and the same procedure was used. Images were captured in grayscale mode and false color was added with a script written in Matlab.

3.5.2 Flow cytometry

Flow cytometry was used to count algae and broken particles. Light scattering measurements were indicative of particle size and morphology. A BD LSR II flow cytometer (BD Biosciences, San Jose, CA) was used with two illumination channels; a 488-nm argon-ion, air-cooled laser (Coherent, Santa Clara, CA) with a 530/30 bandpass filter was used for algal cell excitation, and a 633-nm, red He Ne Uniphase^{TM} Laser (JPS, Milpitas, CA) with a 735-nm longpass and 660/20 bandpass filter was used for detecting fluorescent calibration beads. The fluorescence data were analyzed using FCS Express flow analysis software (De Novo, Los Angeles, CA). Samples were prepared by adding

450 µl to 50 µl of 10-µm Flow-Check^{TM} Fluorosphere calibration beads (Beckman Coulter, Fullerton, CA) at a concentration of 1.35 x 10^6 beads/ml. The flow rate of the machine was measured by counting the number of bead events recorded in a given time period and calculating the volume processed using the bead concentration. Sample tubes were vortexed prior to analysis to ensure homogeneity.

Algal cells were identified in flow-cytometry data by their light-scatter and fluorescence properties. Cells had forward scatter greater than 200, side scatter between 250 and 500, 633-nm fluorescence greater than 300, and 488-nm fluorescence greater than 300; the numbers are unitless measures of the peak area for each cell signal. Separation between the algae and background particulate material occurred most dramatically on the 488-nm channel while separation between algae and calibration beads was best observed on the 633-nm channel. Based on the scatter and fluorescence signals, particles were gated and labeled accordingly. Hemacytometry was used to calibrate the flow cytometry counts and ensure that whole algal cells were properly distinguished from other material.

3.5.3 Bulk fluorescence

A fluorescence microplate reader (Molecular Devices, Sunnyvale, CA) was used for measurement of bulk sample fluorescence. Samples were measured in triplicate (300 µl each) in a 96-well plate. Excitation was set at 450 nm and emission was set at 680 nm with a longpass cutoff of 665 nm.

3.5.4 Ultraviolet absorbance

UV absorbance at 254 nm was measured on a UV-vis spectrophotometer (UV-2450, Shimadzu, Kyoto, Japan). Samples were measured in a 1-cm path-length quartz cell (QS 284, Fisher) and an identical cell with ultrapure water was used as a reference.

3.5.5 Total organic carbon

Total organic carbon (TOC) was measured with an analyzer using an oxidative combustion-infrared method (Shimadzu TOC-VCPN, Kyoto, Japan). A known volume of sample was injected into a combustion tube maintained at 680°C. Ultrapure air carried the sample through the combustion tube and past a platinum catalyst where the sample was oxidized to carbon dioxide. The carbon dioxide was measured by an infrared detector. A calibration curve made from potassium hydrogen phthalate TOC standards was used to determine sample concentrations.

3.5.6 Carbohydrates

Organic matter was also characterized as to its carbohydrate composition. Both monosaccharides and polysaccharides were measured using a procedure slightly modified from that of Myklestad (1997). Three reagents were prepared for the analysis, all with ACS-grade stock chemicals. Reagent A was 0.7 mM potassium ferricyanide (Fisher Scientific, Pittsburgh, PA) in 10-mM sodium hydroxide (Fisher) and 0.19-M sodium carbonate (Fisher). Reagent A was stabile, so one solution was used throughout the experiments. Reagent B was made in two parts. The first part was 5-M acetic acid (J.T. Baker, Phillipsburgh, NJ), 1.2-M sodium acetate (Fisher), and 0.2-M citric acid (Fisher). This solution was stabile and only re-made when depleted. The second part of reagent B was 2-mM ferric chloride (anhydrous, Fisher), which was prepared daily. Reagent C was 2.5 mM TPTZ (2,4,6-Tripyridyl-*s*-triazine, Sigma-Aldrich, St. Louis, MO) in 3-M acetic acid. This was also prepared daily. For monosaccharide measurement, one ml of sample was placed in a glass digestion vial (Hach, Loveland, CO) followed by one ml of Reagent A. The vial was capped and placed in a 105°C oven for 20 minutes. One ml of Reagent B was then added, followed by two ml of Reagent C. After 20 minutes of incubation in the dark at room temperature, the 595-nm absorbance was measured with a spectrophotometer (DR/4000U, Hach, Loveland, CO) blanked against deionized water. Standards of 0.25, 0.5, 1, and 2 mg/l glucose were prepared by serial dilution of a glucose stock solution (Ricca Chemical Co., Arlington, TX). To determine polysaccharide concentration, samples were hydrolyzed before measurement. A 0.9-ml sample was placed in a digestion vial followed by 0.1 ml of 1-M HCl. Vials were capped and incubated at 105°C for 24 hours, then neutralized by addition of 0.1 ml of 1-M NaOH. Measurement then proceeded as for monosaccharides. Glucose standards were treated alongside the samples.

3.5.7 Proteins

Protein concentration was measured with the bicinchoninic acid protein assay (Smith et al. 1985) using a prepared kit (Thermo Scientific). The protein concentration in bulk water samples was below the method detection limit of 5 mg/l, so bulk measurements could not be made. However, it was possible to measure proteins either by desorbing them with 0.01-M NaOH or by adding the reagents directly to a small membrane sample. A similar direct-measurement procedure was performed previously for seawater conditioning films on glass slides (Garg et al., 2009). Two 0.8-cm^2 membrane samples were cut from each coupon of interest and placed in replicate digestion vials with 150 µl of ultrapure water (to bring the total reagent volume up to that of the standards). Smaller samples, 0.1 cm^2, were used when glass-fiber filters were measured since the concentration was higher. For each membrane type, two replicates of a clean membrane were also measured to control for reactions between reagent and membrane polymers. Three milliliters of the bicinchoninic acid working solution was added to each vial and the samples were incubated for 30 minutes in a 60°C water bath. Samples were then cooled in a room-temperature bath and their 562-nm absorbance was measured in a Shimadzu UV-vis spectrophotometer (Shimadzu X250) with 1-cm path length quartz cuvettes. Standards were prepared with bovine serum albumin (BSA; Sigma). Different proteins have variable reactivity so the concentrations reported here are "as BSA."

3.5.8 Size-exclusion chromatography

Size exclusion chromatography (SEC) was performed on a Shimadzu VP instrument. The column had a molecular weight separation range of 2 to 80 kDa (Protein-Pak 125, Waters, Milford, MA). Size calibration standards were polystyrene sulfonate (Polysciences, Inc, Warrington, PA). Detection was by ultraviolet absorbance in the range of 200 to 300 nm, with a resolution of 1 nm using a photodiode array.

3.5.9 Visual image analysis of fouled membranes

Membrane coupons were dried and scanned on a desktop scanner to obtain a digital image. A resolution of 600 dots per inch was used. Color images were comprised of red, green, and blue channels. The blue channel proved to be the best indicator of fouling. Horizontal transects (in the direction of flow) of the blue-channel image data were converted into the frequency domain using a Fourier transform with scripts written in Matlab. The transformation resulted in a power spectrum for that transect. Power spectra of all of the transects were averaged to minimize noise and the averages were reported.

3.5.10 Laser-scanning cytometry

Laser-scanning cytometry (LSC) is a method for surface scanning to detect particles and cells. An LSC instrument was previously built in our laboratory for use as a particle detector for low-pressure membrane integrity tests and was calibrated with fluorescent microspheres (Ladner et al. 2007). Because algal cells show strong fluorescence, LSC was evaluated for its usefulness as an algal foulant detection device. Strictly speaking, the method is not “cytometry” as this term indicates single-cell counting or analysis, but we retain the LSC designation for consistency.

For LSC analysis a small (2.5-cm square) section of membrane was cut out of the coupon and mounted on a microscope coverslip with double-sided tape. The specimen was placed on a movable stage onto which laser light (635 nm) was directed. Scanning proceeded in a helical path similar to a compact disk or DVD. Fluoresced light was detected with a photomultiplier tube (PMT). A cutoff filter in front of the PMT ensured that most of the detected light was indeed fluoresced and not reflected. Data were processed with Matlab to generate a histogram of raw PMT readings as well as an image with spatial information.

3.5.11 Infrared spectroscopy

Attenuated total reflectance Fourier transform infrared spectroscopy (ATR-FTIR) was used to evaluate organic foulants accumulated on the membranes after seawater experiments, as has been done in other membrane fouling studies (Kim et al. 1997; Zhu and Nystrom 1998; Howe et al. 2002). Infrared measurements were performed with a Nexus 670 instrument from Thermo Nicolet supplemented with a Smart Golden Gate ATR accessory with a diamond crystal and zinc-selenium focusing element (Waltham, MA). The crystal was washed with 100% ethanol and rinsed with distilled water prior to each measurement. Membrane samples were pressed against the diamond crystal and 32 scans were recorded and averaged with a resolution of 4 cm^{-1}. This was repeated on at least five separate locations in the fouled portion of the membranes. Clean membranes or the clean edge of fouled membranes (protected from foulants by o-rings) were used for obtaining the background membrane spectra.

3.5.12 Scanning electron microscopy

For scanning electron microscopy (SEM) membrane samples stored in a dessicator were sectioned into small (about 2-mm by 6-mm) strips and mounted with carbon tape on an SEM stage. Sputter coating was performed for 30 seconds with gold palladium. A JEOL 6060 SEM was employed in high vacuum mode at a voltage of 20 kV and images were taken at 10,000 times magnification.

3.5.13 Atomic force microscopy

Membrane surface roughness was determined by atomic force microscopy (AFM). Tapping mode AFM measurements were made using an etched silicon probe on an MFP-3D instrument (Asylum Research, Santa Barbara, CA). Clean membrane coupons were allowed to dry for 24 hours in a desiccator before AFM scans were performed. The RMS roughness is given by the standard deviation of the individual height measurements.

3.6 TABLES

Table 3-1. Components of bench-scale RO testing unit.

Description	***Manufacturer***	***Model/Catalog #***
Membrane test cell	GE Osmonics, Minnetonka, MN	SEPA II
Hydraulic hand pump	Brand Hydraulics, Champaign, IL	HP-121DA50
Pump	Cat Pumps, Minneapolis, MN	231
Motor	Marathon Electric, Wausau, WI	MicroMAX 145THFR5329/Y368
Phase inverter	Toshiba, New York, NY	S-11
Pressure transducer (P_f)	Cole Parmer, Vernon Hills, IL	68072-14
Stainless steel tubing	Swagelok, Solon, OH	SS-T6-S-035-20
Elbows, Ts, Couples	Swagelok, Solon, OH	SS-600 series
Regulating needle valve	Swagelok, Solon, OH	SS-1RS6
Pressure relief valve	Swagelok, Solon, OH	SS-4R3A5; spring kit 177-R3A-K1-C
Permeate Flow meter	Alicat Scientific, Tucson, AZ	L-10CCM-D
Balance	Mettler Toledo, Columbus, OH	PB3002-S
Temperature controller	Cole Parmer, Vernon Hills, IL	EW-12101-00
Data acquisition card	National Instruments, Austin, TX	PCI 6024E
Shielded I/O Connector Block	National Instruments, Austin, TX	SCB-68
Programming software	National Instruments, Austin, TX	Labview 7.0

3.7 FIGURES

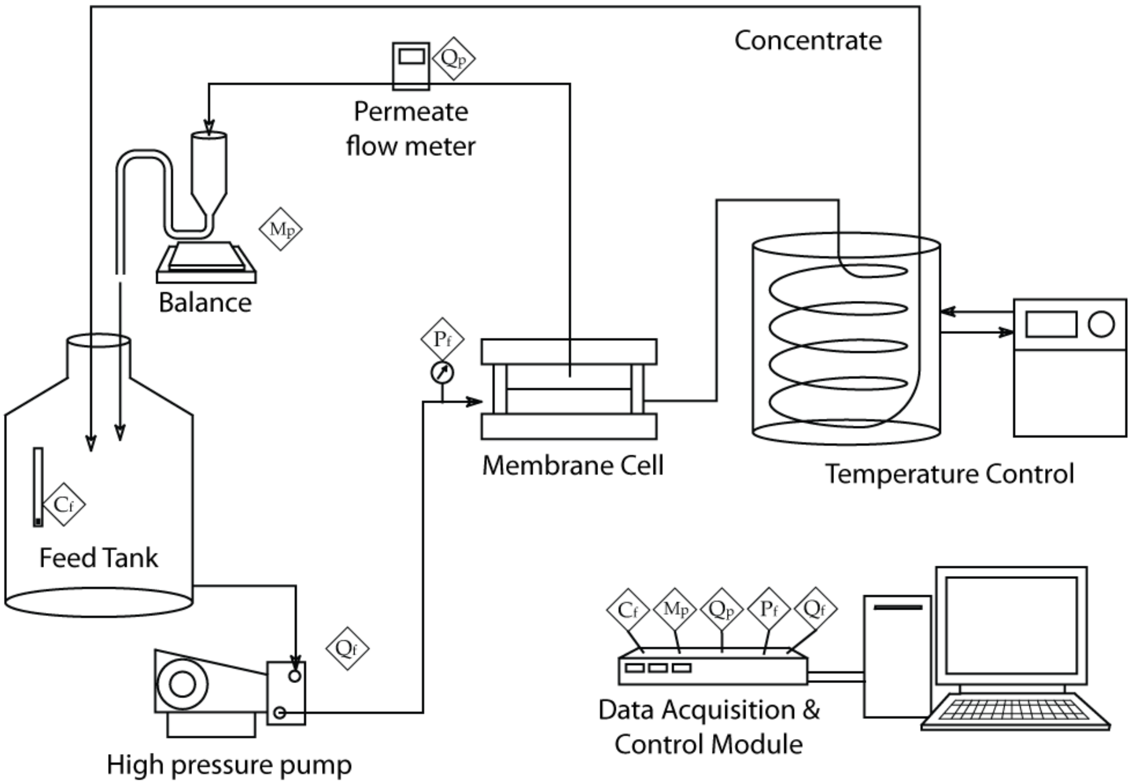

Figure 3-1. Diagram of the bench-scale SWRO membrane testing unit. Diamond symbols indicate electronic interface between the computer and components. Automated data acquisition locations are shown for feed conductivity (Cf), feed pressure (Pf), permeate flow rate (Qp), and permeate mass (Mp). Automated control of the high-pressure pump, and thereby the feed flow rate (Qf), is also indicated.

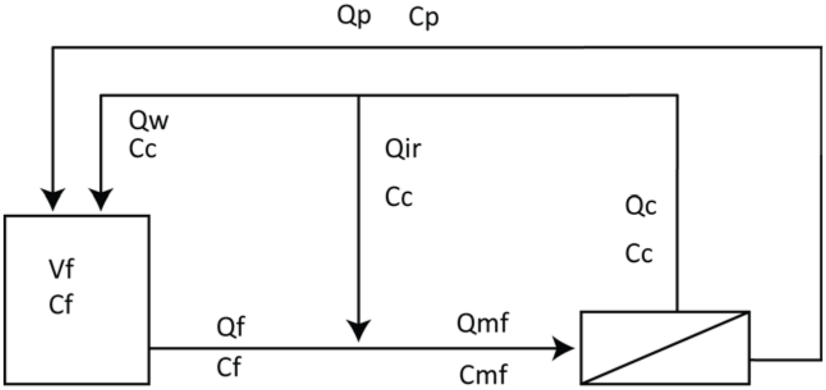

Figure 3-2. Batch internal recycle membrane test (BaIReMT) schematic. Flow rates are designated Q and concentrations C. Subscripts indicate feed (f), membrane feed (mf) concentrate (c), internal recycle (ir), waste (w), and permeate (p). The feed tank volume is Vf.

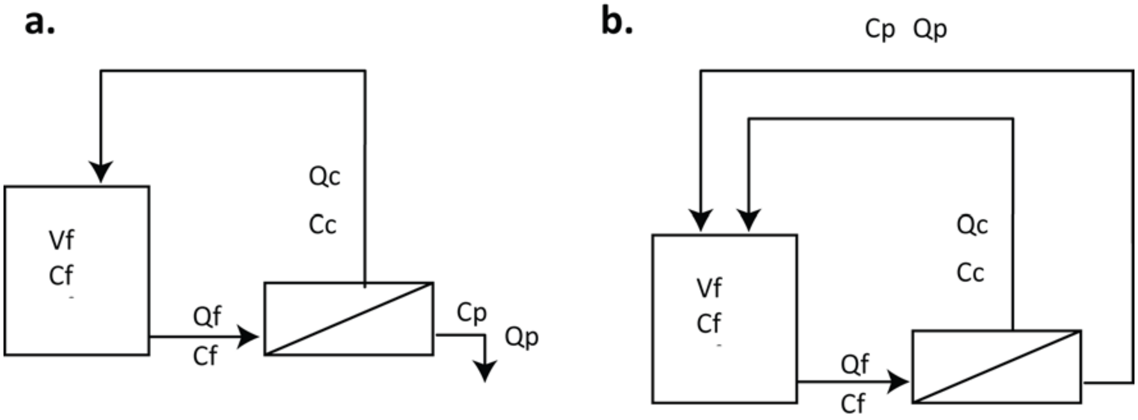

Figure 3-3. Schematics for transient recovery membrane tests. (a) During the initial phase the permeate was wasted to increase the feed tank concentration. (b) After the desired concentration was reached, the permeate was fed back to the feed tank for a full recycle operation. Definitions of variables are given in Figure 3-2.

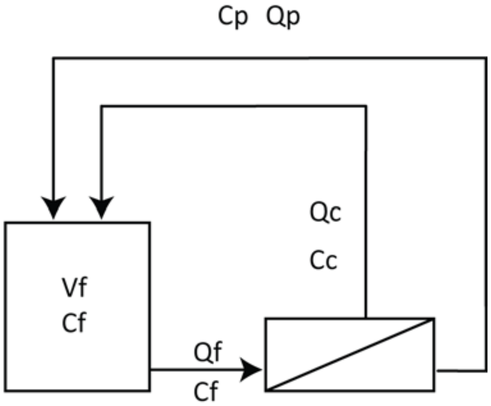

Figure 3-4. Schematic of flows for the full recycle test. Definitions of variables are given in Figure 3-2.

4 BENCH-SCALE EVALUATION OF REVERSE OSMOSIS

The present chapter begins with an evaluation of three testing configurations to determine their usefulness in evaluating reverse osmosis fouling by seawater. These were the Batch Internal Recycle Membrane Test (BaIReMT), the transient recovery test, and the full recycle test. The hypothesis was that the BaIReMT and transient recovery tests would provide a rapid procedure for determining fouling propensity of natural waters. These two tests involve elevated foulant concentrations to mimic later elements in a full-scale treatment train. The full recycle test did not provide an increase in foulant concentration so it was expected to be less useful.

In evaluating various test configurations an understanding of concentration polarization was critical for determining sources of flux variation, whether from fouling, compaction, or osmotic pressure changes. Rigorous modeling of concentration polarization is difficult because of the complex geometries and flow regimes in RO modules; typically, concentration polarization must be measured. However, concentration polarization measurement usually requires knowledge of membrane permeability, which can vary from coupon to coupon. Through manipulation of transport equations a method was devised for determining membrane permeability and concentration polarization in a single experimental run and under appropriate pressure and flux conditions. The key to the method was to allow the salt concentration to increase over time by wasting permeate. Salt concentration, pressure, and flux were monitored during the experiment and the data were supplied to appropriate models for transport parameter determination. The method was most often employed for constant-pressure cases (where flux declines over time), but constant-flux cases (where pressure increases over time) were also evaluated. Results from the two methods are here compared.

After determining transport parameters, natural seawater experiments were performed. The main hypothesis was that short-term bench-scale tests could be used to compare water sources and measure the fouling potential of the dissolved and particulate natural organic matter. Organic-matter foulants in the seawater were fractionated into several size classes and fouling results were compared. By appropriately accounting for the concentration polarization, and through control experiments, it was possible to distinguish flux decline due to fouling from flux decline due to enhanced osmotic pressure. In subsequent experiments, three different seawater sources were tested to evaluate their bench-scale performance.

4.1 EVALUATION OF TEST CONFIGURATION OPTIONS

4.1.1 BaIReMT

The experimental design first attempted in this project was the BaIReMT. The main reason for using this approach was to concentrate the foulant material in the membrane system and simulate later stages of a full-scale RO treatment train. It was anticipated that such a method would lead to more rapid fouling and more realistic results than a simple full-recycle setup.

The basic schematic of the BaIReMT was shown in Figure 3-2. The concept was simple but several key elements had to be incorporated in the design in order to make the RO unit function at appropriate flow rates and pressures to mimic a full-scale RO system. The most important full-scale parameter to mimic was recovery, defined as the amount of clean water produced per salt water entering the system. Higher recovery meant a higher salt and foulant concentration in the concentrate stream. The membrane feed, C_{mf}, had to be higher than the feed tank concentration, C_f. A mathematical model was developed to give the steady-state flow rates and concentrations for a desired recovery.

Through modeling it was found that the amount of concentrate wasted back to the feed tank (Q_w) was very small; to model 50% recovery, Q_w was only 4.0 ml/min. Further, the waste flow rate was highly dependent on the recovery; decreasing recovery to 30% only increased Q_w to 9.8 ml/min. Compared to an anticipated crossflow rate (Q_c) of 1300 ml/min, tweaking a valve to accurately deliver a waste flow of 9.8 ml/min was a difficult proposition. The model also showed that the feed flow (Q_f) would be quite small because it would be equal to the small waste flow (Q_w) plus the small permeate flow (Q_p; 4.6 ml/min for the flux desired).

Another possible problem in BaIReMT was pump cavitation. The setup would require that the pump be operated in almost a closed-loop configuration where the outlet was returned directly to the inlet. This was dangerous because a slight disturbance would cause the inlet flow rate to drop below the outlet flow rate, starving the pump and causing cavitation. It was more desirable to have an open reservoir under positive pressure at the pump inlet. The solution to the problem was to incorporate a break tank into the design, as shown in Figure 4-1. The break tank was placed in route of the internal recycle line. The high pressure pump was fed directly from the break tank, which was open to the atmosphere. The concentrate stream (Q_c) flowed to the break tank after being cooled. The break tank effectively opened the loop, helping to mitigate pump starvation problems.

The solution to the problem of low waste flow rate (Q_w) was to incorporate a peristaltic pump capable of such flow rates. The peristaltic pump fed Q_w from the break tank to the feed tank. Note that Q_w theoretically should have come directly from the concentrate line, but the break tank was more accessible. This was justified because the break tank composition was the same as the concentrate line, since the feed flow rate (Q_f) was small, the concentrate line flow rate (Q_c) was large, and the break tank was well mixed.

In order to adequately control the feed flow rate (Q_f), the feed tank was elevated and the tubing carrying water from the feed tank to the break tank was open to the atmosphere at the water level in the feed tank. In this way, feed water was gravity fed to the break tank. The feed flow (Q_f), then was always equal to the waste flow (Q_w) plus the permeate flow (Q_p), even though these flows were very small.

The steady-state BaIReMT model was used to calculate flow rates and concentrations needed to achieve the desired system recovery. Further modeling allowed evaluation of the dynamic state at startup of the BaIReMT run. The variable of interest was the break tank concentration, which was also the concentrate stream concentration under the completely mixed tank assumption. After solving mass balances for the system, the concentrate concentration could be modeled as in Equation 4-1, with parameters defined in Equations 4-2 and 4-3.

$$C_{bt} = \frac{\beta}{\alpha} + \left(C_{bt,o} - \frac{\beta}{\alpha} \right) \exp(-\alpha \cdot t) \tag{4-1}$$

$$\alpha = \frac{\frac{Q_w - Q_c}{Q_c}\left(Q_{mf} + Q_p\left(rej - 1\right)\right) - \frac{V_{bt} Q_f}{V_f} - Q_{mf}}{V_{bt}} \tag{4-2}$$

$$\beta = \frac{Q_f M_{tot}}{V_{bt} V_f} \tag{4-3}$$

The measured parameters from which α and β were derived were flow rate (Q), volume (V), membrane rejection (rej), and total solute mass (M_{tot}). Subscripts indicate break tank (bt), concentrate (c), feed tank and feed line (f), waste line back to feed tank (w), membrane feed (mf), and permeate line (p). The time constant of the BaIReMT is α with units of inverse time. If the permeate flow rate or the waste flow rate were increased (thereby increasing the feed flow rate) α would increase and the system would reach steady state more quickly. If the membrane feed flow rate (and thereby the concentrate flow rate) were decreased or if the break tank volume were increased, α would decrease and more time would be required for steady state. The β parameter had units of concentration per time and incorporated the total solute mass in the system. It could be thought of as the mass flow constant, analogous to a mass transfer coefficient. The steady state break tank concentration was determined by β over α.

BaIReMT model parameters were measured during a run with a sodium chloride solution. The model prediction is shown in Figure 4-2. The model overshot the data in this case; however, when α and β were found through a fit to the data using Equation 4-1 a good fit was found. The model was of the correct form and if the parameters were more accurately measured, salt concentration could be predicted *a priori* for experimental runs. Foulant concentration could also be predicted with the adjustment of the *rej* parameter to the appropriate foulant rejection value for the membrane (probably very close to 1 for seawater RO membranes).

4.1.2 Transient recovery

One drawback to the BaIReMT configuration was insufficient stability. Small perturbations caused wide swings in operating parameters. In an effort to provide more control and repeatability, the transient recovery configuration was utilized. This did indeed help with repeatability, but no flux decline difference was seen in waters with different organic-matter fractions. The transient recovery test, like the BaIReMT, involved high salt concentrations that limited the amount of flux that could be achieved in the system. There was an upper bound to pressure (1000 psi) and at high salt concentrations flux was limited by the heightened osmotic pressure. In other tests where full recycle was employed, salt concentrations were constant at the initial level and flux was maintained at a higher level during the run. There the flux did tend to decline as foulants accumulated. It appeared, then, that high flux was more important than high organic matter concentration when fouling was to be studied in a short time period. For short-term bench-scale tests it is advisable to run at the highest flux possible. That is achieved at the lowest salt concentration, which is obtained in the full recycle test.

4.1.3 Full recycle

The full recycle test schematic was presented in Figure 3-4. This was the setup used for the general bench-scale membrane testing apparatus diagram in Figure 3-1. Permeate and concentrate flows were delivered back to the feed tank, so no modeling of flow rates was required as for the BaIReMT or transient recovery configurations. The full recycle test had another advantage over both the BaIReMT and the transient recovery tests: minimal operator involvement. The BaIReMT and transient recovery configurations demanded that an operator constantly monitor the feed tank conductivity and adjust the pressure to maintain constant flux. It was difficult to make those changes in the exact same manner for each run. With the full recycle test the operator did not need to adjust the valves or tubing and there was no change in crossflow velocity during the run. This resulted in greater stability and repeatability.

4.1.4 Comparison of configurations

A summary of the differences in operating modes among bench-scale testing approaches is given in Figure 4-3. The full recycle configuration involved only one changing parameter, flux, so flux decline due to fouling could be seen directly. In the other two tests both pressure and salt concentration varied so modeling was required to determine the causes of changing membrane performance. The full recycle configuration did not simulate the full-scale system because at full scale a constant flux is maintained. However, the full recycle test was advantageous for lab-scale work because it was easiest to perform and interpret.

The length of a bench-scale test is another important consideration. It will be shown in the testing results that follow that short-term tests (eight hours) for natural waters were insufficient because no significant flux decline was observed. Twenty-four hour tests were more adequate when the organic-matter concentrations were sufficiently high, but even these did not result in large flux declines. For natural waters with lower organic-matter loading, a four-day test at high flux (1000-psi pressure) gave measurable flux decline; however, longer-term tests presented several challenges. For one, the system ran at very high pressure and needed a complex control system to avoid upsets, especially over night when operators were absent. In that sense, the effort and complexity of the bench-scale test setup was almost as great as would be required for a pilot-scale test. If such a large effort is required it decreases the attractiveness of bench-scale work. Secondly, corrosion is a problem. When a batch sample is used and the liquid is constantly recycled, any corrosion products present will increase in concentration over time and cause fouling. A small amount of corrosion typically occurs with high-salinity seawater even on 316 stainless steel. Thus, the longer a system is run, the more likely it is that corrosion products will affect the membranes. Thirdly, suspended biomass is present in all natural waters and will grow over time. For tests with high organic-matter content, bacterial numbers increased significantly over just 24 hours. When the system is run for several days in recycle mode it is quite likely that the organic matter composition will change due to biological activity and biofilms will form. Thus, longer time frames for bench-scale tests are not always advisable.

The volume of seawater used for bench-scale tests is also an important consideration. Twenty liters of seawater was sufficient to observe flux decline due to fouling in 24 hours when the organic-matter concentration was sufficiently high (as in the algal fouling experiments of Chapter 5). For natural waters, there was one case where 20 liters was sufficient to observe flux decline, but four days were required. In many other cases, eight liters were used and no significant flux could be observed. It is quite probable that a foulant limitation existed in that there was not enough organic matter in the water to form a sufficiently thick foulant layer. It is advisable, then, to use as much volume as possible in bench-scale testing so that no foulant limitation is experienced. Ideally, a flow-through system could be employed where the sample is continuously refreshed instead of completely recycled (as was done with the long-term sample throughput test). It is important to note, however, that the volume of seawater did not appear to be as important as the initial flux and foulant concentration. Even for long-term, high-volume experiments, flux decline was not observed with natural seawater if the initial flux was too low.

4.2 TRANSPORT PARAMETER DETERMINATION

Water flux (v_w) in reverse osmosis depends on the intrinsic membrane permeability (A), applied transmembrane pressure (Δp), and transmembrane osmotic pressure ($\Delta\pi$) as shown in Equation 4-4.

$$v_w = A(\Delta p - \Delta\pi_m) \tag{4-4}$$

The transmembrane osmotic pressure depends on the concentration of solute at the wall of the membrane on the concentrate side (c_w) and permeate side (c_p) as shown in Equation 4-5, where f_{os} is a term relating the salt concentration to the osmotic pressure.

$$\Delta\pi_m = f_{os}(c_w - c_p) \tag{4-5}$$

Most of the parameters in Equations 4-4 and 4-5 are available; intrinsic membrane permeability can be determined with a clean-water flux experiment, applied feed and permeate pressures can be measured, and permeate concentration can be measured. The osmotic pressure factor, f_{os}, is available through first-principles calculations or through empirical values in the literature (as described in the next section). The term that has always been problematical is the concentration of solute at the membrane wall, c_w, which depends on the extent of concentration polarization in the system. Concentration polarization can be modeled using film theory or other analytical approaches (Kim and Hoek 2005), but for spacer-filled channels with complex geometries, empirical determination of c_w is necessary. One method to measure c_w is to compare the clean-water and salt-water fluxes under similar hydrodynamic and pressure conditions (Sutzkover et al. 2000). The difference between clean-water flux ($v_{w,c}$) and salt-water flux ($v_{w,s}$) gives the transmembrane osmotic pressure, as in Equation 4-6.

$$\Delta\pi_m = \frac{v_{w,c} - v_{w,s}}{A} \tag{4-6}$$

Knowing the osmotic pressure on the permeate side (π_p), the concentrate-side wall osmotic pressure (π_w) and c_w can be determined. Using c_w and the bulk salt concentration (c_b) the concentration polarization factor (f_{cp}) is obtained as in Equation 4-7.

$$f_{cp} = \frac{c_w}{c_b} \tag{4-7}$$

In the above approach, two separate experiments must be performed: the clean-water test and the salt-water test. For seawater desalting, the flux through the membrane is very different in the two tests because there is no osmotic pressure in the clean water test. For example, for salt-free water at a pressure of 6,900 kPa, a seawater desalting membrane would typically have a flux around 50 liters per meter-squared per hour (lmh). However, for a 32,000-ppm seawater source, the osmotic pressure (about 2,000 kPa) reduces the flux to around 30 lmh. With concentration polarization, the flux is reduced even further. Thus, the flux of the clean-water experiment is quite different from the flux in the salt-water experiment and the membrane permeability obtained from the clean-water experiment may not be representative of the true membrane permeability at lower flux and higher applied pressure where the membrane deforms around the permeate carrier (as will be described in Chapter 5).

An alternative approach for determining A and f_{cp} for salt-rejecting membranes is presented here. A single test can be performed to determine both parameters and the measurements are reliable because the flux and applied pressure during the experiment are close to the actual flux during seawater desalting. An explanation of the theory behind this approach begins with a rearrangement of Equation 4-4 to explicitly include the osmotic pressure terms.

$$v_w = A\left(\Delta p - (\pi_w - \pi_p)\right) \tag{4-8}$$

The permeate osmotic pressure is typically at least two orders of magnitude lower than the feed osmotic pressure, especially when concentration polarization is significant.

Thus the permeate-side osmotic pressure can be neglected. The concentrate-side wall osmotic pressure is simply the bulk osmotic pressure multiplied by f_{cp} because the osmotic pressure varies approximately linearly with salt concentration. Thus, the flux equation can be written as

$$v_w = -A \cdot f_{cp} \cdot \pi_b + A \cdot \Delta p \tag{4-9}$$

where π_b is the bulk osmotic pressure and the other terms have been written so as to elucidate the linear slope-intercept form of the equation (flux varies linearly with bulk osmotic pressure, where the slope is Af_{cp} and the intercept is $A\Delta p$).

Parameters A and f_{cp} were determined for constant-pressure experiments by continuously wasting permeate and allowing the bulk salt concentration to increase. The bulk osmotic pressure was calculated from conductivity measurements of the feed solution. The linear relationship between bulk osmotic pressure and flux allowed calculation of parameters A and f_{cp} in a single test.

A very similar approach was used in other experiments where flux was held constant while pressure and salt concentration varied. In those cases, the slope-intercept form of the equation was

$$\Delta p = f_{cp} \cdot \pi_b + \frac{v_w}{A} \tag{4-10}$$

So f_{cp} and A could be obtained through the linear fit to paired applied pressure and bulk osmotic pressure data.

4.3 OSMOTIC PRESSURE DETERMINATION

In the method described above for determination of concentration polarization it is important to accurately determine the bulk concentrate and permeate osmotic pressures. Empirical values for seawater osmotic pressure can be found in the literature (Kellogg 1971). Those data were used to calculate osmotic pressure for seawater with total dissolved solids (TDS) between 10,000 and 80,000 ppm at 25˚C, as given in Equation 4-11.

$$\pi_b = 1.416 \cdot 10^{-7} c_b^{\;2} + 6.913 \cdot 10^{-2} c_b - 80.64 \tag{4-11}$$

where π_b is the bulk osmotic pressure in kPa and c_b is the TDS in parts per million. Equation 4-11 is very nearly linear in the region of interest but a second-order polynomial form is retained for greatest accuracy. The R-squared value for the data fit is greater than 0.99.

For NaCl solutions the relationship between concentration and osmotic pressure is different than for seawater. NaCl osmotic pressure was found from a separate set of literature data (Stoughton and Lietzke 1965) and a linear fit (R-squared > 0.99) to those data for the 12,000 to 55,000 ppm concentration range is given by Equation 4-12, which is valid at 25˚C.

$$\pi_b = 8.505 \cdot 10^{-2} c_b - 86.61 \tag{4-12}$$

For the permeate-side osmotic pressure the permeate TDS is two orders of magnitude lower than the feed and the composition of dissolved salts are assumed to be mostly sodium and chloride ions since other seawater salts are more readily excluded by the membrane. Because the concentration is lower, the salts act in a more predictable fashion and Equation 4-13, a formulation from van't Hoff, can be employed (Merten 1966).

$$\pi = \frac{nRT}{V} \tag{4-13}$$

Here, *n/V* is the concentration of sodium chloride (moles of sodium plus moles of chloride divided by the volume), *R* is the ideal gas law constant and *T* is temperature. Comparing literature osmotic pressure data (Stoughton and Lietzke 1965) with the values calculated by Equation 4-13 shows a discrepancy of only four percent for a 580-mg/l sodium chloride solution at 25˚C (48 kPa in the reference, 50 kPa calculated here). Permeate concentrations were typically lower than 580 mg/l during testing.

The concentration of solutes during RO experiments was determined via conductivity measurements. The conversion from bulk concentrate conductivity to TDS for seawater is given by

$$c_b = 732.56\sigma_b - 3831.6 \tag{4-14}$$

where c_b is the bulk feed concentration in parts per million and σ_b is the electrical conductivity in milliSiemens per centimeter (mS/cm). Equation 4-14 is a linear fit of data from oceanographic literature (Poisson 1980) and does not apply to sodium chloride solutions. For sodium chloride, the relationship was derived from linear interpolation of data from the conductivity standards manufacturer (Oakton, Vernon Hills, IL) for NaCl concentrations between 8,500 and 48,000 ppm. The TDS versus conductivity relationship for NaCl is given in Equation 4-15.

$$c_b = 613.11\sigma_b - 664.62 \tag{4-15}$$

For the permeate side, the equation is

$$c_p = 512.1\sigma_p - 15.30 \tag{4-16}$$

which is a linear fit of data between 0.084 and 2.76 mS/cm, also from the conductivity standards manufacturer (Oakton). Equation 4-15 was used for both seawater and NaCl permeates because it was assumed that the permeate from seawater was principally composed of NaCl. It should be stressed that the relationships between conductivity and concentration given in Equations 4-14 to 4-16 are empirical formulae that apply only for the concentration and temperature ranges of interest in this study.

4.4 SEAWATER FRACTIONATION EXPERIMENT

San Diego seawater was fractionated to determine the RO fouling potential of different-sized organic material. A similar approach was used previously for fresh-water fractionation (Howe and Clark 2002) and for seawater (Kumar et al. 2006). Seawater was fractionated into different size classes using three ultrafiltration (UF) membranes: 20-kDa poly-ether-sulfone (PES), 30-kDa regenerated cellulose (RC), and 100-kDa regenerated cellulose (all membranes from Millipore). Each flat-sheet membrane coupon was rinsed in deionized water, loaded into a dead-end, unstirred acrylic SEPA cell (GE Osmonics), and placed in an Osmonics cell holder pressurized at 60 psi. A clean water sample was run using ultrapure water (18 MΩ) to establish the membrane’s clean-water flux. A seawater sample was prepared by prefiltration through a glass-fiber filter (AP40, Millipore) to remove large particulate matter. The prefiltered sample was then loaded into a stainless steel feed tank. The tank was pressurized to 200 kPa with a regulated nitrogen tank and a valve was opened allowing flow of seawater through the membrane. Pressure remained close to 200 kPa for the duration of the fractionation run and room temperature was maintained (20 to 21˚C). Approximately ten liters of filtrate were collected for each fraction.

Each fraction of San Diego seawater was run in the bench-scale RO unit using the transient recovery configuration to simulate RO elements in later stages of a full-scale treatment train where module feed concentrations would be elevated. Permeate was wasted from the system to allow the feed salt concentration to increase over time. As the salt concentration increased, the pressure was adjusted manually to achieve a constant flux of 20 lmh. Once the desired recovery (17%) was achieved, permeate was fed to the feed tank to maintain a constant feed salt concentration. Eight liters of fractionated seawater were used for each test. A non-fractionated seawater sample and a synthetic seawater sample were also tested. The non-fractionated seawater was treated only by filtration through an AP40 glass-fiber filter (Millipore).

4.5 TRANSPORT PARAMETER RESULTS

Representative data from a constant-pressure experiment to determine concentration polarization are shown in Figure 4-4. Applied pressure was 6,900 kPa, crossflow velocity was 800 ml/min, and salt rejection was 98.7%. Permeate was removed from the system allowing the feed-side salt concentration and osmotic pressure to increase over time. Bulk osmotic pressure data were determined by conversion from conductivity measurements. From flux versus osmotic pressure data the intrinsic membrane permeability (A) was determined to be 0.0077 lmh/kPa and the concentration polarization factor (f_{cp}) was 1.34. It should be noted that for constant-pressure experiments the f_{cp} reported is an average value. Because flux varied during the run, f_{cp} should have also varied, since solutes are pulled toward the membrane to a greater extent at higher flux. However, in re-plotting run data using the model with constant f_{cp}, the model fit the data quite well, suggesting that the f_{cp} value did not vary significantly as flux decreased over the course of the run.

Representative data from a constant-flux experiment used to determine concentration polarization are shown in Figure 4-5. Flux was 20 lmh, crossflow velocity was 800 ml/min, and salt rejection was 98.4%. As with constant-pressure runs, the permeate was wasted from the system to allow feed-side salt concentration and osmotic pressure to increase over time. As osmotic pressure increased, the pressure was adjusted to maintain constant flux. Pressure adjustments were performed manually, not continuously, resulting in the stair-step pattern in Figure 4-5. Constant-flux experiments were more difficult to perform than constant-pressure experiments because more operator involvement was needed to incrementally increase the pressure. Regardless, reasonable values for A (0.011 lmh/kPa) and f_{cp} (1.48) were obtained.

Data for 26 experiments are summarized by the box plots in Figure 4-6. The average salt rejection for all tests was 98.9% with the lowest rejection being 97.7% and the highest being 99.5%. Permeability varied from coupon to coupon and the extent of the variation is evident in the box plots. There was no significant difference in permeability between Filmtec SW30HR and Hydranautics SWC4 membranes. There appeared to be more variability in permeability with SWC4 membranes, but this is probably due to the low sample size ($n = 6$) for SWC4 compared to the larger sample size ($n = 15$) for SW30HR coupons.

There was a significant difference in permeability determined from constant-flux and constant-pressure experiments; constant-flux experiments resulted in higher intrinsic membrane permeability. This could be due to the lower average pressure (6,000 kPa) in constant-flux runs causing less membrane compaction and deformation than in constant-pressure runs (6,900 kPa). Also, the average f_{cp} was slightly higher for constant-pressure runs. Parameters determined using this method may not be completely independent; as higher concentration polarization occurs, the reported permeability may be elevated as well.

Because of the apparent success in determining transport parameters, it is suggested here that this measurement approach can be used as the first step in a bench-scale desalination test to determine if the membrane coupon transport parameters are similar to those from previous experiments. In this way, performance variability from coupon to coupon can be monitored. Additionally, the method can be used to compare different membrane types. Further, the concentration polarization factor can be determined for the flow characteristics of any given system. This is important for correctly separating the effects of fouling and osmotic pressure in high-salinity experiments.

To illustrate the last point, Figure 4-7 provides three different presentations of data from a San Diego seawater experiment. In the lower curve (a) the normalized measured flux is plotted directly. Flux declines as one would expect for a constant-pressure/increasing-TDS experiment. In the middle curve (b) normalized specific flux (flux per unit driving force) is plotted, but the driving force was calculated by considering only the bulk salt concentration without knowledge of the concentration polarization factor. One might erroneously conclude that the membrane performance declined by over 20% if the data were treated in this manner. In the upper curve (c) the normalized RO specific flux was calculated by taking into account a concentration polarization factor of 1.31 calculated by the methods presented previously. Here it is apparent that the membrane performance did decrease, but only by about 5% over eight hours. Further, the shape of the curve is non-linear, as opposed to the apparent linearity of the other curves. These results suggest that in order to appropriately characterize membrane performance for experiments where salt concentrations vary (like the BaIReMT or transient recovery tests) measurement of the concentration polarization factor is critical.

4.6 SEAWATER FRACTIONATION RESULTS

Operational data for the bench-scale RO runs of each seawater fraction tested with the transient recovery method are presented in Figure 4-8. Salt rejection was between 98.9 and 99.4% for the five experiments. Though permeability declined in all runs, there was no significant difference in the rate of decline among the seawater fractions. Further, the synthetic seawater control showed the same flux decline as the other samples. Permeability decline was most likely due to compaction, since it was seen in all cases. Since no performance difference could be detected for the various fractions, it appears that a sufficient cake layer did not build up in these experiments, even for the water that was treated with only glass-fiber filtration.

4.7 SEAWATER SOURCE COMPARISON

Full recycle tests were used for comparison of seawaters from West Basin, Carlsbad, and Tampa Bay. In full recycle tests, permeate and concentrate were delivered back to the feed tank so that the feed water solute concentration did not vary. Pressure was held constant at 6,900 kPa. The flow rate was 800 ml/min, which gave a crossflow velocity of approximately 0.47 m/s and Reynolds number of 270. Crossflow velocity and Reynolds number were calculated as suggested for RO modules by other workers (Schock and Miquel 1987).

The results from Section 4.4 (seawater fractionation experiments) suggested no flux decline due to fouling, but rather a flux decline due to increasing salt concentration and compaction. This gave impetus for changes in the testing method during further studies with other natural waters. The volume tested was increased from eight liters to 19 liters in order to increase the total amount of foulant. Instead of constant-flux operation that required operator-controlled pressure changes over time, a constant-pressure operation was used. The pressure was set at the maximum recommended pressure for the test cell, 6,900 kPa. This gave the highest flux possible and the greatest chance of foulant accumulation.

Another protocol change implemented in further tests was a 24-hour compaction period instead of the three hour period used previously. As we learned, it was important to consider the membrane compaction characteristics in these bench-scale tests. As the membrane was pressurized, the polymeric structure compressed and water passage was reduced. In addition to compaction, the membrane deformed around the permeate spacer. It is hypothesized that this deformation decreased the surface area available for water passage, which decreased the flux over time. An additional possibility is that local flow characteristics changed as the membrane deformed, which may have increased concentration polarization and further led to reduced flux. Because of differences in module design, membrane deformation in bench-scale systems is different than that experienced in full-scale systems. The exit holes at the center of the test cell through which the permeate passes are rather large compared to the dimples formed by the permeate carrier spacer. The permeate spacer itself deformed into these holes, and the membrane followed suit. Such drastic local deformation may have dramatically increased the permeability of the membrane and could affect its integrity. In fact, on two occasions membranes were punctured and the runs had to be terminated. One improvement to the bench-scale cell would be to reduce membrane deformation through the use of smaller holes for permeate flow.

Figure 4-9 shows the difference between SWC4 and SW30HR membrane compaction characteristics. The SWC4 membrane had a higher initial flux, but its flux declined more than the SW30HR membrane so that after several hours their fluxes were very similar. Interestingly, AFM analysis indicated the SWC4 membrane had a greater roughness (data not shown), which is corroborated in the literature; RMS roughness for an SWC4 membrane was reported to be 129 nm (Louie et al. 2006) and SW30HR roughness was reported to be 87 nm (Hodgkiess et al. 2001). It has been suggested that rougher surfaces may be beneficial in increasing permeate fluxes due to increased surface area (Hodgkiess et al. 2001), which could have been the case for the early stages of the tests shown in Figure 4-9. However, the rougher membrane also experienced more compaction, so the flux benefit was nullified.

Figure 4-10 shows flux results for the three natural waters tested, and raw-water qualities are given in Table 4-1. For each of the three cases, the flux behavior was virtually identical over the 24-hour duration of the experiments. There was a slight flux decline for all three runs at the beginning of the experiments, which was probably due to membrane settling and compaction. Such recompaction occurred because the system was depressurized briefly (~15 minutes) for replacement of the NaCl solution with seawater. During depressurization the membrane relaxed to some degree.

Even though no significant flux decline was apparent, the membranes were autopsied to determine to what extent fouling had occurred. SEM images (Figure 4-11) show that material had indeed accumulated on the membrane surface. Fouling was patchy; the exposed membrane surface can be seen where foulants did not accumulate. This suggests that foulants preferentially deposit where other foulants have previously attached in a nucleation phenomenon. Foulant morphology appeared different among water sources with Tampa Bay giving the largest foulant aggregates, West Basin showing less aggregation and more granular material, and Carlsbad having patchiness similar to

Tampa Bay but with smaller aggregates. Similar qualitative observations were made for other SEM images taken of the same samples.

Infrared spectroscopy was also used as an autopsy technique. Figure 4-12 shows infrared spectra in the “fingerprint region” where the clean-membrane spectra (obtained from the edge of the coupon that received no permeate flow) were subtracted from the fouled-membrane spectra. Peaks were interpreted by comparison to literature and representative protein and polysaccharide spectra were also collected for comparison (Figure 4-13). It appeared that the foulants were partly made up of polysaccharidic material, as the triplet peak at 1,003, 1,051, and 1,090 cm^{-1} is qualitatively very similar to the triplet peak in the polysaccharide spectrum. Protein-like material is also indicated by the peak at 1,643 cm^{-1} which is the proper location for amide I vibrations (Mayo et al. 2004). Figure 4-14 shows that there was also high infrared absorbance in the 2,800 to 3,600 wavenumber region, which could be due to N-H stretching vibrations in proteins or O-H stretching vibrations in polysaccharides or bound water. All three waters had similar foulant infrared spectra.

4.8 CONCLUSIONS REGARDING BENCH-SCALE TESTING

Some conclusions can be drawn about the advantages and disadvantages of various bench-scale RO testing configurations. The BaIReMT and transient recovery tests enabled a simulation of full-scale recovery and constant flux conditions. The transient recovery test was easier to control than the BaIReMT because the salt concentration and pressure changed more steadily. In both the BaIReMT and transient recovery tests flux decline must be modeled taking into consideration the changing pressure and salt concentration. The full recycle test could be run at higher initial pressure and flux than the BaIReMT and transient recovery tests. Flux decline was measured directly, since pressure and salt concentration were constant. The full recycle test did not simulate the full-scale system, but it was advantageous for bench-scale studies because of its ease of use and high flux leading to more rapid flux decline than in the other tests.

Regarding transport parameters, a method has been presented here to determine both the permeability and concentration polarization using a single test where salt concentration was allowed to increase over time. Transport parameters were extracted by fitting a flux model to the data. Such a test could be performed for any reverse osmosis system to empirically determine the transport parameters under the flux and pressure conditions of interest. Use of such a method will greatly simplify laboratory efforts at determining transport parameters. Additionally, data can be collected for several runs to determine the coupon-to-coupon variability and provide quality control during experiments; defective membranes can be easily detected and replaced.

For seawater experiments it was found that flux decline due to fouling was not discernable, leading to the conclusion that natural cake layers were not sufficiently thick or dense to cause flux decline during short-term tests. This differs from the results presented in other work where flux decline was seen in eight hours and was attributed to fouling (Kumar et al. 2006). It is likely that in that work the measured specific flux decline in the BaIReMT experiments was caused by an inappropriate calculation of driving force as salt concentrations varied. The authors did not specify how their driving force was calculated when determining specific flux.

Even though flux decline was not observed, examination of the membranes after desalination runs showed that foulants had indeed accumulated on the membrane surface. The cake layers that developed did not provide sufficient resistance to cause flux decline; intrinsic membrane resistance was so large that the resistance from organic-matter cake layers was negligible. For Tampa Bay, Carlsbad, and West Basin seawaters the foulant material detected by infrared spectroscopy was quite similar, comprised of proteinaceous and polysaccharidic material. It is hypothesized that the organic matter deposition observed here represents the early stages of fouling that would be seen in a full-scale facility. Further, the early organic deposition could enhance bacterial attachment and provide substrate for biofilm formation. It has been shown that conditioning films of aqueous organic matter can in some cases promote bacterial attachment, though in other cases they protect against attachment (Ghayeni et al. 1998). Whether the organic matter present here would promote or protect against attachment is uncertain. In fact, the material present could be the early stages of biofilm development and not simply organic deposition, since natural waters were used with no effort at sterilization.

A question remains for future researchers and designers as to the usefulness of bench-scale studies for determining full-scale membrane performance. In the short-term tests presented here, no true flux decline due to fouling was apparent for any of the natural waters tested. One may consider increasing the testing time, which would necessitate an increase in seawater volume. Considering the complexity of such tests, the effort required would approach that of a pilot system, so engineers may choose to skip bench-scale studies and move directly to pilot tests. However, it has been shown here that even when no flux decline is apparent, materials do accumulate on the membrane surface. Bench-scale studies, then, can be used to characterize such initial deposition.

Where bench-scale studies will be employed, it is important to characterize and allow for membrane compaction. At least 24 hours of compaction was needed for flux to level off, with the rougher membrane compacting more than the smoother membrane. In addition it is important to recognize that compaction may not be the only factor affecting permeability because gross membrane deformation also occurs as the membrane and permeate carrier are molded to the geometry of the test cell. The membrane coupons tested here compacted in a very repeatable manner suggesting that compaction need not be determined for each coupon from the same membrane sheet.

4.9 TABLES

Table 4-1. Raw water quality for the three seawaters tested in the bench-scale RO unit.

Analyte	Method	Units	WestBasin	TampaBay	Carlsbad
Alkalinity	SM 2320B/310.1	mg/l	114	155	92
Bicarbonate Alkalinity	SM 2330B	mg/l	140	190	110
Ammonia Nitrogen	EPA 350.1	mg/l	ND	0.1	0.1
Sulfate	EPA 300.0	mg/l	2700	2000	3000
pH	SM 4500H+	pH Units	8	7.8	7.9
Aluminum	SM 2320B/310.1	ug/l	ND	ND	ND
Barium	EPA 200.8	ug/l	ND	ND	ND
Boron	EPA 200.7	mg/l	4.7	3.8	2.4
Bromide	EPA 300	ug/l	62600	56200	66400
Calcium	EPA 200.7	mg/l	390	360	200
Chloride	EPA 300.0	mg/l	19000	16000	19000
Copper	EPA 200.8	mg/l	ND	ND	ND
Fluoride	SM 4500F-C	mg/l	1	0.9	0.9
Iron	EPA 200.7	mg/l	ND	ND	ND
Magnesium	EPA 200.7	mg/l	1300	1100	650
Nickel	EPA 200.8	mg/l	ND	ND	ND
Potassium	EPA 200.7	mg/l	380	320	190
Silica	EPA 200.7	mg/l	ND	6.7	3.5
Sodium	EPA 200.7	mg/l	11000	8800	5200
Strontium	EPA 200.7	mg/l	7.3	6.6	7.4
Fecal Coliform	SM 9221C	MPNM	<2.0	<2.0	17
Total Coliform	SM 9221B	MPNM	<2.0	<2.0	17
SDI	ASTM, D4189-95	-	4.3	6.3	4

4.10 FIGURES

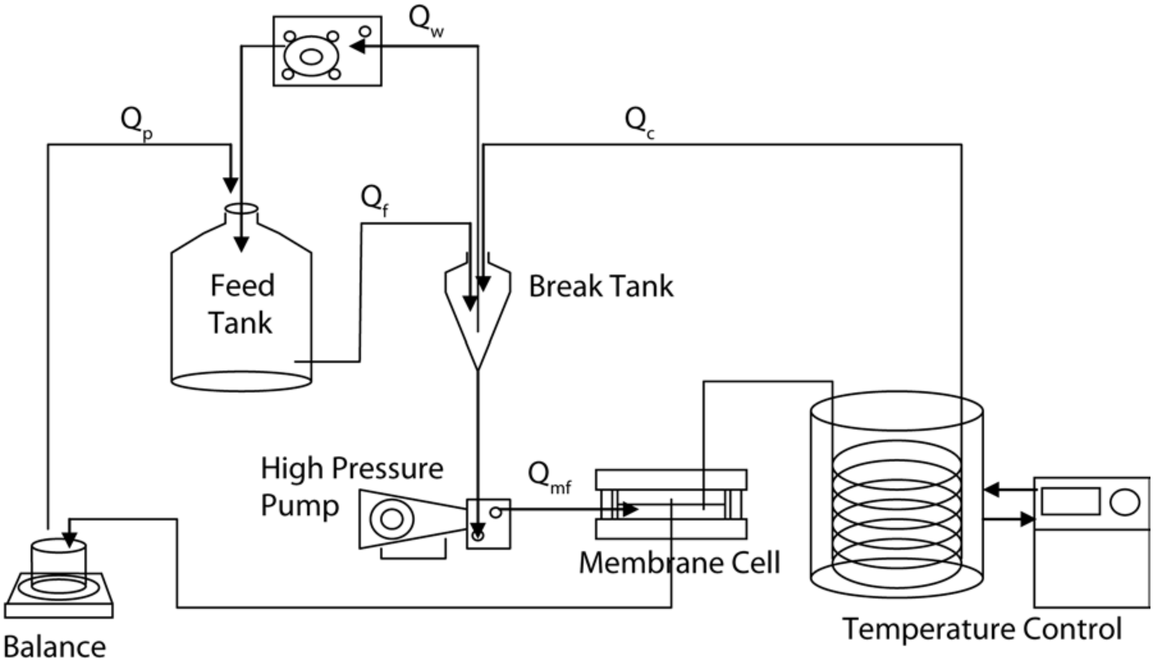

Figure 4-1. Bench-scale RO unit setup for the batch internal-recycle membrane test (BaIReMT).

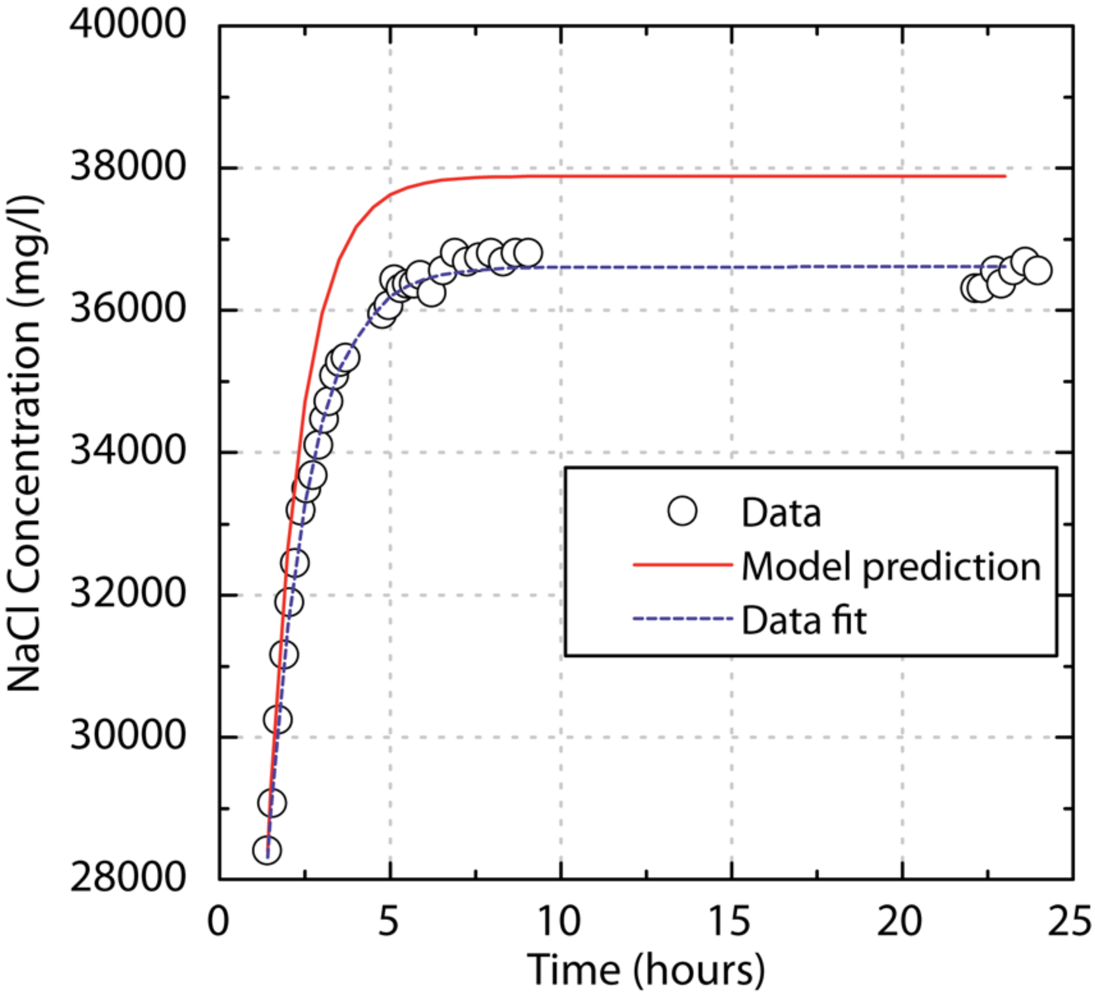

Figure 4-2. NaCl concentration during a 24-hour BaIReMT run. The model prediction was found using measured parameters. The data fit was found by adjusting α and β.

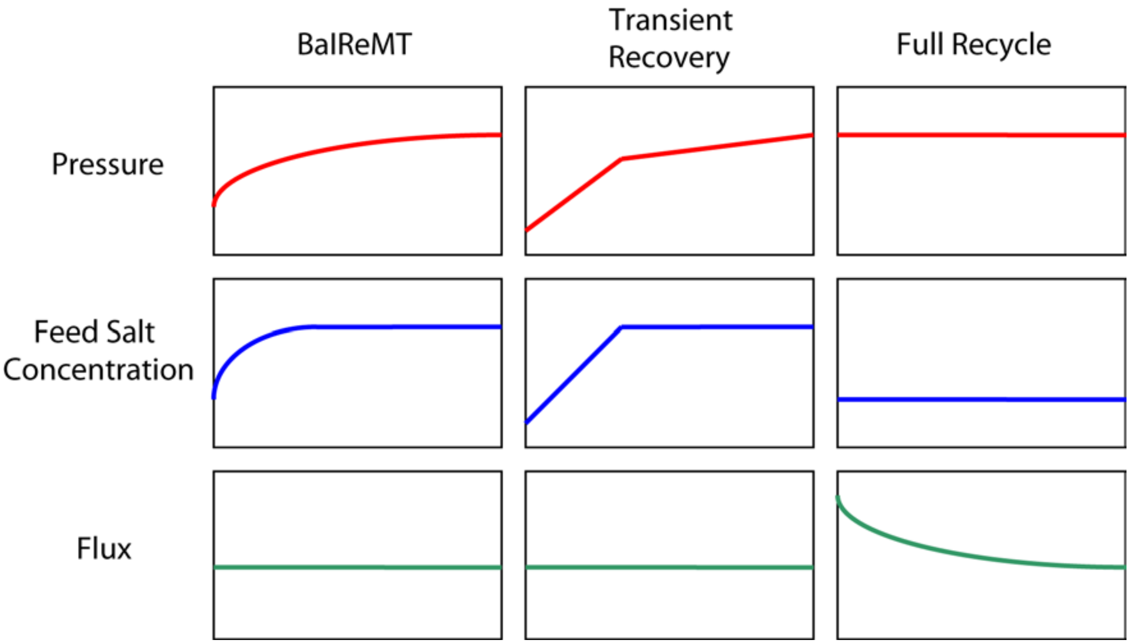

Figure 4-3. Diagram of operating conditions over time (horizontal axes) for three bench-scale RO testing schemes.

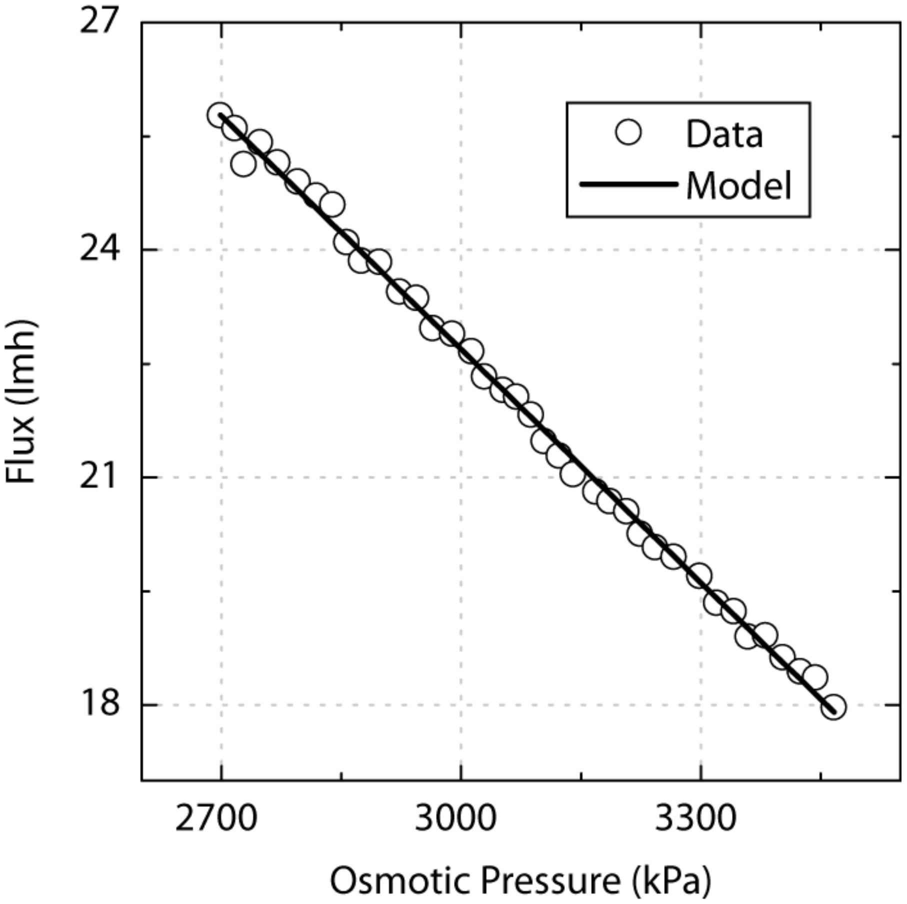

Figure 4-4. Representative data showing flux versus osmotic pressure for a constant-pressure RO experiment. Target applied pressure was 6900 kPa. R-squared for the linear fit was 0.997. Parameters derived from this test were A = 0.0077 lmh/kPa and f_{cp} = 1.34.

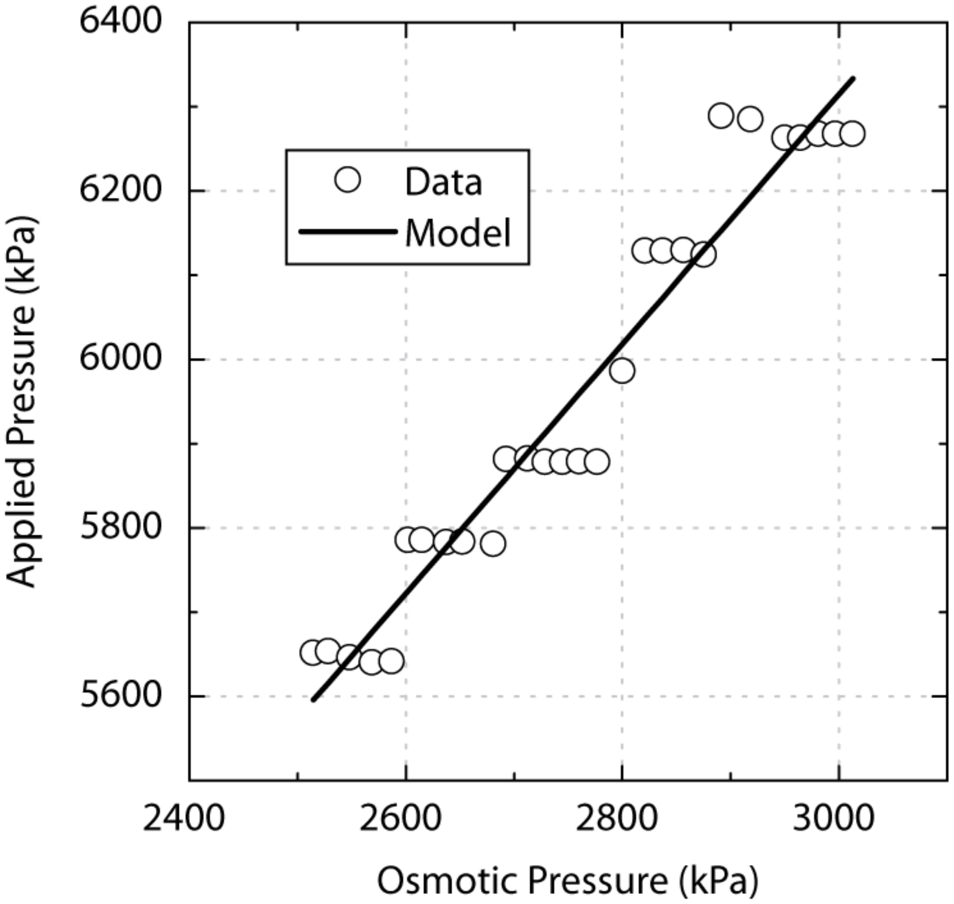

Figure 4-5. Representative data showing osmotic pressure versus applied pressure for a constant-flux RO experiment. Target flux was 20 lmh. R-squared for the linear fit was 0.94. Parameters derived from this test were A = 0.011 lmh/kPa and f_{cp} = 1.48.

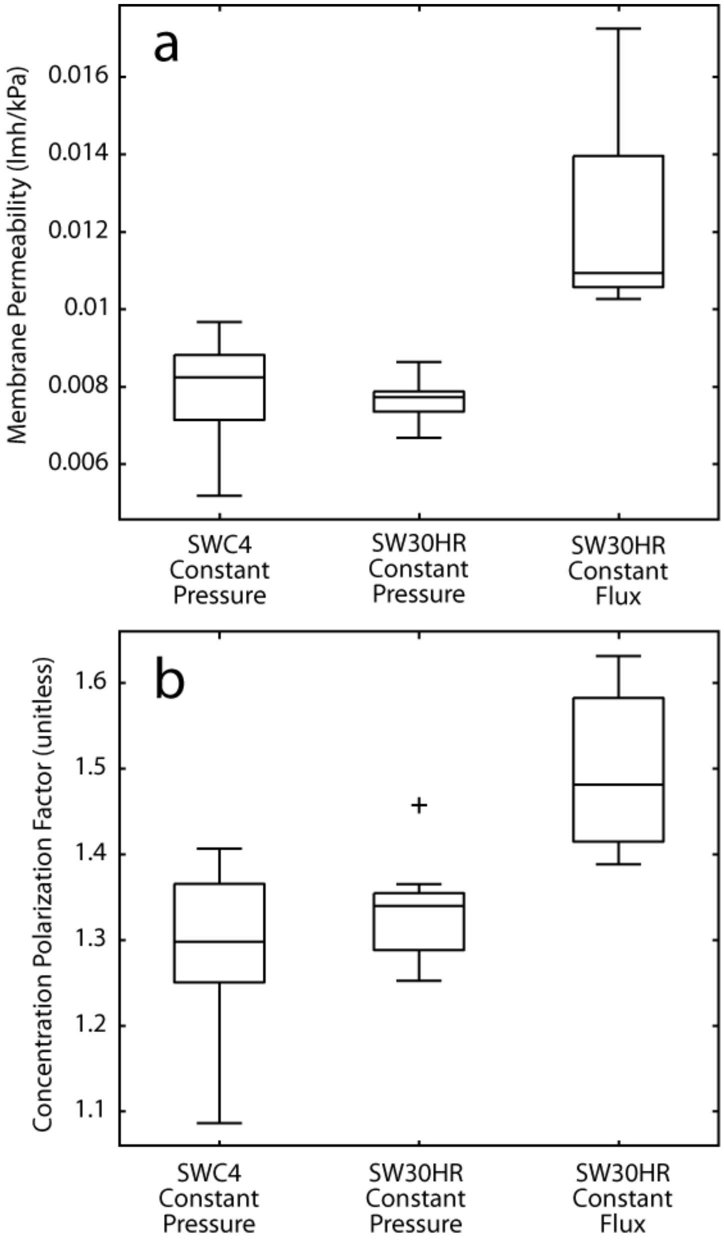

Figure 4-6. Box plots of intrinsic membrane permeability (a) and concentration polarization factor (b) found in 26 experiments where salt concentration varied during the course of the RO run. Constant-pressure experiments were performed at 6,900 kPa. Constant-flux experiments were performed at 20 lmh. Sample sizes were 6, 15, and 5 left to right. Boxes cover the interquartile range (from 25th to 75th percentile) with the median designated by the interior line. Whiskers extend to the most distant data points that are not outliers. Outliers are defined as greater than Q_3 + 1.5(Q_3-Q_1) or less than Q_1 - 1.5(Q_3-Q_1) where Q_1 is the 75th percentile and Q_3 is the 25th percentile.

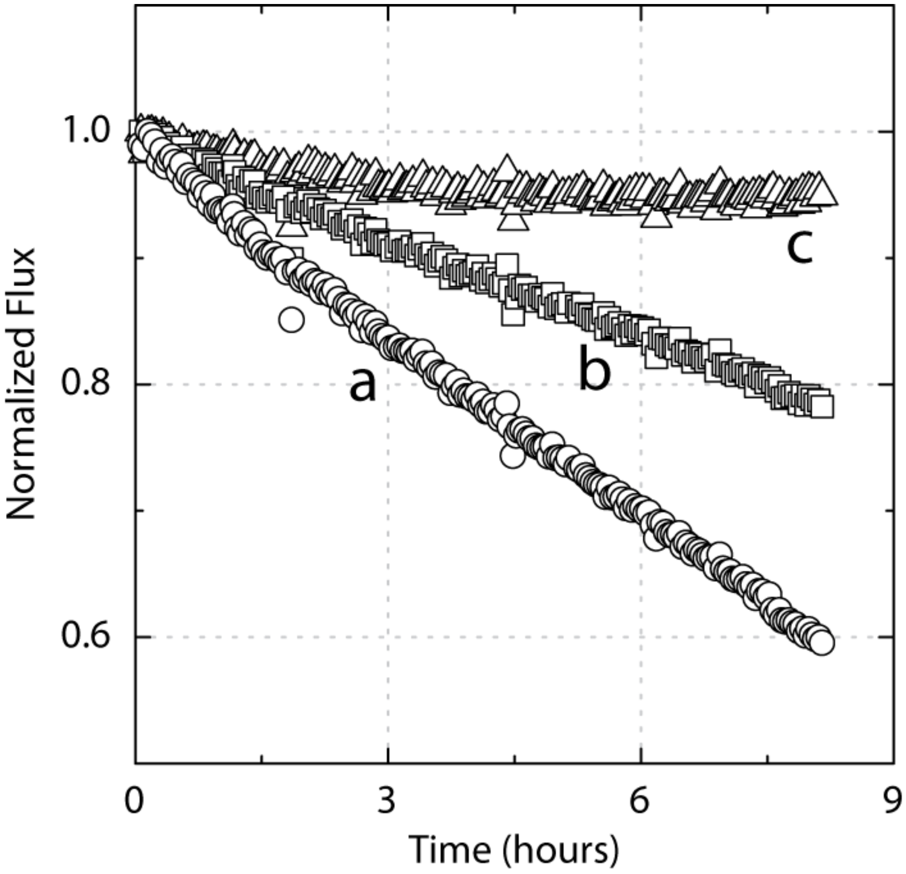

Figure 4-7. Comparison of data treatment methods for a San Diego seawater experiment where permeate was wasted to increase the concentration of feed salts. In (a) the flux is plotted directly. In (b) the concentration polarization factor was ignored and the bulk feed osmotic pressure was used to calculate specific flux. In (c) the specific flux was calculated with a concentration polarization factor of 1.31. All curves were normalized to their initial flux values.

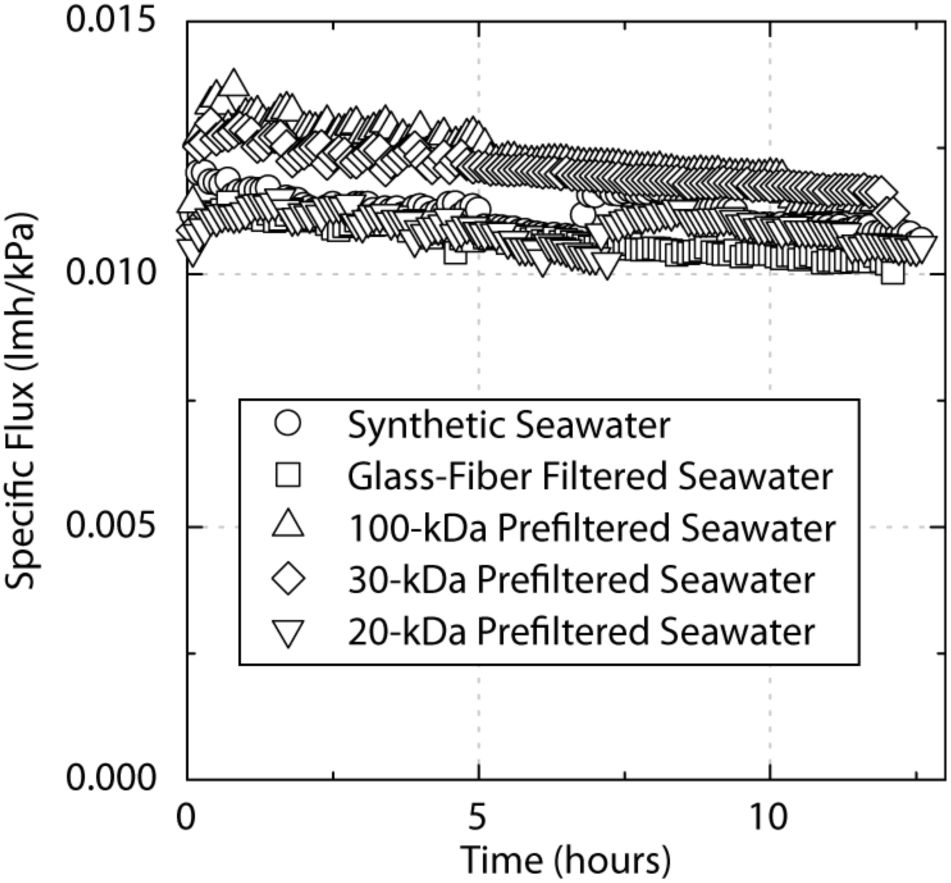

Figure 4-8. Membrane permeability over time for five transient recovery RO tests on seawater prefiltered with various size cutoff membranes. Synthetic seawater was used as a control containing no organic matter.

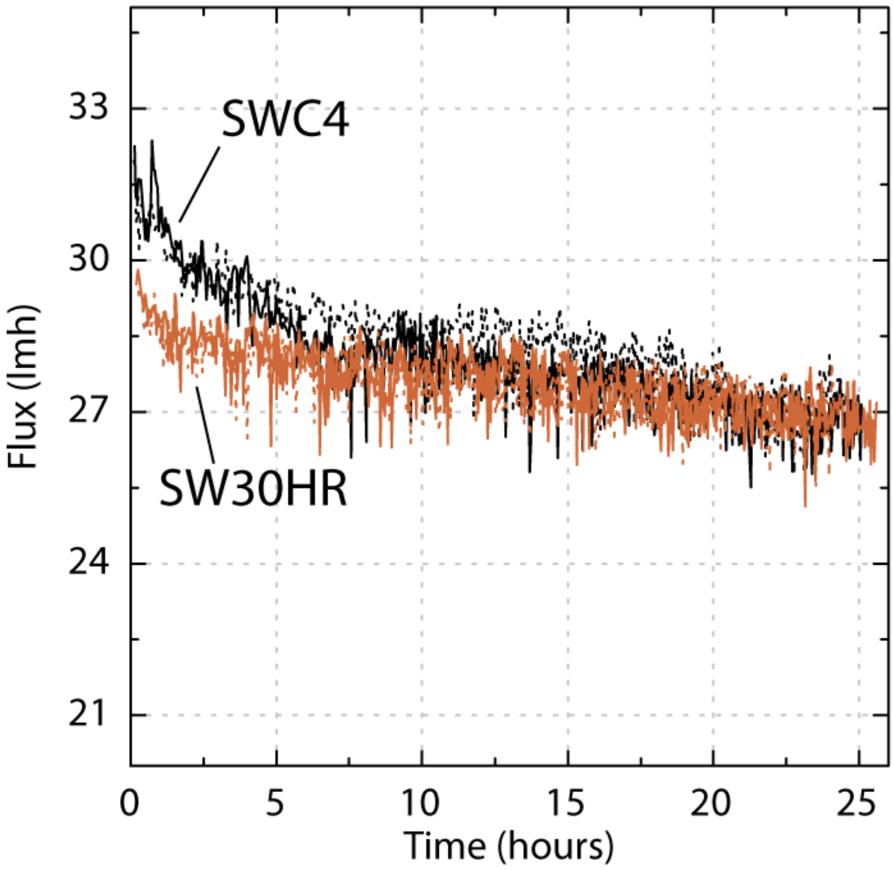

Figure 4-9. Comparison of compaction characteristics for SWC4 and SW30HR RO membrane coupons. Two runs are displayed for each coupon. SWC4 membranes had a higher initial flux than SW30HR, but the final flux values were very similar, indicating that SWC4 experienced more compaction. All runs were performed with a solution of 32 g/l NaCl in DI water at a constant pressure of 6,900 kPa. Salt rejection was between 99.4 and 99.7% for the four experiments.

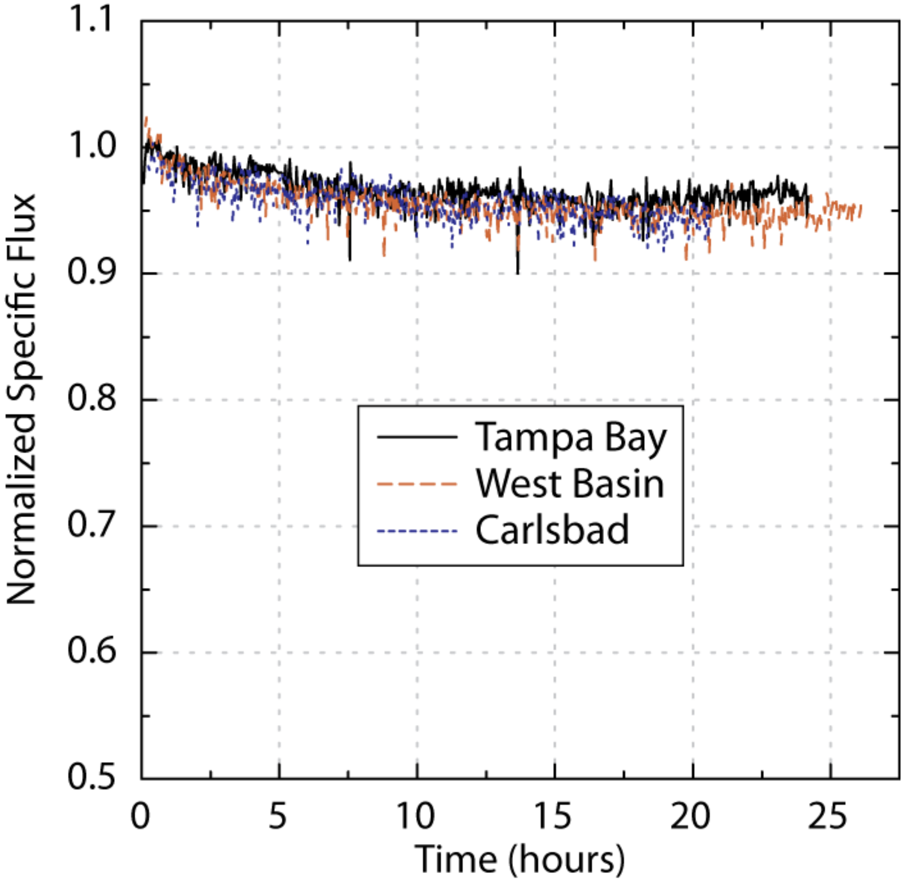

Figure 4-10. Flux data for three seawater sources in full recycle RO experiments. Before each run, the water was prefiltered through a 0.45-µm microfiltration membrane. Runs were performed at 6,900 kPa and 800 ml/min concentrate flow rate. Calculated crossflow velocity was 47 cm/sec and Reynolds number was 270. Salt rejections were 99.7, 99.5, and 99.8%, respectively. Initial specific flux values were 0.0058, 0.0062, and 0.0062 lmh/kPa, respectively.

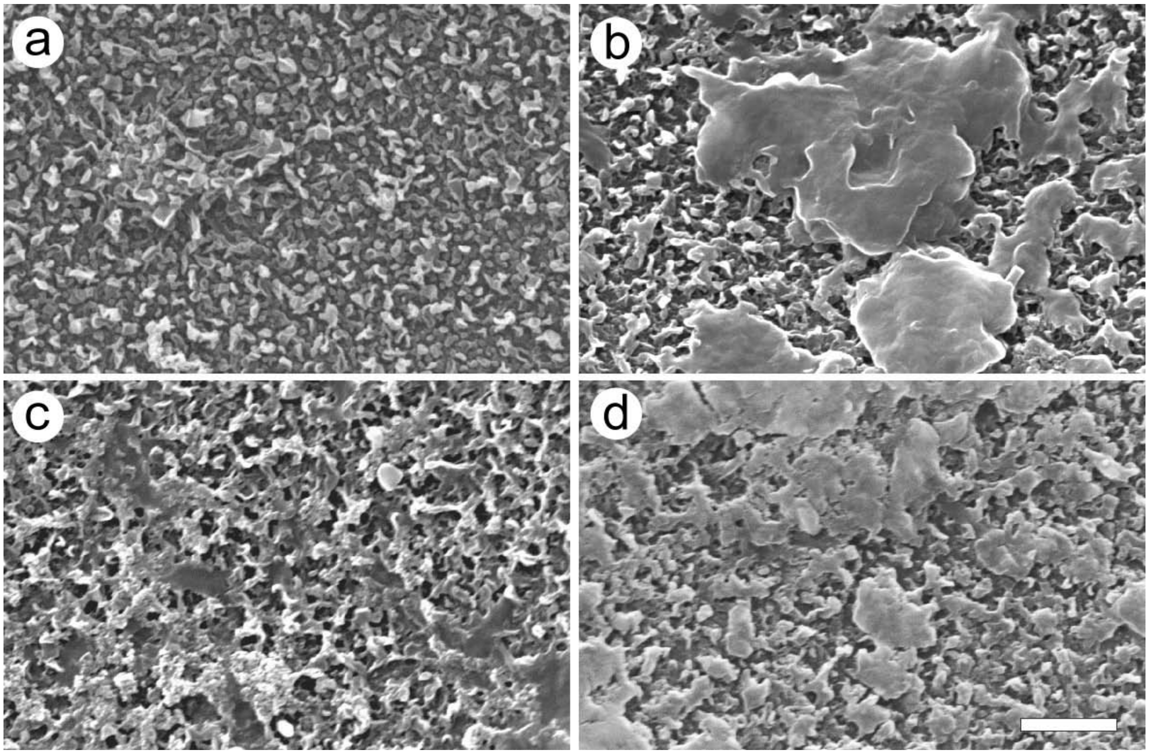

Figure 4-11. (a) Clean RO membrane. (b) Membrane fouled with Tampa Bay seawater. (c) Fouled with West Basin seawater. (d) Fouled with Carlsbad seawater. White bar is 2 μm.

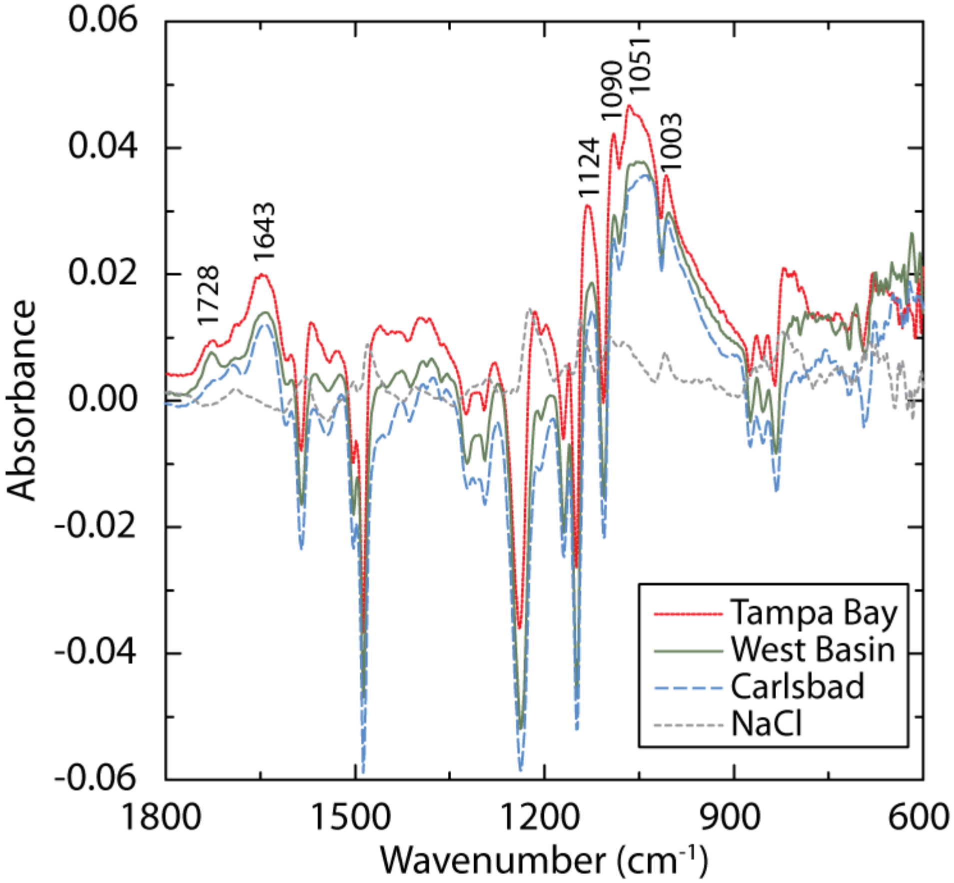

Figure 4-12. Infrared spectra of foulant material on RO membrane coupons tested with three natural seawaters. Background (the underlying membrane absorbance spectrum) was subtracted. For comparison, the same method was employed for a membrane that was used only for filtering a solution of 32,000 ppm NaCl in deionized water.

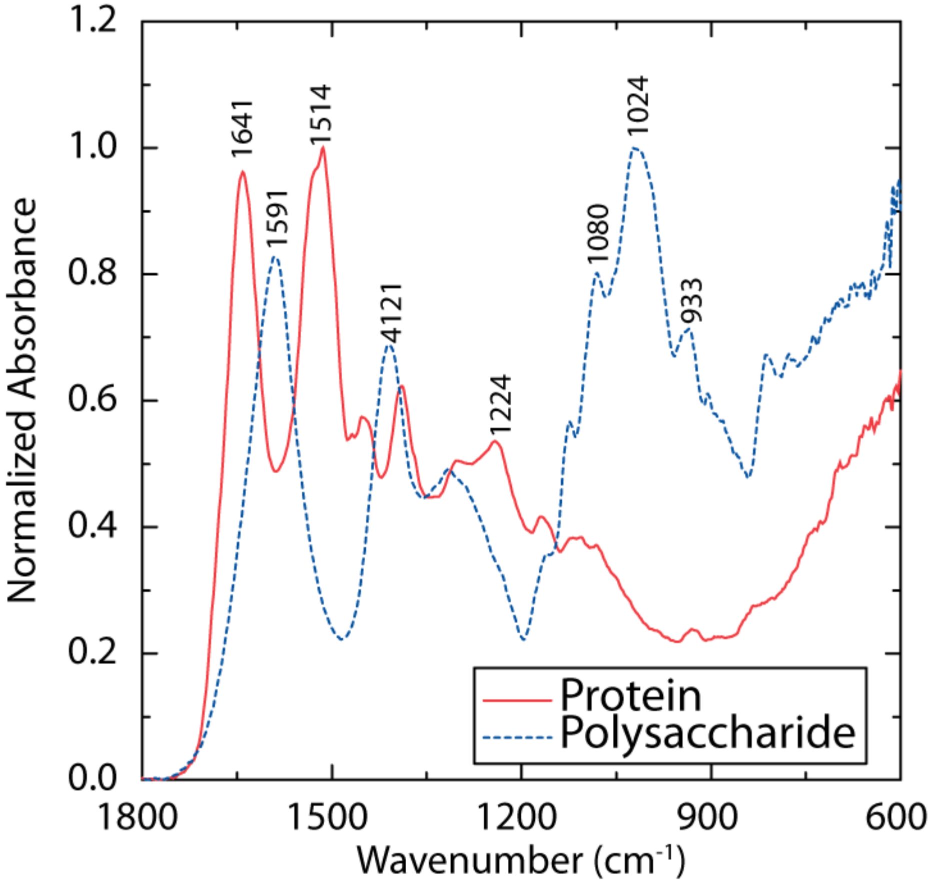

Figure 4-13. Infrared absorbance spectra of protein and polysaccharide for comparison to fouled membrane absorbance spectra. The protein sample was BSA. The polysaccharide sample was sodium alginate.

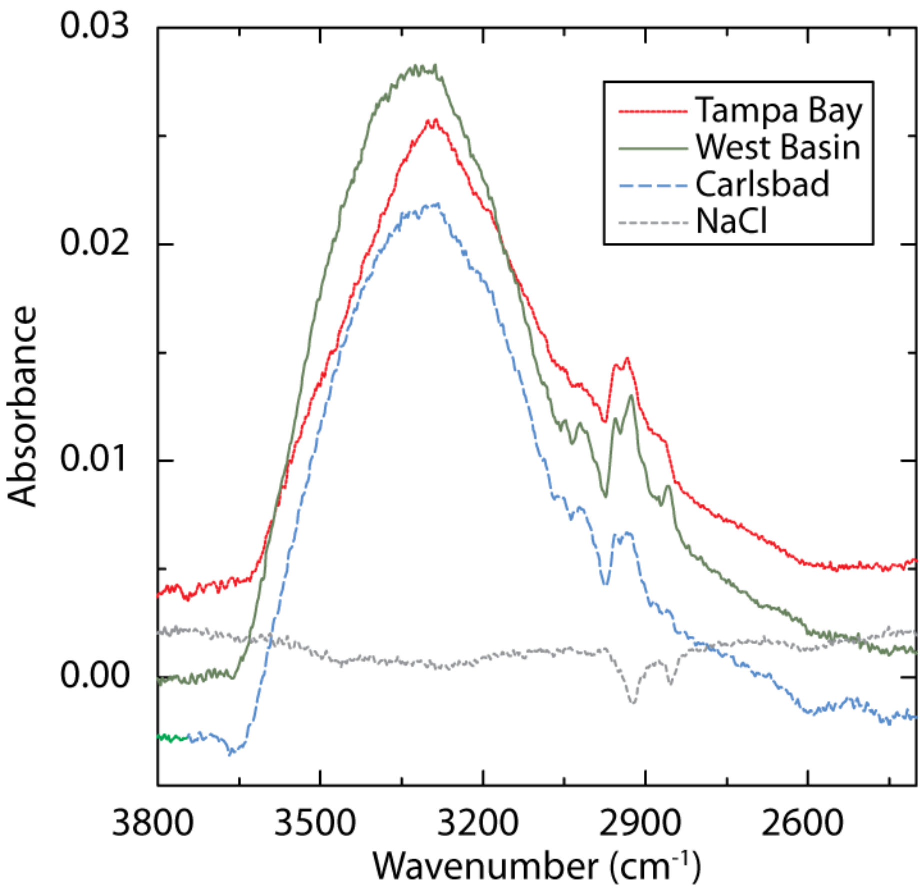

Figure 4-14. Infrared absorbance spectra in the region 2,400 to 3,800 cm^{-1} for RO membranes fouled with three natural seawaters. The background membrane spectra have been subtracted in each case. For comparison, the same method was employed for a membrane that was used only for filtering a solution of 32,000 ppm NaCl in deionized water.

5 REVERSE OSMOSIS FOULING BY MARINE ALGAE

Natural waters caused very little organic fouling of RO membranes in the bench-scale results of the previous chapter, though some organic matter did deposit on the membranes. A question arose, then, as to whether situations could occur when sufficient organic matter was present to cause measurable flux decline. One situation where high levels of organic matter would be present is during an algal bloom. As noted in the literature review, fouling by marine algae and AOM is a cause of concern for desalination facilities. Red tide events have severely damaged pilot MF/RO systems (Ishida 2006) and full-scale RO systems with dual media filtration pretreatment (Petry et al. 2007; Kim et al. 2007; Sambidge 2008). In these reports little information was collected as to the extent to which AOM fouling occurred. The laboratory experiments described in this chapter elucidate the magnitude of fouling by AOM on RO membranes.

The main hypothesis of this chapter was that dissolved AOM would cause significant RO fouling. This was expected because several literature reports discuss fouling by colloids and natural organic matter on RO membranes (i.e. Zhu and Elimelech 1997; Kumar et al 2006; Chong et al 2007) and high concentrations of colloids and organic matter are present in an algal bloom scenario. Dissolved AOM is the material most relevant to a full-scale RO process because it can pass through many pretreatment processes. Experiments were performed to determine the extent of dissolved AOM fouling compared to fouling by bulk algal material (comprised with a combination of cells, cell-derived particles, and dissolved AOM).

The second hypothesis was that a coarse permeate carrier would cause more exacerbated fouling than a fine permeate carrier. The coarse permeate carrier had a wider gap between fibers that allowed a greater degree of membrane deformation. Foulants were expected to more easily deposit in the relatively deep valleys caused by the coarse permeate carrier. Membrane autopsy was performed after fouling runs to determine the extent of foulant deposition.

The third hypothesis evaluated in this chapter dealt with fouling mechanism. It was expected that cake-enhanced concentration polarization (CECP) would be more important than cake hydraulic resistance. CECP has been previously reported as the main fouling mechanism for salt-rejection membranes (Hoek and Elimelech 2003). Flux data were modeled to elucidate the interplay between CECP and hydraulic resistance fouling mechanisms.

5.1 DESIGN OF EXPERIMENTS

Heterocapsa pygmaea, a bloom-forming dinoflagellate algal species, was cultured in the laboratory according to methods in Section 3.4. *H. pygmaea* culture and AOM were spiked into the RO unit feed and flux was measured over time at constant pressure. The RO unit configuration was shown in Figure 3-1. Experiments were performed with the two commercial membranes studied in Chapter 4: SW30HR and SWC4. Two types of permeate spacer were also tested, one having a finer mesh spacing than the other. The coarse permeate spacer was provided by GE Osmonics with the SEPA II crossflow testing apparatus. The fine permeate spacer was cut from the permeate carrier of a commercial spiral-wound nanofiltration module (ESNA-1 LF, Hydranautics, Oceanside, CA; this was the same spacer used for extra support in the dead-end low-pressure experiments of Chapter 6). The two permeate carriers are shown in Figure 5-1.

Two experiment types were performed: a direct algal spike and a spike of microfiltered AOM. Direct algal spikes proceeded by adding algal culture to prefiltered (0.45 μm) San Diego seawater to make a 20-liter batch of algae at 40,000 cells/ml. Cells were harvested during their active growth phase and were observed to be swimming vigorously in the seawater matrix. The spiked seawater sample was run on the bench-scale reverse osmosis unit in full recycle mode (permeate and concentrate fed back to the feed tank), at 6,900 kPa pressure and a flow rate of 800 ml/min (which translates roughly to a crossflow velocity of 0.47 m/s and Reynolds number of 270). Temperature was held at 20 ± 1˚C. Before each run, the membrane was compacted and greater than 98% salt rejection was verified using a 32 g/l NaCl solution.

After performing the direct algal spike experiment the sample was removed and filtered through 0.45-μm membranes (Millipore MCE) in the dead-end low-pressure filtration apparatus. The resulting sample was then used for the microfiltered AOM experiment with the same operating conditions as the direct algal spike.

Algae were counted and fluorescence was measured over the course of the experiments to determine changes in feed-water composition. Fouled membranes were removed and examined using visual imaging, laser-scanning cytometry (LSC), scanning electron microscopy, and infrared spectroscopy to determine the extent and spatial patterns of fouling.

A fouling model was applied to help elucidate flux decline mechanisms. The flux decline contributions of hydraulic cake resistance and cake-enhanced concentration polarization (CECP) were determined.

5.2 FLUX DECLINE CAUSED BY ALGAE

Direct algal spikes caused greater flux decline than microfiltered AOM for all three membrane/permeate carrier combinations (Figure 5-2). This was expected, since the direct spikes contained algal cells and higher concentrations of AOM. Microfiltered AOM caused slightly more flux decline (five percent) on the coarse permeate carrier than it did on the fine permeate carriers (two to three percent).

No significant difference in fouling was apparent between the two membranes tested; both the direct algal spikes and the microfiltered AOM experiments resulted in similar flux decline for each membrane type. This is interesting since roughness values measured by AFM were quite different between the two membranes; 78.3 ± 7.8 and 150.5 ± 5.4 nm for SW30HR and SWC4 membranes, respectively. It seems that macroscale roughness (on the order of millimeters) caused by the shape of the permeate carrier membrane was more important than nanoscale roughness. The difference in membrane shape caused by fine and coarse permeate carriers is evaluated in Section 5.3.

5.3 AOM CHARACTERIZATION

During the direct algal spike into the RO system a dramatic drop in cell number was observed. Cells first showed signs of damage in that they ceased swimming. As the run continued, cell number decreased until only a few intact cells could be observed. Subsequent experiments showed that the cells were broken apart as they passed through the concentrate valve. Pressure drop over the valve was high (about 6,400 kPa) and the hydraulic residence time in the valve was quite small (about 2×10^{-4} seconds) so the hydrodynamic shear was quite high, causing the observed algal breakup. These initial results on cell breakup led to a more detailed investigation into the effects of shear on algal cells and on their subsequent fouling in microfiltration and ultrafiltration. The results of that investigation are found in Section 6.2.

Figure 5-3 shows the change in cell concentration during one of the direct algal spike runs; results were similar for all of the direct algal spike experiments. Approximately half of the cells were broken apart in the first hour then the cell breakup rate flattened as the run progressed. In Section 6.2 the hypothesis is presented that the algal cells removed in the early period were the weaker cells in the population. The algal cells that remained for a longer time (and thus a higher number of passes through the valve) were the structurally stronger cells.

Internal organelles, biopolymers, and dissolved AOM were released as algal cells broke apart. Much of the released organic matter was fluorescent material that caused an increase in bulk fluorescence of the sample (Figure 5-3). The bulk fluorescence increase was likely due to the release of light-harvesting pigments peridinin and chlorophyll *a*. The total concentration of pigment did not increase, but before shear self-shading in algal cells resulted in lower fluorescence; this self-shading is called the “package effect” (Kirk 1994). As the cells were broken apart the pigments were released and the package effect was minimized. Most of the released fluorescent material was dissolved as confirmed by the fluorescence readings of 0.45-µm filtered samples shown in Figure 5-3. Filtered fluorescence was negligible at the beginning of the run, but as cells were sheared the filtered fluorescence and bulk fluorescence increased and decreased at similar rates.

Fluorescence peaked and began to decay at about four hours for the unfiltered sample and seven hours for the filtered sample. This decrease in fluorescence with time could be due to adsorption of fluorescent material on the membrane during the run. Alternatively, bacteria may have been actively metabolizing the fluorescent pigments. During one of the runs bacteria levels were measured using the techniques in Section 3.6.2. Bacteria more than doubled during the run, from 5×10^5 to 1.2×10^6 cells per ml confirming that biological activity was occurring. The extent to which pigments were degraded biologically, however, is unknown.

5.4 FOULED MEMBRANE AUTOPSY

5.4.1 Visual and fluorescence image analysis

A distinct brown coloration was observed in scanned images of RO membranes fouled by a direct algal spike in Figure 5-4 (column 1, *a*-*c*). When the coarse permeate carrier was used (*a*), foulants preferentially deposited in a pattern caused by the feed spacer. With the fine permeate carrier the SW30HR membrane (*b*) showed a slight pattern in the visual image and a more apparent pattern in the LSC fluorescence image (column 2). No discernable feed spacer pattern was seen in the SWC4 fine permeate carrier case (*c*). Microfiltered AOM caused a distinct foulant pattern in the coarse permeate carrier case (*d*), but no obvious pattern could be seen in either of the fine permeate carrier samples (*e*, *f*).

Fluorescence histograms (Figure 5-4 column 3) show that the mean fluorescence readings were higher and the foulants were more evenly distributed (histograms were more Gaussian-shaped) for direct algal spikes when the fine permeate carrier was used (*b*, *c*). With the coarse permeate carrier (*a*) the distribution showed a strong tail toward higher fluorescence readings. This tail represents the locally high fluorescence data points, while the overall fluorescence (mean) was lowered because some regions had lower foulant accumulation and lower fluorescence.

With microfiltered AOM the fluorescence histogram for the coarse permeate carrier (*d*) had a tail toward high fluorescence from the locally elevated patches of foulant. With the fine permeate carrier (*e*, *f*), however, the fluorescence histograms were sharp and narrow. A control scan of a membrane used to filter an organic-free sodium chloride solution gave an almost identical histogram as those in Figure 5-4 *e*3 and *f*3 indicating that the mean fluorescence of 660 was the background fluorescence reading for a non-fouled membrane. Thus it was concluded that no measurable foulants were detected by the LSC when a fine permeate carrier membrane was used with microfiltered AOM. There was little to no deposition of fluorescent material.

The fact that LSC was able to detect AOM foulants lends insight into the nature of the organic matter. Strict carbohydrates (starches, dextrans, or other polymers containing only sugar monomers) would not be expected to display significant fluorescence. Aminosugars or proteins, however, could potentially exhibit fluorescence and chlorophyll and peridinin would yield a positive response.

Fouled membrane images were analyzed by Fourier transform analysis. Power spectra of horizontal transects (in the direction of feed-water flow) were obtained. Figure 5-5 shows spectra for the six fouled membranes of interest and two control samples (coarse and fine permeate carriers run with non-fouling water). The direct algal spike with the coarse permeate carrier (*a*) resulted in strong peaks at 1.94, 3.87, and 10.38 wavenumbers (cm^{-1}). Wavenumbers are the frequency of a repeating feature on the images. Reciprocal wavenumbers give the length (i.e. wavelength) of those features. Thus the peak at 1.94 resulted from the foulant pattern caused by the 0.5-cm mesh feed spacer. The 3.87 cm^{-1} peak was a harmonic of the foulant pattern peak; harmonics are usually found in power spectra at halves and multiples of a strong peak (Smith 1999). A second harmonic was evident at 5.81 cm^{-1} in the coarse permeate carrier direct algal spike spectrum. The other strong peak of interest at 10.38 cm^{-1} was caused by dimples in the membrane where it deformed into the permeate carrier. The reciprocal indicates that the coarse carrier had a repeating length scale of about 0.09 cm. This peak was stronger than that found for a control sample run with sodium chloride only (*g*) because foulants had preferentially deposited in the dimples giving them a darker color and stronger power spectrum signal.

Foulant patterns caused by the feed spacer were markedly reduced in the fine-permeate carrier direct spike power spectra (Figure 5-5 *b* and *c*). Peaks in the 1.9 cm^{-1} region were slightly evident but were much less intense than in the coarse feed spacer sample. This was due to the foulant material being more evenly distributed across the membrane surface instead of preferentially depositing around the feed spacer. The fine permeate carrier caused a characteristic peak at 17.1 cm^{-1} indicating that the fine permeate carrier dimples had a length scale of 0.06 cm, which was 2/3 the mesh size of the coarse permeate carrier. The fine permeate carrier peaks were small in the direct algal spike case because foulants had covered the dimples.

Microfiltered AOM on a coarse permeate carrier (*d*) resulted in similar peak locations as those for the direct algal spike (*a*). The 2.01, 3.80, and 5.65 cm^{-1} peaks were smaller in magnitude because the feed spacer pattern was not as prominent. The 10.92

cm^{-1} peak was about as high as in the direct spike, indicating that the permeate carrier pattern was just as strong. The peak was stronger than the control case (*g*) indicating that foulants had preferentially accumulated in the dimples and made the pattern more obvious.

Microfiltered AOM run on the fine feed spacer (*e*, *f*) resulted in prominent peaks at 17.1 and 8.55 cm^{-1} which can be compared with the fine carrier control sample (*h*) to show that they arose from the dimple pattern. The SW30HR membrane (*e*) also showed a small peak at 2.0 cm^{-1} indicating that some foulant material had deposited in the feed-spacer pattern. The SWC4 membrane did not show that peak so feed-spacer-pattern fouling was not evident.

In short, image analysis clearly distinguished between the coarse and fine permeate carrier membranes based on their dimple pattern. More importantly, the coarse permeate carrier caused foulants to deposit according to the feed spacer pattern. This is a very interesting result suggesting that the shape of the permeate carrier is important in determining how foulants accumulate around the feed spacer. Both the permeate carrier and feed spacer were important in defining the crossflow hydrodynamics and foulant deposition.

5.4.2 Scanning electron microscopy

SEM images (Figure 5-6) reveal foulant accumulation at the micron scale. Letters *a* through *f* in Figure 5-6 designate the same samples as *a* through *f* in Figure 5-4. Letters *g* and *h* show new, clean SW30HR and SWC4 membranes, respectively. In the direct algal spike fouled membranes (*a*, *b*, *c*) foulant material completely covered the membrane surface. The SEM images were taken at locations where a crack was present in the dried sample in order to provide a qualitative picture of the depth and thickness of the foulant layer; the membrane surface could not be seen in any of the images. The smooth foulant surfaces around the cracks show what was found over the majority of the sample coupon surface. Foulant material created a relatively smooth, thick layer. No algal cells were identified in any of the samples examined suggesting that whole-cell deposition was less important than colloidal and dissolved organic matter deposition; however, it is unclear whether whole cells would be identifiable by this technique, since the samples were not prepared in a way in which whole cells would be preserved.

For the microfiltered AOM experiments (*d*, *e*, *f*) SEM images showed some organic-matter accumulation on the membrane surfaces in all three cases. Fouling was not spatially homogeneous, but Figure 5-6 *d*, *e*, and *f* give typical observations. By comparison with clean membranes (*g* and *h*) it can be surmised that the microfiltered AOM foulant was not thick enough to completely mask the underlying membrane features. All three microfiltered AOM cases had qualitatively similar amounts of material present. The coarse permeate carrier (*d*) seemed to result in slightly more organic matter accumulation, but the effect was not quantifiable. Foulants accumulated in patches, with clumps of material found next to clean membrane surfaces. This suggests a nucleation phenomenon where incoming foulants had a higher affinity for pre-adsorbed foulant regions as opposed to the clean membrane; foulants may adhere better to other foulants than they do to the membrane.

5.4.3 Infrared spectroscopy

ATR-FTIR spectra give information about the chemical character of foulants. In Figure 5-7 three regions of interest are plotted and two clean-membrane spectra are given for comparison. All the curves here are averages of at least three and usually five locations on the membrane. The large peak between 3,000 and 3,600 cm^{-1} is in an area sensitive to N-H stretching of proteins or O-H stretching of polysaccharides and adsorbed water (Mayo et al. 2004). The direct algal spikes had the highest absorbance in this region due to the high concentration of mass deposited. The coarse membrane was highest of all indicating a greater foulant concentration than the others, which is perhaps inconsistent with the visual and LSC fluorescence observations; the coarse permeate carrier had more patchy foulant and the underlying membrane was visible so one would expect that some measurements would be taken from cleaner areas than others and the average absorbance would be decreased. Microfiltered AOM (*d*, *e*, *f*) showed intermediate absorbance indicating that a significant amount of foulant material had deposited and was detectable by infrared spectroscopy. Note, however, that the spectra are only semi-quantitative; the evanescent infrared wave passing through the ATR apparatus is most sensitive to material pressed directly on the crystal and material stacked above is blocked. Thus, thick cake layers would not be completely detected.

The FTIR region between 1,800 and 1,300 cm^{-1} is an area where proteins absorb in a characteristic pattern. Proteins are indicated by strong absorbance at the 1,650 cm^{-1} amide I peak, the 1,550 cm^{-1} amide II peak, and the 1,350 to 1,450 cm^{-1} amide III region (Nelson 1991; Mayo et al. 2004). Here the two fine-permeate carrier samples had higher absorbance than the coarse permeate carrier samples for direct algal spikes. This is more in line with visual and LSC fluorescence observations, since the membranes were completely covered with foulants when fine permeate carriers were used. With microfiltered AOM the protein peaks were greater for the coarse permeate carrier, which is consistent with its greater flux decline and its greater visible and fluorescence activity than the microfiltered AOM samples on the fine permeate carrier. Protein measurements from the wet-chemical BCA assay performed with desorbed foulant material (Figure 5-8) corroborate the results of the FTIR data just described. The fine permeate carrier experiments had roughly twice as much protein than the coarse permeate carrier for direct algal spike experiments. For microfiltered AOM the coarse permeate carrier resulted in slightly higher protein numbers, but these were in the low range of the protein assay and not as trustworthy; the control coupon run with only NaCl (Figure 5-8g) gave a similar protein measurement as the microfiltered AOM runs.

Carbohydrates are indicated in FTIR data by the C-O stretching region from about 900 to 1,100 cm^{-1} (Mayo et al. 2004). As was the case for proteins, the direct algal spikes with fine permeate carriers showed higher absorbance than the coarse permeate carrier sample in the carbohydrate region. Microfiltered AOM showed less absorbance in this region. Though all the fouled samples were higher than the clean-membrane samples, they had very similar absorbance. Thus carbohydrates were evident in microfiltered AOM, but they were only slightly above background.

5.5 FOULING MECHANISMS

Flux decline in RO should not occur by a pore blocking mechanism since water passage is diffusional and the “pores” are too small for foulants to penetrate. Foulant cake-layer hydraulic resistance is a more probable mechanism, since foulants are located on the membrane surface. Another mechanism for flux decline is cake-enhanced concentration polarization (CECP) which occurs because back-diffusion of ions is hindered by the tortuous foulant cake. The cake also reduces crossflow velocity at the membrane surface so salts are not as easily swept away. It is difficult to determine whether hydraulic resistance or CECP is the major foulant mechanism because the resultant flux decline is similar; in fact, it is likely that both mechanisms operate simultaneously. Here the theory behind the two mechanisms is explored to help determine which is dominant.

An approach for determining the relative contributions of hydraulic resistance and CECP is presented here, building on work by Hoek and Elimelech (2003). Hydraulic resistance is modeled using the Carman-Kozeny equation written as

$$\Delta P_c = \frac{180 v \mu (1-\varepsilon)^2}{d_p^2 \varepsilon^3} \delta_c \tag{5-1}$$

Here ΔP_c is the pressure drop (kPa) due to hydraulic resistance, v is the flux (m/s), μ is viscosity of water (1.00 x 10^{-6} kPa·s at 20°C), ε is the porosity (unitless), d_p is the particle size (m) and δ_c is the cake thickness (m).

CECP results in a reduced, or hindered diffusion coefficient D^* that arises because solute molecules must travel a longer, more tortuous path to diffuse away from the membrane. D^* is related to the bulk diffusion coefficient, D_∞, by

$$D^* = \frac{\varepsilon D_\infty}{\theta^2} \tag{5-2}$$

where θ is the tortuosity and θ^2 is called the tortuosity factor. Note that Hoek and Elimelech (2003) defined θ^2 as the tortuosity, but here we use the nomenclature as set forth in previous work (Boudreau 1996). It is important to recognize that tortuosity is not strictly defined by pore geometry. The term arises from a modification of Fick's First Law given in unidimensional form as

$$F = -\frac{\varepsilon D_\infty}{\theta^2} \frac{\partial C}{\partial x} \tag{5-3}$$

where F is the solute flux at a concentration C and location x. Thus the tortuosity factor is a term that acts on the diffusion coefficient to account for hindrances and it must be evaluated experimentally. The tortuosity factor should, of course, be related to pore geometry and one relationship that fits many data sets is (Boudreau 1996)

$$\theta^2 = 1\text{-}ln(\varepsilon^2) \tag{5-4}$$

The tortuosity factor defined here is related only to the porosity, but in reality the tortuosity will vary according to other geometrical properties like grain shape and pore-size heterogeneity.

Hindered diffusion and crossflow velocity in the cake layer result in a diminished mass transfer coefficient, k^*.

$$k^* = \left[\delta_c\left(\frac{1}{D^*} - \frac{1}{D_\infty}\right) + \frac{1}{k}\right]^{-1} \tag{5-5}$$

Here k is the mass transfer coefficient obtained when no foulant cake is present. Using k^* the concentration polarization factor f_{cp} can be determined by

$$f_{cp} = \frac{C_m}{C_b} = \left(1 - R_i + R_i \exp\left(-\frac{V}{k^*}\right)\right)^{-1} \tag{5-6}$$

The CECP model predicts that the salt concentration at the membrane surface C_m will be elevated compared to the bulk salt concentration C_b when a cake is present so the observed salt rejection R_o should be diminished according to

$$R_o = 1 - \frac{C_m - R_i C_m}{C_b} \tag{5-7}$$

where R_i is the intrinsic membrane salt rejection.

The pressure drop $\Delta\pi^*$ caused by CECP is given by

$$\Delta\pi_m{}^* = f_{os} C_b R_o \exp\left(\frac{V}{k^*}\right) \tag{5-8}$$

where f_{os} is a factor relating salt concentration to osmotic pressure. In Chapter 4 an empirical relationship for f_{os} was used (Equation 4-11) and the same is retained here. Salt concentrations were determined from conductivity measurements as shown in Equation 4-14.

The sum of cake-resistance pressure drop, CECP pressure drop, and intrinsic membrane pressure drop must be equal to the applied pressure ΔP, so

$$\Delta P = \Delta P_c + \Delta \pi_m * + \Delta P_m \tag{5-9}$$

where $\Delta P_m = v\mu R_m$ with R_m being the intrinsic membrane resistance. Note that $\Delta \pi_m*$, the result of CECP, is elevated compared to the osmotic pressure from concentration polarization without a cake layer, $\Delta \pi_m$. To quantify the degree of additional pressure drop $\Delta \pi_a$ caused by CECP we will here use

$$\Delta \pi_a = \Delta \pi_m * - \Delta \pi_m \tag{5-10}$$

The AOM in our studies was not well characterized and we are left without accurate knowledge of particle size, porosity, or cake layer thickness. Further, the relationship between tortuosity and porosity may not be the same as Equation 5-4. Because of these uncertainties we cannot strictly determine whether cake layer resistance or CECP was most important in the observed flux decline. We can, however, ask the model to tell us which mechanism would be more important over a range of possible particle sizes, porosities, and tortuosities. To do this we used an iterative equation solver script written in Matlab. An initial guess at cake thickness was made followed by calculation of pressure drop from hydraulic resistance ΔP_c using Equation 5-1. At the same time the hindered mass transfer coefficient $k*$ was calculated with Equation 5-5 and f_{cp} was determined with Equation 5-6. The new membrane wall concentration ($C_m = f_{cp}C_b$) was fed to Equation 5-7 for determining the observed salt rejection R_o and the cake-enhanced osmotic pressure $\Delta \pi*$ was found with Equation 5-8. These steps were repeated with varying cake layer thickness until the sum of hydraulic resistance pressure drop, CECP pressure drop, and intrinsic membrane pressure drop was equal to the applied pressure.

With the above modeling procedure we found the pressure drops associated with hydraulic resistance and CECP for the direct algal spike on the SWC4 membrane with a fine permeate spacer. Measured operating conditions at the end of the run (when flux had declined to its lowest level) were input to the model. Flux decline was ten percent (27.1

lmh initial, 24.4 lmh final), pressure was 6,880 kPa, and intrinsic membrane salt rejection was 99%. The pre-fouling mass transfer coefficient (k) was calculated using a rearrangement of Equation 5-6 with f_{cp} equal to 1.32 as determined during the clean-water flux run with procedures from Chapter 4. Intrinsic membrane resistance R_m was also determined during the clean-water flux run. Other parameters were $D_\infty = 1.61 \times 10^{-9}$ m^2/s, $\mu = 1.00 \times 10^{-6}$ kPa-s (at 20°C), and bulk conductivity $\sigma_b = 50.0$ mS/cm.

Figure 5-9 shows the modeling results for varying particle size, porosity, and tortuosity. Similar results would be obtained for the other fouled membrane cases except that the cake thickness and total pressure drop would change with the level of fouling. The first interesting finding is that for a given porosity and tortuosity there exists a maximum cake thickness obtained when particle size is large and CECP dominates (see Figure 5-9a). This maximum exists because any thicker cake (with the same porosity and tortuosity) would cause more CECP resistance than was found in the experiment. The cake can only be thicker if the porosity is higher (Figure 5-9b) making the hindered diffusion coefficient (D^*) greater, as is described in Equation 5-2. Coupled with that effect, a high porosity means a lower hydraulic resistance, as described in Equation 5-1; thus very porous cakes are much more likely to cause CECP resistance than hydraulic resistance. If the tortuosity is high the cake thickness must be smaller (Figure 5-9c). Tortuosity has an inverse effect on cake thickness because higher tortuosity gives a lower D^*. Pressure drop does not vary as much with tortuosity changes as it does with particle size or porosity changes, so pressure drop seems less sensitive to tortuosity.

In general Figure 5-9 shows that hydraulic resistance is the dominant mechanism at low particle size, porosity, or tortuosity. As any of these increase CECP becomes dominant. A crossover point exists where hydraulic resistance and CECP contribute equally to the pressure drop. For the analyses in Figure 5-9 the crossover point was at $d_p = 10$ nm, $\varepsilon = 0.39$, and $\theta^2 = 2.5$; however, these values are only valid for the conditions of the modeling (described in the caption). To see how the crossover point changes as conditions vary, further modeling was performed.

For a given flux decline measurement there exists only one particle size and cake thickness combination that fits the model at the crossover point for each porosity and tortuosity value. Plots of cake thickness and particle size versus porosity at the crossover points for several values of tortuosity are shown in Figure 5-10; these are here called crossover point curves. The curves give information about the relative importance of hydraulic resistance and CECP for cakes with different properties. For example, a cake that is 20 μm thick and has a tortuosity factor (θ^2) of 2 will have equal pressure drops from hydraulic resistance and CECP when the porosity is about 0.9. If the porosity or tortuosity were lower, hydraulic resistance would dominate (as we know from Figure 5-9). A cake made up of 20-nm particles with a porosity of 0.4 would be at its crossover point if the tortuosity were one. If the tortuosity is higher than one, CECP will dominate.

From the crossover point curves a few suppositions can be made about the importance of hydraulic resistance compared to CECP for this experimental run (and the other fouled-membrane tests performed here under similar conditions). First if we assume a set of reasonable cake parameters such as a cake porosity of 0.4 (what would be found in a random assemblage of spherical particles) and a tortuosity factor of 2.83 (found from the $\theta^2 = 1\text{-}\ln(\varepsilon^2)$ relationship given by Boudreau (1996)) then hydraulic resistance would only dominate if the particle size were less than about 15 nm. The cake thickness in that case would be limited to about six μm. It is certainly possible that such a thin, densely packed cake could form at the membrane surface. SEM images (Figure 5-6) of dried foulants show a homogeneous layer with no large particles present. However, there is much more room for possibility on the other side of the crossover point. The flux in these experiments, though high for RO, was much lower than the crossflow velocity and would likely yield a loosely packed cake. Indeed much of the wet foulant material imediately after the experiment could be rinsed away easily so it appeared to have only a loose attachment (the apparently tight, homogeneous cake in SEM images may have formed upon drying). This would mean a higher porosity and much more likelihood that CECP would dominate as a resistance mechanism.

One significant piece of evidence to shed light on the fouling mechanism is the salt rejection data. The model presented here suggests a 1% decrease in salt rejection if CECP dominates while if hydraulic resistance is dominant no change in rejection would be expected. Observed salt rejections for our experiments are plotted in Figure 5-11; observed rejection increased in all cases. The increase was similar for all six experiments, whether flux decline was observed or not. The coarse permeate carrier resulted in slightly lower rejection than the fine permeate carrier, perhaps because the membrane deformed to a greater extent and structural stability was not maintained; however, greater than 99.5% rejection was achieved by the end of the experiments, which was still very good for bench-scale tests.

Non-decreasing salt rejection data support the hydraulic resistance model and suggest that CECP did not dominate; however, it is possible that CECP did occur, but the membranes were still able to reject the salts and hide its effect. In Hoek and Elimelech's study (2003) a nanofiltration membrane with 70-80% salt rejection showed the biggest decrease in observed salt rejection and the greatest evidence for cake-enhanced concentration polarization. The RO membranes had 94 to 98% salt rejection and the observed salt rejection decreased very little so the evidence for CECP was not as strong, though they cited another of their studies where rejection was observed to decrease more significantly over a longer time period with the same membranes and similar colloidal foulants (Hoek et al. 2002). In our study the observed rejections were between 98.8 and 99.9% and always increased even as flux declined. Perhaps our highly rejecting membranes did not allow observation of the cake-enhanced concentration polarization phenomenon. Another possibility is that the increasing rejection due to membrane compaction masked the decrease in rejection that would have been observed with elevated feed salt concentration. Even though the membranes were compacted before the fouling runs it is possible that some degree of compaction was still occurring and the membrane rejection tightened over time.

In summary, there was not enough evidence to conclude whether hydraulic resistance or CECP was the dominant fouling mechanism in our experiments. Hoek and Elimelech (2003) assert that CECP will dominate for salt-rejecting membranes and in their study with 100-nm spherical particles CECP certainly did dominate. We used their data in our model and showed that for 100-nm particles CECP dominates for any porosity (0.1 to 1) and tortuosity (1 to 5). For the AOM in our experiments, however, there was a wide range of particle size, from dissolved up to the size of the algal cells themselves (10 to 15 μm). Such material could form dense cakes with low porosity; hydraulic resistance would then be more important than CECP.

5.6 CONCLUSIONS REGARDING REVERSE OSMOSIS FOULING BY AOM

Some important aspects of reverse osmosis fouling by bloom-forming algae have been elucidated. Deposition of AOM did not result in drastic flux decline even though significant amounts of material were present. Resistance to flux from the AOM cake layer was small compared to the inherent membrane resistance so water flux was only slightly impeded by the cake. These results strengthen the findings from Chapter 4 where natural waters were tested. In natural waters there was no apparent flux decline even though some organic matter deposition was found. Here we showed that much more organic matter—microfiltered algogenic organic matter—could attach to the membrane with very little change in flux. The case where significant flux decline did occur was when algae were spiked directly into the system and AOM concentrations were greatly elevated. Also, particulate matter (greater than 0.45 μm) was present, which was more easily deposited on the membranes. It is important for operators to recognize that this pre-fouling deposition is occurring long before it is apparent in operational data.

These experiments showed that feed spacer morphology played an important role in fouling. Foulants tended to deposit in a pattern created by the feed spacer, suggesting that dead or low-flow zones were present. Perhaps modifications in spacer design could be implemented to reduce dead zones and minimize foulant deposition. More interestingly, however, the permeate carrier membrane had a marked effect on foulant deposition. The coarse permeate carrier caused foulants to deposit in a more obvious feed-spacer pattern, suggesting an interplay between the membrane shape (caused by the permeate carrier) and the feed spacer shape that determined the hydrodynamics and deposition rates. The fine permeate carrier resulted in more homogeneous fouling where the feed spacer pattern was not as apparent.

It remains unclear which permeate carrier was better. The coarse permeate carrier left some of the membrane surface clean during the direct algal spike, suggesting it was better than the fine permeate carrier. But microfiltered AOM deposited more readily and flux declined greater with the coarse permeate carrier, suggesting the fine permeate carrier was optimal. The feed water composition, then, may determine which permeate carrier is best. The significant result here is that the permeate carrier shape is an important consideration when designing RO modules for reducing fouling.

Some insight into AOM foulant composition was obtained. Proteins gave a stronger signal than carbohydrates in the infrared spectra, especially for the microfiltered AOM runs. This perhaps suggests a preferential deposition of protein over carbohydrate in the early stages of fouling; however, the FTIR spectra are not strictly quantitative, so further work would be needed to determine if proteins do indeed preferentially adsorb. The foulant material contained fluorescent organic matter, probably from the light-harvesting pigments chlorophyll and peridinin. In the algal cell these pigments are part of the Peridinin-Chlorophyll *a*-Protein (PCP) light-harvesting complex and it is likely that the PCP complex remains intact during cell breakup. Fluorescence could then be an indicator for not only the pigments but the apoprotein (the protein in which pigments are held) as well. Fluorescence, wet-chemical protein detection, and FTIR detection all correlated. These may all have been detecting the same PCP complex in the foulant layer. The PCP complex makes up between 5 and 30% of total cellular protein, depending on culture conditions. High light exposure results in lower PCP content and our exposure was a continuous, fairly high dose. So while PCP is certainly present, other proteins could have played a bigger role in fouling. An interesting future research question is whether some cellular proteins are more prone to membrane deposition than others.

It should be recognized that changes in organic matter composition over the course of the bench-scale experiment may mean quite different fouling results for algal blooms at full scale. Algae broke apart in the concentrate valve and the fluorescence changed dramatically due to adsorption or biological activity in this batch recycle system. Membrane autopsy of full-scale fouled elements could be performed to make comparisons with our data. Two of the autopsy techniques used here have not been previously reported: Fourier transform image analysis and laser-scanning cytometry. These techniques help determine the spatial distribution and fluorescence intensity of foulants, which can help quantify the extent of fouling and identify the material present.

There was no conclusive evidence as to whether hydraulic resistance or CECP was the dominant fouling mechanism. The heterogeneous AOM present may have formed a dense enough cake to provide significant hydraulic resistance. Permeate salt concentration did not decrease over time, suggesting that CECP was not occurring. It is still possible, however, that CECP was dominant, but the highly rejecting membranes masked the effect. The closest we could approach to a solution was to model the cake layer properties (particle size, porosity, and tortuosity) that would be present for each mechanisms. Though others have reported that CECP dominates for salt-rejecting membranes, here a dominant hydraulic resistance could not be completely ruled out.

In a full-scale desalination system the pretreatment step (be it conventional media filtration or low-pressure membrane filtration) would be expected to adequately remove particles and high-concentrations of organic matter. Thus it is unlikely that the RO membranes would receive water with algal concentrations as high as those in our direct algal spike. The microfiltered AOM experiments were more realistic, though even these would represent fairly extreme conditions. It may be surmised, then, that fouling by cake-layer deposition of AOM would not be a principal concern at full-scale. However, AOM deposition could enhance bacterial deposition by changing the membrane surface properties. Also, AOM could be used as substrate for biofilm growth. So while AOM cake layers may not be the principle cause of flux decline, AOM could be an indirect culprit via biofilm enhancement.

The feed spacer was an important component in determining foulant deposition in these bench-scale tests. Curiously, many investigators do not install a feed spacer into their bench-scale test equipment because they want to make the flow conditions as well-characterized as possible. Here it was shown that the feed spacer was very important in foulant deposition, as would be the case at full scale where all modules have feed spacers. In order to make fouling data relevant to full scale a feed spacer should be used.

5.7 FIGURES

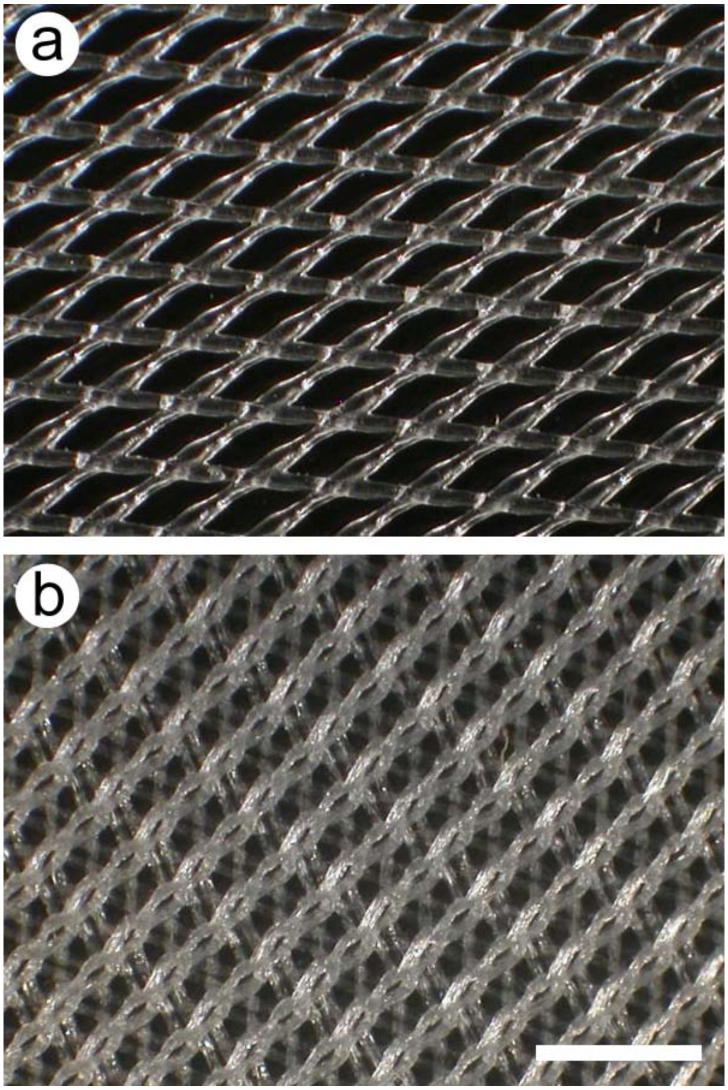

Figure 5-1. (a) Coarse permeate carrier. (b) Fine permeate carrier. Scale bar is 2 mm.

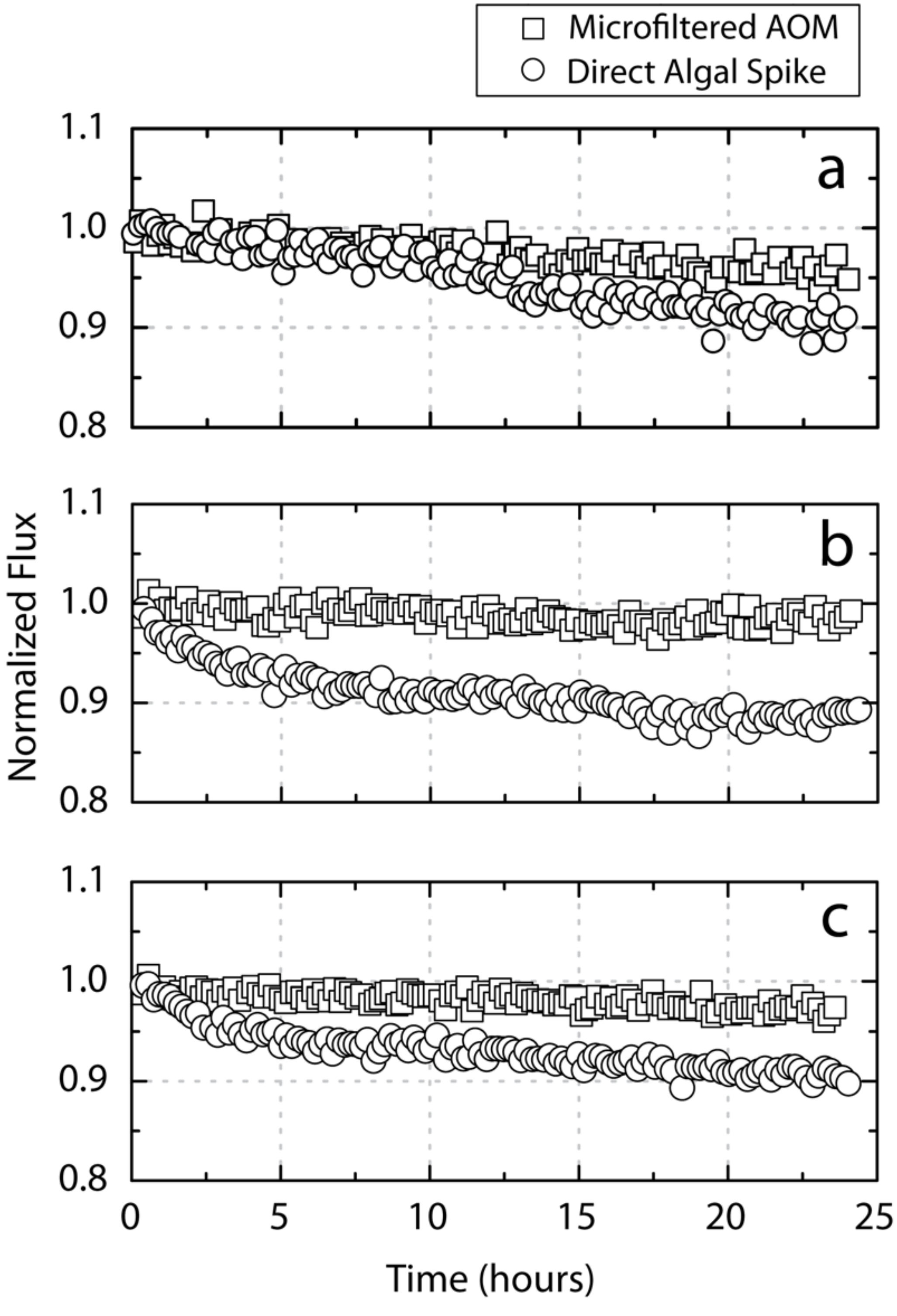

Figure 5-2. Normalized RO specific flux for microfiltered AOM and direct algal spikes (40,000 cells/ml) on (a) coarse permeate carrier with SW30HR membranes (b) fine permeate carrier with SW30HR membranes, and (c) fine permeate carrier with SWC4 membranes.

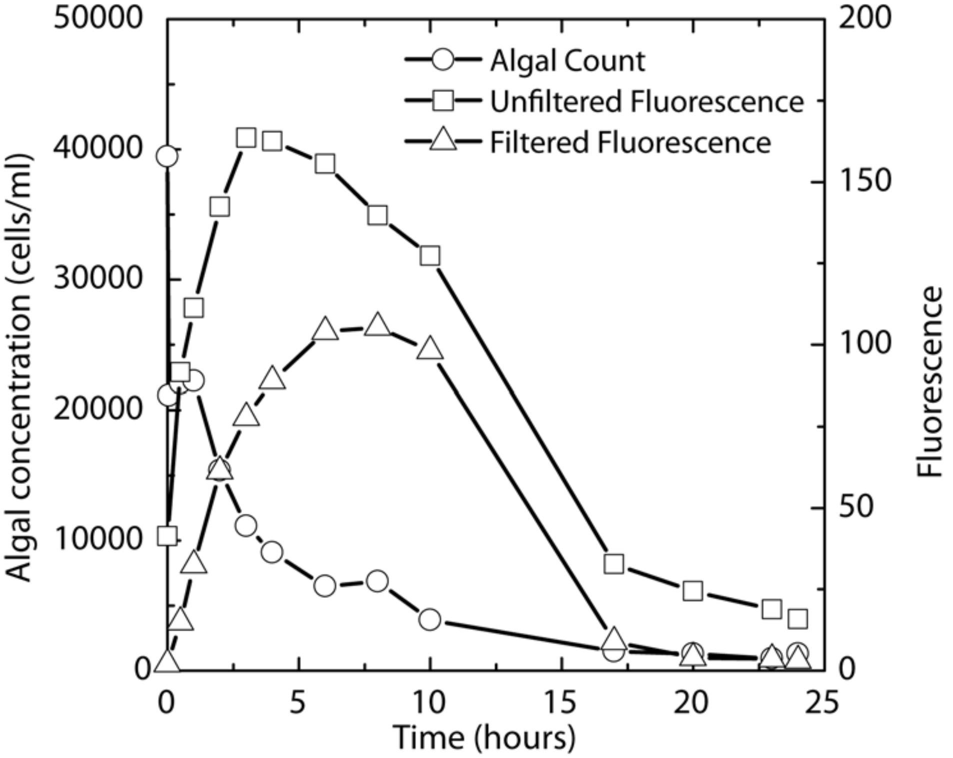

Figure 5-3. Cell concentration determined by hemacytometer during a direct-spike algal fouling experiment along with fluorescence of filtered (0.45 µm) and unfiltered samples.

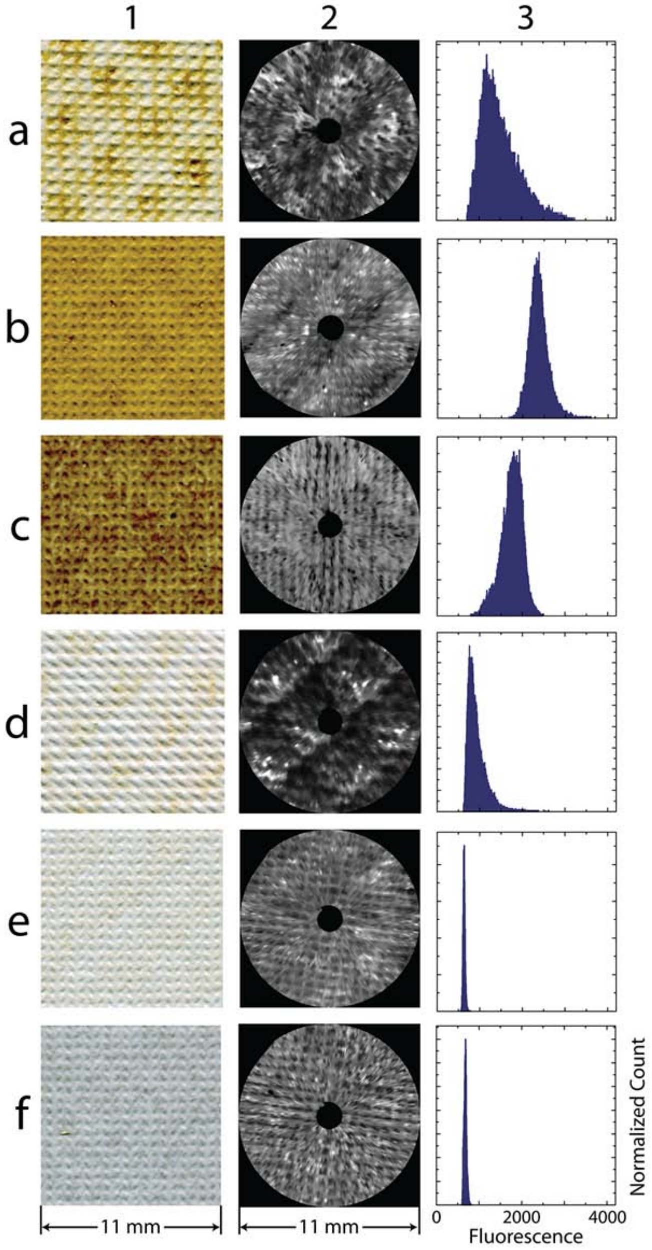

Figure 5-4. (Column 1) Visual images, (Column 2) LSC fluorescence images, and (Column 3) fluorescence histograms of RO membranes fouled by algogenic organic matter. (a) Direct algal spike, SW30HR, coarse permeate carrier. (b) Direct algal spike, SW30HR, fine permeate carrier. (c) Direct algal spike, SWC4, fine permeate carrier. (d) Microfiltered AOM, SW30HR, coarse permeate carrier. (e) Microfiltered AOM, SW30HR, fine permeate carrier. (f) Microfiltered AOM, SWC4, fine permeate carrier. In LSC images (2) contrast was adjusted to highlight notable features so grey levels are not comparable among images. Histogram heights in (3) were normalized to the maximum peak heights.

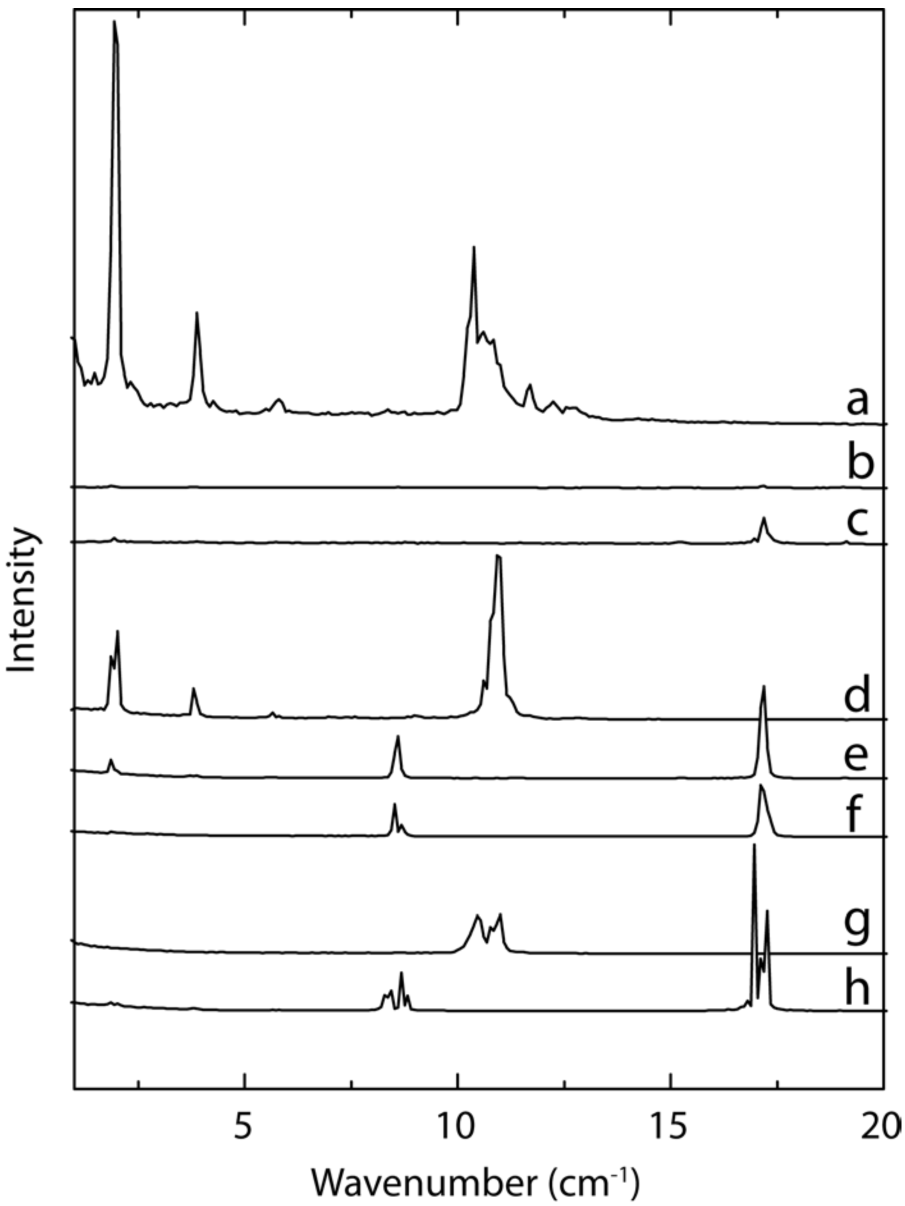

Figure 5-5. Power spectra from image analysis of fouled membranes. (a-f) Samples as designated in Figure 5-4. (g) Non-fouled control from a coarse permeate carrier run. (h) Non-fouled control from a fine permeate carrier run. Intensity is in arbitrary units and spectra are offset on the vertical axis for clarity.

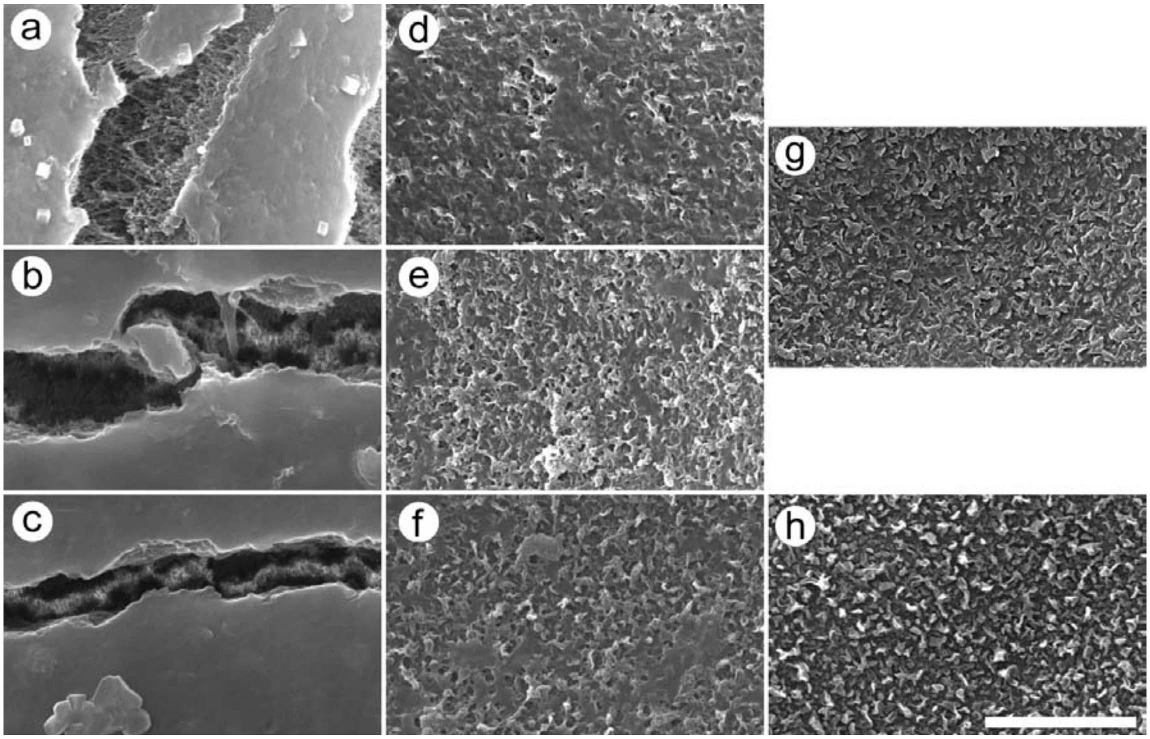

Figure 5-6. SEM images of fouled RO membranes. Letters (a-f) designate the samples listed in Figure 5-4. (g) Clean SW30HR. (h) Clean SWC4. Images were taken at 20 kV in secondary electron imaging mode with 20 kV acceleration voltage. White scale bar spans five µm.

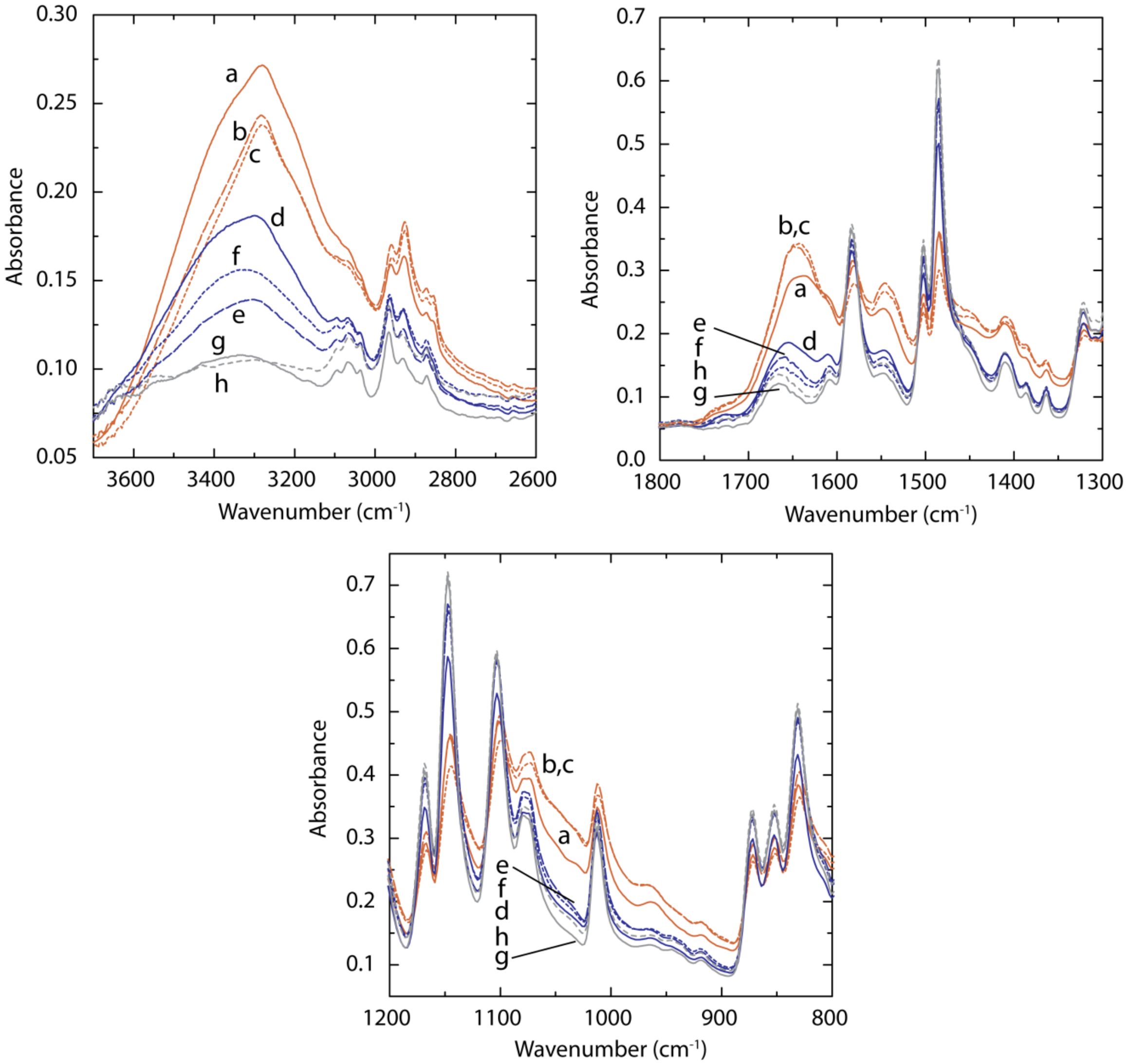

Figure 5-7. Infrared absorbance spectra of fouled and clean RO membranes in the wavenumber regions 3700 to 2600 cm^{-1}, 1800 to 1300 cm^{-1}, and 1200 to 800 cm^{-1}. Letters (a-f) designate the samples listed in Figure 5-4. (g) Clean SW30HR. (h) Clean SWC4.

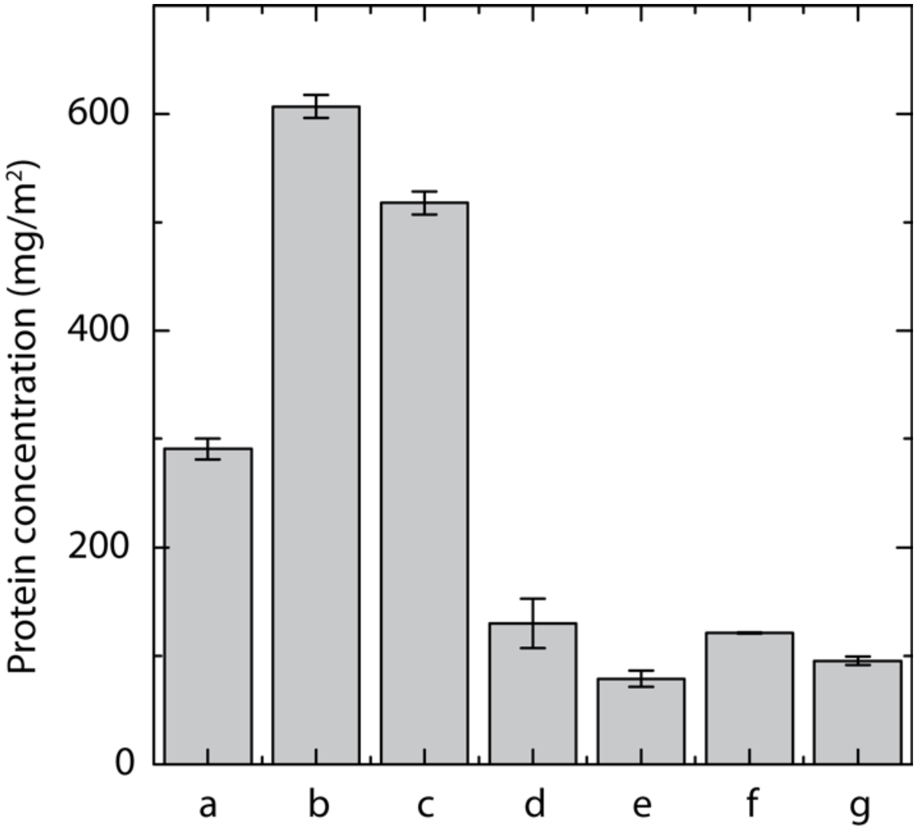

Figure 5-8. Surface protein concentrations of fouled RO membranes. Letters (a-f) designate the samples listed in Figure 5-4. (g) Non-fouled control from a fine permeate carrier run. Error bars span standard error of triplicate measurements.

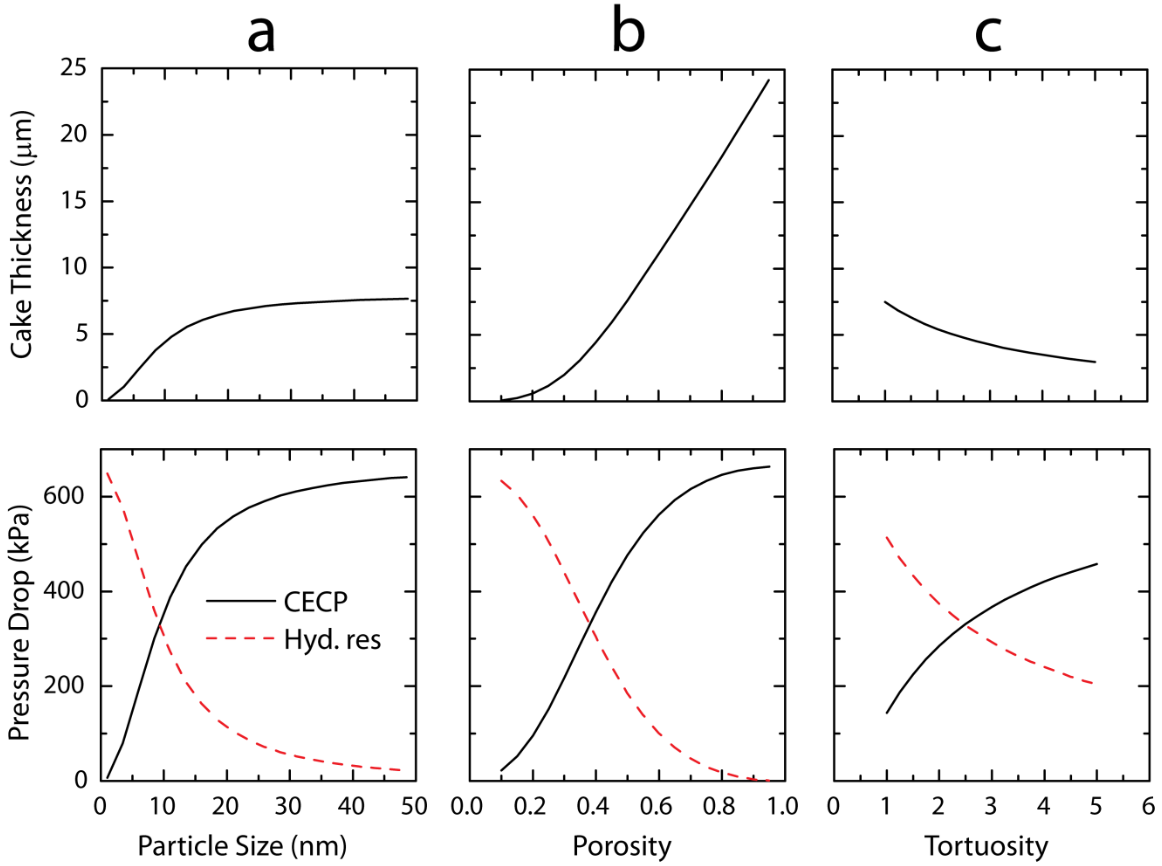

Figure 5-9. Top row: modeled cake thickness compared to other cake properties for a direct-spike fouling test (SWC4 fine permeate carrier). Bottom row: contributions of hydraulic resistance (broken line) and CECP (solid line) to the foulant-layer pressure drop from the model for the same fouling test. (a) Varying particle size (d_p) with constant porosity ($\varepsilon = 0.4$) and tortuosity ($\theta^2 = 1\text{-ln}(\varepsilon^2) = 2.83$). (b) Varying porosity with constant particle size ($d_p = 10$ nm) and tortuosity ($\theta^2 = 2.83$). (c) Varying tortuosity with constant particle size ($d_p = 10$ nm) and porosity ($\varepsilon = 0.4$).

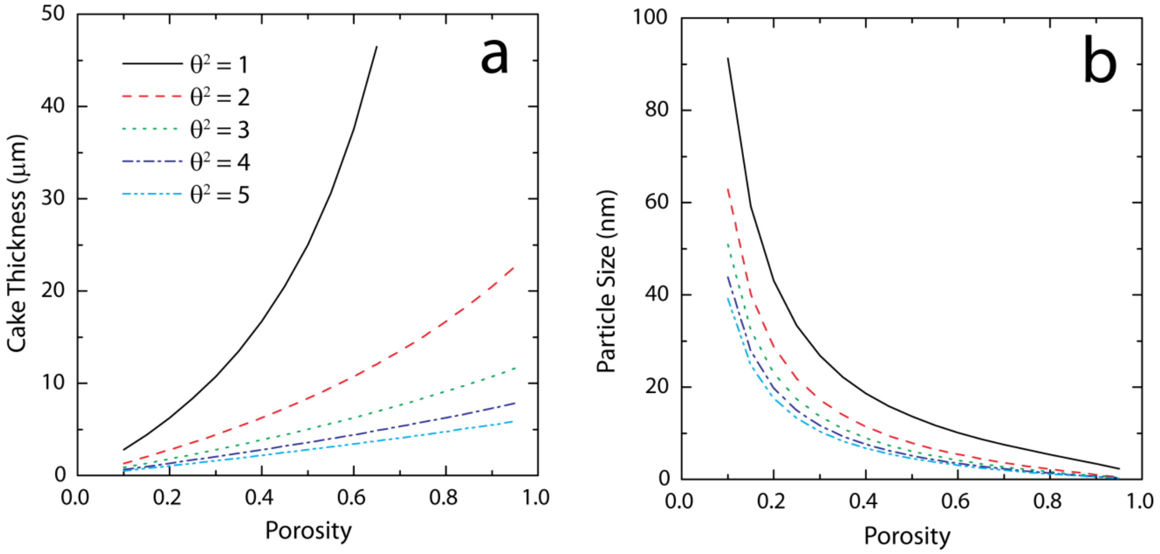

Figure 5-10. Crossover point curves (where CECP and hydraulic resistance yield equal pressure drops) for a direct-spike fouling test (SWC4 fine permeate carrier). (a) Cake thickness and (b) particle size are given for varying porosity and tortuosity.

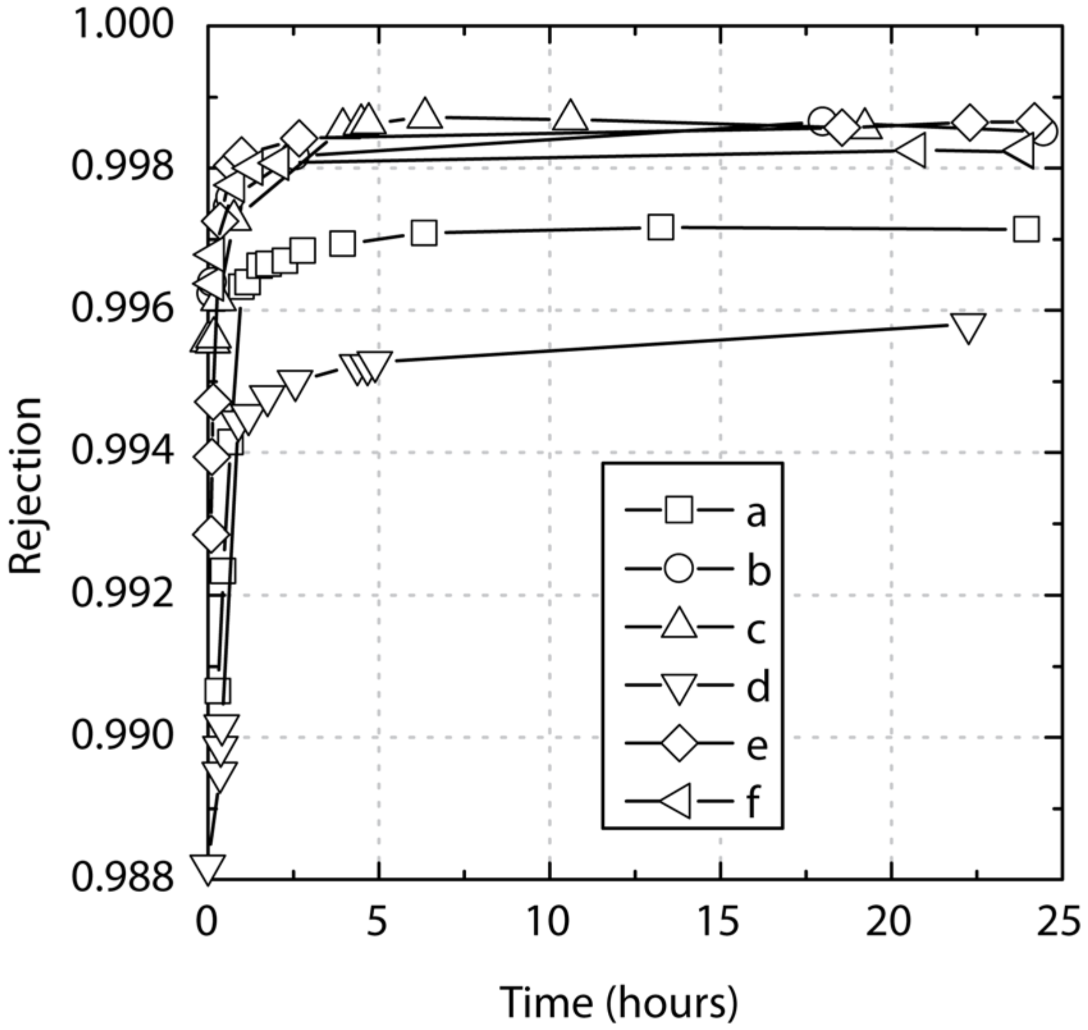

Figure 5-11. Salt rejection data for direct algal spikes and microfiltered AOM on coarse and fine permeate carriers for two RO membrane types. Letters indicate samples as designated in Figure 5-4.

6 LOW-PRESSURE MEMBRANE FOULING BY MARINE ALGAE

Pretreatment of seawater for desalination can be accomplished with microfiltration (MF) or ultrafiltration (UF) membranes. One problem with MF and UF pretreatment is fouling by marine algae, which is most prevalent during algal blooms. Algal cells quickly block MF and UF pores and decrease permeability. The objective of this chapter is to discuss important considerations concerning low-pressure membrane fouling by marine algae.

Direct filtration of algae was first tested to determine the extent of flux decline and investigate mechanisms. It was hypothesized that MF fouling would occur by a pore blocking mechanism because the relatively large pore size of MF membranes would enable foulants to penetrate. In contrast, UF fouling was expected to occur by a cake filtration mechanism since much of the algal material was too large to enter the membrane pores and would thus build up on the surface. Data from filtration experiments were modeled using the methods described by Hermia (1982) to elucidate the mechanisms.

The second hypothesis of this chapter was that shear would exacerbate flux decline by releasing AOM that was more detrimental to the membranes than the whole algal cells. The most highly fouling size fraction was expected to be in the colloidal or high-molecular-weight size class. This fraction would be released with shear and fouling would be worsened. Experiments were performed to test whether shear did cause exacerbated flux decline. AOM was subsequently fractionated into different size classes to test the fouling propensity of each and determine the highly fouling fraction.

Directly related to the ideas above was a third hypothesis that rejection of organic matter would decrease after shear. As dissolved material was released it would be better able to pass through the membranes. Feed and permeate samples were measured to determine the change in rejection with shear.

The final hypothesis was that bacteria would be important during fouling in an algal bloom scenario. Bacteria are smaller than the algal cells and thus could potentially be better pore blockers. Also, bacteria are more abundant than algae, especially toward the end of an algal bloom. A simulated algal bloom was created and fouling was measured over time as the bloom progressed. Algal and bacterial numbers were monitored to determine which were more important for fouling.

6.1 FOULING BY DIRECT ALGAL FILTRATION

As reported in Chapter 5, high-pressure RO bench-scale tests resulted in minimal flux decline due to algae. The situation was different for low-pressure filtration; algae caused quick and dramatic flux decline. This section investigates the mechanisms of flux decline by algae on microfiltration and ultrafiltration membranes. Experiments were performed in the 50-ml dead-end cell at a constant pressure of 200 kPa (30 psi) following the MF/UF filtration protocol in Section 3.2.1. Two membranes were used: 0.45-µm MF membranes made of mixed cellulose esters (Millipore) and 100-kDa UF membranes made of regenerated cellulose (Millipore). Algae were fed at a concentration of 70,000 cells/ml. After flux declined the membranes were rinsed with deionized water and another flux decline test was performed. This was repeated five times for the MF membrane and three times for UF.

Flux verses time plots for direct algal filtrations on the MF membranes are shown in Figure 6-1 where it is clear that algae caused rapid flux decline. After the first rinse only about half (53%) of the clean-water flux was recovered, so 47% of the flux decline was reversible. In subsequent stages irreversible flux decline continued; flux recovered to 30, 26, and 20 percent of the clean-water flux with subsequent backwashes. Note, however, that irreversible flux decline becomes less important with each subsequent stage. Stage *b* recovered 59% of the flux in stage *a*, stage *c* recovered 57% of stage *b*, stage *d* recovered 87% of stage *c*, and stage *e* recovered 77% of stage *d*. This is consistent with a fouling model where some pores were irreversibly blocked in the early stages of filtration then in later stages many of the remaining active pores were small enough or had a suitable geometry so that foulants were not lodged in the pores and could be rinsed away.

An often-used method of characterizing porous membrane fouling is the approach of Hermia (1982) who considered four conceptual blocking filtration models: cake filtration, intermediate blocking, standard blocking (pore constriction), and complete blocking. The four models can be presented in a characteristic form given by Equation 6-1.

$$\frac{d^2t}{dV^2} = k\left(\frac{dt}{dV}\right)^n \tag{6-1}$$

Here V is the permeate volume, t is time, and the exponent n depends on the model; $n = 0$ for cake filtration, $n = 1$ for intermediate blocking, $n = 3/2$ for standard blocking, and $n = 2$ for complete blocking. Values of n falling between these levels suggest a combination of mechanisms. The units of the constant k also vary depending on the model.

Equation 6-1 can be written in linear form by taking the logarithm of both sides

$$\ln\left(\frac{d^2t}{dV^2}\right) = n\ln\left(\frac{dt}{dV}\right) + \ln(k) \tag{6-2}$$

Plotting $\ln(d^2t/dV^2)$ versus $\ln(dt/dV)$ and finding the slope gives evidence for the mechanism at play in the fouling process (Crittenden et al. 2005). Equation 6-2 was used to analyze MF flux decline data; resulting plots are shown in Figure 6-2. Solid lines indicate the best linear fit of the data with the exponent n reported at the side. In the first filtration, n was 1.4, which was close to the standard blocking (pore constriction) model. Subsequent filtrations gave a decreasing trend with n equal to 1.3, 1.0, 0.8, and 0.7. This supports the idea presented above that pore blocking (higher n) was more dominant at the beginning and cake filtration (lower n) was more dominant as fouling progressed. In fact, the first filtration appears to have two segments, as shown by the broken lines in Figure 6-2a. Segment *a* followed the complete blocking model ($n = 2$) and the later segment followed the intermediate blocking model ($n = 3/2$). It seems that the pores blocked during the first segment were not cleared with rinsing, since subsequent filtrations did not show the early pore blocking segment.

Another way to visualize the fouling mechanism at play is to compare flux vs. time plots against the four model fits. Each model was expressed in a form where permeate flow (which is directly proportional to flux) was given as a function of time. Model parameters were lumped into a single term for data fitting. The cake filtration model was given by

$$Q = \frac{Q_0}{(1 + K_{cf}\, t)^{1/2}} \tag{6-3}$$

where Q is the permeate flow rate, Q_0 is the initial flow rate, and K_{cf} is the lumped fitting parameter for cake filtration. The intermediate blocking model was given by

$$Q = \frac{Q_0}{1 + K_{ib} t} \tag{6-4}$$

where K_{ib} is the fitting parameter for intermediate blocking. Standard blocking was given by

$$Q = \frac{Q_0}{\left(1 + K_{sb} t\right)^2} \tag{6-5}$$

where K_{sb} is the standard blocking fitting parameter. Finally, the complete blocking model took the form

$$Q = Q_0 \exp(-K_{cb} t) \tag{6-6}$$

where K_{cb} is the fitting parameter for complete blocking.

The four fouling models were fitted to flux data using a script written in Matlab. First the data were normalized to the initial flow rate (Q_0) then an iterative solver function found the *K* parameter that minimized the sum of squares error for each model. The results are plotted in Figure 6-3. By comparing the data to the closest fitting model it was confirmed that a combination of complete blocking and standard blocking best represented flux curve *a*. Curve *b* was represented well by standard blocking. Curves *c*, *d*, and *e* were well represented by the intermediate blocking model.

UF flux data versus volume filtered are plotted in Figure 6-4. Similar to MF, algae caused rapid flux decline in UF; however, more of the flux was recoverable. Stage *b* recovered 70% of the stage-*a* flux and stage *c* recovered 97% of the stage-b flux. This suggests that much of the flux decline was due to cake-layer formation and pore blocking by material that did not penetrate or adsorb within the UF membrane pores; the foulants were mainly larger than the pores (100-kDa). Also noteworthy is that the irreversible portion of fouling (30% of the overall flux decline) occurred mainly in the first stage (*a*). With stage *b* only 3% was irreversible fouling.

Fouling mechanism analysis plots for UF filtrations are shown in Figure 6-5. The characteristic blocking law terms, *n*, for UF were 2.3, 2.8, and 1.9. These would suggest that pore blocking ($n = 2$) was the principal mechanism at play during the fouling process; however, this result is counterintuitive since algal cells (10 to 15 μm in size) were much larger than the pores and much of the fouling was reversible. Cake filtration was expected as the dominant mechanism. When the flux versus time plots were compared to the predictions of the four blocking models (Figure 6-6) cake filtration did give the best fit in all cases. It is felt that the $\ln(d^2t/dV^2)$ vs. $\ln(dV/dt)$ plots (Figure 6-5) was less reliable than the flux versus time plots (Figure 6-6) in this case, since the former had significant scatter and $\ln(dV/dt)$ did not vary over a wide enough extent to make the analysis meaningful. Cake filtration was the more likely flux decline mechanism for UF.

6.2 EFFECTS OF SHEAR ON LOW-PRESSURE MEMBRANE FOULING BY ALGAE

6.2.1 Shearing

Algal cells were exposed to shear by pumping samples through a valve (SS-2MG4, Swagelok, Solon, OH). The valve geometry is given in Figure 6-7. Shear in the valve can be characterized by determining the energy density E_v applied to the fluid. E_v is the specific volumetric energy input by the system and is often given as the parameter of interest for homogenizers, typically in units of joules per cubic meter (J/m^3) (Stang et al. 2001; Schultz et al. 2004). In emulsification of oils, droplet diameters correlated with E_v, where higher E_v produced smaller droplets (Karbstein and Schubert 1995). E_v is equivalent to the pressure drop ΔP over the homogenizing valve (Stang et al. 2001).

Energy density, or pressure drop, is a useful parameter for comparing shear in different valves of a single homogenizer system because it is assumed that the flow rate and valve size are comparable. But pressure drop alone is certainly insufficient for characterizing shear in other systems, especially when the system is scaled. A different approach at characterizing shear for valve systems was made specifically for a photobioreactor growing an algal culture (Vandanjon 1999). Here the authors used a head-loss term (with units of length) for characterizing valve shear

$$\frac{\Delta P}{\rho g} = \frac{K_v u^2}{2g} \tag{6-7}$$

where ρ is the density of water, g is the acceleration of gravity, and u is the velocity of water in the valve. The parameter of greatest interest was the unitless pressure drop coefficient K_v (i.e. valve coefficient) which was found to be a good indicator of the level of hydrodynamic shear on microalgae; as K_v increased, so did algal damage. K_v may be more appropriate than E_v because the velocity of the fluid is taken into consideration. However, the authors noted that K_v was only useful for varying flow and pressure through a single valve; different valves performed differently at the same K_v.

In order to better characterize shear caused by different types of valves and systems it may be more appropriate to use a power density term, Φ_m

$$\Phi_m = \frac{E_v}{\bar{t}_{res}} \tag{6-8}$$

which is found by dividing the energy density by the average residence time ($\bar{t}_{res}$) over which the liquid experiences the pressure drop. It has been noted in the homogenization literature that drop breakup is proportional to Φ_m (Karbstein and Schubert 1995); where Φ_m is denoted as $\overline{P_v}$). When two systems have the same energy density the one with higher power density (due to its smaller valve opening and liquid residence time) produces more shear and droplet breakup (Stang et al. 2001).

The level of shear in the valve was characterized by all three methods mentioned above (E_v, K_v, and Φ_m). Algal cells also experienced some degree of shear as they passed through the pump, so this was characterized by applying similar concepts. The pump used was a three-frame plunger pump (model 231, Cat Pumps, Minneapolis, MN). A schematic of the pump intake and outlet manifold is given in Figure 6-8.

The pump design was such that water could not be completely removed from the manifold, so the system was flushed with 0.45-µm-filtered seawater to ensure that new samples would not experience a salinity gradient after cleaning and flushing. A two-liter algal sample was added to the seawater remaining in the system and mixed at low pressure (10 kPa; 23 psi) for five minutes. After the five-minute mixing period, one liter was withdrawn for two “non-sheared” MF and UF filtrations of 500 ml each (filtration details follow). It is recognized that this “non-sheared” sample had experienced some relatively small level of shear during the pump mixing process. However, this experimental design ensured that the non-sheared sample was exactly the same in initial algal concentration and organic-matter composition as the sheared sample, except for the ensuing high-shear time period. High shear was created by increasing the pressure and flow rate to 6,900 kPa and 800 ml/min, respectively. The system ran in recycle mode with the remaining 2.3-liter sample for 150 minutes, or approximately 50 passes through the valve. A second one-liter sample of “sheared” material was then withdrawn for duplicate MF and UF filtrations.

In a second round of experiments with the same system, the effects of foulant size were studied by fractionating the algal samples. Here the non-sheared algal samples were taken directly from the cultures and diluted to the appropriate algal concentration (100,000 cells per ml) without mixing in the pumping system. The sheared sample in that case was of a higher volume and required a longer shearing time to achieve the same total amount of shear (number of passes through the valve) as the previous set of experiments. Further details for this round of experiments are given in the Size Fractionation section below.

6.2.2 Cell breakup characterization

Cell breakup was monitored using hemacytometry, flow cytometry, and bulk fluorescence measurements. Breakup was modeled with a first-order equation (6-9) used previously for characterization of protein release during yeast breakup in industrial homogenization (Follows et al. 1971; Moore et al. 1990).

$$\frac{dC}{dt} = -kC \tag{6-9}$$

Here C is the algal concentration in cells per ml, t is time, and k is the rate constant. A direct analogy can be drawn between this model and the Chick-Watson kinetic model used for characterizing disinfection (Watson 1908). While the rate constant for disinfection depends on the dose of disinfectant and the time for which the microbes are exposed, the rate constant in the cell breakup model for shear depends on the level of shear and the time it is exposed to shear. In this light, the rate constant could be expanded to

$$k = \frac{1}{\kappa\tau} \tag{6-10}$$

where κ is a strength parameter and τ is the time constant. The time constant is determined by $\tau = V_s/Q_s$ where V_s is the volume of the recirculated fluid and Q_s is the flow rate of recirculation. Note that t/τ is the average number of passes through the valve that each algal cell experiences.

The cell breakup model formulation is most appropriate if all the algal cells have the same structural strength (κ). However, it is possible that there exists a distribution of cell strength with some cells being stronger than others. For a case where two cell classes exist the total cell concentration can be expressed as

$$C = C_s + C_w \tag{6-11}$$

where the subscripts *s* and *w* denote the strong and weak fractions. The breakup model (Equation 6-9) can then be written

$$\frac{dC}{dt} = \frac{dC_s}{dt} + \frac{dC_w}{dt} = -k_s C_s - k_w C_w \tag{6-12}$$

The two cell classes are independent of one another (breakup of weak cells does not depend on the number of strong cells); hence, the solution to the breakup model can be found for each class

$$C_s = C_{so}e^{-k_s t} \text{ and } C_w = C_{wo}e^{-k_w t} \tag{6-13}$$

Taking Equations 6-11 and 6-13 together, we find the total algal cell concentration with respect to time.

$$C = C_{so}e^{-k_s t} + C_{wo}e^{-k_w t} \tag{6-14}$$

The sum of C_{so} and C_{wo} must equal the initial cell concentration. During the fitting procedure the data were normalized and the initial cell concentration was set to one. Thus, C_{so} and C_{wo} must add to unity Equation 6-15 resulted.

$$C = C_{so}e^{-k_s t} + (1 - C_{so})e^{-k_w t} \tag{6-15}$$

The rate constants associated with the first-order breakup model (Equation 6-9) and the two-term model (Equation 6-15) were found by fitting the breakup data from hemacytometry and flow cytometry using a nonlinear least squares method in the curve fitting tool of Matlab.

6.2.3 MF/UF experiments for testing shear effects

MF and UF flux tests were performed as noted in Section 3.2.1. Two MF and two UF membranes were compared: the 0.45-μm and 0.22-μm cellulose acetate membranes and the 100- and 30-kDa regenerated cellulose membranes. Two replicates were performed for each sheared and non-sheared sample and for each membrane type to see the effect of shear on flux decline.

6.2.4 Size fractionation

Sheared and non-sheared algal culture samples were fractionated to determine the effects of different organic-matter size classes on fouling. Figure 6-9 shows a schematic of the fractionation procedure. Algae were collected from culture and diluted to a concentration of 100,000 cells/ml in 3 liters of 0.1-μm-filtered seawater. The non-sheared sample was used directly in the fractionation procedure that follows. Because of the time required to perform all of the fractionation procedures and subsequent flux tests the sheared and non-sheared runs could not be performed on the same day. Instead, one algal batch was used for all of the non-sheared fractionations and a separate algal batch harvested on a different day was used for the sheared fractionations. The same algal cell concentration (100,000 cells/ml) was obtained, but because of variability in the growth cycle from batch to batch it was impossible to ensure that organic matter composition and bacterial numbers were the same for each batch. The effects of shear on a single algal culture for various filtration levels were tested previously. In the size-fractionation experiments it was more important to maintain a single sample for all of the fractionations within each group; distinct samples had to be used for the sheared and non-sheared runs.

The sheared sample was prepared by passing algae through the pump and valve apparatus as described in Section 6.2.1. Algal cells were diluted to 100,000 cells/ml. As noted previously, the pump manifold could not be run dry so some of the sample was used to flush the manifold. This was slightly different than previous experiments where it was important that the before- and after-shear experiments be of the same composition. Here the composition of the sheared and non-sheared samples were different due to their harvesting on different days, so simply flushing the manifold was sufficient. After flushing, the sample volume was 3.8 liters. It was run at 6,900 kPa and 800 ml/min for 300 minutes to achieve the desired 60% cell breakup.

Seven sub-samples of each (sheared and non-sheared) batch were used for subsequent fractionation as shown in Figure 6-9. One sub-sample was left without fractionation. The second sub-sample was centrifuged (5000 G, 5 minutes; designed to selectively remove algal cells) and the supernatant was collected. The third sub-sample was filtered with a glass-fiber filter (Millipore AP-40) to remove particulate matter including algal cells, bacteria, and any other particulate debris rejected by the nominal 0.7-µm pore size. The fourth through seventh sub-samples were also glass-fiber filtered then were filtered through either 0.45-µm cellulose acetate (GE-Osmonics), 0.22-µm cellulose acetate (GE-Osmonics), 100-kDa regenerated cellulose (Millipore), or 30-kDa regenerated cellulose (Millipore) membranes. These were the same cellulose acetate and regenerated cellulose membranes used in previous experiments and are desirable here, as before, because of their low adsorptive fouling potential.

Glass-fiber filtration was performed at roughly 2-kPa vacuum using a flask and filter holder. The first 50 ml was discarded to minimize any effects of organic matter leaching from or binding to the filter. A cleaned and baked (300°C, four hours) vacuum flask collected the remainder of the sample. The filter was replaced after passing 500 ml of solution so that the filtration properties would not change drastically as a cake layer formed. All glass-fiber filtered samples were combined in a single container to ensure sample homogeneity for subsequent fractionation steps.

Fractionation filtrations were performed in the same dead-end cell used for previous experiments at a pressure of 69 kPa (10 psi) for MF (0.22 and 0.45 µm), 207 kPa (30 psi) for 100 kDa-UF, and 276 kPa (40 psi) for 30-kDa UF.

The fouling propensities of each fractionated sub-sample were determined by measuring flux decline on the 0.1-µm PVDF membranes (Millipore type VVLP).

Filtrations were performed in the same manner as the fractionation filtrations above, but with the 22-mm diameter cell. Dead-end operation was used to mimic the operational mode of most full-scale MF and UF facilities.

6.2.5 Determination of the level of shear

The level of shear in our system was characterized with three parameters found in the literature to be indicative of shear. It is not our purpose to exactly characterize the shear forces in the system, but to provide order-of magnitude estimates and comparisons with other systems.

Energy density E_v for the valve was simply the pressure drop over the valve, 6.4x10^6 J/m^3 (the system was run at 6,900 kPa, but 500 kPa of head loss was contributed by the heat exchanger and tubing after the valve; 1 kPa = 1000 J/m^3). The pressure drop coefficient, K_v, for our valve was calculated to be 0.003. For this we assumed that the area of greatest shear was around the needle inserted in its seat. We assumed the cross-sectional flow area was 10% of maximum (90% of the flow area was taken up by the needle) resulting in a velocity of 62 m/s. K_v was then calculated with Equation 6-7 using the velocity, pressure drop, and density of seawater (1030 kg/m^3). To calculate the power density Φ_m we further assumed that the needle was inserted 10 mm for a flow volume around the needle of 2.1 mm^2. With the flow volume and residence time, Φ_m could be calculated with Equation 6-8. The power density was 4x10^{10} W/m^3.

For the pump E_v was expected to be greatest at the point of greatest constriction, which appeared to be where the valves met the manifold (see Figure 6-8). The extent to which the valves were open was variable during the piston cycle making it difficult to calculate the flow velocity. Further, the pressure drop over the valve openings could not be measured. For the purposes of estimation, we assumed the pump manufacturers would minimize pressure drop in the valves to decrease energy demand for the pump and we took 500 kPa as a conservatively high pressure drop estimate. Next we assumed that during operation the valves were open to their full extent, as shown in Figure 6-8. The resulting parameter estimates for the pump were E_v, 5x10^5 J/m^3; Kv, 1x10^2; and Φ_m, 2x10^7 W/m^3.

Our values were compared with values calculated from the literature for other systems (Table 6-1) to evaluate the appropriateness of each parameter. Our valve E_v falls between the E_v for valves of a photobioreactor (Vandanjon 1999) and the E_v that is typical for an industrial milk homogenizer (Thiebaud et al. 2003). Our pump E_v was similar to the phobioreactor valve. It appears that E_v provided a reasonable estimate for shear, since our high-pressure system was designed to produce more algal breakup than would be expected in the photobioreactor, but not as much as would be expected in a milk homogenizer.

The calculated K_v value for our pump was lower than but similar to the photobioreactor valve K_v. Our valve K_v was five orders of magnitude lower than the photobioreactor valve and the same order of magnitude as the homogenizer. If K_v were truly an indicator of shear as suggested by Vandanjon (1999) the photobioreactor had the highest shear and the homogenizer and our valve were similar in shear. This was a counterintuitive result because our high-pressure-drop valve intended for cell breakup should have induced more shear than the lower-pressure-drop photobioreactor valve. Also, the homogenizer shear should have been much greater than the other two systems since homogenizers are specifically intended to induce shear and cause droplet breakup. It appeared, then, that K_v was a poor parameter for comparing shear among different systems. Typically one would use K_v to determine head loss while designing pipe networks (Munson et al. 2006). K_v correlated with cell breakup in the cited photobioreactor study (Vandanjon 1999) because different valves were tested in a single system. Flow velocities were comparable for the different valve configurations making the K_v parameter a simple measure of head loss or energy density. In the various systems compared here, however, the flow velocities were orders of magnitude different and K_v became an inappropriate parameter for quantifying shear.

The power density term, Φ_m, for our valve was between the photobioreactor and homogenizer. The pump Φ_m was the same as the photobioreactor valve. These results are consistent with expectations; low shear in the photobioreactor, higher shear for our system and the homogenizer. It appeared that power density was a useful term for shear estimation. In fact, power density (energy/time-volume) may be more appropriate than energy density (energy/time). The energy density, being simply the pressure drop over the valve, could misrepresent the shear level if the system size varies greatly. For example, a very high energy density could be calculated for a very long tube even if the flow rate were low and actual shear forces minimal. The power density term would be more appropriate because it takes into account the residence time of the fluid in the system; only if the energy is dissipated very quickly (as in high-shear, turbulent conditions) will the power density be high. Thus power density is accepted here as the more appropriate parameter for evaluating shear.

The power density also had the advantage that it could be calculated for non-valve systems, like a rapid-mix coagulation tank in water treatment. The power density for a typical rapid mix tank would be roughly $1x10^2$ W/m^3. This is much lower than our valve or the photobioreactor valve used for comparison and helps conceptualize the difference in shear between a mixing tank and a valve system for engineers familiar with coagulation mixing systems. It is recognized that it may not be strictly accurate to compare shear in the valve with the average or characteristic shear in a rapid-mix tank based on power density. Energy dissipation is uneven in the mixing tank so it would be more appropriate to rigorously determine the flow patterns near the impeller as the most likely location of shear and particle disruption, which could have locally much higher power density (Clark 1988; Ducoste and Clark 1998). But the average power dissipation calculated for the whole mixing volume is a first approximation for comparison of shear among different systems.

We determined that most of the shear in our system was due to the valve instead of the pump. This was verified in one experiment where a single-pass run was performed and algae were counted in the tubing between the pump and valve. No algal breakup was found after the pump, while algae were broken after the valve.

6.2.6 Effects of shear on algal cells

Shear forces in the pump and valve system caused cell lysis and release of internal organelles and organic matter. Figure 6-10 shows several views intact cells and cells that whose internal organic matter have been released by crushing under a microscope slide. We were unable to show broken fragments from cells sheared in the valve because they were too small to be readily detected by visible-light microscopy; once cells were breached the cellular material was scattered and the pieces were too small to identify. However, some fragments were detected by flow cytometry.

Figure 6-11 displays flow cytometry data for one experiment before and after 150 minutes of exposure to shear. Light-scatter parameters are indicative of particle size and the side-scatter and front-scatter readings of the background matter were markedly lower than those of whole algal cells making it possible to distinguish whole cells from fragments. A particle was confirmed to be a cell by its 488-nm fluorescence. Cell numbers dropped significantly while the number of “background” data points (having low forward-scatter and side-scatter) increased significantly. It is noteworthy that even in the sheared-sample plot of Figure 6-11 there was clear separation between the whole-cell and background data clouds. This was consistent with the visual observation that cells did not break into mid-size pieces, but dissociated into very small fragments upon breakup.

Bulk sample fluorescence increased over time with shear. This was an interesting result because fluorescence measurements typically correlated very well with cell number; in fact, culture growth was monitored with fluorescence. However, as material was delocalized upon breakup there was less self-shading. Self-shading is known to be a factor in fluorescence measurements; fluorescence is always lower in a whole-cell suspension than in a solution of pigments with the same total pigment concentration due to the package effect mentioned in Section 5.3 (Kirk 1994; Johnsen et al. 1997).

For one run a time series of flow cytometry sub-samples was taken, as displayed in Figure 6-12. At each time step the number of points in the “whole cell” data cloud and the “background” data cloud were counted. The same sub-samples were examined with hemacytometry, which confirmed that flow cytometry was appropriately identifying whole cells. As expected, whole cell numbers declined and background material increased over the course of the shearing run. The number of background particles measured by flow cytometry did not rise very far above the initial algal cell concentration even though it was suspected that cells ruptured into multiple parts. This was most likely due to the broken segments and released organic matter being smaller than the lower size detection threshold of the flow cytometer. The actual lower size limit of detection for our flow cytometry setup was unknown, but other workers have reported that the smallest observable particles were 0.1 μm in one case (Tocchetti et al. 2001) and 0.3 μm in another case (B. R. Robertson 1989). In those references the photomultiplier (PMT) detector settings were adjusted for sensitivity to the small particle size, while in our case the PMT gains were set to observe larger cells. Thus, our detection limit was probably higher than the 0.1 or 0.3 μm reported by other workers.

Algal cell breakup was characterized using the first-order model given in Equation 6-9. The data were normalized to the initial concentration before analysis so C_o was set to unity. This resulted in a fitted breakup constant (k) of 0.0158 and a cell strength (κ) of 15 (τ was 4.26 min^{-1}). However, the data fit (not shown) overestimated cell number in the early stages and underestimated cell number in the later stage of the experiment. A better data fit was obtained with the two-term first-order model (Equation 6-12) plotted in Figure 6-12. It was not surprising that a model with more terms would yield a better fit, but there is physical meaning in the extra parameters. It is suggested here that there exists a distribution of cell structural strength with some cells being stronger than others. The two-term model describes a dichotomy of cell class: a structurally strong fraction and a structurally weak fraction. C_{so} was 0.56 suggesting that a little over half the cells were of the strong class. C_{wo} (constrained by the model to be $1-C_{so}$) was 0.44 and represented the weaker cell fraction. The κ_s value for the strong-cell class was 29 and the weak-cell constant κ_w was 3.1, suggesting an order of magnitude difference in strength between the two cell classes (note that a higher κ indicates stronger cells).

After forming this hypothesis about cell strength we found in the literature an analogous strong/weak population hypothesis for cryptosporidium oosyst inactivation during disinfection (Rennecker et al. 2001). It was shown there that a two-term first-order model appropriately fit the inactivation data and it was hypothesized that strong and weak oosyst populations were present. Our model (Equation 6-15) is slightly different from that of Renneker et al. in that they separated the data into two segments (early and late time periods) for fitting of each decay term separately. Here we fit both decay terms simultaneously over the entire data set, which is consistent with the idea that both strong and weak cells experience breakup over the entire time period. Rennecker et al. (2001) did not investigate the reasons for varying structural strength, but they did note that older oocyst lots were weaker. Algae may grow weaker with age, as well. Also, actively dividing cells may have less structural stability.

6.2.7 Effects of shear on flux

Flux data for the four sets of algal-laden membrane fouling experiments (one set for each membrane pore size) are presented in Figure 6-13. Here the flux (J) is normalized to the initial clean-water flux (J_o). In all cases flux decline was more drastic after shear than before shear. The difference in flux was quite dramatic for 0.45-µm membranes (Figure 6-13a); before shear flux declined by 40 to 50 percent and after shear flux declined by over 95 percent. There was less difference in flux before and after shear for the 0.22-µm membrane (Figure 6-13b). In the 100-kDa UF experiment (Figure 6-13c), the curves had an almost linear region toward the middle of the run before shear. After shear, however, flux decline was more decaying-exponential in nature. In the 30-kDa UF experiment (Figure 6-13d) the before-shear fouling was quite odd in that the rate of flux decline increased with mass filtered (i.e. the curve dropped downward instead of leveling out). This was counterintuitive because as flux decreased, less material should have been deposited on the membrane, so the rate of flux decline should have flattened, as it did in all other cases. It is hypothesized that some sort of cake thickening or compaction occurred to decrease the permeability of the already-deposited cake layer and exacerbate flux decline late in the run. Perhaps the whole algal cells deposited in a haphazard manner in the beginning, then adjusted their positioning to a more ordered and less porous structure as the cake developed. It is expected that if the filtration continued for a longer period of time, the curve shape would flatten as the cake reached its minimum porosity. Note that a similar phenomenon may have occurred during the 100-kDa before-shear runs. The linear region in the middle of the run—which is also counterintuitive by the same reasoning just described—could be explained with cake-compression physics.

6.2.8 Flux modeling results

It was quite clear by simple observation of the flux curves (Figure 6-13) that shear increased the rate of algal fouling. However, it was also interesting to investigate the way in which the mathematical description of the fouling behavior changed. Figure 6-14 shows the best-fit curves for the 100-kDa fouling runs before and after shear for the four fouling models defined by Hermia (1982). Table 6-2 gives the coefficient of determination and the root mean squared error of model fits for all 16 of the flux tests (duplicates before and after shear for four membranes). Shaded values in Table 6-2 indicate the best fit model judged by coefficient of determination and root-mean-squared error. The actual values found for the fitting parameters (K_{cf}, K_{ib}, K_{sb}, and K_{cb}, for Equations 6-3 through 6-6) are not the focus of the current discussion, but they are presented in Table 6-3.

In three of the four cases (0.22 µm, 100 kDa, and 30 kDa) the best fit model shifted before and after shear. The shift was always in the direction of decreasing n, which went against our expectations. Hermia terms the model with the highest n-value (2) “complete blocking,” meaning that flux declines because material enters the pores and blocks them completely. The model with the lowest n-value (0) is termed “cake filtration” because all material deposits on the filter surface. The other models fall somewhere in between; pore blocking is coupled with cake filtration. It was expected that before shear the cake filtration model would dominate, since algal cells are approximately 10 to 15 µm in diameter and should not be able to access the pores. However, small particles and colloidal material resulting from shear were expected to enter the pores so the models would shift toward complete blocking (higher n). Instead, a lower n-value was found after shear for three of the four membrane types.

To understand the difference in models, the shape of the curves can be evaluated. The $n = 0$ model (cake filtration) is characterized by a very steep initial flux decline that levels off over time (see Figure 6-14). As n increases, the flux decline is gentler in the beginning but drops further by the end of the run. From this perspective, it makes sense that the more drastic flux decline caused by sheared cells would be characterized by a model with lower n.

It appears that caution must be taken in interpreting fouling mechanism based solely on the best-fitting Hermia model. To say that “pore blocking” or “cake filtration” occurred simply because the data fell on one or the other curve is an oversimplification. In reality, a combination of mechanisms was probably occurring in all cases, since even before shear the composition was heterogeneous, having different-sized cells and background material from cells that died and lysed naturally in culture or in sample preparation. Many investigators use two Hermia models: pore-blocking to describe the early data and cake filtration to describe the later data (Blanpain and Lalande 1997; Hwang and Lin 2002; Ye et al. 2005). Pore blocking and cake filtration models have also been combined for a more comprehensive model that fits data for the entire run (Ho and Zydney 2000). Such efforts to completely describe the flux curves are not the focus of this work; here the models are used simply to support the hypothesis that the flux decline mechanism changes after shear and that the change can be described mathematically. Further, the descriptions are consistent since duplicate filtration runs gave the same result.

A final note concerning flux models is that in the 0.45-µm fouling case, the cake filtration model was the best fit to both the before- and after-shear cases. This was an anomaly, since the extent of flux decline was actually quite different (see Figure 6-13a). The before-shear experiment had a linear flux trend and it just so happened that the cake filtration model was the best mathematical fit to that data shape. In reality, a linear trend is not well represented by any of the models. A similar situation occurred for the 30-kDa before-shear run. Certainly none of the models can well describe a curve where flux decline is exacerbated over time, but the cake filtration model happened to come closest.

6.2.9 Organic-matter rejection

In the preceding experiments the organic-matter compositions of samples for each membrane type were variable because the tests had to be performed on different days to accommodate four runs per membrane type. More reliable organic-matter rejection data were collected in a second set of experiments with a single sample on the same day so that the feed was the same for all membrane types. One filtration of non-sheared and sheared cases for each membrane type was performed. This required a higher volume than the previous experiments so the time constant τ was lower. The time of shear was lengthened so that the sample experienced the same total amount of shear; (i.e. the same number of passes through the valve).

Total carbohydrates, monosaccharides, UV absorbance, and fluorescence for feed and permeate samples are presented in Table 6-4. Rejection values calculated from these data are presented in Table 6-5. Rejection decreased with shear in almost every case. Without shear a significant portion of organic matter was held within the algal cells that were large enough to be rejected by the membranes, but shear released organic material from the cells and this was able to permeate the membranes.

Rejection numbers varied for different water quality parameters giving information about the nature of the AOM before and after shear. Feed concentrations of total carbohydrates and monosaccharides were actually lower after shear than before shear. Measurement error is likely, especially for the total carbohydrate feed sample, but even in other data sets (not shown) total carbohydrates and monosaccharides did not increase after shear. The wet-chemical assay is responsive to both inter- and extra-cellular carbohydrates. Cells were perfectly rejected by all membranes, but carbohydrates were not, so much of the carbohydrate material was extracellular. With shear the amount of extracellular carbohydrates increased.

UV absorbance was more sensitive to extracellular organic matter than intracellular material. This was probably due to the package effect described in Section 5.3. Rejection calculated from UV measurements were quite similar before and after shear and in the 0.45-μm membrane case rejection *increased* after shear. This was not due to the permeate having lower UV absorbance (in fact it was significantly higher), but because the feed UV absorbance was so much higher after shear that the calculated rejection was higher. We see from this that even before shear there existed a significant amount of extracellular UV-absorbing compounds (having double bonds or aromatic rings) and these were greatly increased after shear. Strict carbohydrates would not fall into this class, so these materials are more likely proteins, aminosugars, light-harvesting molecules chlorophyll *a* and peridinin, or nucleic acids.

Fluorescence measurements proved to be the most sensitive to shear. Fluorescence was almost perfectly rejected before shear by all membrane types, since algal cells do not typically release dissolved fluorescent material into the water matrix. After shear, however, the total fluorescence increased by 3.3 times, from 150 to 499 (arbitrary units). Much of the material after shear was dissolved, as it permeated all four membrane types. Fluorescence was most likely due to chlorophyll *a* and peridinin, since the excitation and detection wavelengths were set specifically for their detection.

These organic matter rejection results make it clear that shear caused an increase in dissolved material that was able to pass through the membranes; however, the data were insufficient to indicate whether the exacerbated flux decline was caused by the dissolved material or by other constituents. The subsequent fractionation experiments were designed to shed light on the makeup of the foulants and the mechanisms at play.

6.2.10 Fractionation Flux Results

Flux data for fouling of 0.1-μm PVDF membranes by different size fractions of algogenic organic matter are presented in Figure 6-15 where the flux (J) is normalized to the initial clean-water flux (J_o), as done earlier (Figure 6-13). In order to make quantitative comparisons in the discussion of these results, we will consider the percentage fouling caused by each fraction. We will make the comparisons at 200 L/m^2 specific volume filtered since all samples were run at least up to that point. The non-fractionated algal culture was comprised of all possible foulant material and thus is defined as 100% fouling. The centrifuged sample caused 71% of the fouling in the non-sheared case and 91% of fouling after shear. The glass-fiber filtered sample caused 59% of fouling before shear and 76% after. We can see, then, that the majority of foulant material was not removable by either centrifugation or glass-fiber filtration and that shear caused an increase in the relative importance of these fractions.

The trend was not as clear for smaller fractions. Material able to permeate 0.45-μm membranes caused 28% of the fouling for non-sheared samples, but only 13% after shear. The sub-0.22-μm fraction caused 7% fouling before shear and 5% after. These results are counterintuitive because it was expected that shear would release a large amount of dissolved material and fouling would be exacerbated for these fractions. It is important to remember here that the samples for sheared and non-sheared cases were different, taken from separate algal cultures. Also, the fractionation procedure was not expected to be perfect; material smaller than the membrane pore size can possibly be retained. As cake layers build on the membrane surface, rejection can be enhanced to capture smaller particles. Further, though the regenerated cellulose and cellulose acetate membranes used here were hydrophilic and resistant to adsorption, some adsorption could still occur. Thus it is important to evaluate the organic matter contained in each fraction to determine to what extent the fractionation procedure changed the sample. Such characterization is given in the next section.

Material smaller than 100-kDa and 30-kDa caused no discernable flux decline either before or after shear. From this it appears that fouling of 0.1-μm PVDF membranes did not occur by adsorption of dissolved material. Only the fractions larger than the membrane pore size were capable of causing flux decline.

6.2.11 Fractionation Analytical Results

The starting point for characterizing the various fractions of algogenic organic matter was to determine algal removal in each stage (Figure 6-16). Though the samples were harvested and brought to the same concentration of 100,000 cells/ml, the sheared sample had lower algal cell numbers due to their breakup in the shearing system. Algal cells were removed effectively by centrifugation, though some cells remained. Glass-fiber filtration allowed only a few cells to pass in the non-sheared sample and no cells were detected in the glass-fiber filtered sheared sample. The fact that some algal cells passed through the glass-fiber shows that these depth filters cannot remove everything larger than the nominal 0.7 μm pore size stated by the manufacturer. All of the MF and UF membranes completely removed algal cells.

Bacterial numbers were also counted (Figure 6-17). Surprisingly, the sheared sample contained double the bacterial concentration as the non-sheared sample. This was due to sample variability as noted previously; the samples were collected on different days from different batches of algae. The algal concentration was adjusted to 100,000 cells/ml (before shear), but the bacterial concentration could not be simultaneously controlled.

Centrifugation was effective in removing about half of the bacteria. From analysis of the images used for counting it appears that bacterial aggregates (as opposed to individual bacterial cells) were more easily removed by centrifugation, as would be expected. Glass-fiber filtration removed bacteria slightly better than centrifugation. Some bacteria remained in the sample even after 0.45-μm microfiltration. Observed bacterial cells were larger than 0.45 µm, but the membranes have variable pore size and could have compromised integrity to allow some bacterial passage. Also, the system was not sterile so bacteria may have multiplied in the time between fractionation and analysis. Samples were refrigerated to minimize bacterial growth, but it could not be halted completely, especially for these organic-matter rich samples. While it is was not expected to find bacteria in the 0.45-µm fractionated samples, their presence did not hinder the experiments; bacterial concentrations were measured at the time of filtration on the PVDF membranes, so their contribution to flux decline can be assessed.

SEC data (Figure 6-18) indicate changes in size distribution that occurred with each fractionation step. Note that the SEC procedure required filtration through 0.45-µm syringe filters before analysis so these data represent only dissolved and colloidal organic matter able to pass through that filter. The most obvious result is that the concentrations of both low- and high-molecular weight material increased dramatically after shear. This confirms that algal cell breakup released significant amounts of dissolved organic matter.

The SEC data also indicate that much of the high-molecular-weight material was removed by the 30- and 100-kDa fractionation steps. All other fractions contained similar amounts of high-molecular-weight material. The exact size distribution of this material cannot be ascertained since everything larger than 67 kDa eluted together in the first peak. However, it can be surmised that the peak is indicative of dissolved and colloidal material between 67 kDa and 0.45 µm.

Total organic carbon (TOC) was measured for each size fraction and for the corresponding 0.1-µm PVDF permeate (Figure 6-19). Even though the unfractionated TOC levels were the same for the non-sheared and sheared samples, all of the subsequent fractionated samples had higher TOC for sheared than for non-sheared. Because all of the fractionation steps resulted in elevated TOC, it appears that much of the material released by shear was dissolved and smaller than 30 kDa. It is also interesting to note that feed and permeate samples were very similar for all of the non-sheared runs, but in the case of shear the centrifuged and glass-fiber-filtered (GFF) fractions showed detectable differences between feed and permeate samples. This supports the view that shear released some intermediate-sized particles that were not as easily removed with centrifugation or glass-fiber filtration but were removed with subsequent fractionation steps.

UV measurements at 254 nm (Figure 6-20) reveal that without shear the 0.1-μm PVDF permeate had approximately the same UV absorbance regardless of the fractionation level. Further, aside from the algal culture sample, the feed and permeate were all fairly close. This indicates that the algal cells themselves absorbed approximately half of the UV radiation and once they were removed only dissolved material that could pass through all of the fractionation steps remained; i.e. there was not a significant amount of UV-absorbing material between 30-kDa and the size of the algal cells themselves. It is interesting that with shear there arose higher absorbance levels for centrifuged and glass-fiber-filtered fractions, while without shear these fractions were quite similar to smaller fractions. It seems that some UV-absorbing material between 0.45 μm and the algal cell size (about 10 to 20 μm) was created with shear.

Fluorescence (Figure 6-21) proved again to be a very good indicator of shear and was also a good indicator of the degree of fractionation. The sheared algal culture samples had about twice the fluorescence of the non-sheared culture. Centrifugation removed 97% of fluorescence for the non-sheared algal culture, but only 33% after shear. Comparing fluorescence data with algal concentration (Figure 6-16) it appears that most of the fluorescent material was contained within the algal cells before shear, but after shear most of the fluorescence was extracellular. Subsequent fractionation levels removed progressively more material for both non-sheared and sheared cases. Fluorescent material was present in all of the size classes.

Carbohydrate measurements (Figure 6-22) showed similar trends as UV absorbance; a significant portion of carbohydrate material was dissolved and able to pass through all fractionation levels. Also similar to UV, more material in the glass-fiber-filtered and centrifuged fractions was created after shear. It is noteworthy that carbohydrates were similar in concentration even when bacterial numbers were greatly elevated in the sheared sample; it appears that carbohydrates came mostly from the algal cells.

Along with carbohydrates, proteins were suspected to be present in the foulant material. Both raw algal samples and all measured fractions showed protein levels below the detection limit of aqueous analytical methods (5 mg/l). In order to determine the effects of protein on the samples, proteins were measured directly on the fractionation membranes using a modified form of the Pierce-BCA protein assay. The results are given in Figure 6-23; these show a different trend than the results in other figures because here we measured the amount of protein collected by the fractionation membrane as opposed to the concentrations in the fractionation permeate (as in Figures 6-19 through 6-22). The protein concentration given is the amount of material in the feed sample that was collectable by that membrane. Negative control samples (clean membranes) gave readings that were 0.1 mg/l or lower, due either to the reagents reacting with the membrane material or to contamination. A positive control was performed by placing a known quantity of BSA in solution on a 30 kDa membrane coupon and allowing it to dry before measuring adsorbed protein. The protein recovery was 114% and would have resulted in an extrapolated feed water concentration of 0.1 mg/l higher than expected. Thus it appears that all of the protein was recovered in the positive control and the background reading was consistent with the negative control readings. The negative control readings were subtracted from the fouled membrane readings in the protein concentrations reported.

The protein data (Figure 6-23) show that more proteinaceous material was collected as the pore size decreased. This indicated that proteinaceous material existed in a distribution of size classes; some was large enough to be retained on loose membranes, while other material could only be retained by tighter membranes. The sheared samples had significantly higher protein levels than the non-sheared sample, indicating that proteins were able to pass through the glass-fiber filter after shear more readily than before shear. The data are suspect because the bacterial concentration was elevated in the sheared sample; it could be thought that this was a measurement of the protein in the bacteria. However, if the measurement were dominated by bacteria, the concentrations would all be similar because bacteria were almost completely rejected by all membranes.

The data of Figures 6-19 through 6-22 can be compiled to produce the algogenic organic matter size distributions displayed in Figure 6-24 (the protein data of Figure 6-23 cannot be included here because of its distinct measurement method). These plots make it readily apparent that shear changed the size distribution of organic matter. The non-sheared samples were comprised of at least 55% material that was large enough to be removed with centrifugation; this is apparent with any of the four measurement methods. On the other hand, only an average of 35% of the material could be removed with centrifugation after shear. Before shear there was more of a dichotomy of organic matter size; the very large and very small size classes dominated and little intermediate-sized material was present. However, shear caused the distribution to spread and intermediate-sized material became available. This helps explain one possible reason that shear caused exacerbated flux decline in all cases; a sample with a heterogeneous size distribution would be more likely to contain pore-plugging material and would be more likely to form dense cake layers.

Examining the flux decline data of Figure 6-15 in light of the organic matter characterization data the role of each size fraction can be ascertained. The algal cells themselves appear to be important before shear since the unfractionated sample (containing the most algal cells) had the most dramatic flux decline. However, after shear the algal concentration was not so important, since the centrifuged and glass-fiber filtered fractions had similarly low flux results even without algal cells present. The bacterial concentration does seem to be important for flux decline. Where the bacterial concentration was elevated, flux decline was exacerbated. The bacterial concentration could have been the reason for the odd result that the 0.45-μm non-sheared sample had more fouling than the 0.45-μm sheared sample; the non-sheared sample turned out to have more bacteria. These bacterial data call into question the conclusions about shear. Was the release of organic matter truly the cause of extreme flux decline or were bacteria the culprits? For this set of fractionation data it remains unclear; however, it should be remembered that the original round of flux decline experiments was performed with the same sample on the same day so the bacterial levels would not have been different there. In those experiments shear caused more extreme fouling in every case, so the hypothesis stands.

Algae and bacteria are members of the particulate size class, operationally defined as greater than 0.45 μm in size. Fouling certainly correlates with that size fraction, but the question remains whether fouling also correlates with the dissolved material. Particularly, dissolved biopolymers and small colloidal material would be suspect as foulants. Figure

6-18 shows that high-molecular weight dissolved and colloidal material (the peak between 6 and 7 minutes) was very similar in concentration for all the size fractions bigger than 100 kDa, yet fouling was very different. Also, the 100 kDa and 30 kDa sheared fractions had more high-molecular-weight material than all of the non-sheared fractions, yet no flux decline was seen for these samples. Though this material was in high abundance and increased with shear, it apparently passed through the microfiltration membranes without adsorbing to the pores and causing flux decline. This does not rule out the possibility that the dissolved material could have interacted with the particulates to in a synergistic way; such a phenomenon has been seen in other fouling studies (Li and Elimelech 2006). However, without particulate matter present the high-molecular weight dissolved material was not able to cause fouling in these short-term tests. This is contradictory to other studies where adsorptive fouling was found to play an important role (Howe and Clark 2002; Koh et al. 2005; Howe et al. 2006). Those studies were performed with fresh waters whose humic materials may have a stronger affinity for adsorption than our algogenic organic matter. Also, here we used a hydrophilic PVDF membrane while previous work was done with polypropylene which is hydrophobic and polyethersulfone which is moderately hydrophobic (Cheryan 1998). Membrane manufacturers are turning more and more toward hydrophilic membranes, like the modified PVDF used in this study. Thus, adsorption is expected to be a less important short-term fouling mechanism at full scale. A gradual process where adsorptive fouling would occur over several backwashes in a full-scale facility could still be important; longer-term experiments would be needed to asses that possibility.

The chemical makeup of the highly fouling fractions was determined by carbohydrate and protein measurements. Carbohydrates accounted for 34% and 31% of the total organic carbon for unfractionated non-sheared and sheared samples, respectively. After centrifugation, the carbohydrate content dropped to 18% and 21%. Glass fiber filtration gave similar results, 19 and 19%, respectively. Further fractionation left the ratio at 12 and 13% for the 0.45 μm fraction, 14 and 15% for 0.22 μm, 14 and 17% for 100 kDa, and 5 and 14% for 30 kDa. It appears, then, that the particulate organic matter has a higher carbohydrate content per mass of TOC than does the dissolved material; this was true for both non-sheared and sheared samples. Also, it is apparent in the centrifuged and glass-fiber-filtered cases that carbohydrates were retained on the PVDF membrane, since there was a measurable difference between feed and permeate samples.

The protein content of the foulant material was not as easy to elucidate, since proteins could not be measured in solution. However, Figure 6-23 shows the amount of protein in the glass-fiber-filtered sample that was collectable on each membrane. The tightest membrane (30 kDa) collected the most material, indicating the upper limit of the verifiable protein concentration in the glass-fiber-filtered sample. Thus, at a minimum, the non-sheared glass-fiber-filtered sample had roughly 0.35 mg/l of protein and the sheared sample had 0.85 mg/l. These represent 13 and 19% of the non-sheared and sheared TOC, respectively, which was in the same range as found for carbohydrates (19 and 19%). These data represent our best estimate for the composition of the highly-fouling material, since the glass-fiber filtered sample contained the highly-fouling fraction, but did not contain larger particulates and algal cells. It is interesting to note that even though the total organic carbon concentrations were different for non-sheared and sheared samples (2.7 and 4.4 mg/l, respectively) the carbohydrate and protein ratios were quite similar. This suggests that the highly fouling particulate fraction is composed of similar material whether it be released naturally or through engineered shear.

The distributions of organic matter shown in Figure 6-24 help to determine the quantity of foulant material present. It is noteworthy that centrifuged and glass-fiber-filtered fractions together made up only seven percent of the total organic matter and 10% of the carbohydrates before shear. Despite these low mass-percentages, these fractions contributed most of the flux decline. After shear, the mass percentages increased to 13% of TOC, 23% of carbohydrates. Along with this increase in mass percentage, the flux decline was exacerbated. This supports the hypothesis that the material in these fractions are the principal foulants. Further, it suggests that the majority of the organic matter (that which is larger or smaller than this size fraction) is not heavily responsible for flux decline. A similar result was found for filtration of surface waters, except that the highly fouling fraction was determined to be colloidal material between 20 and 100 kDa (Howe and Clark 2002). This could suggest that the existence of a highly-fouling fraction is a general phenomenon, while the exact fraction that is highly fouling depends on the foulant source, membrane pore size, and membrane material.

In the just-concluded discussion of size distribution the fluorescence data were intentionally ignored. Fluorescence data were unique compared to other characterization techniques in that the difference in apparent size distribution between sheared and non-sheared samples was extreme. As noted previously, before shear almost all the fluorescent material was within the algal cells. After shear it had been released and spread over the entire size distribution. Some of the material was contained in the highly fouling fraction (centrifuged and GFFed fractions) but there was clear separation into the other fractions, as well. This is interesting because fluorescence is specifically an indicator of the light-harvesting pigments chlorophyll and peridinin. Instead of being released entirely upon cell breakup, and instead of being retained in only one of the size classes, the chlorophyll and peridinin are distributed throughout the matrix.

Based on the size distributions, and keying in on the pigments as a good indicator, some hypotheses can be drawn here about the cellular components of *H. pygmaea* that were scattered upon cell breakup and caused the exacerbated flux decline. *H. pygmaea* has a theca (covering) of plates that give rigidity and protection. As shown Figure 6-25 there are 35 thecal plates per cell and their average width is roughly three microns (Loeblich et al. 1981). When the cell is disrupted these plates could separate and remain in solution as three-micron particles made up principally of carbohydrates (cellulose). Fibers have been found that run throughout the cells and appear to provide structural strength and thecal plate alignment (Roberts et al. 1987). These fibrous structures, though broken apart from the cell, could also remain intact and form small particles. The situation could be similar for chloroplasts, pyrenoids, and mitochondria that are roughly one to three microns in size (Bullman and Roberts 1986). The pyrenoids are locations of starch production/collection. If they remain intact, they would be pore-blocking particles and if they are broken apart they could be a source of dissolved or colloidal carbohydrates.

Another organelle, the chloroplast, is interesting because it contains several levels of structure. Chromoprotein complexes containing light-harvesting pigments have molecular weights between 17 and 32 kDa (Jovine et al. 1995). The most abundant structure of this class is the Peridinin-Chl *a*-Protein complex (PCP) that gives the algae their brick-red color (Jovine et al. 1992). These are located in the thylakoids which are arranged in grana stacks that are 0.1 to 0.5 microns. Thus when chloroplasts are released from the cells they could be broken down into smaller units of grana, thylakoids, and/or protein complexes. Further, it has been shown that cell disruption and thylakoid release results in the creation of thylakoid micelles that retain intact chromoprotein complexes and have greater light absorbance and fluorescence than whole cells (Johnsen et al. 1997). The increased absorbance arises because the micelles are not subject to the package effect. These observations are very much in line with our own observations that bulk fluorescence increases with cell breakup. It is quite reasonable to assume that cell breakup results in chloroplast fragments of varying size because of different degrees of damage. This could account for the wide distribution of size classes evident in fluorescence measurements.

6.3 THE IMPORTANCE OF BACTERIA

The life cycle of an algal bloom involves a lag phase, a rapid increase in phytoplankton cell number, and a subsequent rapid increase in bacterial cell number. The seawater organic matter composition changes drastically from pre-bloom background material to algal cells and AOM to bacterial cells and bacterial organic matter. This makes for a particularly challenging situation when pre-treatment strategies are being considered for seawater desalination facilities; operators must deal with feed water that changes greatly from day to day in terms of organic-matter and microbiological concentration and composition.

To provide some insight into how the varying concentration and composition of organic matter may affect pretreatment membranes, a simulated algal bloom was created in the laboratory and filtration performance was measured during the various stages of bloom development. Water quality was monitored over time and compared to the flux decline experiments to determine which factors would be of greatest concern to membrane filtration plant operators. The importance of bacteria during this bloom life cycle was investigated.

6.3.1 Simulated algal bloom

Algae were cultured as reported in Section 3.4. Ten bottles with a volume of 500 ml each were spiked on the same day and grown side-by-side for seven weeks. The seven-week period encompassed the simulated algal bloom; it began with a small algal concentration then algal numbers peaked and decayed. Three times each week two bottles were measured via hemacytometry and fluorescence microscopy to determine algal cell concentration. Fluorescence microscopy was also used for bacterial counts. Additionally, ultraviolet (UV) absorption and bulk fluorescence were measured three times per week. Approximately each week (sometimes twice per week) a culture bottle was removed and used for membrane performance experiments.

6.3.2 Membrane Filtration Tests

Membrane filtration tests during the algal bloom life cycle experiment were performed using two 22-mm diameter dead-end test cells for side-by side replication. Membranes were 0.1-µm hydrophilic PVDF (Millipore type VVLP) that represent full-scale hollow-fiber filtration. The filtration protocol of Section 3.2 was used with the following modifications. After the clean-water flux test, the feed was switched from ultrapure water to a one-liter pressure vessel containing 200-ml of algal culture. The culture was collected by siphoning from the top of the culture bottle to avoid collecting settled material. Forty milliliters of feed were saved for analysis. A magnetic stir bar was used in the pressure vessel to ensure entrainment of algal cells. Filtration was performed at 69 kPa (10 psi). The sample was filtered until exhausted or until flux dropped below 100 liters per meter squared per hour (lmh).

After filtration of the algal culture, the membrane was rinsed by adding about 25 ml of 0.1-µm filtered and autoclaved seawater (clean seawater) to the vessel, shaking for ten seconds and discarding. Rinsing was performed three times. The membrane was then inverted and placed back in the filtration cell. The support screen was helpful in facilitating membrane inversion; without a support screen the membrane deforms more and is harder to remove from the cell without damage. Membrane backwash was done with 100-ml of clean seawater. The membrane was then inverted again and another 100-ml of clean seawater was filtered to measure the flux recovery. The reason clean seawater was used instead of nanopure water for rinsing, backwashing, and flux recovery is that nanopure water could break algal cells due to osmotic shock. All flux experiments were done at room temperature (22 ± 2°C). Each test was performed twice using the dual-filtration-cell setup.

6.3.3 Algal bloom life cycle results

Algal concentration during the simulated algal bloom followed a fairly classic pattern of lag phase and exponential growth. This was evident in both the hemacytometry and fluorescence microscopy data given in Figure 6-26. The expected stationary and decline phases were difficult to determine due to scatter in the data. The latter data seemed to be a combination of stationary and declining phases; though the algal numbers had dropped from their peak, they experienced a slow decline instead of remaining steady or dropping completely.

Bacterial measurements (Figure 6-27) showed a lag phase for ten to fourteen days then cell numbers began to increase dramatically. Bacteria continued to increase in number up to the 46-day end of the experiment, though in later stages the growth rate appeared to taper. These data are consistent with the idea of a bacterial bloom following the algal bloom. Algal numbers started increasing dramatically at about eight days. Organic matter from the algal bloom was then available for the bacterial bloom that began about one week later. As the algal bloom peaked and cell numbers started declining, bacteria fed on the algal remains. There was sufficient organic matter for the bacteria to continue feeding through the end of the experiment, but since algal numbers had dropped, bacterial growth rates also declined. It is presumed that had the experiment continued, bacterial numbers would have reached a peak and also begun to decline.

In enumerating algal and bacterial cells it is important to note their morphology. The fluorescence microscope images in Figure 6-28 show the way bacteria and algae interact in culture. Bacteria often attach to an algal cell and form a globular biofilm as in Figure 6-28a. Alternatively, bacteria can enter into an algal cell and feed off organic matter from within (Figure 6-28b). When bacteria were enumerated, these globular biofilms and invaded algal cells were not considered; only planktonic bacteria were enumerated, keeping floc-associated biofilms separate. Thus, the actual biomass in a sample was underestimated, since it did not include floc-associated bacteria.

The simulated algal bloom was also tracked using optical techniques. UV absorbance at 254 nm (Figure 6-29) showed a slight decrease during the first seven days of the experiment. The reason for the decrease is unknown, since algal and bacterial numbers were both rising (though slowly) during that time period, but UV-absorbing vitamins in the nutrient medium may have been utilized by algae or consumed by bacteria in the early stage.

After the initial decrease, UV absorbance increased in a linear fashion as time progressed. This was the case for both unfiltered and filtered (0.22 μm) samples. The trend follows the bacterial growth pattern. Since algal numbers showed a different pattern (they decreased after 20 days) UV absorbance is more correlated to bacteria than it is to algae. There was a linear relationship between unfiltered and filtered UV absorbance. Assuming that the difference between unfiltered and filtered samples is caused by the presence or absence of cells (bacterial or algal), it appears that cells released UV-absorbing extracellular material at a constant rate throughout the experiment.

Fluorescence data shed further light on the nature of organic matter present during the algal bloom simulation. Fluorescence of bulk (non-filtered) samples (Figure 6-30) followed the algal cell numbers for the first thirty days of the experiment; the increase in algal cell numbers starting around day eight is evident in the non-filtered fluorescence plot. Further, the peak in algal numbers at about day 20 is also evident via fluorescence. The pattern broke down, however, after day 34 when unfiltered fluorescence was dramatically higher than any other day of the experiment, even though algal numbers were on the decline.

In order to better understand the fluorescence information the data were plotted according to the bottle measured. As noted previously, during the experiment culture bottles were removed for membrane tests. Thus, on days two to ten bottle *a* was measured, but after the first membrane test on day 11, bottle *b* was used. This pattern continued through the experiment and in Figure 6-30 the bottle measured is indicated. It turns out that the anomalously high fluorescence data occurred in bottles *g* and *h*. It is presumed that in those bottles the bacterial bloom involved a strain with extremely fluorescent cellular components; for example, a strain that produced large quantities of fluorescent proteins similar to the green fluorescent protein found in jellyfish. Even though the culture bottles were all spiked at the same time and with the same mixture of algae and bacteria, the bacterial population is heterogeneous and the population dynamics among bacterial species is random so that different strains can take over the culture. In fact, it appears that the fluorescent bacteria in culture bottle *g* bloomed and decayed over the eight days it was monitored, while fluorescence in bottle *h* was slightly increasing.

Fluorescence data for filtered samples shed further light on the organic-matter composition in culture bottles. Figure 6-31 shows that filtered fluorescence intensity was quite low for the first ten days, then began increasing after day 16. This follows the bacterial trend much more closely than the algal trend, indicating that dissolved-matter fluorescence is correlated with bacterial abundance. Even though the algae are very fluorescent, they do not appear to release their fluorescent material when they are in growth stage. For the culture bottles that had very high unfiltered fluorescence, the filtered fluorescence also spiked. In fact, the increase was so intense that the data had to be plotted on a broken y axis in Figure 6-31. The trends in filtered fluorescence for bottles *g* and *h* follow the trend for non-filtered fluorescence indicating that dissolved fluorescent material was the reason for elevated bulk fluorescence. For bottle *g* the filtered fluorescence was as much as 90 percent of the unfiltered fluorescence (on days 37 and 39) and for bottle *h* filtered fluorescence reached 71 percent of the unfiltered fluorescence (day 46). One hypothesis is that the bacterial cells in those bottles released a fluorescent extracellular product. An alternative hypothesis is that culture vessels *g* and *h* contained bacteria that had a propensity to lyse and release material from algal cells. It was seen during shear experiments that fluorescence increased with shear as the cells broke apart. If bacteria were able to lyse the cells, this could have been a mechanism for release of algal fluorescent organic matter.

Flux measurements along the life cycle of the algal bloom (Figure 6-32) showed an expected trend; flux decline was more rapid with each successive experiment. As algal numbers increased, flux decline also increased. However, as the algal population peaked and decayed, flux decline continued to increase. It appears that bacteria were the culprits in this continued exacerbation of fouling.

6.4 CONCLUSIONS REGARDING LOW-PRESSURE FOULING

This chapter evaluated mechanisms by which planktonic algae and their associated organic matter foul MF and UF membranes. Algae are a cause for concern in seawater desalination pretreatment because they quickly block membrane pores and cause severe fouling. However, the algal cells themselves are not the only cause for concern; organic matter released by algal cells is also a major contributor to fouling. We showed this by exposing the algal cells to hydrodynamic shear and evaluating subsequent flux decline. Though algal cell numbers decreased dramatically after shear, flux decline was exacerbated in all of the membranes tested.

When cells are sheared and break apart the cell structure disintegrates and the resulting cellular particles are much smaller than the cells themselves. This was made clear through flow cytometry analysis that resulted in very few “mid-size” particles. Breakup of *Heterocapsa pygmaea* cells in our system followed a first-order model, except that in the very early stages a dramatic decline in cell number was not accounted for. By combining two first-order models the breakup could be more adequately characterized. A fit of the model to the data suggests that about half the cells have strong structural strength and half are weak and more easily disrupted.

Shear of algal cells was detrimental to membrane productivity for all four pore sizes tested (0.45-μm, 0.22-μm, 100 kDa, and 30 kDa). Even though algal numbers decreased during shear, the released organic matter and small cellular particulate material caused more exacerbated flux decline. This was likely due to increased pore blocking and tighter-porosity cake deposits.

Organic-matter rejection was diminished after shear. Carbohydrates, UV-absorbance, and fluorescence were all elevated in permeate samples after shear compared to the before-shear cases. The majority of carbohydrates, UV-absorbing material, and fluorescent material was contained in the algal cells in culture samples. With shear the organic matter was released and permeated the MF and UF membranes. Fluorescence was the best indicator of organic matter released by shear.

Experiments were performed to determine the size fraction of organic matter most responsible for fouling of 0.1-μm PVDF membranes. In both sheared and non-sheared algal cultures the majority of flux decline was caused by material that was small enough to remain in solution after centrifugation and glass-fiber filtration, but large enough to be retained on a 0.45-μm microfilter. Smaller material—that which was able to permeate 0.45-μm and tighter membranes—had lesser fouling effects. This suggests that adsorptive fouling inside the membrane pores was not as important as pore blocking and cake buildup on top of the membrane surface. The highly-fouling material had very similar protein and carbohydrate composition before and after shear; 13% protein and 19% carbohydrate before shear, 19% protein and 19% carbohydrate after shear.

Bacterial cells are included in the size range that was most responsible for fouling. During our simulated algal bloom the bacterial numbers increased steadily even as algal numbers declined and membrane flux continued to deteriorate. Bacteria, then, may be more detrimental to membrane flux than the algal cells in an actual bloom.

These results on fouling by algae and algogenic organic matter have implications for full-scale application of MF and UF as pretreatment to RO for seawater desalination. When blooms occur the algae are easily observed and obvious membrane foulants. However, algal cells could potentially experience sufficient shear for cell lysis in intake and pumping systems so that the cell bodies are broken down into smaller particles. The membrane elements themselves may also have hydrodynamic regimes where shear could be problematic. Perhaps dead-end, open tank membrane configurations similar to those used for membrane bioreactors would be more appropriate than crossflow modules. Studies of local shear stresses in different systems would be needed to determine which configurations were indeed optimal.

By comparison with other systems we determined that our algae were exposed to a higher level of shear than would be seen in typical valves and pumps in a water treatment system (which would be expected to have shear levels similar to the photobioreactor or flocculation tank described here). This makes the experiments a "worst-case scenario" for algal breakup by cells similar to *Heterocapsa pygmaea*. However, *H. pygmaea* is a fairly small dinoflagellate armored with thecal plates that give it substantial rigidity. Other bloom-forming dinoflagellate species like *Karenea brevis*, the principal bloom-forming species in the Gulf of Mexico, are larger and unarmored so they would break apart much more easily. The red-tide former *Heterosigma akashiwo* that recently shut down a seawater desalination plant in Fujairah had large cells (50 to 100 μm) and no cell wall. It is possible that *K. brevis* or *H. akashiwo* would experience cell breakup even in lower-shear treatment systems. Measurements of actual breakup properties among various species should be performed to determine the levels of shear they can withstand.

Even when shear is not sufficient for cell breakup, algal cells naturally lyse during their cycle of growth and death. Additionally, bacteria can exist at concentrations much higher than the algae and are in the size range that makes them principal foulants. Thus it behooves designers to consider not only algal cells, but the particulate material smaller than algal cells as the more problematic foulant.

Some engineers have considered additional steps for algal removal before MF or UF membranes. Dissolved air floatation (DAF) has been put forward as one possible solution. Coagulation and flocculation could be another alternative. In these or other approaches it will be important that the systems not only remove the algal cells, but that they do it in a manner which minimizes cell lysis. For maximum effectiveness, the pretreatment approach should be able to remove algal cells as well as the smaller particulate and bacterial matter that accompanies the algal bloom.

6.5 TABLES

Table 6-1: Comparison of three potential shear-characterizing parameters in various systems.

System	E_v (J/m^3)	K_v	Φ_m (W/m^3)
Coagulation tank	NA	NA	1 E+02
Photobioreactor valve	4 E+05	8 E+02	2 E+07
Our pump	5 E+05	1 E+02	2 E+07
Our valve	6 E+06	3 E-03	4 E+10
Homogenizer	4 E+07	7 E-03	8 E+12

Table 6-2. Goodness of fit values for fouling models applied to MF and UF filtration for two replicates on each of the four membranes of interest, before and after shear (16 total flux tests are represented). The models are delineated by their *n* value (see caption to Figure 6-14). R^2 is the coefficient of determination. RMSE is the root mean squared error with units of percent initial flux. Shading indicates the highest R^2 and the lowest RMSE (the best model fit) for the flux test.

		n = 0		n = 1		n = 3/2		n = 2	
		R^2	RMSE	R^2	RMSE	R^2	RMSE	R^2	RMSE
0.45 µm	Before Shear	0.938	2.9	0.952	2.6	0.956	2.5	**0.957**	**2.4**
		0.907	5.0	0.947	3.8	0.963	3.1	**0.976**	**2.5**
	After Shear	0.652	11.7	0.864	7.3	0.940	4.8	**0.972**	**3.3**
		0.642	12.2	0.853	7.8	0.931	5.4	**0.966**	**3.8**
0.22 µm	Before Shear	0.847	9.8	0.947	5.7	0.983	3.2	**0.993**	**2.0**
		0.831	10.7	0.939	6.4	0.980	3.7	**0.996**	**1.6**
	After Shear	0.742	9.5	0.932	4.9	**0.982**	**2.5**	0.975	2.9
		0.767	11.0	0.931	6.0	**0.983**	**3.0**	0.982	3.1
100 kDa	Before Shear	0.887	6.0	**0.989**	**1.8**	0.970	3.1	0.850	6.9
		0.901	5.5	**0.992**	**1.6**	0.960	3.5	0.819	7.5
	After Shear	**0.987**	**1.5**	0.913	3.8	0.685	7.2	0.305	10.7
		0.994	**1.1**	0.907	4.2	0.688	7.8	0.276	11.8
30 kDa	Before Shear	0.856	3.5	0.880	3.2	0.891	3.1	**0.902**	**2.9**
		0.896	4.1	0.931	3.3	0.947	2.9	**0.961**	**2.5**
	After Shear	0.973	3.0	**0.996**	**1.1**	0.976	2.8	0.919	5.2
		0.956	3.8	**0.993**	**1.5**	0.991	1.7	0.966	3.4

Table 6-3. Lumped fitting parameter values for fouling models applied to MF and UF filtration for two replicates on each of the four membranes of interest, before and after shear (16 total flux tests are represented). The models are delineated by their *n* value (see caption to Figure 6-14). Also reported is the half width of the 95% confidence interval ($CI_{1/2}$) given as a percentage of the fitting parameter value. Shading indicates the parameter associated with the best model fit (as in Table 6-2).

		n = 0		n = 1		n = 3/2		n = 2	
		K_{cf} (s^{-1})	$CI_{1/2}$ (%)	K_{ib} (s^{-1})	$CI_{1/2}$ (%)	K_{sb} (s^{-1})	$CI_{1/2}$ (%)	K_{cb} (s^{-1})	$CI_{1/2}$ (%)
0.45 µm	Before Shear	1.13 E-2	8.6	4.81 E-3	6.6	2.21 E-3	5.9	**4.06 E-3**	**5.4**
		1.53 E-2	11.6	6.14 E-3	7.4	2.74 E-3	5.5	**4.89 E-3**	**4.0**
	After Shear	1.75 E-1	22.2	2.74 E-2	9.7	8.62 E-3	5.4	**1.19 E-2**	**3.2**
		1.60 E-1	22.4	2.55 E-2	10.0	8.04 E-3	5.8	**1.11 E-2**	**3.5**
0.22 µm	Before Shear	1.98 E-2	18.1	5.55 E-3	7.9	2.07 E-3	3.7	**3.07 E-3**	**1.9**
		2.21 E-2	20.5	6.13 E-3	9.2	2.28 E-3	4.4	**3.36 E-3**	**1.5**
	After Shear	6.01 E-2	18.7	9.81 E-3	6.7	**3.09 E-3**	**2.9**	4.28 E-3	2.9
		5.04 E-2	22.5	9.85 E-3	8.8	**3.23 E-3**	**3.6**	4.43 E-3	3.1
100 kDa	Before Shear	1.16 E-2	6.0	**2.29 E-3**	**1.3**	7.44 E-4	1.8	1.01 E-3	3.4
		9.66 E-3	5.0	**1.92 E-3**	**1.0**	6.24 E-4	1.9	8.46 E-4	3.3
	After Shear	**2.00 E-2**	**1.7**	3.64 E-3	3.2	1.18 E-3	5.2	1.77 E-3	6.8
		1.95 E-2	**1.3**	3.85 E-3	3.8	1.25 E-3	5.9	1.77 E-3	7.6
30 kDa	Before Shear	1.14 E-4	2.5	5.10 E-5	2.0	2.40 E-5	1.8	**4.50 E-5**	**1.6**
		1.88 E-4	2.4	8.00 E-5	1.7	3.70 E-5	1.4	**6.70 E-5**	**1.1**
	After Shear	6.66 E-4	1.2	**2.12 E-4**	**0.4**	8.40 E-5	0.8	1.32 E-4	1.2
		5.52 E-4	1.6	**1.86 E-4**	**0.5**	7.60 E-5	0.5	1.23 E-4	0.8

Table 6-4. Measured values of feed and permeate total carbohydrates, monosaccharides, UV absorbance, and fluorescence for non-sheared and sheared algal samples on four membrane pore sizes. ± indicates standard error of triplicate measurements.

		Measured Values			
		Total Carbohydrates (mg/l as glucose)	Monosaccharides (mg/l as glucose)	UV absorbance	Fluorescence
Feed	Non-sheared	5.84 ± 0.13	1.14 ± 0.02	0.10	150.4 ± 2.2
	Sheared	3.67 ± 0.3	1.07 ± 0.03	0.18	499 ± 7.2
0.45 μm permeate	Non-sheared	0.74 ± 0.17	0.57 ± 0.06	0.05	1.3 ± 0.1
	Sheared	0.95 ± 0.05	0.61 ± 0.07	0.08	151.7 ± 2.6
0.22 μm permeate	Non-sheared	0.82 ± 0.24	0.21 ± 0.01	0.04	1.4 ± 0.1
	Sheared	0.99 ± 0.34	1.00 ± 0.03	0.08	249.1 ± 1.1
100 kDa permeate	Non-sheared	0.34 ± 0.09	0.26 ± 0.02	0.03	1.3 ± 0.1
	Sheared	0.85 ± 0.07	0.47 ± 0.03	0.07	129.6 ± 4.3
30 kDa permeate	Non-sheared	0.34 ± 0.09	0.18 ± 0.02	0.04	1.3 ± 0.2
	Sheared	1.10 ± 0.04	0.53 ± 0.03	0.07	107.8 ± 0.5

Table 6-5. Rejection calculated for total carbohydrates, monosaccharides, UV, and fluorescence for four membrane pore sizes.

		Calculated Rejection			
		Total Carbohydrates	Monosaccharides	UV	Fluorescence
0.45 μm	Non-sheared	0.87	0.50	0.55	0.99
	Sheared	0.74	0.43	0.56	0.70
0.22 μm	Non-sheared	0.86	0.82	0.64	0.99
	Sheared	0.73	0.06	0.54	0.50
100 kDa	Non-sheared	0.94	0.77	0.66	0.99
	Sheared	0.77	0.56	0.59	0.74
30 kDa	Non-sheared	0.94	0.84	0.65	0.99
	Sheared	0.70	0.51	0.61	0.78

6.6 FIGURES

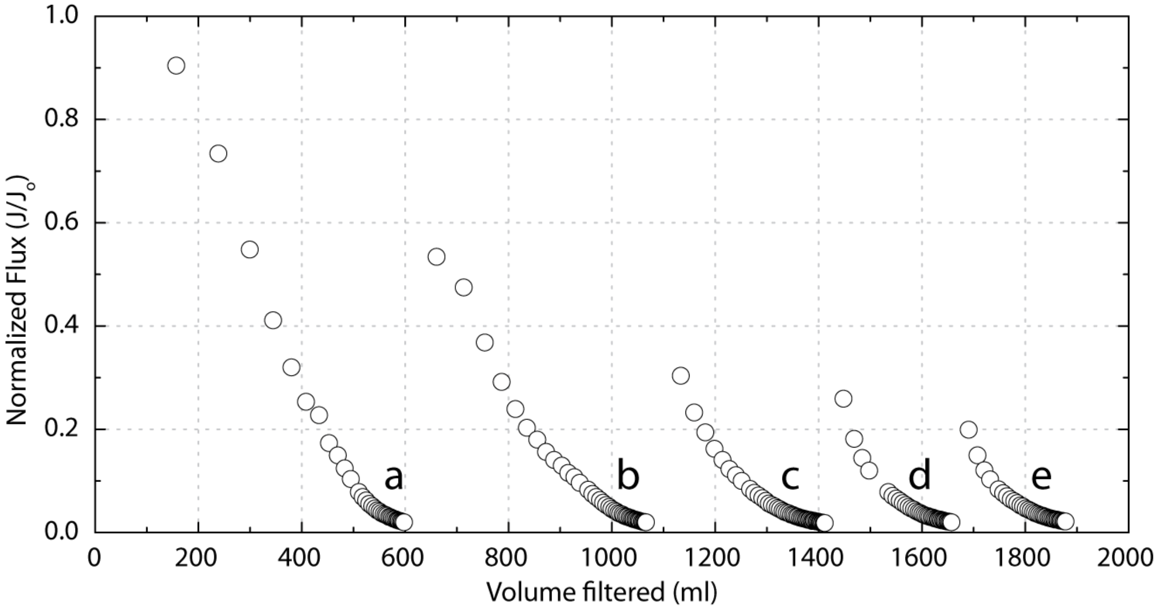

Figure 6-1. Normalized flux for filtration of an algal-laden sample (70,000 cells/ml) on a 0.45-µm MF membrane. The five stages (*a*, *b*, *c*, *d*, *e*) are separated by breaks where the membrane was rinsed. Clean-water flux (J_o) was 22,400 lmh.

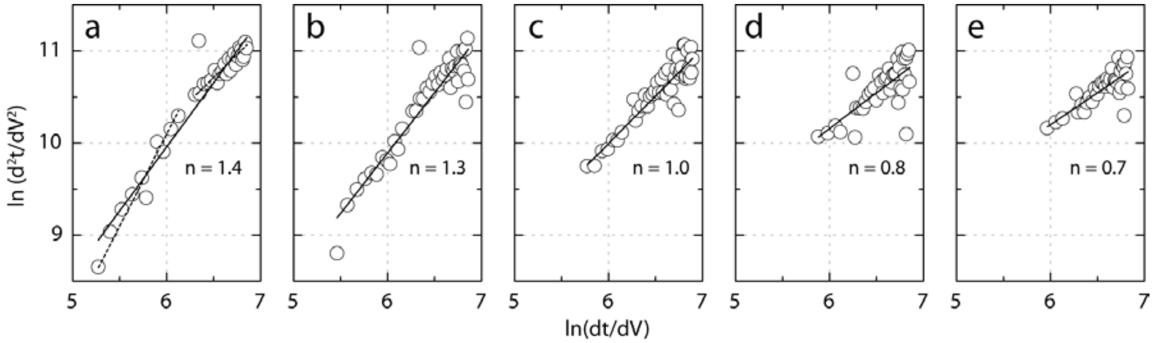

Figure 6-2. Fouling mechanism analysis plots for the five MF algal filtration flux curves (*a*, *b*, *c*, *d*, *e*) presented in Figure 6-1. Solid lines show the linear fit, the slope of which (n) is also given. Curve *a* has two additional fits indicated by broken lines; $n = 2$ for the first segment and $n = 1$ for the second segment.

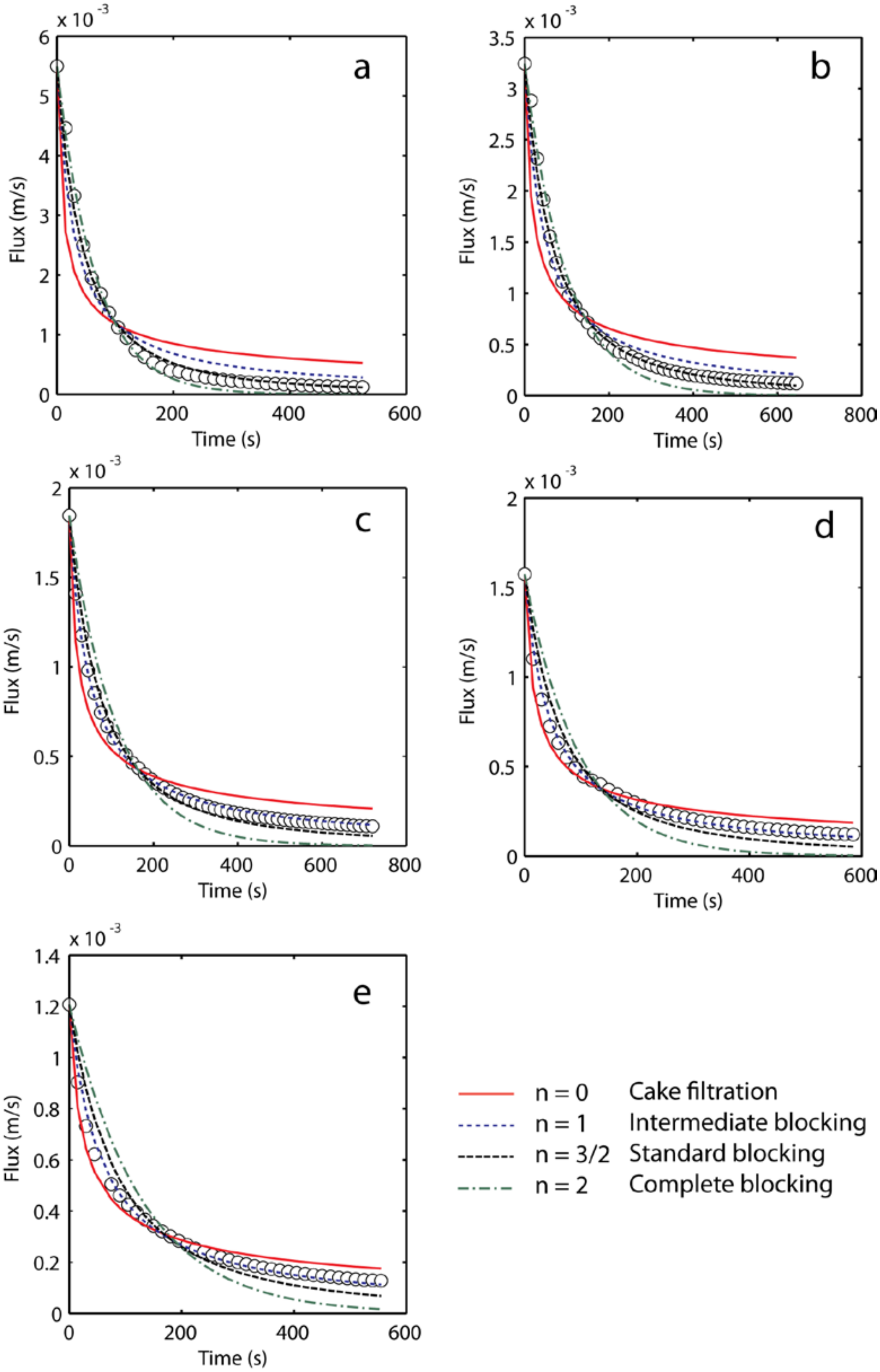

Figure 6-3. Flux versus time plots for the five regions (*a*-*e*) shown in Figure 6-1. Data are indicated by circles and data fits for four fouling models are also shown.

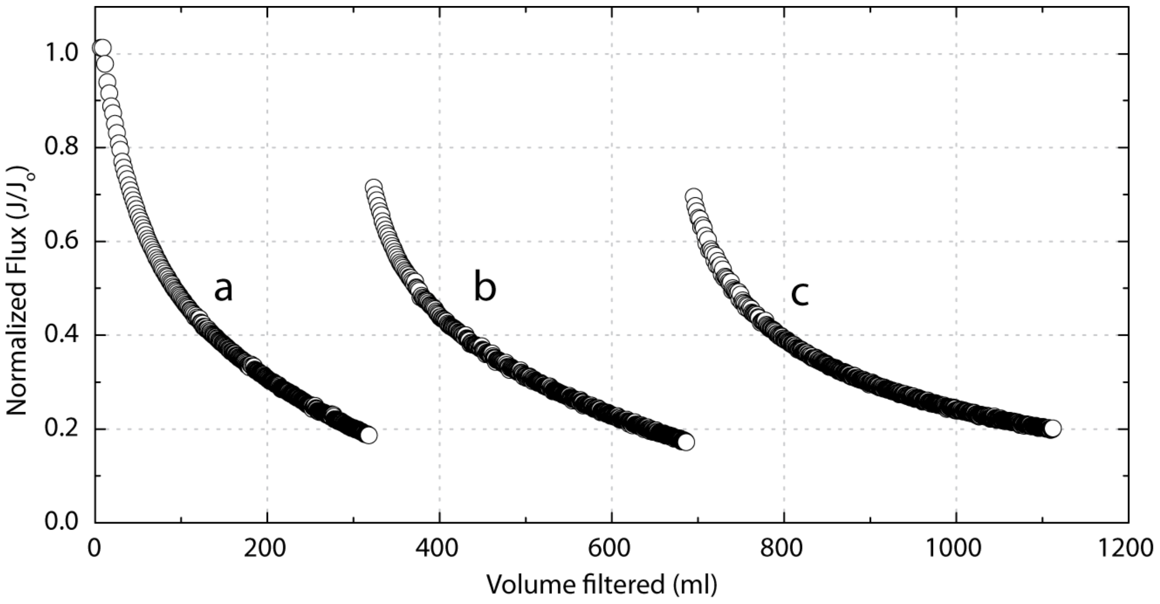

Figure 6-4. Normalized flux for filtration of an algal-laden sample (70,000 cells/ml) on a 100-kDa UF membrane. The three curves (*a*, *b*, *c*) are separated by breaks where the membrane was rinsed. Clean-water flux (J_o) was 520 lmh.

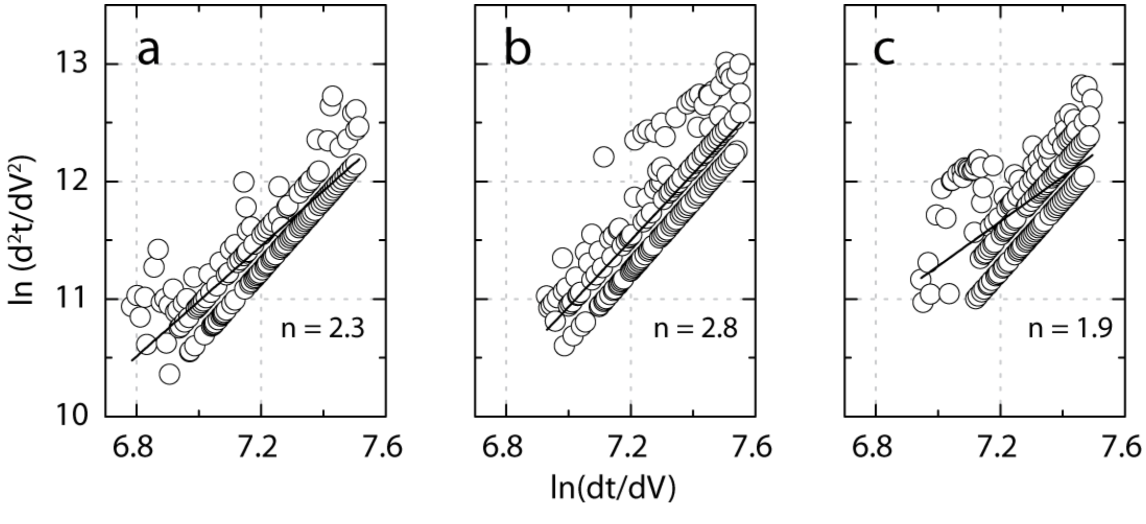

Figure 6-5. Fouling mechanism analysis plots for the three UF algal filtration flux curves (*a*, *b*, *c*) presented in Figure 6-4. Solid lines show the linear fit, the slope of which (*n*) is also given.

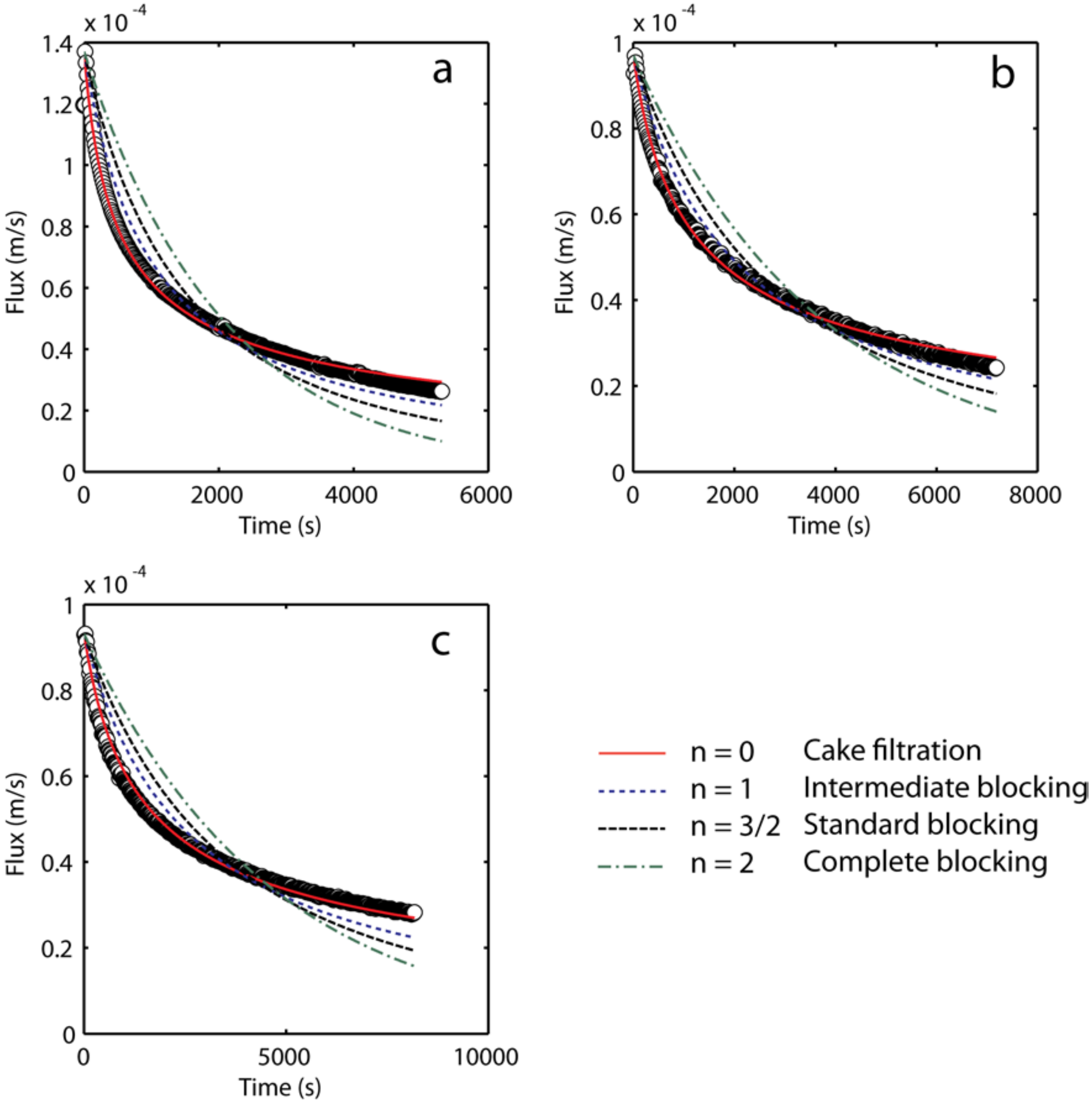

Figure 6-6. Flux versus time plots for the three UF filtration regions (a-c) shown in Figure 6-4. Data are indicated by circles and data fits for four fouling models are also shown.

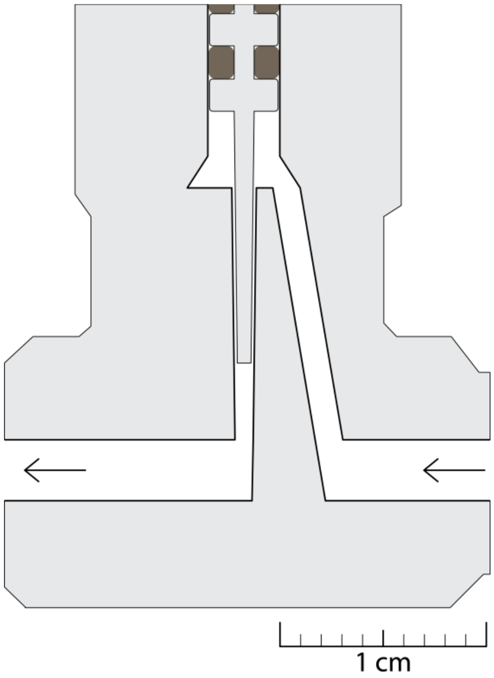

Figure 6-7. Geometry of the valve through which algal samples were passed. Arrows indicate flow direction.

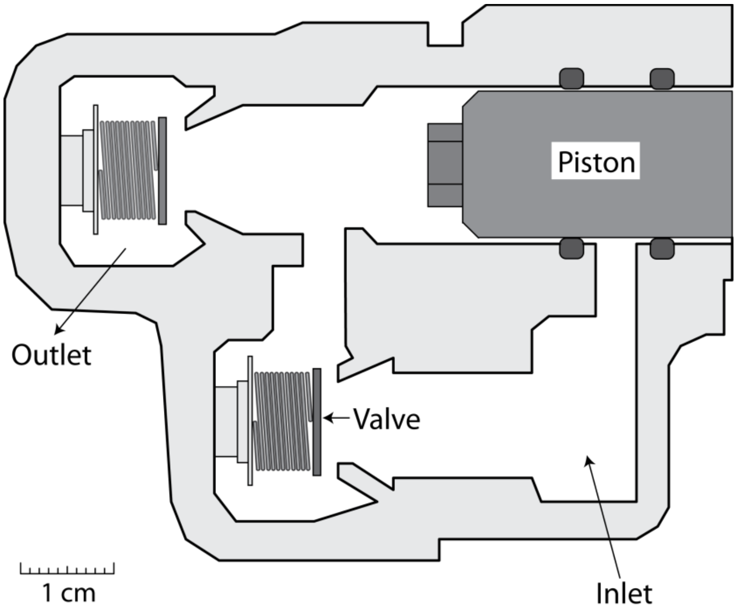

Figure 6-8. Pump manifold schematic. Both valves are in their open state to show the geometry of water passage.

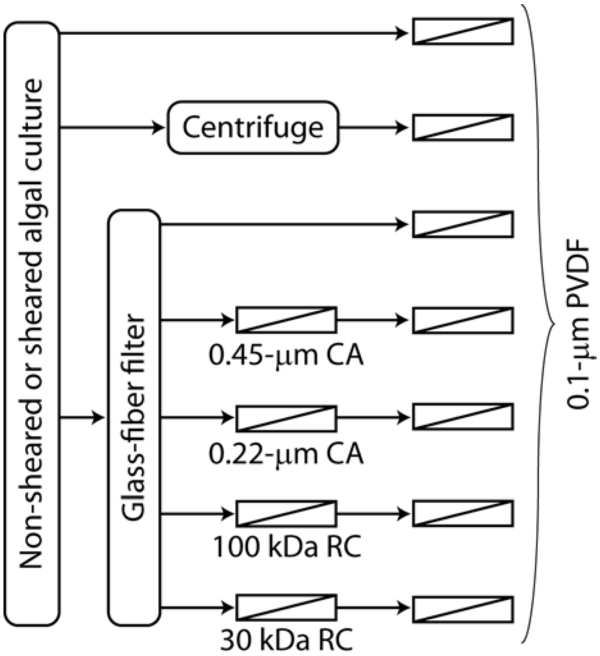

Figure 6-9. Schematic of the fractionation procedure. The procedure was repeated twice; once for a non-sheared algal culture sample and once for a sheared sample. CA: cellulose acetate. RC: regenerated cellulose. PVDF: polyvinilidene fluoride.

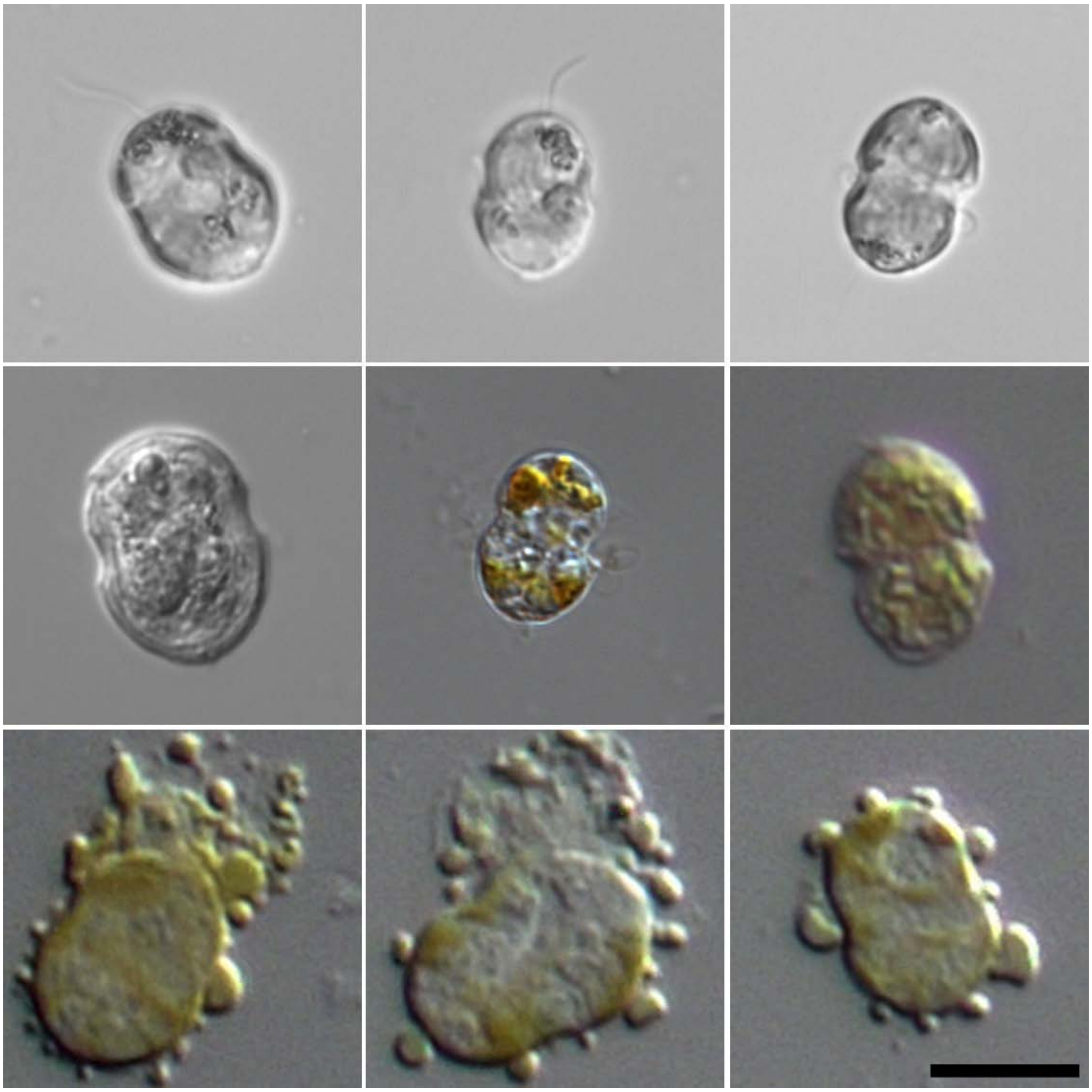

Figure 6-10. Intact *H. pygmaea* cells (top two rows) compared with cells that were deliberately crushed under a microscope coverslip. The images were taken with visible-light microscopy in differential interference contrast (DIC) mode. Scale bar is ten micrometers.

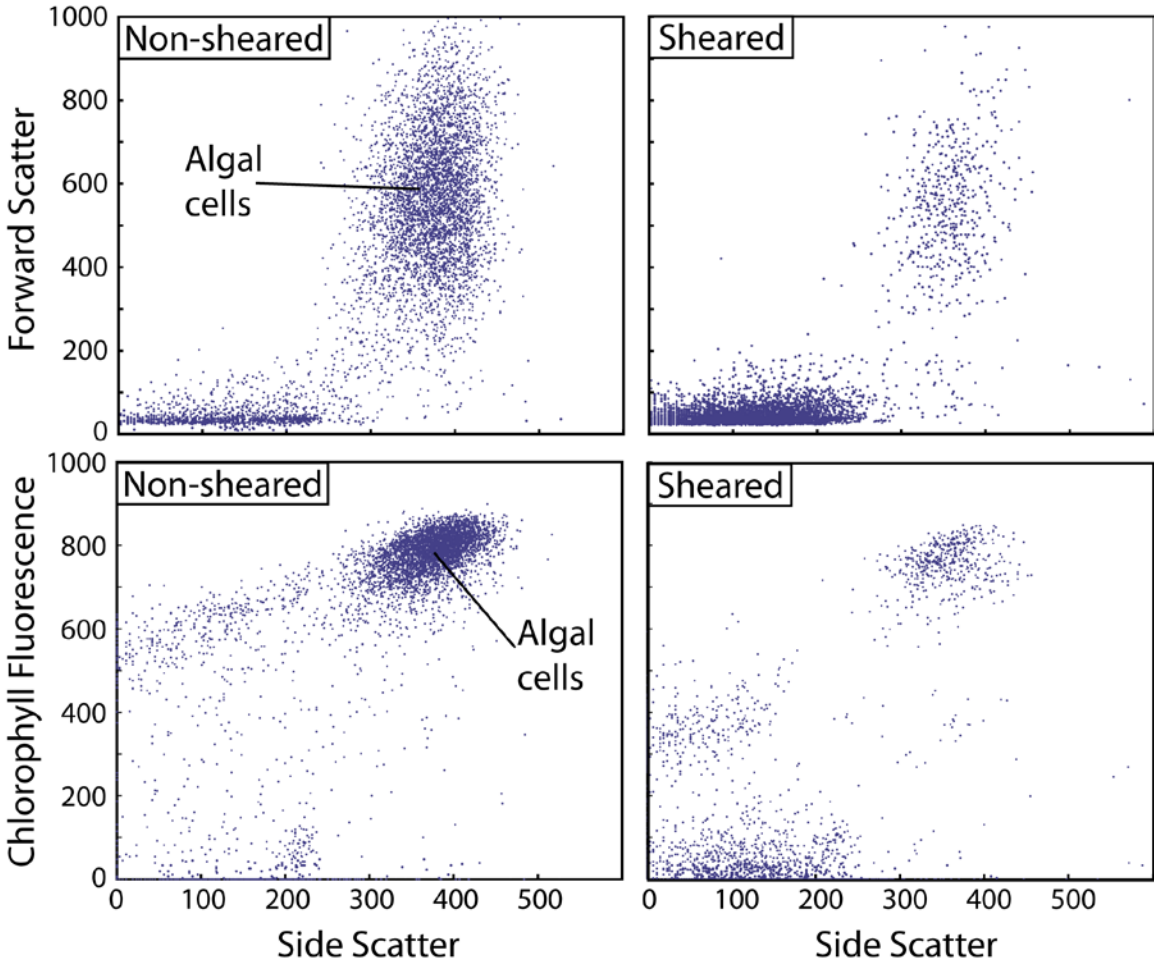

Figure 6-11. Flow cytometry scatter plots for non-sheared and sheared algal samples. Sheared samples experienced 150 minutes of shear through the pump and valve. Light scatter and fluorescence parameters were measured to determine sample composition. Cell concentration (labeled as algal cells in the figure) significantly decreased during shear as background particle detection increased proportionately.

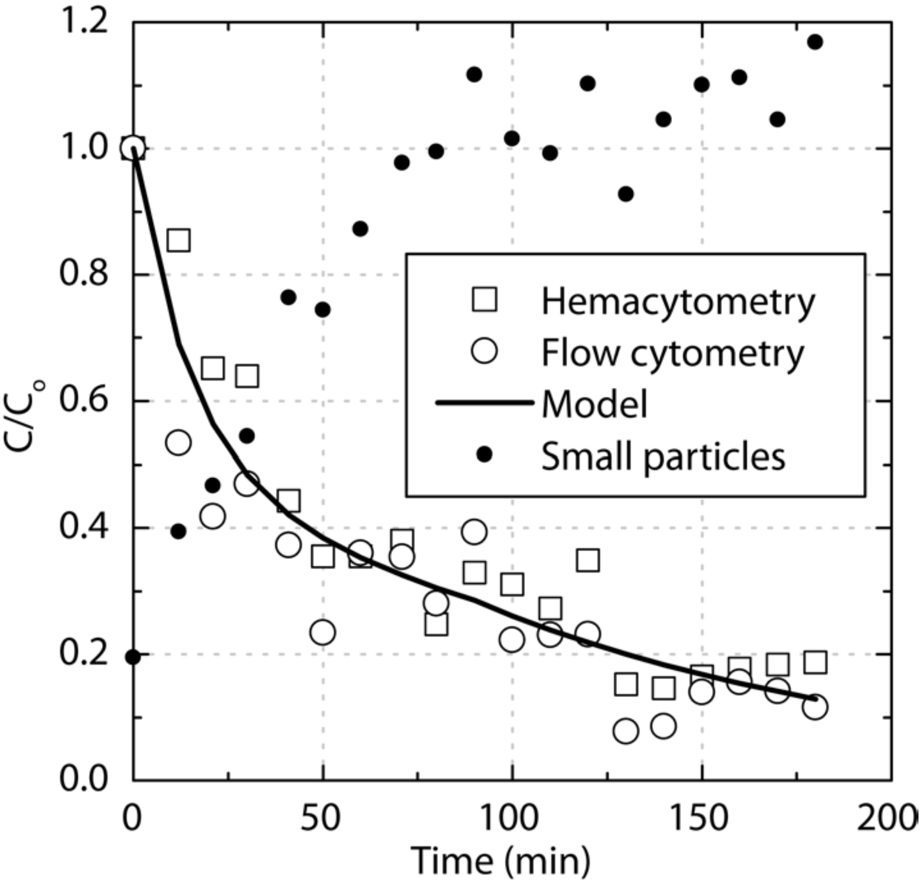

Figure 6-12. Algal counts by hemacytometry and flow cytometry during shear. Algal counts (C) were recorded in units of cells/ml and normalized to their initial concentration (C_o). Background material was normalized to the initial flow cytometry algal count in order to make a direct comparison with algal concentrations. The model is the best fit to the combined data set, with $C_{so} = 0.51$, $C_{wo} = 0.49$, $k_s = 0.031$ passes^{-1}, and $k_w = 0.32$ passes^{-1}. Background particulate material was enumerated by flow cytometry.

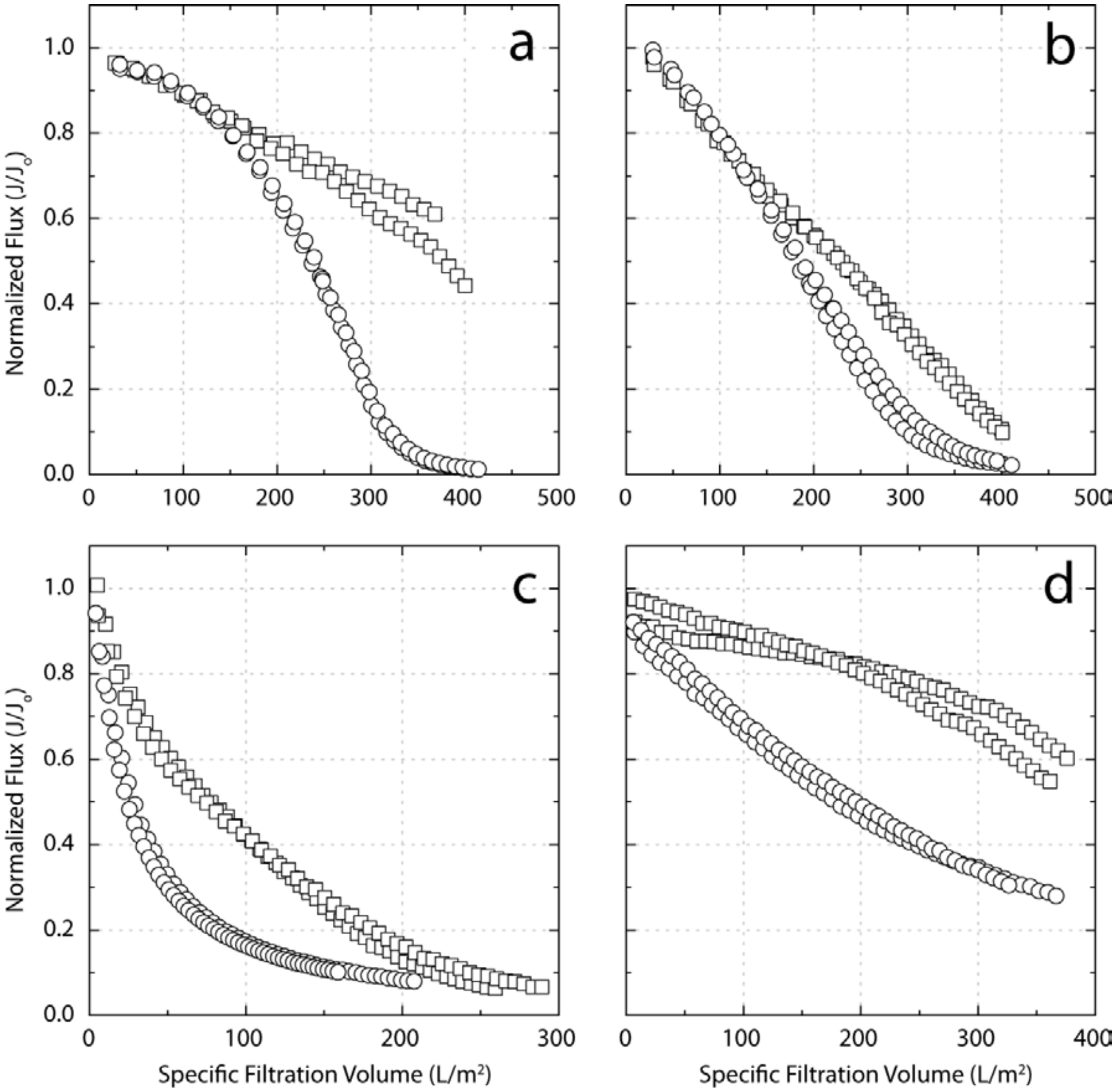

Figure 6-13. Flux curves for (a) 0.45 µm, (b) 0.22 µm, (c) 100 kDa, and (d) 30 kDa experiments. Two runs were performed with non-sheared samples (squares) and two runs were performed with sheared samples (circles) for each membrane type. Flux declined more rapidly after shear in all cases.

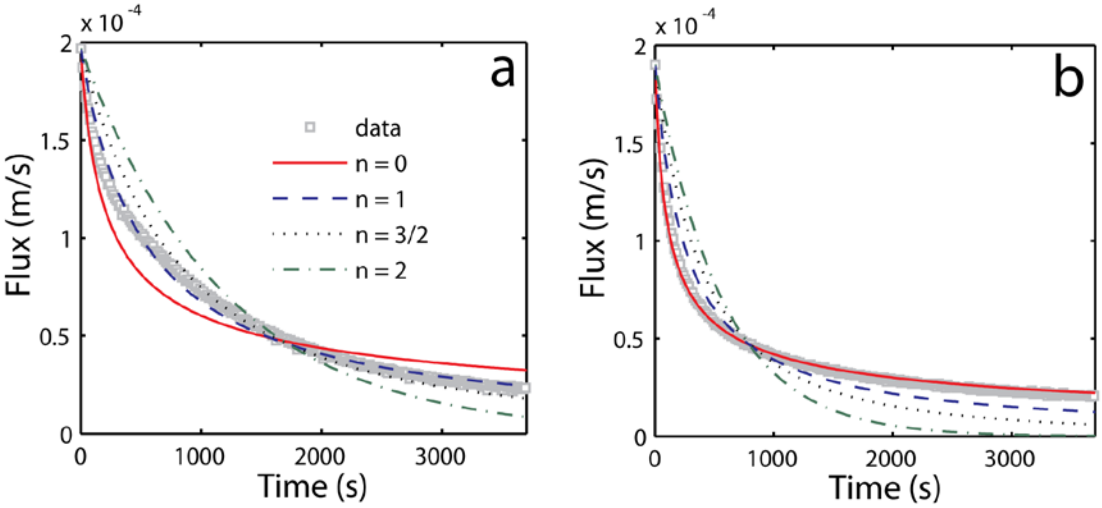

Figure 6-14. Model fits for algal fouling runs before shear (a) and after shear (b) on a 100-kDa membrane. The four models were defined by Hermia (1982) and can be characterized by the value of *n* from Equation 6-1; *n* = 0 for cake filtration, *n* = 1 for intermediate blocking, *n* = 3/2 for standard blocking, and *n* = 2 for complete blocking. The intermediate blocking model was the best fit to the data before shear (R^2 = 0.992, RMSE = 1.6%) while the cake filtration model gave the best fit after shear (R^2 = 0.994, RMSE = 1.1%).

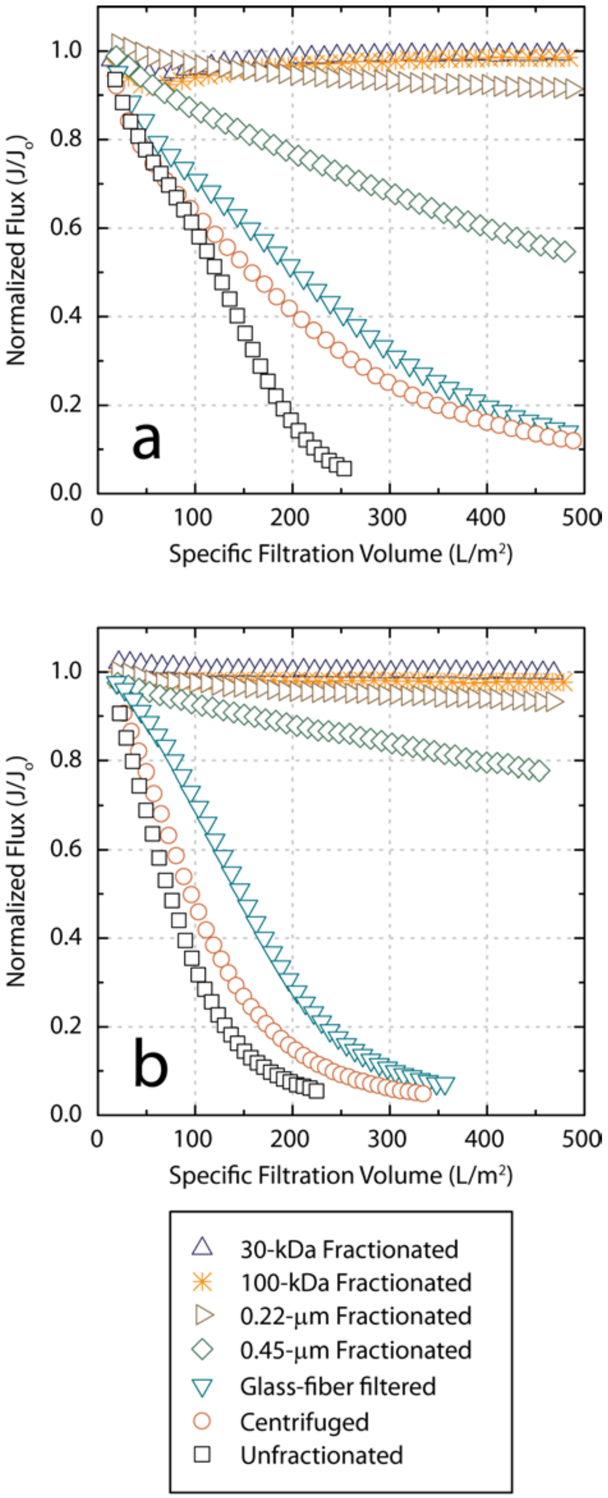

Figure 6-15. Flux results for various size fractions of (a) non-sheared algal culture and (b) sheared algal culture filtered on a 0.1-µm PVDF membrane.

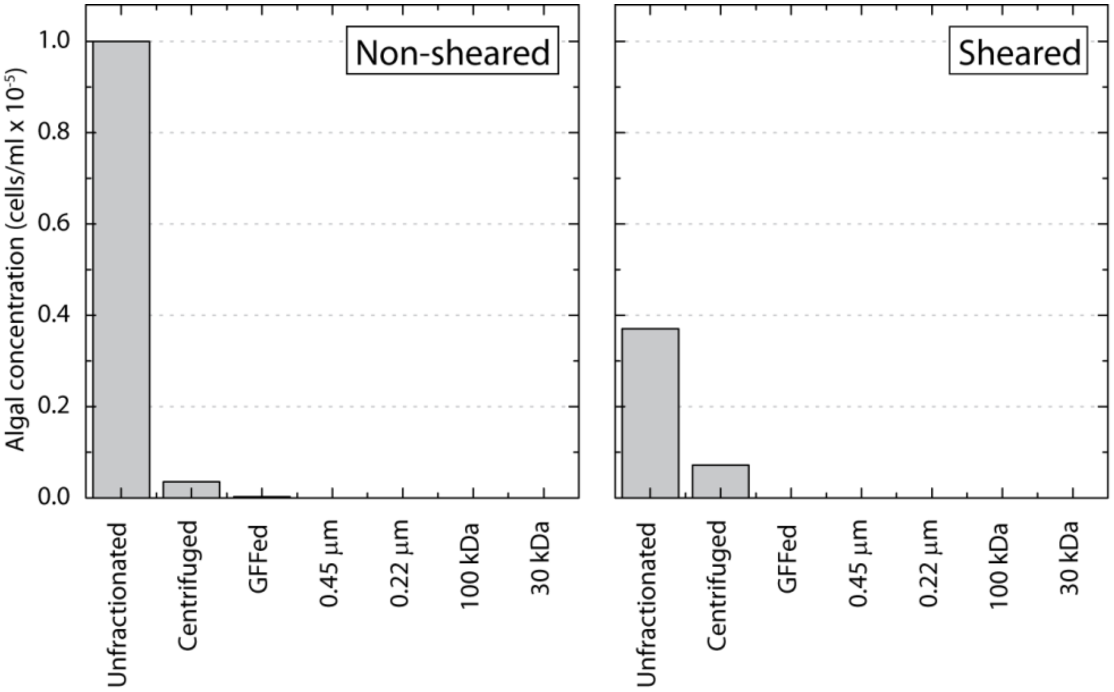

Figure 6-16. Algal concentrations for non-sheared and sheared fractionated samples.

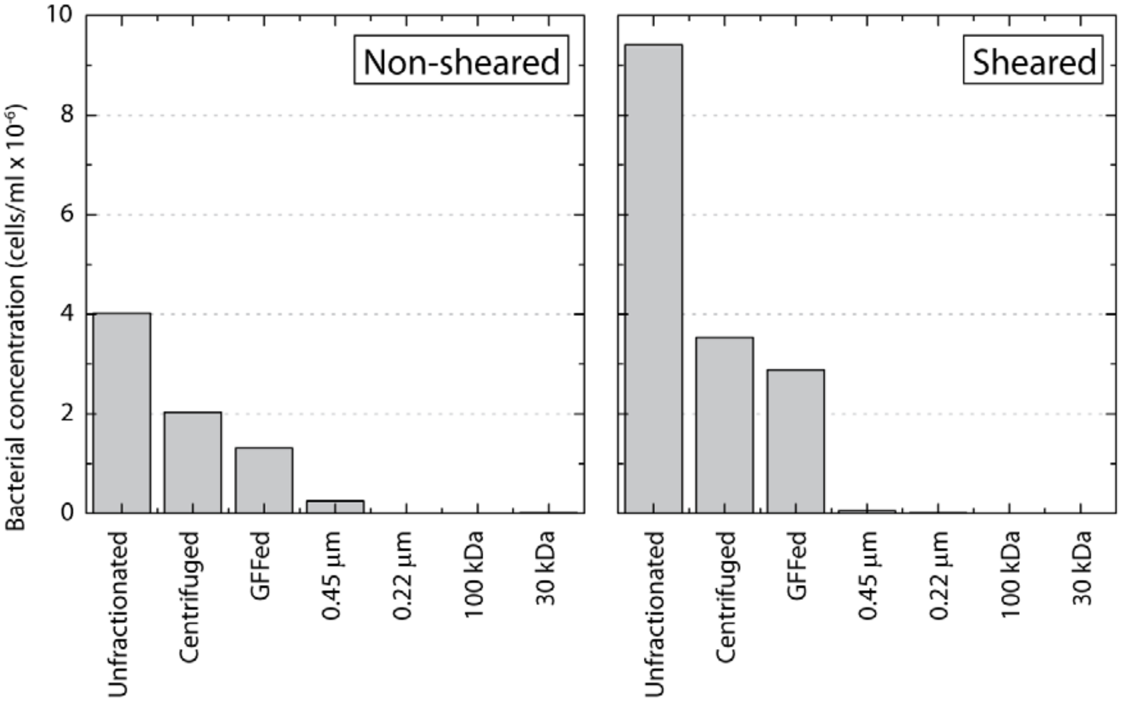

Figure 6-17. Bacterial concentrations for non-sheared and sheared fractionated samples.

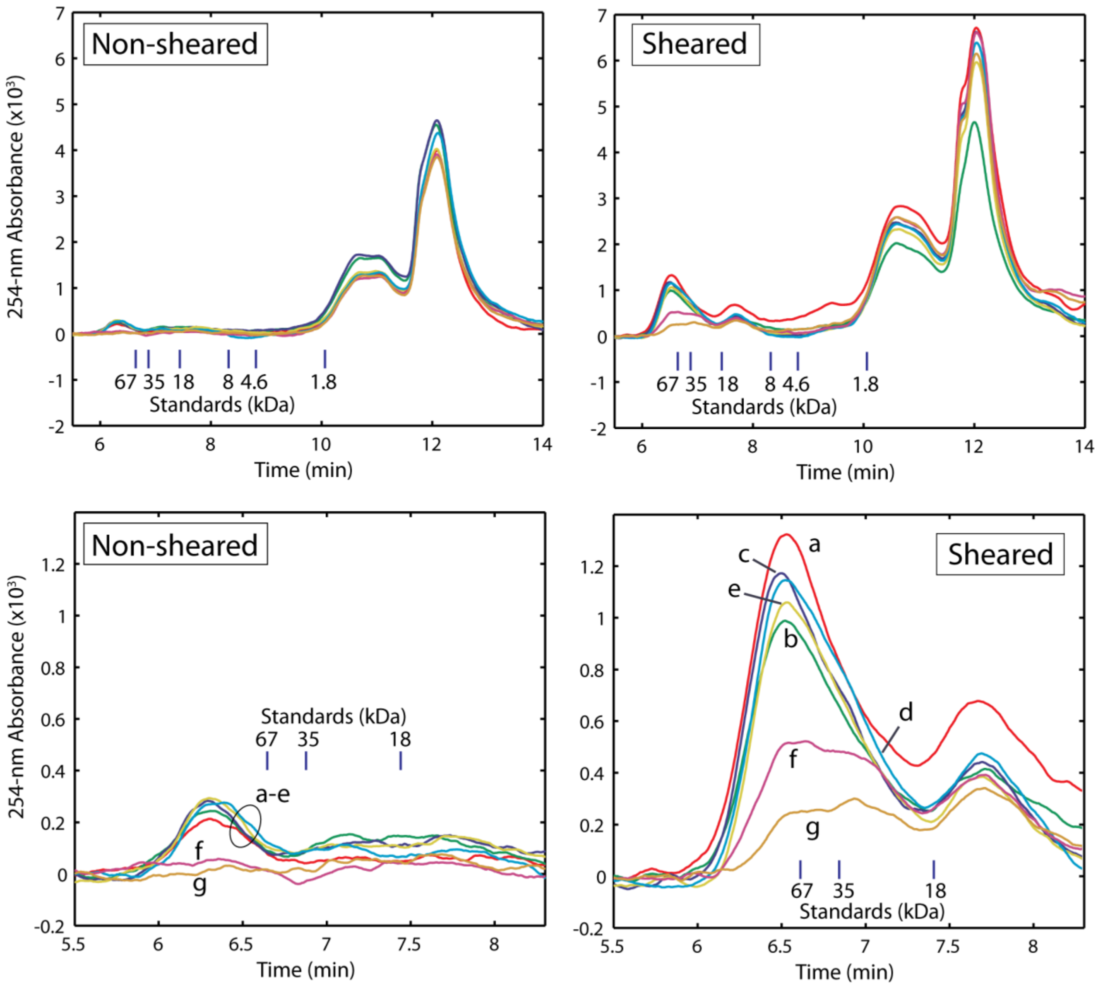

Figure 6-18. Size exclusion chromatograms for fractionated algae. The full range is presented in the top two plots and a narrower range (magnified view) in the lower plots. Both non-sheared and sheared algal samples were fractionated into various size classes: unfractionated (a), centrifuged (b), glass-fiber filtered (c), 0.45 µm (d), 0.22 µm (e), 100 kDa (f), and 30 kDa (g). Note that the upper limit of separation for this SEC column was 80 kDa so all material 80 kDa and above eluted in the peak near 6.5 minutes. The lower limit was 1 kDa so all material below 1 kDa eluted in the peak near 12 minutes.

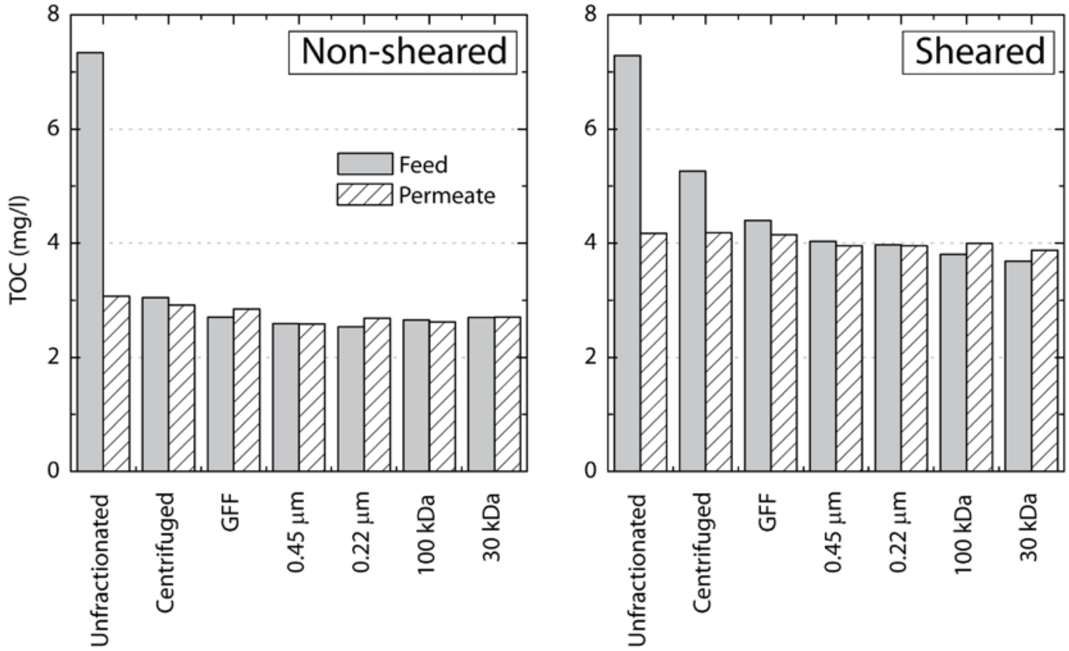

Figure 6-19. Total organic carbon (TOC) for size fractions of non-sheared and sheared algal culture. Feed (solid bars) and permeate (hatched bars) are given for each sample filtered through 0.1-μm PVDF membranes.

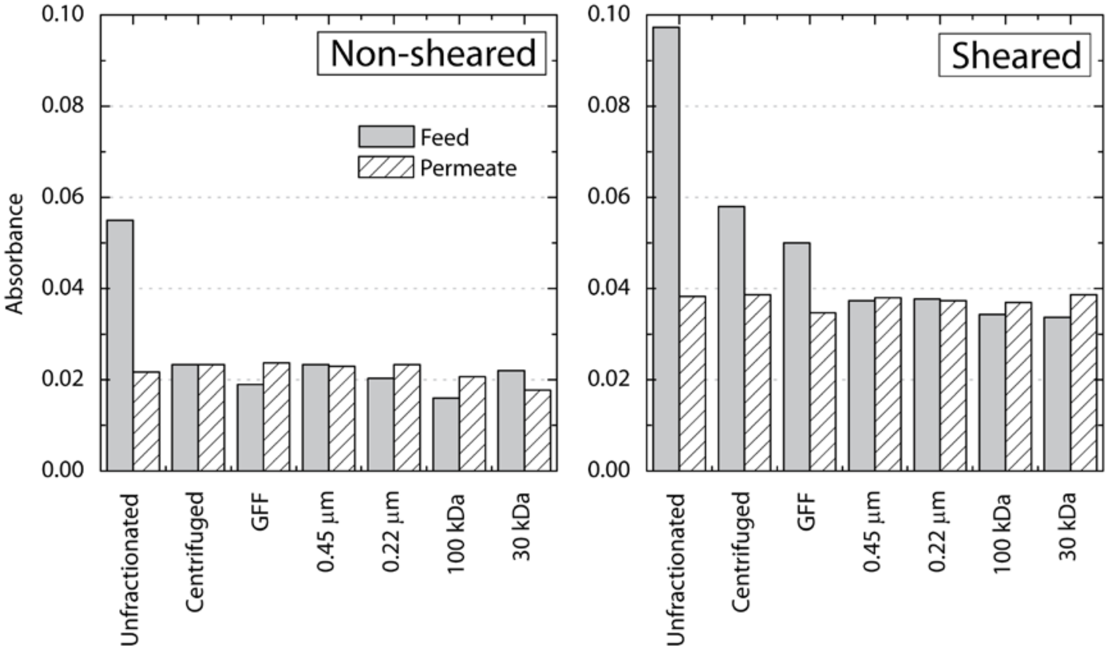

Figure 6-20. UV absorbance at 254 nm for size fractions of non-sheared and sheared algal culture. Feed (solid bars) and permeate (hatched bars) are given for each sample filtered through 0.1-μm PVDF membranes.

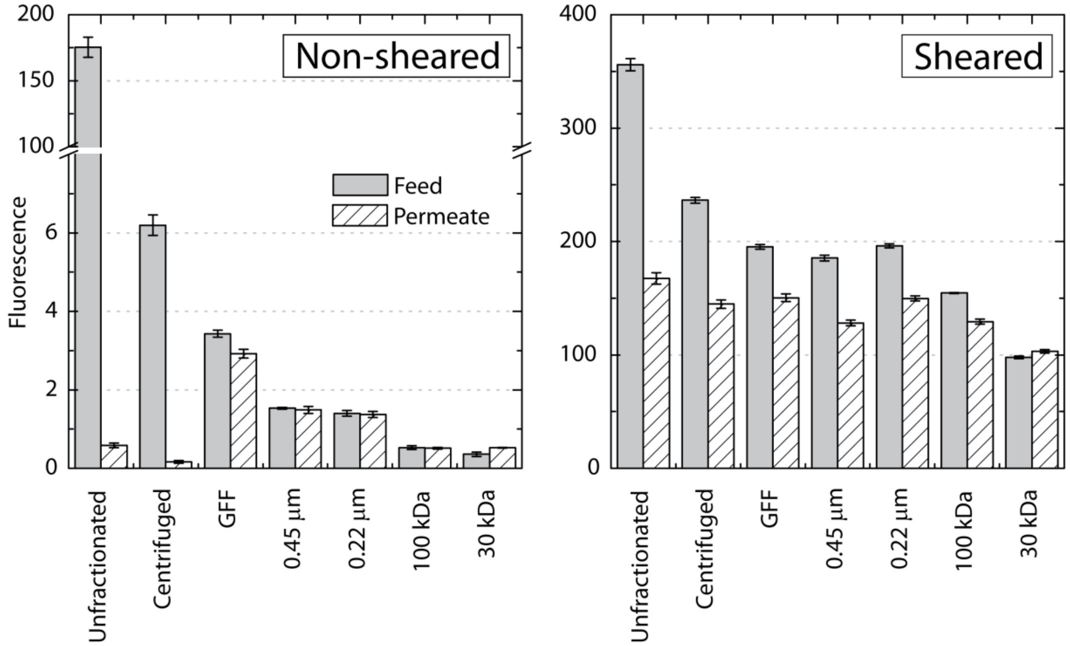

Figure 6-21. Fluorescence at 450-nm excitation and 680-nm detection for size fractions of non-sheared and sheared algal culture. Feed (solid bars) and permeate (hatched bars) values are given for each sample filtered through 0.1-µm PVDF membranes. Error bars span the standard error of triplicate measurements.

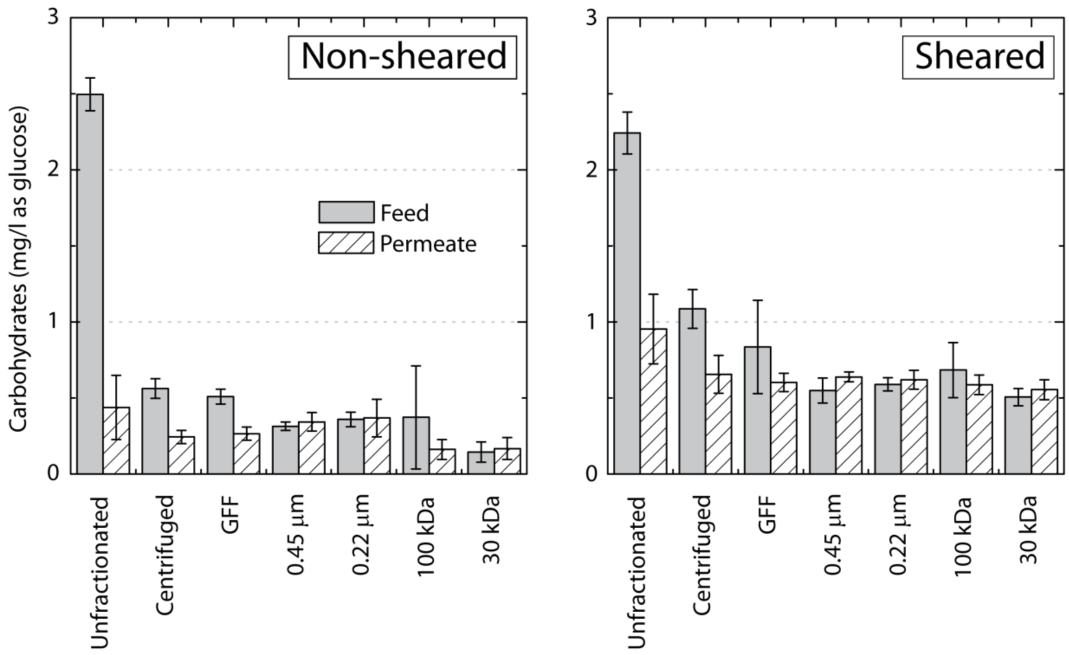

Figure 6-22. Carbohydrate concentrations for size fractions of non-sheared and sheared algal culture. Feed (solid bars) and permeate (hatched bars) are given for each sample filtered through 0.1-µm PVDF membranes. Error bars span the standard error of triplicate measurements.

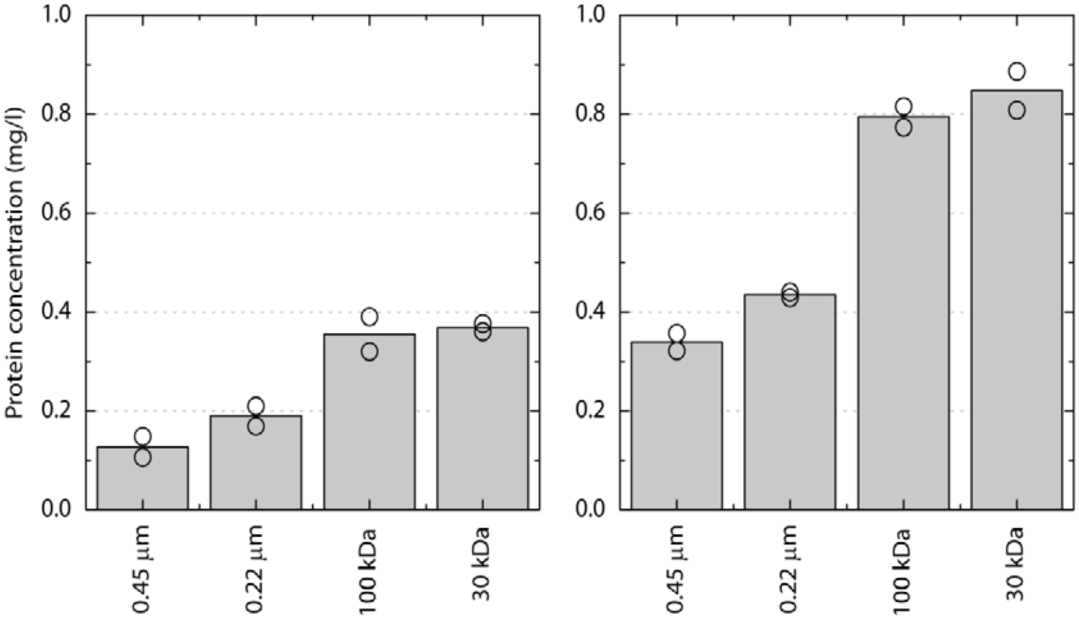

Figure 6-23. Protein concentrations extrapolated from direct measurement of fractionation membranes. The concentration shown is the amount of protein in the feed water that was collectable by that membrane. Circles give actual measurements (2 repetitions per sample) and bars show averages.

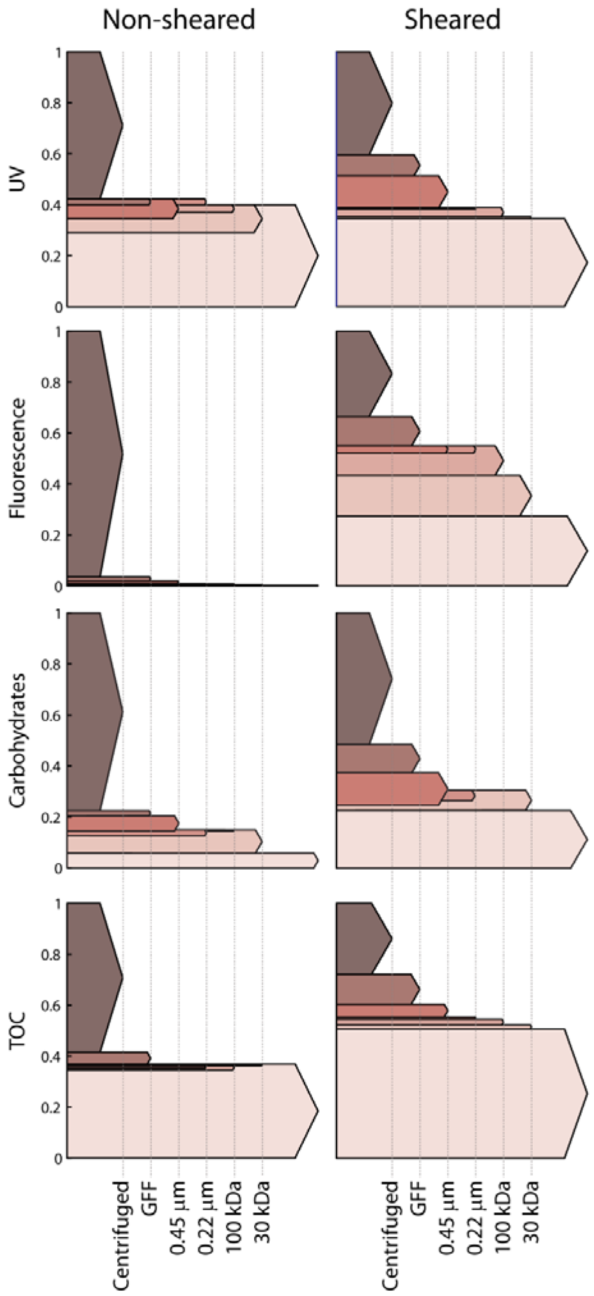

Figure 6-24. Organic matter size distributions for non-sheared and sheared algal samples based on four analytical methods. The data are normalized to the concentration measured in the unfractionated sample. The lowest (light color) bar represents the smallest-sized material that was able to pass through all six fractionation steps. The top bar (dark color) represents the largest-sized material that was removed by centrifugation. Intermediate bars represent material that permeated some fractionation step but was retained in subsequent steps. Bar widths are indicative of the weight of the given size class; i.e. 37% of TOC passed through all fractionation levels without shear and 50% passed through after shear. Overlapping bars result from measurement uncertainty.

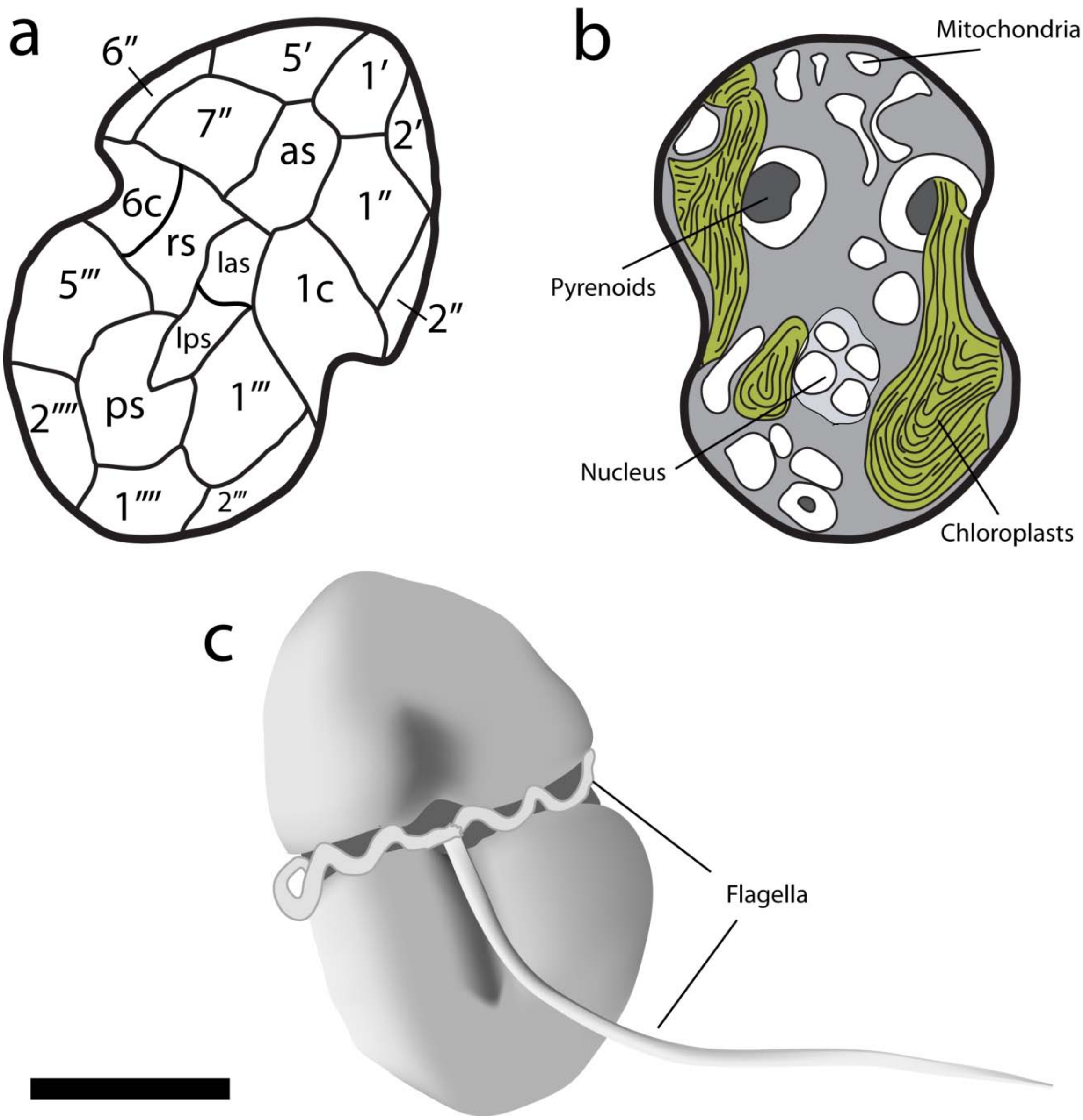

Figure 6-25. Structural features of *H. pygmaea.* (a) Thecal plates and their designations; ’: apicals, ’’: precingulars, ’’’: postsingulars, ’’’’: antapicals, as: anterior sulcal, rs: right sulcal, las: left anterior sulcal, lps: left posterior sulcal, ps: posterior sulcal. Plate locations and designations are from Loeblich et al. (1981). (b) Cross-sectional view of internal organelles as seen in TEM images (Bullman and Roberts 1986). (c) Typical morphology and orientation of flagella as seen in SEM images (Roberts et al. 1987). Scale bar is five microns.

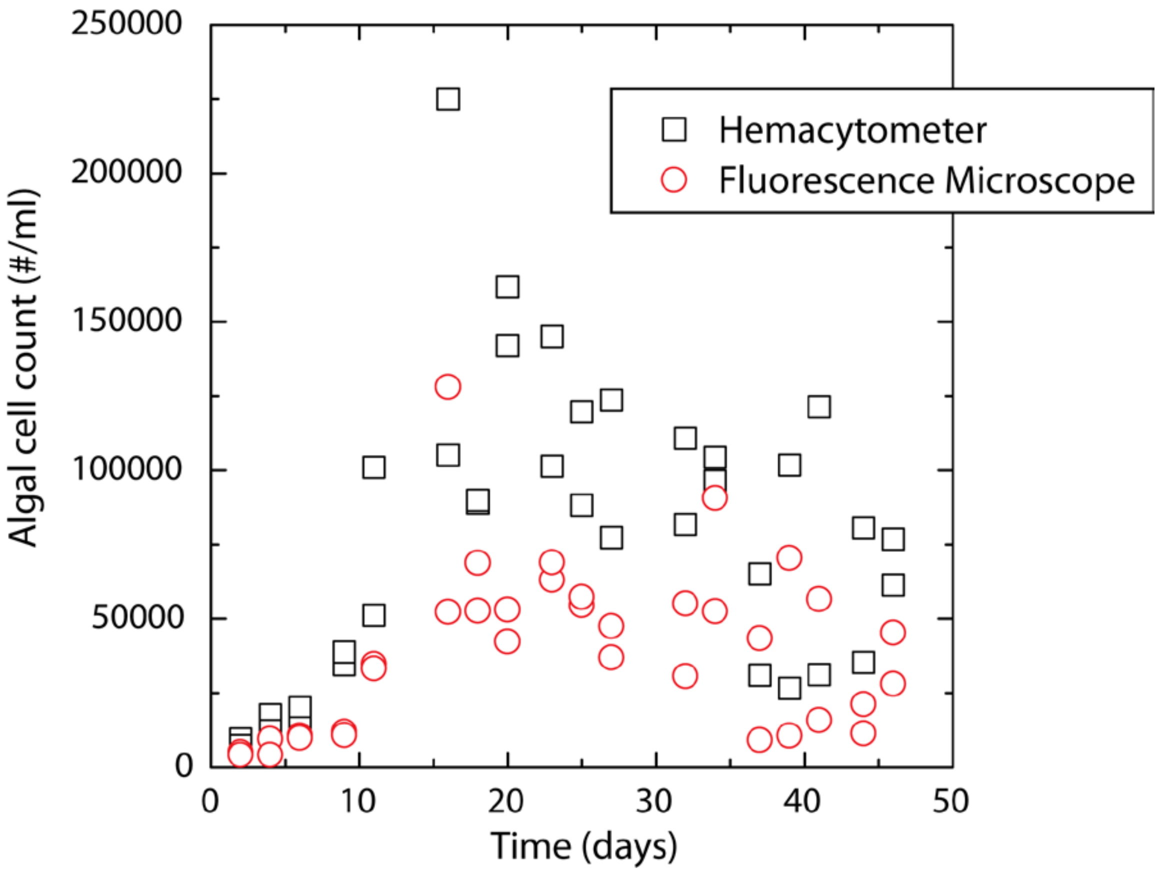

Figure 6-26. Algal concentration as measured with hemacytometry and fluorescence microscopy over the course of the simulated algal bloom

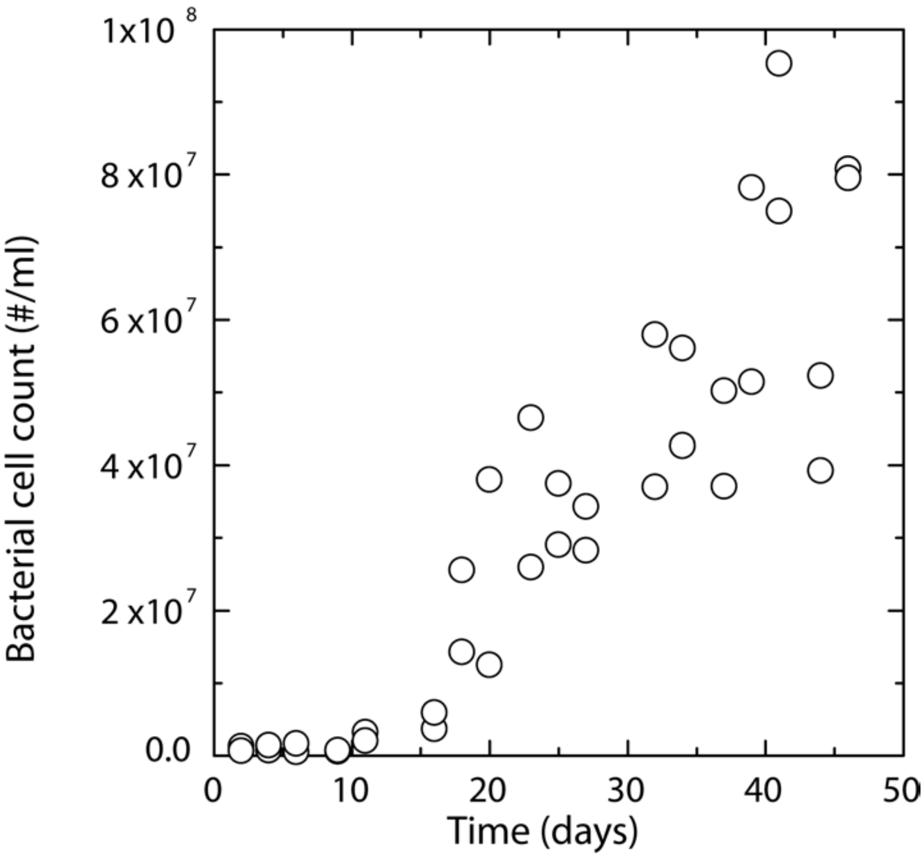

Figure 6-27. Bacterial concentration as measured by fluorescence microscopy during the simulated algal bloom.

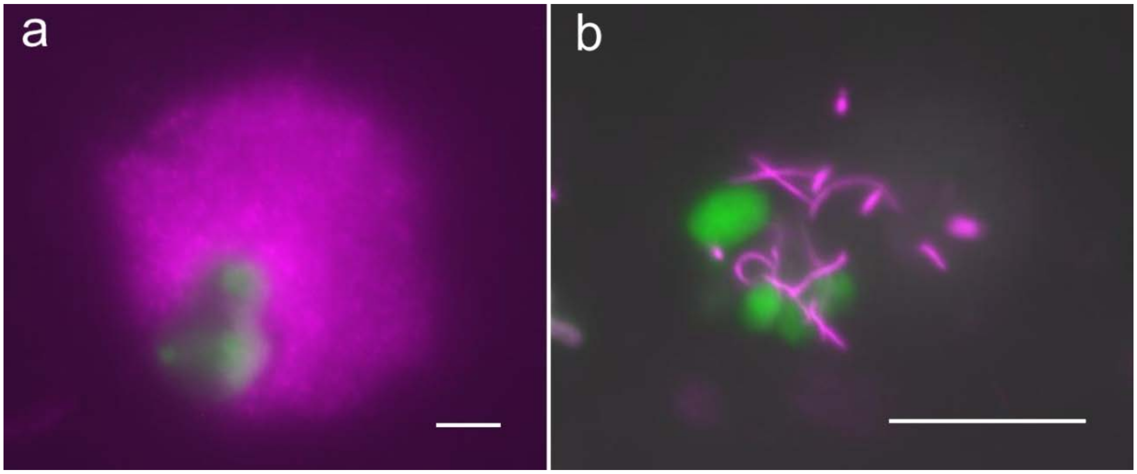

Figure 6-28. Fluorescence microscope images of bacteria interacting with algae. Bacteria are visible by DAPI staining and have been colored purple in these pseudo-color images. Algae are autoflurescent and have been colored green. a) Globular biofilm surrounding an algal cell. b) An algal cell into which bacteria have entered. The outline of the cell is not readily apparent; only a few chloroplasts remain intact and are fluorescing. White bars represent ten micrometers.

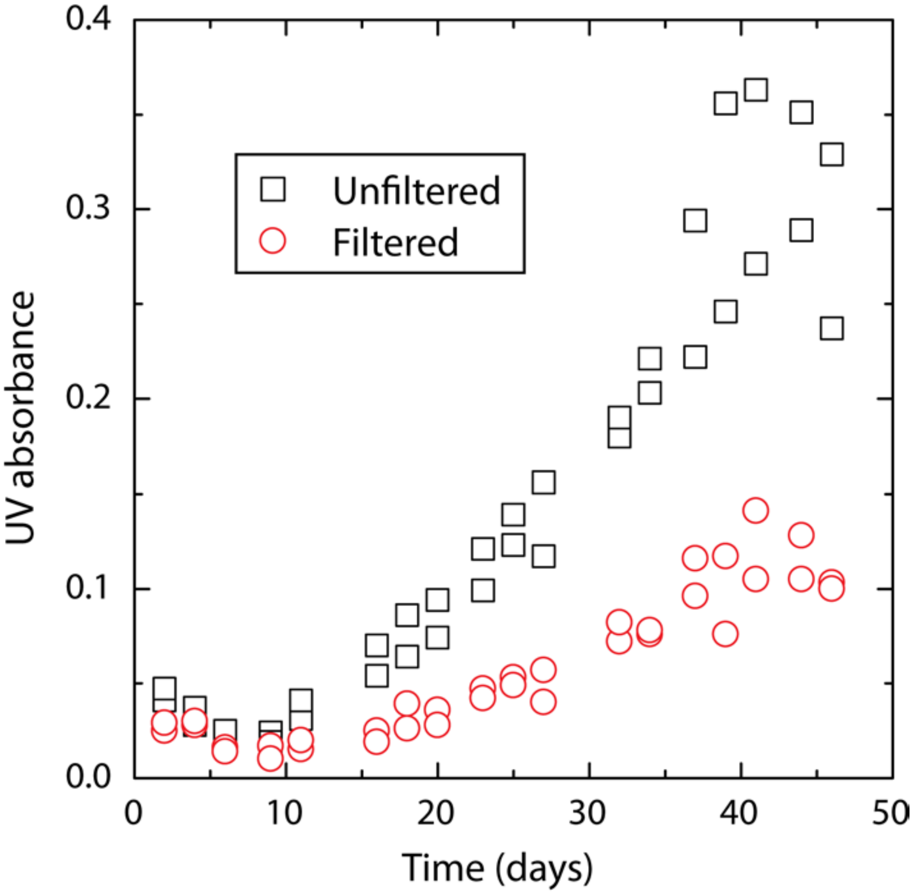

Figure 6-29. UV absorbance of raw (unfiltered) and filtered (0.22 µm) samples drawn from culture vessels over the time period of the simulated algal bloom.

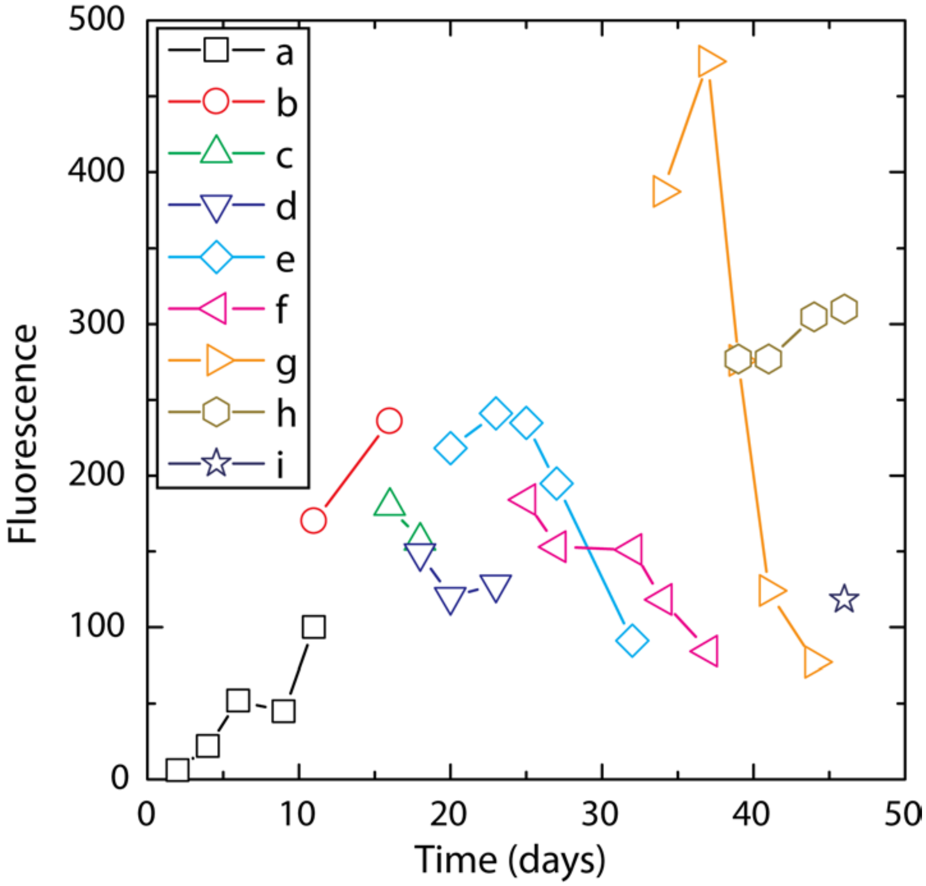

Figure 6-30. Fluorescence data for bulk (non-filtered) samples during the simulated algal bloom. Letters *a*-*i* are the bottle labels.

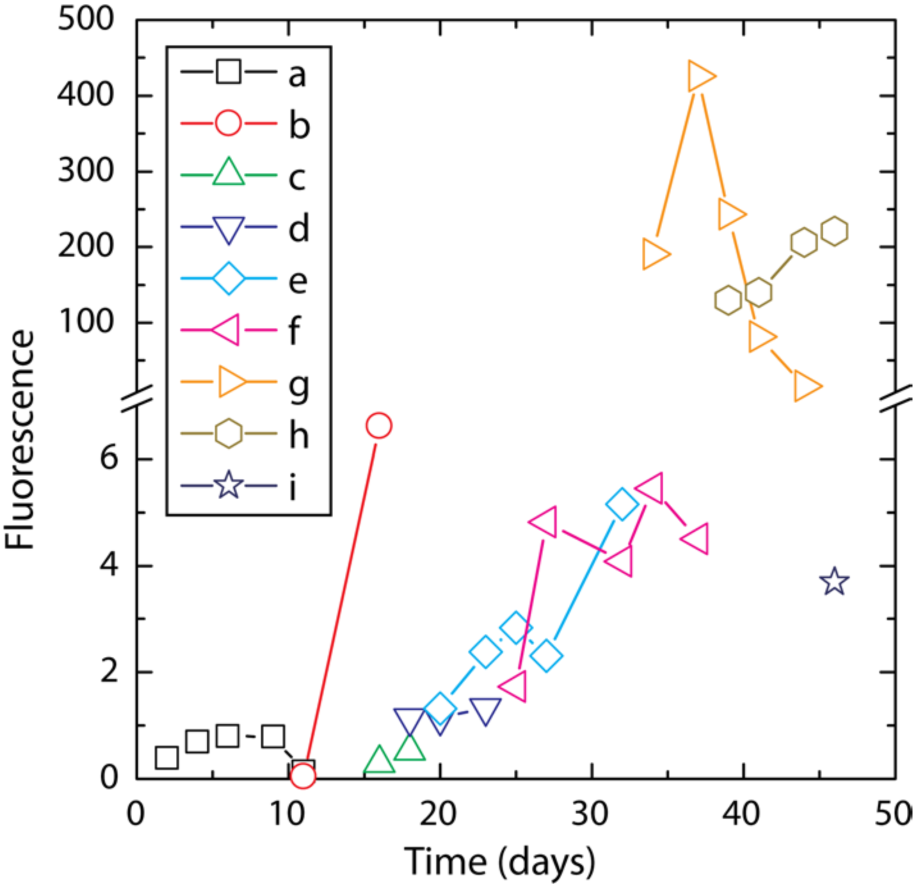

Figure 6-31. Fluorescence data for filtered samples during the simulated algal bloom. Letters *a*-*i* are the bottle labels.

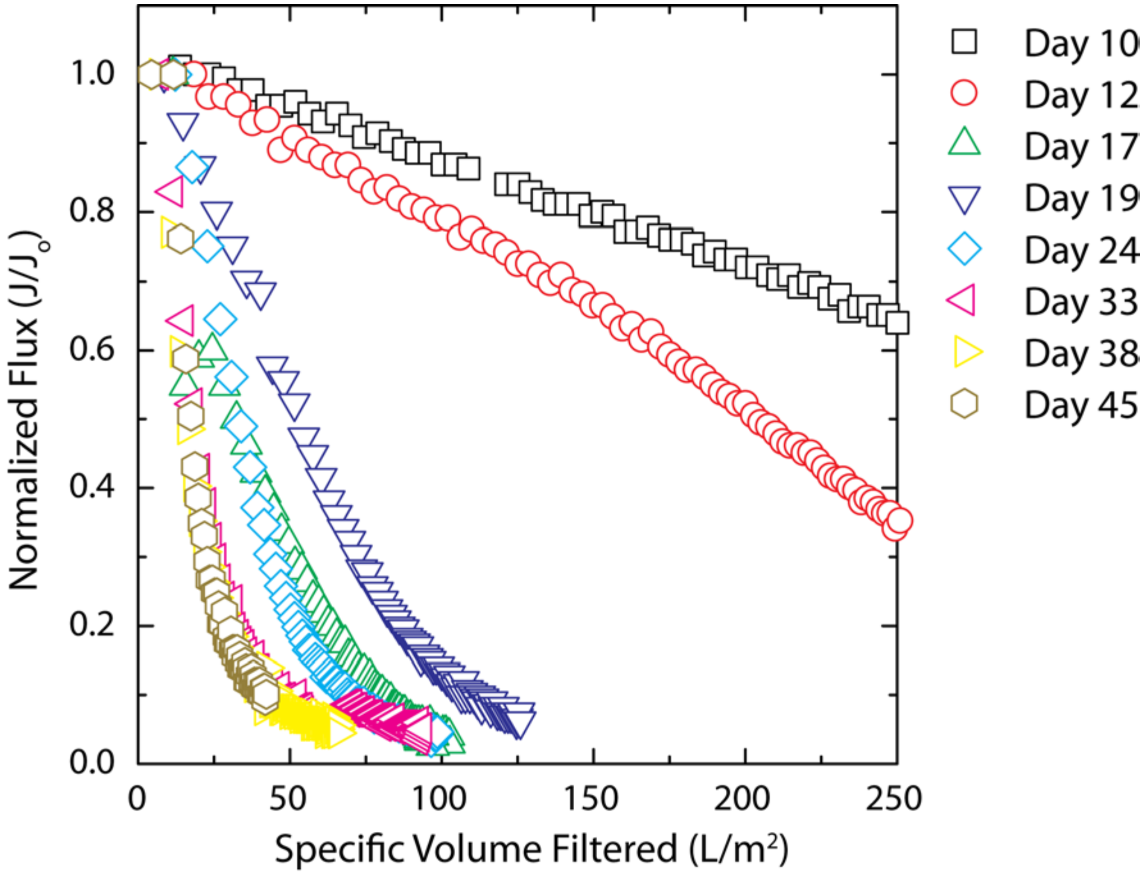

Figure 6-32. Flux data for filtrations performed during the simulated algal bloom.

7 CONCLUSIONS AND SUGGESTIONS FOR FUTURE RESEARCH

This dissertation has uncovered new information regarding membrane fouling by marine algae. In the present chapter the findings will be summarized and their potential usefulness and future application will be explored.

7.1 OVERVIEW OF THE PROJECT

This endeavor into studying fouling in an integrated membrane system occurred largely in the order presented in the preceding chapters. The work began with high-pressure membranes because the researcher was most interested in questions dealing with desalination and first attempted to study the salt-removing process itself. The most reasonable introductory step to take was to repeat what prior investigators had done in using the BaIReMT system to study fouling with natural waters. The BaIReMT seemed necessary since it was capable of concentrating the foulant material and providing a short-term analytical tool. It became clear soon into the work, however, that any fouling effects in the BaIReMT were overshadowed by the flux decline caused by the concentration of salts. It was critical to accurately determine the level of concentration polarization so that the salt concentration effects could be modeled and true flux decline from fouling could be determined. Our method for determining concentration polarization (and intrinsic membrane permeability at the same time) was subsequently developed.

The BaIReMT protocol was modified and became the transient recovery protocol, which allowed for more careful control of operating parameters. When the system was well controlled and the concentration polarization accounted for there was no fouling problem from organic matter. This was contrary to the literature where flux decline due to organic fouling had been reported. Those investigators did not account for concentration polarization so their flux decline data are suspect.

The final bench-scale RO testing effort was to modify the protocol yet again and perform full recycle tests. These had the advantage of running at the highest possible flux for the system, since salts were not concentrated during the run. Still, natural waters did not cause significant flux decline, even though some foulant material had accumulated on the membrane surfaces. Along with this, it was determined that full recycle tests functioned well enough for RO testing and the complexity of BaIReMT and transient recovery protocols was unnecessary and provided no real benefit.

With RO testing tools at hand, the project proceeded to the study of algal blooms. Algae did prove to be problematic foulants, but not to the extent that the researchers expected. It became apparent that high-pressure RO membranes were inherently good at maintaining their flux because their resistance was already so high that any added hydraulic resistance from foulants was only a fraction of the total. Further, the initial flux was so low that pressure drop in the cake layer was minimal. Drastic flux decline by dissolved AOM in a full-scale system would probably by caused more by bacterial growth on the membrane surface than by the AOM itself. Thus AOM would be an indirect cause of flux decline.

In the above work with RO fouling by algae it was clear that algae fouled the membranes in a pattern according to the feed spacer. A technique was sought to characterize this qualitative observation in a quantitative way and Fourier transform image analysis was used. Further, it was found that foulant deposition patterns could be studied with LSC. This is the first time these methods have been used in foulant characterization. They were useful in showing that the foulant deposition pattern depended not only on the feed spacer, but on the permeate spacer, as well.

In order to prevent fouling of RO membranes the water must be pretreated for algal removal. The next logical question, then, was how algae would affect the pretreatment process. It stood to reason that algae would cause fouling problems during pretreatment, but several questions had not yet been addressed in the fouling literature. The first question came about because of observations during the RO fouling experiments. Algal numbers declined greatly during the high-pressure experiments and it was presumed that cell breakup was occurring due to shear in the pump and valve. It was hypothesized that AOM derived from sheared algae could be more problematic than the algal cells themselves. Experiments were then undertaken to determine the extent of algal breakup and the size distribution of material released through shear. It was observed that shear did exacerbate flux decline in low-pressure membranes and that the particulate matter derived from cells was the culprit.

The final experiments undertaken for the project were to investigate the role of bacteria in an algal bloom. Bacteria had been suspect as possible key players during the early AOM work with RO membranes. Bacterial numbers were observed to increase during the tests since AOM was a good substrate. Bacteria also fell into the size class that was most responsible for fouling in the low-pressure experiments. Projecting our thinking toward a full-scale desalination facility we asked whether it would truly be the algal bloom that would be worrisome or whether the bacterial bloom might be more problematic. A simulated algal bloom showed that indeed fouling continued after algae had decline because bacteria persisted.

From the research chronology just described it can be seen that this project evolved from a question of RO fouling by natural seawater to a study of RO fouling by algae to a study of algal effects on low-pressure membranes. The question of fouling by algal blooms in seawater desalination has only been lightly addressed by previous researchers. The main contribution of this work was to identify which aspects of algal bloom fouling might be truly important. Here is established a groundwork for future engineers and investigators in this field, including the author. Specific conclusions from this work and the ways that this research can enhance future efforts are described below.

7.2 BENCH-SCALE EVALUATION OF REVERSE OSMOSIS

7.2.1 Conclusions

Three bench-scale testing protocols were compared: BaIReMT, transient recovery, and full recycle. The main hypothesis was that the BaIReMT and transient recovery tests would result in more rapid fouling because they represented later elements of a full-scale system where foulant concentrations are elevated. This hypothesis was rejected because organic matter concentrations still were not sufficiently elevated to cause measurable flux decline in the short-term (24-hour) tests performed. Also, the flux was higher in the full recycle test because the salt concentration was lower. High flux was more important than elevated foulant concentration for measuring fouling.

During the bench-scale testing it was important to accurately determine the level of concentration polarization and the intrinsic membrane permeability. Experimental protocols were developed to determine these transport parameters. Both concentration polarization and membrane permeability were determined in a single experiment with either a constant-flux or a constant-pressure test. The permeate was wasted so the feed salt concentration increased over time and linear models could then be fit to the data to extract transport parameters.

Using the above bench-scale testing methods natural seawater was evaluated to determine its fouling potential. We hypothesized that short-term bench-scale experiments could be used to compare water sources and measure the fouling potential of the organic matter present. We also expected that natural-water foulants could be fractionated into different size classes to determine which size was the most highly fouling. These hypotheses were rejected because no natural-water tests resulted in substantial flux decline and the various organic-matter fractions all performed similarly. Some organic matter did accumulate on the membranes, but it did not cause reduced membrane performance.

7.2.2 Future research

Though the bench-scale testing done here was not useful as an indicator of fouling potential by natural waters, modifications to the testing can be envisioned. Instead of using a recycle configuration with a small batch (20 liters) of water, it may be useful to have a continuous-flow arrangement with the equipment located next to the water source. In this way the system could be operated for longer time periods with no foulant limitation and no change in composition over time (except natural changes). Autopsy techniques can then be used to determine fouling potential without the need for the higher cost and effort of a pilot system.

The scheme for transport parameter determination has a great deal of application in future work. Bench-scale tests can begin with an experiment to determine the transport parameters for the installed coupon and flow conditions. This can provide a control measure for coupon variability and will detect integrity breaches. Further, one can envision coupling the transport parameter determination methodology with fouling experiments for identifying the fouling mechanism at play. The membrane permeability and concentration polarization factor could be determined over time during a fouling run.

A change in apparent membrane permeability would be a measure of hydraulic resistance and a change in concentration polarization factor would be a measure of CECP.

7.3 REVERSE OSMOSIS MEMBRANE FOULING BY MARINE ALGAE

7.3.1 Conclusions

It was hypothesized that dissolved AOM would cause significant fouling of RO membranes during seawater desalination. Dissolved AOM is the material that would be most likely to pass through pretreatment and reach the RO membranes in a full-scale system. The hypothesis did not hold here because dissolved AOM did not cause severe flux decline in this bench-scale study. Only when algal-derived particulate material (greater than 0.45 µm) was present did flux decline occur. A significant amount of material was deposited before flux decline was noted. The intrinsic resistance of RO membranes is substantial and the flux is low (relative to other membrane processes) so foulant layers must be significant in order to add measurably to the resistance.

Another hypothesis was that permeate carrier morphology would affect foulant deposition; a coarse permeate carrier would lead to exacerbated foulant deposition compared to a fine permeate carrier because of the larger peaks and valleys created as the membrane was pressed on the permeate carrier. This hypothesis was confirmed in the dissolved AOM case. More material deposited and flux declined to a greater extent when a coarse permeate carrier was used. In the direct-algal-spike case, when particulate material was present, both permeate carriers caused similar flux decline, but the deposition pattern was different. The coarse permeate carrier caused foulants to deposit in a pattern that matched the feed-spacer morphology while the fine permeate carrier resulted in more homogeneous, less patterned deposition. The significant result here is that both the permeate carrier and the feed spacer morphologies are important for foulant deposition.

The final hypothesis regarding AOM fouling of RO membranes was that CECP would be the dominant fouling mechanism instead of hydraulic resistance since CECP has been reported to dominate for salt-rejecting membranes (Hoek and Elimelech 2003). However, the heterogeneous nature of particulate and dissolved AOM results in cake layers with low porosity and particle size. With such cake layers hydraulic resistance can be just as important as CECP. The concept of the “crossover point” has been presented; for any given combination of flux decline and particle size there exists a single crossover point where hydraulic resistance and CECP give equal resistance. At that point cake thickness, porosity, and tortuosity are defined. This sets the stage for applying future experimental data to verify that the equations and assumptions used in the modeling are accurate.

7.3.2 Future research

It has been reported in pilot studies that algal fouling is detrimental to the system, but over longer time periods (several days) than tested here. It is possible that AOM cake layers build up over time to cause more significant resistance. More likely, bacterial growth enhanced by AOM may be the principal fouling mechanism. Examining the interplay between adsorbed AOM and biofouling would be a useful area of future research.

Since AOM does adsorb to the membrane and form a conditioning film, an important question is whether there exists a highly-fouling fraction of AOM on RO membranes (analogous to the highly-fouling AOM material observed in low-pressure membranes). It is possible that some class of protein, carbohydrate, or lipid material is the highly-fouling fraction and selectively adsorbs to the membrane surface. The PCP protein complex would be a good candidate for initial examination since it is well-characterized and we have already observed that it deposits on the membrane surface. LSC could be used to help determine PCP deposition since PCP fluorescence is detectable by LSC.

Further development of the LSC technique for foulant characterization could also be useful. The LSC technique could supplement visual image analysis by providing a measure of fluorescent material. It could be used in full-scale autopsy to determine whether algal pigments are present in the foulant layer. The method could be expanded by including additional fluorescence channels indicative of other components, like humic acid. Further, foulant layers could be stained with chemical-specific dyes and the LSC could measure their spatial distribution. A live-dead stain for bacterial activity or a 16S-rRNA stain for species specificity could be envisioned.

Another future need is improvement in RO module hydrodynamics. Full-scale modules should be designed without feed spacers to minimize foulant deposition. Such a design would require some other method of decreasing concentration polarization. A module with high crossflow velocity achieved by lengthening the flow path could be effective. The permeate carrier morphology should be taken into consideration to minimize foulant deposition in this next-generation module design.

7.4 LOW-PRESSURE MEMBRANE FOULING BY MARINE ALGAE

7.4.1 Conclusions

The first hypothesis with regard to low-pressure fouling was that MF fouling would exhibit a pore blocking mechanism and UF fouling would exhibit a cake filtration mechanism. The hypothesis was confirmed except that MF fouling changed from pore blocking to intermediate blocking over several filtration cycles. The model suggests that MF pores were irreversibly plugged over time so that the remaining pores were smaller and foulants accumulated on the surface.

The second hypothesis was that shear stress applied to an algal sample would exacerbate fouling through the release of AOM. Some portion of the released AOM would constitute a highly fouling fraction that would be more detrimental to flux than the whole algal cells. This hypothesis was confirmed first by tests with four different membrane pore sizes that all showed exacerbated flux decline after shear. It was further confirmed by fractionating the organic matter into different size classes and testing the fouling potential of each class. The highly fouling fraction was material that was not removed with centrifugation or glass-fiber filtration, but was largely removed with 0.45-μm filtration and 95% removed with 0.22-μm filtration; thus it was material larger than 0.22 μm but smaller than the algal cells themselves. Bacteria (typically one to two μm) were included in this highly-fouling size class. Adsorption of dissolved organic matter, even large biopolymers, was not a significant fouling mechanism. This conclusion was reached because even in sheared samples where high concentrations of large-molecular weight material were present (as determined by SEC) only minimal fouling was observed.

Along with effects of shear on flux, we hypothesized that shear would cause reduced organic-matter rejection. This was confirmed since rejection was diminished after shear in all four membrane pore sizes tested. This was due to the release of dissolved organic matter that was small enough to pass through all of the membranes.

As part of the effort to test shear effects, algal cell breakup kinetics were evaluated. A steep decline in cell number was observed at the beginning of the shear exposure, with breakup rate tailing off over time. Breakup data could be modeled by considering two cell classes: a structurally strong class and a structurally weak class. Thus, members of the same algal cell population have different structural strengths.

The final hypothesis tested here was that bacteria are an important factor in low-pressure fouling during an algal bloom. The hypothesis was partially confirmed above when bacteria were found to be in the highly-fouling size class. Further confirmation was obtained when fouling increased along with bacterial numbers even as algal numbers decreased.

A final conclusion that was indirectly tested during this project is that low-pressure membranes are much more dramatically fouled by algae than high-pressure membranes in the first several hours or days of filtration. Productivity of the RO membranes never declined below 90% even after 24 hours, but MF and UF membrane performance was drastically diminished in a matter of minutes. In an integrated membrane system the pretreatment membranes would be expected to fail first during an algal bloom.

7.4.2 Future research

Though the highly-fouling fraction of AOM was identified here as material larger than 0.22 μm and adsorption of biopolymers was not indicated as a fouling mechanism, it is recognized that these short-term experiments may not be representative of the longer-term case. Future work should be performed to determine if adsorption of biopolymers and colloids causes fouling over many backwash cycles as full-scale plants are operated.

Several future research projects could be performed regarding the effects of shear on algae. On one hand, the structural strength of different algal species should be determined, since the *H. pygmaea* cells used here have different morphology than many found in nature. On the other hand, the full-scale treatment train should be evaluated to determine the magnitude of shear in the intake systems, pumps, valves, and membrane modules. These studies will help to determine how much cell breakup—and thus release of highly-fouling organic matter—is occurring at full scale. During such tests, fluorescence measurements can be used as an effective indicator of shear.

Lastly, because algae rapidly foul low-pressure membranes, alternative removal strategies should be sought. Coagulation before filtration may be an effective strategy since large flocs should have lower fouling potential. Dissolved air floatation is another possibility, since cells do not settle well. Whatever the case, an algal-removal strategy should be designed to minimize shear and cell breakup.

7.5 FINAL THOUGHTS

This dissertation is anticipatory. The problem it studies is only currently applicable to a few people around the world, but as seawater desalination increases and as algal blooms are expected to become more prevalent due to climate change, the problem will need to be addressed. As engineers move forward to design future desalination treatment schemes it will be important to realize that pretreatment membranes can be severely affected by an algal bloom. It will be advantageous to design an algal removal strategy ahead of the low-pressure membranes and any such strategy will need to be capable of removing not only the algal cells but also their AOM and bacteria, since these are more detrimental to the filtration process. AOM passing through pretreatment and reaching the RO elements will likely not be observed to cause significant flux decline in the system, but AOM will adsorb and could exacerbate biofouling.

In planning for and testing different algal removal techniques, bench-scale testing and membrane autopsy can be employed. Testing protocols developed here will help investigators distinguish fouling effects from other system variables like concentration polarization. Autopsy methods presented here will help to examine fouling behavior to make accurate determination of the best pretreatment techniques and operating conditions. These tools and the knowledge gained here have the potential to enable sustainable application of seawater desalination even in the event of algal blooms.

REFERENCES

Ahn, W. Y., A. G. Kalinichev and M. M. Clark (2008). "Effects of background cations on the fouling of polyethersulfone membranes by natural organic matter: Experimental and molecular modeling study." Journal of Membrane Science **309**(1-2): 128-140.

Allgeier, S. C. and R. S. Summers (1995). "Evaluating NF for DBP Control with the RBSMT." Journal American Water Works Association **87**(3): 87-99.

Aluwihare, L. I., D. J. Repeta and R. F. Chen (1997). "A major biopolymeric component to dissolved organic carbon in surface sea water." Nature **387**(6629): 166-169.

Andersen, R. A. (2005). Algal culturing techniques. Burlington, Mass., Elsevier/Academic Press.

Asatekin, A., A. Menniti, S. T. Kang, M. Elimelech, E. Morgenroth and A. M. Mayes (2006). "Antifouling nanofiltration membranes for membrane bioreactors from self-assembling graft copolymers." Journal of Membrane Science **285**(1-2): 81-89.

B. R. Robertson, D. K. B. (1989). "Characterizing aquatic bacteria according to population, cell size, and apparent DNA content by flow cytometry." Cytometry **10**(1): 70-76.

Bhattacharyya, D., S. L. Back, R. I. Kermode and M. C. Roco (1990). "Prediction of Concentration Polarization and Flux Behavior in Reverse-Osmosis by Numerical-Analysis." Journal of Membrane Science **48**(2-3): 231-262.

Blanpain, P. and M. Lalande (1997). "Investigation of fouling mechanisms governing permeate flux in the crossflow microfiltration of beer." Filtration & Separation **34**(10): 1065-1069.

Boerlage, S. F. E., M. Kennedy, M. P. Aniye and J. C. Schippers (2003). "Applications of the MFI-UF to measure and predict particulate fouling in RO systems." Journal of Membrane Science **220**(1-2): 97-116.

Bonnélye, V., L. Guey and J. Del Castillo (2008). "UF/MF as RO pre-treatment: the real benefit." Desalination **222**(1-3): 59-65.

Boudreau, B. P. (1996). "The diffusive tortuosity of fine-grained unlithified sediments." Geochimica et Cosmochimica Acta **60**(16): 3139-3142.

Braghetta, A., F. A. DiGiano and W. P. Ball (1998). "NOM accumulation at NF membrane surface: Impact of chemistry and shear." Journal of Environmental Engineering **124**(11): 1087-1097.

Brehant, A., V. Bonnelye and M. Perez (2003). "Assessment of ultrafiltration as a pretreatment of reverse osmosis membranes for surface seawater desalination." Water Science and Technology: Water Supply **3**(5-6): 437-445.

Bullman, V. and K. R. Roberts (1986). "Structure of the flagellar apparatus in *Heterocapsa pygmaea* (Pyrrophyta)." Phycologia **25**(4): 558-571.

Cheryan, M. (1998). Ultrafiltration and Microfiltration Handbook. Lancaster, Pennsylvania, Technomic.

Chong, T. H., F. S. Wong and A. G. Fane (2007). "Enhanced concentration polarization by unstirred fouling layers in reverse osmosis: Detection by sodium chloride tracer response technique." Journal of Membrane Science **287**(2): 198-210.

Clark, M. M. (1988). "Drop breakup in a turbulent flow--II. Experiments in a small mixing vessel." **43**(3): 681-692.

Cloern, J. E., T. S. Schraga, C. B. Lopez, N. Knowles, R. G. Labiosa and R. Dugdale (2005). "Climate anomalies generate an exceptional dinoflagellate bloom in San Francisco Bay." Geophysical Research Letters **32**(14).

Crittenden, J. C., R. R. Trussell, D. W. Hand, K. J. Howe and G. Tchobanoglous (2005). Chapter 12: Membrane Filtration. Water Treatment Principles and Design
John Wiley & Sons, Inc.**:** 955-1034.

Da Costa, A. R., A. G. Fane and D. E. Wiley (1994). "Spacer characterization and pressure drop modelling in spacer-filled channels for ultrafiltration." Journal of Membrane Science **87**(1-2): 79-98.

DiGiano, F. A., S. Arweiler and J. A. Riddick (2000). "Alternative tests for evaluating NF fouling." Journal American Water Works Association **92**(2): 103-115.

Drioli, E., F. Lagana, A. Criscuoli and G. Barbieri (1999). "Integrated membrane operations in desalination processes." Desalination **122**(2): 141-145.

Ducoste, J. J. and M. M. Clark (1998). "The Influence of Tank Size and Impeller Geometry on Turbulent Flocculation: I. Experimental." Environmental Engineering Science **15**(3): 215-224.

Duranceau, S. J., Ed. (2001). Membrane Practices for Water Treatment. AWWA Trends in Water Series. Denver, American Water Works Association.

Edzwald, J. R. (1993). "Algae, bubbles, coagulants, and dissolved air flotation." Water Science and Technology **27**(10): 67-81.

Elimelech, M., X. Zhu, A. E. Childress and S. Hong (1997). "Role of membrane surface morphology in colloidal fouling of cellulose acetate and composite aromatic polyamide reverse osmosis membranes." Journal of Membrane Science **127**(1): 101-109.

Escobar, I. C., E. M. Hoek, C. J. Gabelich, F. A. DiGiano, Y. A. Le Gouellec, P. Berube, K. J. Howe, J. Allen, K. Z. Atasi, M. M. Benjamin, P. J. Brandhuber, J. Brant, Y. J. Chang, M. Chapman, A. Childress, W. J. Conlon, T. H. Cooke, I. A. Crossley, G. F. Crozes, P. M. Huck, S. N. Kommineni, J. G. Jacangelo, A. A. Karimi, J. H. Kim, D. F. Lawler, Q. L. Li, L. C. Schideman, S. Sethi, J. E. Tobiason, T. Tseng, S. Veerapanemi and A. K. Zander (2005). "Committee Report: Recent advances and research needs in membrane fouling." Journal American Water Works Association **97**(8): 79-89.

Follows, M., P. J. Hetherington, P. Dunnill and M. D. Lilly (1971). "Release of enzymes from bakers' yeast by disruption in an industrial homogenizer." Biotechnology and Bioengineering **13**(4): 549-560.

Ghayeni, S. B. S., P. J. Beatson, R. P. Schneider and A. G. Fane (1998). "Adhesion of waste water bacteria to reverse osmosis membranes." Journal of Membrane Science **138**(1): 29-42.

Glucina, K., A. Alvarez and J. M. Laine (2000). "Assessment of an integrated membrane system for surface water treatment." Desalination **132**(1-3): 73-82.

Grasshoff, K., M. Ehrhardt and K. Kremling (1983). Methods of Seawater Analysis. Weinheim, Verlag Chemie GmbH.

Harrison, C. J., Y. A. Le Gouellec, R. C. Cheng and A. E. Childress (2007). "Bench-scale testing of nanofiltration for seawater desalination." Journal of Environmental Engineering-Asce **133**(11): 1004-1014.

Heil, C. A., P. M. Glibert and C. L. Fan (2005). "Prorocentrum minimum (Pavillard) Schiller - A review of a harmful algal bloom species of growing worldwide importance." Harmful Algae **4**(3): 449-470.

Her, N., G. Amy, H. R. Park and M. Song (2004). "Characterizing algogenic organic matter (AOM) and evaluating associated NF membrane fouling." Water Research **38**(6): 1427-1438.

Hermia, J. (1982). "Constant Pressure Blocking Filtration Laws - Application to Power-Law Non-Newtonian Fluids." Transactions of the Institution of Chemical Engineers **60**(3): 183-187.

Herzberg, M. and M. Elimelech (2007). "Biofouling of reverse osmosis membranes: Role of biofilm-enhanced osmotic pressure." Journal of Membrane Science **295**(1-2): 11-20.

Himberg, K., A. M. Keijola, L. Hiisvirta, H. Pyysalo and K. Sivonen (1989). "The effect of water treatment processes on the removal of hepatotoxins fromMicrocystis andOscillatoria cyanobacteria: A laboratory study." Water Research **23**(8): 979-984.

Ho, C. C. and A. L. Zydney (2000). "A combined pore blockage and cake filtration model for protein fouling during microfiltration." Journal of Colloid and Interface Science **232**(2): 389-399.

Hodgkiess, T., W. T. Hanbury, G. B. Law and T. Y. Al-Ghasham (2001). "Effect of hydrocarbon contaminants on the performance of RO membranes." Desalination **138**(1-3): 283-289.

Hoek, E. M. V. and M. Elimelech (2003). "Cake-Enhanced Concentration Polarization: A New Fouling Mechanism for Salt-Rejecting Membranes." Environmental Science and Technology **37**(24): 5581-5588.

Hoek, E. M. V., A. S. Kim and M. Elimelech (2002). "Influence of crossflow membrane filter geometry and shear rate on colloidal fouling in reverse osmosis and nanofiltration separations." **19**(6): 357-372.

Howe, K. J. and M. M. Clark (2002). "Fouling of microfiltration and ultrafiltration membranes by natural waters." Environmental Science & Technology **36**(16): 3571-3576.

Howe, K. J., K. P. Ishida and M. M. Clark (2002). "Use of ATR/FTIR spectrometry to study fouling of microfiltration membranes by natural waters." Desalination **147**(1-3): 251-255.

Howe, K. J., A. Marwah, K.-P. Chiu and S. S. Adham (2007). "Effect of membrane configuration on bench-scale MF and UF fouling experiments." Water Research **41**(17): 3842-3849.

Howe, K. J., A. Marwah, K. P. Chiu and S. S. Adham (2006). "Effect of coagulation on the size of MF and UF membrane foulants." Environmental Science & Technology **40**(24): 7908-7913.

Hwang, K. J. and T. T. Lin (2002). "Effect of morphology of polymeric membrane on the performance of cross-flow microfiltration." Journal of Membrane Science **199**(1-2): 41-52.

Hyung, H. and J. H. Kim (2006). "A mechanistic study on boron rejection by sea water reverse osmosis membranes." Journal of Membrane Science **286**(1-2): 269-278.

Ishida, K. P. (2006). Email concerning red tide fouling of an integrated membrane system. D. A. Ladner. Urbana, IL.

Jaouen, P., L. Vandanjon and F. Quéméneur (1999). "The shear stress of microalgal cell suspensions (Tetraselmis suecica) in tangential flow filtration systems: the role of pumps." Bioresource Technology **68**(2): 149-154.

Jarusutthirak, C. and G. Amy (2006). "Role of soluble microbial products (SMP) in membrane fouling and flux decline." Environmental Science and Technology **40**(3): 969-974.

Jenkins, D., L. L. Medsker and J. F. Thomas (1967). "Odorous compounds in natural waters. Some sulfur compounds associated with blue-green algae." Environ. Sci. Technol. **1**(9): 731-735.

Johnsen, G., B. B. Prezelin and R. V. M. Jovine (1997). "Fluorescence excitation spectra and light utilization in two red tide dinoflagellates." Limnology and Oceanography **42**(5): 1166-1177.

Joshi, J. B., C. B. Elias and M. S. Patole (1996). "Role of hydrodynamic shear in the cultivation of animal, plant and microbial cells." The Chemical Engineering Journal and the Biochemical Engineering Journal **62**(2): 121-141.

Jovine, R. V. M., G. Johnsen and B. B. Prezelin (1995). "Isolation of membrane bound light-harvesting-complexes from the dinoflagellates *Heterocapsa pygmaea* and *Prorocentrum minimum*." Photosynthesis Research **44**(1-2): 127-138.

Jovine, R. V. M., E. L. Triplett, N. B. Nelson and B. B. Prezelin (1992). "Quantification of chromophore pigments, apoprotein abundance and isolectric variants of Peridinin-Chlorophyll *a*-Protein complexes (PCPs) in the dinoflagellate *Heterocapsa pygmaea* grown under variable light conditions." Plant and Cell Physiology **33**(6): 733-741.

Jucker, C. and M. M. Clark (1994). "Adsorption of aquatic humic substances on hydrophobic ultrafiltration membranes." Journal of Membrane Science **97**: 37-52.

Kahru, M. and B. G. Mitchell (1998). "Spectral reflectance and absorption of a massive red tide off southern California." Journal of Geophysical Research-Oceans **103**(C10): 21601-21609.

Kamp, P. C., J. C. Kruithof and H. C. Folmer (2000). "UF/RO treatment plant Heemskerk: from challenge to full scale application." Desalination **131**(1-3): 27-35.

Karbstein, H. and H. Schubert (1995). "Developments in the continuous mechanical production of oil-in-water macro-emulsions." Chemical Engineering and Processing **34**(3): 205-211.

Kellogg (1971). Saline water conversion engineering data book. Washington, U.S. Dept. of the Interior.

Kim, A. S. and H. Chen (2006). "Diffusive tortuosity factor of solid and soft cake layers: A random walk simulation approach." Journal of Membrane Science **279**(1-2): 129-139.

Kim, A. S., H. Chen and R. Yuan (2006). "EPS biofouling in membrane filtration: An analytic modeling study." Journal of Colloid and Interface Science **303**(1): 243-249.

Kim, K. J., A. G. Fane, M. Nystrom and A. Pihlajamaki (1997). "Chemical and electrical characterization of virgin and protein-fouled polycarbonate track-etched membranes by FTIR and streaming-potential measurements." Journal of Membrane Science **134**(2): 199-208.

Kim, S. and E. M. V. Hoek (2005). "Modeling concentration polarization in reverse osmosis processes." Desalination **186**(1-3): 111-128.

Kim, S. H., S. H. Lee, J. S. Yoon, S. Y. Moon and C. H. Yoon (2007). "Pilot plant demonstration of energy reduction for RO seawater desalination through a recovery increase." Desalination **203**(1-3): 153-159.

Kim, S. H. and J. S. Yoon (2005). "Optimization of microfiltration for seawater suffering from red-tide contamination." Desalination **182**(1-3): 315-321.

Kirk, J. T. O. (1994). Light and photosynthesis in aquatic ecosystems. New York, Cambridge University Press.

Kirkpatrick, B., L. E. Fleming, L. C. Backer, J. A. Bean, R. Tamer, G. Kirkpatrick, T. Kane, A. Wanner, D. Dalpra, A. Reich and D. G. Baden (2006). "Environmental exposures to Florida red tides: Effects on emergency room respiratory diagnoses admissions." Harmful Algae **5**(5): 526-533.

Kirkpatrick, B., L. E. Fleming, D. Squicciarini, L. C. Backer, R. Clark, W. Abraham, J. Benson, Y. S. Cheng, D. Johnson, R. Pierce, J. Zaias, G. D. Bossart and D. G. Baden (2004). "Literature review of Florida red tide: implications for human health effects." Harmful Algae **3**(2): 99-115.

Koh, M., M. A. Clark and K. J. Howe (2005). "Filtration of lake natural organic matter: Adsorption capacity of a polypropylene microfilter." Journal of Membrane Science **256**(1-2): 169-175.

Koseoglu, H., N. Kabay, M. Ynksel and M. Kitis (2008). "The removal of boron from model solutions and seawater using reverse osmosis membranes." Desalination **223**(1-3): 126-133.

Kumar, M., S. Adham, J. Decarolis and W. Pearce (2007). "Comparative seawater RO pretreatment evaluation using bench- and pilot-scale testing." Journal American Water Works Association **99**(9): 168-181.

Kumar, M., S. S. Adham and W. R. Pearce (2006). "Investigation of seawater reverse osmosis fouling and its relationship to pretreatment type." Environmental Science & Technology **40**(6): 2037-2044.

Kwon, B., N. Park and J. Cho (2005). "Effect of algae on fouling and efficiency of UF membranes." Desalination **179**(1-3): 203-214.

Ladner, D. A., B. W. Lee and M. M. Clark (2007). "Laser scanning cytometry for enumeration of fluorescent microspheres." Journal / American Water Works Association **99**(3): 110-117.

Laine, J. M., J. P. Hagstrom, M. M. Clark and J. Mallevialle (1989). "Effects of Ultrafiltration Membrane-Composition." Journal American Water Works Association **81**(11): 61-67.

Lechuga-Deveze, C. H. and M. D. Morquecho-Escamilla (1998). "Early spring potentially harmful phytoplankton in Bahia Concepcion, Gulf of California." Bulletin of Marine Science **63**(3): 503-512.

Lee, N., G. Amy, J. P. Croue and H. Buisson (2004). "Identification and understanding of fouling in low-pressure membrane (MF/UF) filtration by natural organic matter (NOM)." Water Research **38**(20): 4511-4523.

Lee, S., J. Cho and M. Elimelech (2005). "A novel method for investigating the influence of feed water recovery on colloidal and NOM fouling of RO and NF membranes." Environmental Engineering Science **22**(4): 496-509.

Lee, Y. and M. M. Clark (1998). "Modeling of flux decline during crossflow ultrafiltration of colloidal suspensions." Journal of Membrane Science **149**(2): 181-202.

Li, Q. and M. Elimelech (2006). "Synergistic effects in combined fouling of a loose nanofiltration membrane by colloidal materials and natural organic matter." Journal of Membrane Science **278**(1-2): 72-82.

Li, Q. L. and M. Elimelech (2006). "Synergistic effects in combined fouling of a loose nanofiltration membrane by colloidal materials and natural organic matter." Journal of Membrane Science **278**(1-2): 72-82.

Li, Q. L., Z. H. Xu and I. Pinnau (2007). "Fouling of reverse osmosis membranes by biopolymers in wastewater secondary effluent: Role of membrane surface properties and initial permeate flux." Journal of Membrane Science **290**(1-2): 173-181.

Loeblich, A. R., III, R. J. Schmidt and J. L. Sherley (1981). "Scanning electron microscopy of Heterocapsa pygmaea sp. nov., and evidence for polyploidy as a speciation mechanism in dinoflagellates." J. Plankton Res. **3**(1): 67-79.

Louie, J. S., I. Pinnau, I. Ciobanu, K. P. Ishida, A. Ng and M. Reinhard (2006). "Effects of polyether-polyamide block copolymer coating on performance and fouling of reverse osmosis membranes." Journal of Membrane Science **280**(1-2): 762-770.

Lyster, E. and Y. Cohen (2007). "Numerical study of concentration polarization in a rectangular reverse osmosis membrane channel: Permeate flux variation and hydrodynamic end effects." Journal of Membrane Science **303**(1-2): 140-153.

Ma, S. W. and L. F. Song (2006). "Numerical study on permeate flux enhancement by spacers in a crossflow reverse osmosis channel." Journal of Membrane Science **284**(1-2): 102-109.

Mariñas, B. J. and R. I. Urama (1996). "Modeling concentration-polarization in reverse osmosis spiral-wound elements." Journal of Environmental Engineering **122**(4): 292-298.

Marquis, E. and C. G. Trick (2008). Preliminary Report--Harmful Algal Bloom in Dibba/Fujairah coastal waters. Tokyo, United Nations University.

Maso, M. and E. Garces (2006). "Harmful microalgae blooms (HAB); problematic and conditions that induce them." Marine Pollution Bulletin **53**(10-12): 620-630.

Mayo, D. W., F. A. Miller and R. W. Hannah (2004). Course notes on the interpretation of infrared and Raman spectra, Wiley-Interscience Hoboken, NJ.

Merten, U. (1966). Desalination by Reverse Osmosis. Cambridge, Massachusetts Institute of Technology Press.

Momtaz, M., J. L. Dewez and J. Marchand-Brynaert (2005). "Chemical reactivity assay and surface characterization of a poly(vinylidene fluoride) microfiltration membrane ("Durapore DVPP")." Journal of Membrane Science **250**(1-2): 29-37.

Moore, E. K., M. Hoare and P. Dunnill (1990). "Disruption of baker's yeast in a high-pressure homogenizer: New evidence on mechanism
" Enzyme and Microbial Technology **12**(10): 764-770.

Moorthi, S. D., P. D. Countway, B. A. Stauffer and D. A. Caron (2006). "Use of quantitative real-time PCR to investigate the dynamics of the red tide dinoflagellate Lingulodinium polyedrum." Microbial Ecology **52**(1): 136-150.

Mulder, M. (1991). Basic Principles of Membrane Technology. Boston, Kluwer Academic Publishers.

Myklestad, S. M., E. Skanoy and S. Hestmann (1997). "A sensitive and rapid method for analysis of dissolved mono- and polysaccharides in seawater." Marine Chemistry **56**(3-4): 279-286.

Nelson, W. H. (1991). Modern techniques for rapid microbiological analysis, VCH.

Ng, H. Y. and M. Elimelech (2004). "Influence of colloidal fouling on rejection of trace organic contaminants by reverse osmosis." Journal of Membrane Science **244**(1-2): 215-226.

Petry, M., M. A. Sanz, C. Langlais, V. Bonnelye, J. P. Durand, D. Guevara, W. M. Nardes and C. H. Saemi (2007). "The El Coloso (Chile) reverse osmosis plant." Desalination **203**(1-3): 141-152.

Pierce, R. H., M. S. Henry, C. J. Higham, P. Blum, M. R. Sengco and D. M. Anderson (2004). "Removal of harmful algal cells (Karenia brevis) and toxins from seawater culture by clay flocculation." Harmful Algae **3**(2): 141-148.

Poisson, A. (1980). "Conductivity/salinity/temperature relationship of diluted and concentrated standard seawater." **5**(1): 41-50.

Rennecker, J. L., J. H. Kim, B. Corona-Vasquez and B. J. Mariñas (2001). "Role of disinfectant concentration and pH in the inactivation kinetics of Cryptosporidium parvum oocysts with ozone and monochloramine." Environmental Science & Technology **35**(13): 2752-2757.

Roberts, K., P. Timpano and A. Montegut (1987). "The apical pore fibrous complex: a new cytological feature of some dinoglagellates." Protoplasma **137**(1): 65-69.

Rosenberger, S., C. Laabs, B. Lesjean, R. Gnirss, G. Amy, M. Jekel and J. C. Schrotter (2006). "Impact of colloidal and soluble organic material on membrane performance in membrane bioreactors for municipal wastewater treatment." Water Research **40**(4): 710-720.

Sambidge, A. (2008) "'Red tide' forces desalination plant closure." ArabianBusiness.com.

Schafer, A. I., U. Schwicker, M. M. Fischer, A. G. Fane and T. D. Waite (2000). "Microfiltration of colloids and natural organic matter." Journal of Membrane Science **171**(2): 151-172.

Schock, G. and A. Miquel (1987). "Mass-Transfer and Pressure Loss in Spiral Wound Modules." Desalination **64**: 339-352.

Schultz, S., G. Wagner, K. Urban and J. Ulrich (2004). "High-pressure homogenization as a process for emulsion formation." Chemical Engineering & Technology **27**(4): 361-368.

Sengco, M. R. and D. M. Anderson (2004). "Controlling harmful algal blooms through clay Flocculation." Journal of Eukaryotic Microbiology **51**(2): 169-172.

Sengco, M. R., A. S. Li, K. Tugend, D. Kulis and D. M. Anderson (2001). "Removal of red- and brown-tide cells using clay flocculation. I. Laboratory culture experiments with Gymnodinium breve and Aureococcus anophagefferens." Marine Ecology-Progress Series **210**: 41-53.

Sherwood, T. K., P. L. T. Brian, R. E. Fisher and L. Dresner (1965). "Salt concentration at phase boundaries in desalination by reverse osmosis." Industrial and Engineering Chemistry Fundamentals **4**(2): 113-118.

Shimizu, Y., K. Matsushita and A. Watanabe (1994). "Influence of shear breakage of microbial cells on cross-flow microfiltration flux." Journal of Fermentation and Bioengineering **78**(2): 170-174.

Smith, S. W. (1999). The Scientist and Engineer's Guide to Digital Signal Processing. San Diego, California Technical Publishing.

Stang, M., H. Schuchmann and H. Schubert (2001). "Emulsification in High-Pressure Homogenizers." Engineering in Life Sciences **1**(4): 151-157.

Steuck, M. J. (1984). Porous membrane having hydrophilic surface and process. United States of America, Millipore Corporation.

Stoughton, R. W. and M. H. Lietzke (1965). "Calculation of Some Thermodynamic Properties of Sea Salt Solutions at Elevated Temperatures from Data on NaCI Solutions." Journal of Chemical & Engineering Data **10**(3): 254-260.

Subramani, A., S. Kim and E. M. V. Hoek (2006). "Pressure, flow, and concentration profiles in open and spacer-filled membrane channels." Journal of Membrane Science **277**(1-2): 7-17.

Sutzkover, I., D. Hasson and R. Semiat (2000). "Simple technique for measuring the concentration polarization level in a reverse osmosis system." Desalination **131**(1-3): 117-127.

Tarabara, V. V. and M. R. Wiesner (2003). "Computational fluid dynamics modeling of the flow in a laboratory membrane filtration cell operated at low recoveries." **58**(1): 239-246.

Teng, C. K., M. N. A. Hawlader and A. Malek (2003). "An experiment with different pretreatment methods." Desalination **156**(1-3): 51-58.

Thiebaud, M., E. Dumay, L. Picart, J. P. Guiraud and J. C. Cheftel (2003). "High-pressure homogenisation of raw bovine milk. Effects on fat globule size distribution and microbial inactivation." International Dairy Journal **13**(6): 427-439.

Tocchetti, E. V., R. L. Flower and J. V. Lloyd (2001). "Assessment of In Vitro-Generated Platelet Microparticles Using a Modified Flow Cytometric Strategy." Thrombosis Research **103**(1): 47-55.

Trigueros, J. M. and E. Orive (2000). "Tidally driven distribution of phytoplankton blooms in a shallow, macrotidal estuary." Journal of Plankton Research **22**(5): 969-986.

Vandanjon, L., Rossignol, N., Jaouen, P., Robert, J. M., Quéméneur, F. (1999). "Effects of shear on two microalgae species. Contribution of pumps and valves in tangential flow filtration systems." Biotechnology and Bioengineering **63**(1): 1-9.

Vrijenhoek, E. M., S. Hong and M. Elimelech (2001). "Influence of membrane surface properties on initial rate of colloidal fouling of reverse osmosis and nanofiltration membranes." Journal of Membrane Science **188**(1): 115-128.

Wang, J., J. Guan, S. R. Santiwong and T. D. Waite (2008). "Characterization of floc size and structure under different monomer and polymer coagulants on microfiltration membrane fouling." Journal of Membrane Science **321**(2): 132-138.

Watson, H. E. (1908). "A Note on the Variation of the Rate of Disinfection with Change in the Concentration of the Disinfectant." The Journal of Hygiene **8**(4): 536-542.

Whipple, S. J., B. C. Patten and P. G. Verity (2005). "Life cycle of the marine alga Phaeocystis: A conceptual model to summarize literature and guide research." **57**(1-2): 83-110.

Wilf, M. and K. Klinko (1998). "Effective new pretreatment for seawater reverse osmosis systems." Desalination **117**(1-3): 323-331.

Ye, Y., P. Le Clech, V. Chen, A. G. Fane and B. Jefferson (2005). "Fouling mechanisms of alginate solutions as model extracellular polymeric substances." Desalination **175**(1): 7-20.

Yiantsios, S. G. and A. J. Karabelas (2003). "An assessment of the Silt Density Index based on RO membrane colloidal fouling experiments with iron oxide particles." Desalination **151**(3): 229-238.

Zhu, H. and M. Nystrom (1998). "Cleaning results characterized by flux, streaming potential and FTIR measurements." **138**(2-3): 309-321.

Zhu, X. and M. Elimelech (1997). "Colloidal fouling of reverse osmosis membranes: Measurements and fouling mechanisms." Environmental Science and Technology **31**(12): 3654-3662.

AUTHOR’S BIOGRAPHY

David Allen Ladner was born in Albuquerque, New Mexico, on November 13, 1977. He graduated from the New Mexico Institute of Mining and Technology (New Mexico Tech) in 2003 with a Bachelor’s degree in Environmental Engineering. He proceeded directly to graduate school and received his Master’s degree from the University of Illinois at Urbana-Champaign in 2005. After finishing his PhD, David will serve as a Postdoctoral Research Associate at Arizona State University. David married Miriam Nibley in 2005 and they have one child, Isaac Kenneth Ladner, born in 2008.